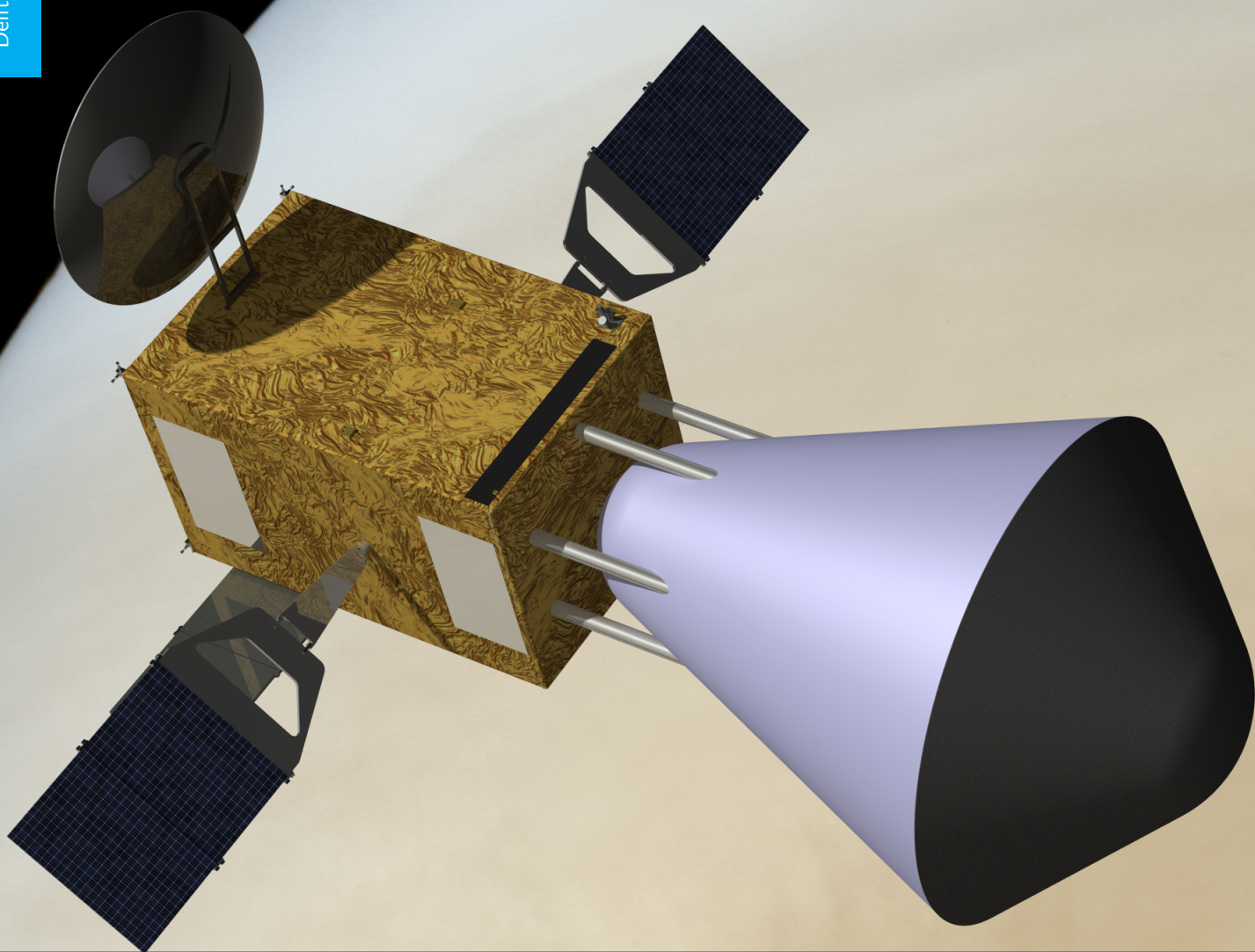


# Final Report

Design Synthesis Exercise  
Finding Venusian Volcanoes

AE3200: Group 14

Delft University of Technology





# FINAL REPORT

DESIGN SYNTHESIS EXERCISE

FINDING VENUSIAN VOLCANOES

PROJECT MATRYOSHKA

BY

<b>MATHIJS DEN BOER</b>	(4303768)
<b>ALEXANDER DE BRUIN</b>	(4209001)
<b>CHAGGAI GANANI</b>	(4293126)
<b>AKHIL GUNESSEE</b>	(4204662)
<b>STEFAN HARMSSEN</b>	(4277872)
<b>MAX HENGER</b>	(4091221)
<b>JEFFREY HUANG</b>	(4234677)
<b>THOMAS KROES</b>	(4267044)
<b>YUYANG LUAN</b>	(4233522)
<b>JULIUS WEINMILLER</b>	(4277597)

JUNE 29, 2016

PRINCIPAL TUTOR:	DR. D.M. STAM	DELFT UNIVERSITY OF TECHNOLOGY
COACHES:	DR. S. TEIXEIRA DE FREITAS	DELFT UNIVERSITY OF TECHNOLOGY
	MSc. Z.HONG	DELFT UNIVERSITY OF TECHNOLOGY

# EXECUTIVE SUMMARY

This report details the design of a mission aimed to find and analyse active Venusian volcanoes, if they exist. These volcanoes are interesting because active volcanism would significantly contribute to the understanding of the Venusian atmosphere, its extreme climate and geological processes. This knowledge would in turn help us understand Earth better. The design is based on the concept selected previously in the Midterm report and consists of five vehicles: a spacecraft, an aeroshell, an aircraft and two landers.

The spacecraft with aeroshell will be launched into a Hohmann transfer orbit to Venus in 2023. Upon arrival, the satellite will map the surface, and find the most promising region for volcanic activity. It will then deploy the aeroshell containing the aircraft and landers. The satellite then changes its orbit to one that allows for it to act as a relay between the Venusian vehicles and Earth. After entry and having slowed down sufficiently to deploy a parachute, the first lander will be dropped. This lander will act as a reference for the lander inside the aircraft. Next, the aircraft is deployed after which it will start following flight tracks that allow for it to stay in the Sunlight. These tracks are designed by taking into consideration the power systems, thermal system and propulsion system, and then optimising such that the electronics do not overheat and that the battery size is reasonable. While flying, the aircraft will take measurements to locate volcanoes. Once a very promising location is found, the aircraft will deploy the second lander from an altitude of about 32 km. This lander will then descend further down and land on the surface where it will perform measurements. Combining the measurements of all vehicles it is expected that the mission can also complete a number of secondary objectives to further improve the knowledge of Venus.

Both landers have the same design with pressurised double shell structure that allows for reducing its weight, compared to past Venusian landers. They have a thermal system that provides each with a surface lifetime of approximately one hour. For these measurements it will use a multispectral camera and laser induced breakdown spectrometer. The lander will communicate directly with the spacecraft, so it should be in range when the landers are deployed. The weight of the lander is 93.22 kg, and is expected to cost about €45.8 million.

The aircraft consists of a body that contains the lander, batteries, and scientific equipment, which is blended with the main wing with a 40 m<sup>2</sup> area and a wingspan of about 16 m. For stabilisation, it has a horizontal stabiliser of 14 m<sup>2</sup> and two small vertical stabilisers of 3 m<sup>2</sup> each that connect the horizontal stabiliser to two booms. These booms and the main wing each have a folding mechanism that allows the aircraft to fit inside the 4.6 m diameter aeroshell which is compatible with current launchers. The aircraft will have a camera, Venus Emissivity Mapper and Spectropolarimeter as its main scientific equipment. The aircraft weight is 729 kg and is expected to cost about €158.5 million.

The spacecraft will serve two phases, a mapping phase using a Synthetic Aperture Radar, and relay phase. It also has a Venus Emissivity Mapper and Doppler Wind Lidar to take other measurements for secondary objectives during both phases. The aeroshell will be connected to the spacecraft by six struts which can be cut by pyrotechnic fasteners when the aeroshell has to be released. During transfer and mapping, the spacecraft will also provide the vehicles in the aeroshell with power. To perform the mission the spacecraft has 2910 m/s of  $\Delta V$ , and combined with the launch vehicle adapter and aeroshell, a weight of 5616.1 kg. The spacecraft cost is about €288.5 million.

The vehicles will also require a number of other steps, such as verification and validation, further research, production and launch. These will all require additional resources in the form of employees, materials, etc. It is found that all these steps will cost €461.4 million, making the design and production costs total €999.9 million. This means that the requirement set by the client has not been exceeded. Also, for launch and operations, an additional €164.35 million will be required. This also includes the ground support and a contract with NASA's Deep Space Network to have communications with the spacecraft.

The complete mission design presented has successfully met all of the requirements that were set by the client, and if funded, shall provide much more information about Venus to the scientific community.

# CONTENTS

<b>Executive summary</b>	<b>i</b>
<b>List of Figures</b>	<b>iv</b>
<b>List of Tables</b>	<b>vii</b>
<b>Nomenclature</b>	<b>ix</b>
<b>List of Symbols</b>	<b>x</b>
<b>1 Introduction</b>	<b>1</b>
<b>2 Mission overview</b>	<b>2</b>
2.1 Mission goals . . . . .	2
2.2 Venusian Atmosphere . . . . .	4
2.3 Venusian Geology . . . . .	5
2.4 Design description . . . . .	6
2.5 Functional analysis . . . . .	7
<b>3 Astrodynamics</b>	<b>12</b>
3.1 Planetary and orbital characteristics . . . . .	12
3.2 Orbital transfer . . . . .	13
3.3 Orbit trade-off . . . . .	16
3.4 Coverage . . . . .	24
3.5 Visiting frequency . . . . .	26
3.6 $\Delta V$ Budget . . . . .	26
3.7 Launcher selection . . . . .	27
<b>4 Lander</b>	<b>28</b>
4.1 Scientific payload . . . . .	28
4.2 Layout . . . . .	28
4.3 Thermal control . . . . .	31
4.4 Power system . . . . .	31
4.5 Communications . . . . .	31
4.6 Block diagrams . . . . .	33
4.7 Budgets . . . . .	35
<b>5 Aircraft</b>	<b>37</b>
5.1 Scientific payload . . . . .	37
5.2 Mission Profile . . . . .	38
5.3 Aerodynamics . . . . .	52
5.4 Propulsion . . . . .	54
5.5 Materials . . . . .	56
5.6 Structure . . . . .	60
5.7 Stability and control . . . . .	73
5.8 Thermal control . . . . .	81
5.9 Communications . . . . .	82
5.10 Aircraft block diagrams . . . . .	83
5.11 Budgets . . . . .	85
<b>6 Entry</b>	<b>87</b>
6.1 Aeroshell design . . . . .	87
6.2 Entry simulation . . . . .	88
6.3 Deployment sequence . . . . .	89

<b>7</b>	<b>Spacecraft</b>	<b>92</b>
7.1	Payload . . . . .	92
7.2	Configuration . . . . .	92
7.3	Structure . . . . .	93
7.4	Thermal . . . . .	95
7.5	Propulsion . . . . .	95
7.6	Communications . . . . .	96
7.7	ADCS . . . . .	98
7.8	EPS . . . . .	99
7.9	Aeroshell deployment . . . . .	100
7.10	Budgets . . . . .	100
7.11	Block diagrams . . . . .	100
<b>8</b>	<b>Sensitivity</b>	<b>105</b>
8.1	Lander . . . . .	105
8.2	Spacecraft . . . . .	105
<b>9</b>	<b>Operations and Logistics</b>	<b>106</b>
9.1	Ground support . . . . .	106
9.2	Communication . . . . .	106
9.3	Data processing . . . . .	107
9.4	Logistic flow block diagram . . . . .	109
<b>10</b>	<b>Risk analysis</b>	<b>110</b>
10.1	Risk analysis method . . . . .	110
10.2	Initial risk analysis . . . . .	110
10.3	Risk mitigation . . . . .	113
<b>11</b>	<b>RAMS</b>	<b>115</b>
11.1	Reliability . . . . .	115
11.2	Availability . . . . .	115
11.3	Maintainability . . . . .	116
11.4	Safety . . . . .	116
<b>12</b>	<b>Verification and Validation</b>	<b>117</b>
12.1	General program procedures . . . . .	117
12.2	Program verification and validation . . . . .	118
12.3	System verification . . . . .	120
12.4	System validation . . . . .	122
<b>13</b>	<b>Sustainable Development Strategy</b>	<b>123</b>
<b>14</b>	<b>Project development</b>	<b>125</b>
14.1	Activities . . . . .	125
14.2	Timeline . . . . .	126
14.3	Costs . . . . .	126
<b>15</b>	<b>Compliance matrix</b>	<b>128</b>
<b>16</b>	<b>Follow-up research</b>	<b>130</b>
<b>17</b>	<b>Conclusion</b>	<b>131</b>
	<b>Acknowledgments</b>	<b>132</b>
	<b>Bibliography</b>	<b>133</b>
<b>A</b>	<b>Appendix Source code</b>	<b>136</b>
<b>B</b>	<b>Appendix Work allocation</b>	<b>136</b>

# LIST OF FIGURES

2.1	The temperature, pressure and density of the Venusian atmosphere . . . . .	4
2.2	Variations of zonal wind speed in the Venusian atmosphere . . . . .	4
2.3	Potential hotspot activity . . . . .	6
2.4	Concept of operations . . . . .	6
2.5	Spacecraft functional flow diagram . . . . .	8
2.6	Aircraft and lander functional flow diagram . . . . .	9
2.7	Spacecraft Functional Breakdown part 1 . . . . .	9
2.8	Spacecraft Functional Breakdown part 2 . . . . .	10
2.9	Aircraft Functional Breakdown part 1 . . . . .	10
2.10	Aircraft Functional Breakdown part 2 . . . . .	11
2.11	Lander Functional Breakdown . . . . .	11
3.1	Type II Hohmann transfer of spacecraft using launch window 3 . . . . .	15
3.2	Characteristic energy versus launch dates for window 1 type-II Hohmann transfer . . . . .	16
3.3	Field of view and swath width of Orbiter . . . . .	17
3.4	Orbiter viewing geometry . . . . .	17
3.5	Relief map of Venus . . . . .	19
3.6	Volcano locations . . . . .	19
3.7	Previous landing sites . . . . .	20
3.8	Ground track for circular mapping phase (single orbit) . . . . .	21
3.9	Orbit geometry for half a cycle of circular mapping phase . . . . .	22
3.10	Ground track for elliptical mapping phase (single orbit) . . . . .	22
3.11	Orbit geometry for elliptical mapping phase . . . . .	23
3.12	Orbit geometry for telecommunication phase (single orbit) . . . . .	23
3.13	Ground track of telecommunication relay phase . . . . .	24
3.14	Computational geometry for footprint parameters . . . . .	25
3.15	SAR access area . . . . .	25
3.16	VEM access area . . . . .	25
3.17	Telecom antenna access area . . . . .	25
4.1	Lander . . . . .	29
4.2	The altitude and vertical velocity of the lander over time during the descent . . . . .	32
4.3	The altitude and equipment temperature of the lander over time . . . . .	32
4.4	Lander H/W diagram . . . . .	34
4.5	Lander S/W diagram . . . . .	34
4.6	Lander data handling block diagram . . . . .	35
4.7	Lander electrical block diagram . . . . .	36
5.1	The variation of dynamic pressure $q_\infty$ with inertial speed $V_I$ , altitude $h$ and the atmospheric severity $\zeta$ . From left to right $\zeta = -1.5$ , $\zeta = 0.0$ and $\zeta = 1.5$ . . . . .	38
5.2	Overview of flight forces and geometry during climbing . . . . .	40
5.3	Overview of flight forces and geometry during cruise . . . . .	41
5.4	Overview of flight forces and geometry during diving . . . . .	41
5.5	Results of a numerical climbing efficiency analysis at a maximum propeller power $P_A$ of 32 kW at a latitude $\phi$ of 0°, a solar longitude $\lambda_S$ of 0° and a weather severity factor $\zeta$ of 0.0. Displayed are the climbing efficiency on the left and the vertical velocity on the right. The green lines indicate the optimum ascent path to any given height. . . . .	46
5.6	Maps of the power required for atmospheric severity factors $\zeta$ of, from left to right, $-1.55$ , $0.0$ and $1.8$ . In each plot a contour is drawn in which all flight parameters are within the required bounds for a given available propeller power. . . . .	47

5.7	Example of flight parameters generated by simulating a diving maneuver (on the left) and a climbing maneuver (on the right)	48
5.8	Available upward and downward power produced by solar panels due to available solar flux and considered efficiencies. The sharp corner at 60 km height is there because above that point the influence of the atmosphere is considered negligible.	48
5.9	The flight track parameters as a function of lower segment cruising time $t_l$ in the left two figures and ground track geometry in the right figure.	52
5.10	The variation of the Reynolds number $Re$ and freestream dynamic pressure $q_\infty$ with height $h$ and velocity $V_{I,hor}$ for the atmospheric severity values $\zeta$ of 0 at a solar longitude $\lambda_S$ of $0^\circ$ and a latitude $\phi$ of $0^\circ$	53
5.11	Geometrical parameters associated with the aeroshell and the wing planform	53
5.12	Graphical depiction of the wing planform design	54
5.13	Propeller efficiency	56
5.14	Airfoil polar	56
5.15	FBD: launch vehicle during launch	60
5.16	FBD: wing during launch	60
5.17	Loading and moment diagram of the wing during launch	60
5.18	FBD: Wing loading during cruising, front view	61
5.19	FBD: Wing loading during cruising, top view	61
5.20	Vertical loading and moment diagram of the wing during cruise	61
5.21	Horizontal loading and moment diagram of the wing during cruise	61
5.22	Vertical loading and moment diagram of the wing during ascent	62
5.23	Horizontal loading and moment diagram of the wing during ascent	62
5.24	FBD: Wing loading during climb-out in the descent phase, top view	62
5.25	FBD: Wing loading during climb-out in the descent phase, side view	62
5.26	Vertical loading and moment diagram of the wing during the climb-out of descent phase	62
5.27	Horizontal loading and moment diagram of the wing during the climb-out of descent phase	62
5.28	Loading and moment diagram of the wing during entry. Note that this is identical to that of the launch case.	63
5.29	FBD: Wing loading during turning, front view	63
5.30	FBD: Wing loading during turning, side view	63
5.31	Vertical loading and moment diagram of the wing during turning	63
5.32	Horizontal loading and moment diagram of the wing during turning	63
5.33	FBD Fuselage, F1 and F2 are supported loads, the other forces represent acceleration forces	64
5.34	Fuselage moment and shear load diagram	64
5.35	FBD Fuselage cross section	64
5.36	Configurations, 8 booms to 12 booms	65
5.37	Configurations (continued), 14 booms to 16 booms	66
5.38	The flow chart of the structural design of the wing. Meaningful results of the wingbox dimensions are only generated if the current wingbox characteristic passes three criteria, namely light weight, Tsai-Hill, and lastly, critical buckling.	67
5.39	Tsai-Hill value sensitivity analysis, $t_{spar}$ vs. $t_{skin}$ . The Tsai-Hill value the lower the better.	67
5.40	Tsai-Hill value sensitivity analysis, $A_{stringer}$ vs. $t_{skin}$ . The Tsai-Hill value the lower the better.	67
5.41	Illustration of the ordering of the shear stress and shear low results, taking configuration '4/2' as an example.	68
5.42	Shear stress and flow with 1-spar configuration, the configuration used is '8/1'. The load case used is 'turning'. $t_{skin} = t_{spar} = 2mm, A_{flange} = 150mm^2$	68
5.43	Shear stress and flow with 2-spar configuration, the configuration used is '8/2'. The load case used is 'turning'. $t_{skin} = t_{spar} = 2mm, A_{flange} = 150mm^2$	68
5.44	Bending stress from second cut to tip during climb-out in the descent phase	69
5.45	Shear stress (left) and flow (right) form second cut to tip during climb-out in the descent phase	69
5.46	Bending stress form hinge line to second cut during climb-out in the descent phase	69
5.47	Shear stress (left) and flow (right) form second cut to tip during climb-out in the descent phase	69
5.48	Bending stress form root to hinge line during climb-out in the descent phase	69
5.49	Shear stress (left) and flow (right) form second cut to tip during climb-out in the descent phase	69
5.50	Bending stress form second cut to tip during turning	70

5.51 Shear stress (left) and flow (right) form second cut to tip during turning . . . . .	70
5.52 Bending stress form hinge line to second cut during turning . . . . .	70
5.53 Shear stress (left) and flow (right) form hinge line second cut during turning . . . . .	70
5.54 Bending stress form root to hinge line during turning . . . . .	70
5.55 Shear stress (left) and flow (right) form root to hinge line during turning . . . . .	70
5.56 Shear stress (left) and flow (right) form second cut to tip during entry . . . . .	71
5.57 Shear stress (left) and flow (right) form hinge line second cut during entry . . . . .	71
5.58 Shear stress (left) and flow (right) form root to hinge line during entry . . . . .	71
5.59 Schematic of the wing. Skin of the root torn off for clearance (right) . . . . .	72
5.60 Fuselage moment and shear load diagram . . . . .	72
5.61 First order mass distributing estimation of the aircraft . . . . .	74
5.62 Expected mass against $R_H$ . . . . .	74
5.63 Aircraft scissor plot tail and canard . . . . .	75
5.64 Aircraft scissor plot pure tail . . . . .	75
5.65 Horizontal Tail Configuration . . . . .	76
5.66 Roll time plot . . . . .	76
5.67 Elevator sizing plot example . . . . .	78
5.68 Rudder sizing plot . . . . .	79
5.69 Dynamic response to frontal gust . . . . .	80
5.70 Dynamic response to up gust . . . . .	80
5.71 Dynamic response to side gust . . . . .	81
5.72 Thermal simulation of aircraft . . . . .	82
5.73 Aircraft H/W diagram . . . . .	84
5.74 Aircraft software block diagram . . . . .	84
5.75 Aircraft data handling block diagram . . . . .	85
5.76 Aircraft electrical block diagram . . . . .	86
6.1 Comparison of blunted-cone shapes . . . . .	87
6.2 $C_A$ entry vehicle coefficient vs $\alpha$ . . . . .	89
6.3 $C_N$ entry vehicle coefficient vs $\alpha$ . . . . .	89
6.4 $C_M$ entry vehicle coefficient vs $\alpha$ . . . . .	89
6.5 Entry simulation results . . . . .	90
6.6 Folding of aircraft surfaces . . . . .	91
6.7 Unfolded aircraft, top view . . . . .	91
7.1 Spacecraft configuration . . . . .	93
7.2 Spacecraft configuration . . . . .	94
7.3 Spacecraft hardware diagram . . . . .	102
7.4 Spacecraft software block diagram . . . . .	102
7.5 Spacecraft data handling block diagram . . . . .	103
7.6 Spacecraft electrical block diagram . . . . .	104
9.1 Uplink communication flow diagram . . . . .	107
9.2 Downlink communication flow diagram . . . . .	108
9.3 Data processing . . . . .	108
9.4 Logistic flow block diagram . . . . .	109
14.1 Project Gantt chart . . . . .	126

# LIST OF TABLES

3.1	General features of Venus compared to the Earth and Sun	12
3.2	Orbital characteristics of Venus (J2000)	12
3.3	General interplanetary transfer parameters	13
3.4	General characteristics of fast trajectory transfer	14
3.5	$\Delta V$ characteristics of fast trajectory transfer	14
3.6	Summary of parameters for Hohmann transfer	14
3.7	Previous mission transfer time. Value in bracket represents actual transfer time.	14
3.8	Potential Hohmann transfer launch windows	15
3.9	Specifications for mapping instruments	17
3.10	Maximum possible horizontal distances with respective to elevation angles	18
3.11	Contact time with lander and aircraft	19
3.12	Orbital characteristics of past mission orbiters	21
3.13	Orbital characteristics of mapping and telecommunications phases	21
3.14	Mapping and telecommunication coverage characteristics	26
3.15	Mapping and telecommunication coverage attributes	26
3.16	$\Delta V$ Budget if circular mapping orbit selected	26
3.17	$\Delta V$ Budget if elliptical mapping orbit selected	27
3.18	Launcher specifications	27
4.1	Material properties of the lander	29
4.2	Specifications of spacecraft telemetry system	33
4.3	Linkbudget Lander-Spacecraft	33
4.4	Mass, power, and cost budget of the lander	36
5.1	SAR specifications	37
5.2	Main parameters of the VEM	37
5.3	Specifications of the camera	37
5.4	Aircraft properties determined in the initial feasibility study	47
5.5	OXIS Energy Ultra Light Lithium Sulphur Cells characteristics for 2019	49
5.6	Aircraft battery sizing parameters	50
5.7	Designed flight tracks for a range of latitudes at mean atmospheric weather intensity.	51
5.8	Ranges of Reynolds numbers $Re$ and dynamic pressures $q_\infty$ most commonly experienced by the aircraft during the three powered flight phases	53
5.9	Geometrical parameters associated with the designed wing planform	54
5.10	Specifications of PETI-330 Composite	57
5.11	Lightning prevention: copper mesh weight estimation	58
5.12	CTE values	59
5.13	Variable parameters to experiment with the wingbox	67
5.14	Specification of each section in the wingbox along the span	68
5.15	Specification of each section in the wingbox along the span, extracted from the newest iteration.	72
5.16	Main system mass and their CG with respect to the leading edge	74
5.17	General inputs aileron sizing	75
5.18	Aileron characteristics	77
5.19	Elevator sizing input values	77
5.20	Elevator characteristics	78
5.21	Rudder sizing input values	79
5.22	Rudder characteristics	79
5.23	Aircraft parameters assumed for the simulation	80
5.24	Aircraft longitudinal stability derivatives	80
5.25	Aircraft lateral stability derivatives	81

5.26 Specifications of spacecraft telemetry system . . . . .	83
5.27 Linkbudget Aircraft-Spacecraft . . . . .	83
5.28 Costs for aircraft . . . . .	86
5.29 Aircraft mass and power budgets . . . . .	86
6.1 Initial entry simulation values . . . . .	89
7.1 SAR specifications . . . . .	92
7.2 Specifications of Doppler Wind Lidar . . . . .	92
7.3 Specifications of spacecraft camera . . . . .	93
7.4 Temperatures during different mission phases . . . . .	95
7.5 Tank volume . . . . .	96
7.6 Specifications of spacecraft telemetry system . . . . .	97
7.7 Linkbudget Spacecraft-Ground station . . . . .	98
7.8 parameters solar array sizing . . . . .	99
7.9 Battery specifications . . . . .	100
7.10 Mass budget of the spacecraft . . . . .	101
7.11 Power budget of the spacecraft . . . . .	101
7.12 Cost budget of the spacecraft . . . . .	101
8.1 Sensitivity of the lander design . . . . .	105
8.2 Sensitivity of the spacecraft design . . . . .	105
10.1 The scale of probability . . . . .	110
10.2 The scale of impact of consequences . . . . .	110
10.3 Risk map color descriptions . . . . .	110
10.4 Initial risk map . . . . .	113
10.5 Revised risk map . . . . .	114
11.1 Frequency of spacecraft failures between 1990 and 2008 . . . . .	116
14.1 Monthly costs per engineer . . . . .	126
14.2 Lander and spacecraft costs . . . . .	126
14.3 Launch and DSN contract costs . . . . .	127
14.4 Ground control specialist costs . . . . .	127
14.5 Design and production cost breakdown . . . . .	127
14.6 Launch and operations costs . . . . .	127
15.1 Compliance table . . . . .	128
B.1 Work allocation overview . . . . .	136

# NOMENCLATURE

AC	Aerodynamic Centre	LIBS	Laser Induced Breakdown Spectro- scope
ACR	Area Coverage Rate	MIMU	Miniature Inertial Measurement Unit
ADCS	Attitude Determination and Control System	MLI	Multi-Layer Insulation
AMMOS	Advanced Multi-Mission Operations System	MMC	Metal Matrix Composites
BER	Bit Error Rate	MNF	Modified Newtonian Flow
CAD	Computer Animated Drawings	NASA	National Aeronautics and Space Ad- ministration
CCD	Charge Coupled Device	NF	Newtonian Flow
CDHS	Command and Data Handling System	PAEK	Polyaryletherketones
CG	Centre of Gravity	PDU	Power Distribution Unit
CMC	Ceramic Matrix Composites	PETI	Phenylethynyl Terminated Imides
CP	Centre of Pressure	PMC	Polymer Matrix Composite
CTE	Coefficient of Thermal Expansion	S/C	Spacecraft
DC	Duty Cycle	SAD	Solar Array Drive
DSN	Deep Space Network	SAR	Synthetic Aperture Radar
DWL	Doppler Wind Lidar	SDG	Sustainable Development Goals
EPS	Electronic Power System	SNR	Signal to Noise Ratio
ESA	European Space Agency	SPEX	Spectropolarimeter for Planetary Ex- ploration
FA	Footprint Area	TT&C	Telemetry Tracking and Command
FBD	Free Body Diagram	UAV	Unmanned Aerial Vehicle
FOV	Field Of View	VEM	Venus Emissivity Mapper
GaAs	Gallium-Arsenide	VEXAG	Venus Exploration Analysis Group
GDS	Ground Data System	VIRA	Venus International Reference Atmo- sphere
GS	Ground Station	VNIR	Visual Near-InfraRed
GVO	Geostationary Venus Orbit	VOI	Venusian Orbit Insertion
IAA	Instantaneous Access Area		
IAL	Instantaneous Access Length		
LCP	Liquid Crystal Polymers		

## LIST OF SYMBOLS

Symbol	Physical parameter	Unit
$a$	Acceleration	$m/s^2$
$a_{Earth}$	Semi-major axis of Earth	$km$
$a_{Venus}$	Semi-major axis of Venus	$km$
$a_{tr}$	Semi-major axis of transfer orbit	$km$
$b$	Wingspan	$m$
$c$	Specific heat	$J/kgK$
$c$	Chord	$m$
$C_3$	Characteristic energy	$km^2/s^2$
$C_D$	Drag coefficient	–
$C_L$	Lift coefficient	–
$C_M$	Moment coefficient	–
$C_p$	Pressure coefficient	–
$D$	Drag	$N$
$E$	Young's modulus	$N/m^2$
$E$	Energy	$J$
$F$	Force	$N$
$f$	Safety factor	–
$f$	Frequency	$Hz$
$G$	Conductance	$W/K$
$h$	height	$m$
$i$	Inclination	$deg$
$I$	Mass moment of Inertia	$kg * m^2$
$k$	Thermal conductivity	$W/mK$
$K$	Ballistic parameter	$kg/ms^2$
$L$	Arm	$m$
$L$	Length	$m$
$M$	Molar mass	$g/mol$
$M$	Mach	–
$m/M$	Mass	$kg$
$M_{stability}$	Stability margin	$x/\bar{c}$
$O_{avg}$	Average between the footprint	%
$p$	Pressure	$N/m^2$
$P$	Period	$s$
$Q$	Heat	$J$
$q$	Dynamic pressure	$N/m^2$
$q$	Heat flow	$W$
$r$	Radius	$m$
$r_0$	Earth's radius plus orbital altitude	$km$
$r_3$	Venus' radius plus orbital altitude	$km$
$r_a$	Apocenter distance	$km$
$r_p$	Pericenter distance	$km$
$R_H$	Canard to tail surface ratio	–
$S$	Surface	$m^2$
$T$	Temperature	$^{\circ}C$
$T$	Thrust	$N$
$T_g$	Glass Transition temperature	$K$
$T_{tr}$	Transfer time	$s$

$t$	Thickness	$m$
$t$	Time	$s$
$W$	Weight	$N$
$V$	Velocity	$m/s$
$V_1$	Heliocentric velocity at departure position	$km/s$
$V_2$	Heliocentric velocity at target position	$km/s$
$V_{2,trans}$	Transverse heliocentric velocity at target position	$km/s$
$V_{2,rad}$	Radial heliocentric velocity at target position	$km/s$
$V_0$	Velocity in pericenter of hyperbola around Earth	$km/s$
$V_1$	Heliocentric velocity at departure position	$km/s$
$V_{\infty,1}$	Excess velocity at Earth	$km/s$
$V_2$	Heliocentric velocity at target position	$km/s$
$V_3$	Velocity in pericenter of hyperbola around Venus	$km/s$
$V_{\infty,2}$	Excess velocity at Venus	$km/s$
$V_{c0}$	Circular velocity around Earth	$km/s$
$V_{c3}$	Circular velocity around Venus	$km/s$
$V_{Earth}$	Heliocentric velocity of Earth	$km/s$
$V_{Venus}$	Heliocentric velocity of Venus	$km/s$
$\bar{V}$	Tail volume coefficient	–
$x$	Position in x-direction	$m$
$y$	Position in y-direction	$m$
$z_T$	Engine arm	$m$
$\alpha$	Angle of Attack	$^\circ$
$\beta$	Inverted scale height	$1/m$
$\gamma$	Flight path angle	$^\circ$
$\gamma$	Heat capacity ratio	–
$\delta$	Deflection angle	$^\circ$
$\varepsilon$	Elevation angle	$^\circ$
$\varepsilon$	Downwash	$^\circ$
$\eta$	Efficiency	%
$\eta$	Dynamic pressure ratio	–
$\lambda$	Longitude	$^\circ$
$\lambda$	Wavelength	$m$
$\lambda$	Taper ratio	–
$\phi$	Latitude	$^\circ$
$\phi$	Knockdown factor	–
$\mu$	Standard Gravitational parameter	$m^3/s^2$
$\nu$	Poisson's ratio	–
$\xi$	Weather severity parameter	–
$\rho$	Density	$kg/m^3$
$\tau$	Control surface effectiveness	--
$\theta_1$	True anomaly at departure position	$^\circ$
$\theta_2$	True anomaly at target position	$^\circ$
$\omega$	Rotational rate	$^\circ/s$

# 1

## INTRODUCTION

Venus, Earth's sister planet, has a very unique atmosphere with its thick unbroken cloud deck of carbon dioxide and sulfuric acid. Curiously, the levels of sulfur are varying throughout time, indicating that there are sources and sinks on Venus. The most plausible explanation is active volcanism on Venus, where during eruption, new sulfur is introduced to the atmosphere, which then over time is removed again by solar winds. This led to the mission *Project Matryoshka* with the objective to *unambiguously detect active volcanic activity and characterise the eruption products on Venus, such that the sources and sinks can be identified*. A volcano is active if it has erupted in the past thousand years. The mission shall also launch before 2026.

Currently (June 2016) it is possible to indirectly locate active volcanoes by overlaying the Venusian heat map with the topographical map created by Magellan. This results in locations where both a mountain and a heat source coincide, which is a strong indication for an active volcano. However, due to the thick atmosphere, it is possible that the heat map is faulty and the resolution of the topographical map is in the range 100 m offering only a very rough surface representation. Therefore, while a strong indication, it is by no means proof that it is a volcano. This mission is designed to unambiguously prove active volcanoes, therefore the uncertainty inducing sulfuric clouds need to be circumvented by going beneath them.

The confirmation that active volcanoes exist on Venus would help significantly in the understanding of its atmosphere, climate, internal properties and geological characteristics. Apart from finding active volcanoes, the mission also aims to complete a number of secondary objectives to help further increase the understanding of, among others, the Venusian green house effect. A deeper understanding of Venus' atmosphere and its runaway greenhouse effect will help to improve the climate prediction models for Earth, and, in addition, raise awareness about the effects of climate change among the public.

Project Matryoshka is an ambitious mission designed to be able to comply with the strict requirements. It consists of two main phases, with five mission vehicles. The spacecraft, the first mission vehicle, will map Venus with a higher accuracy than Magellan to determine changes in the topography. Once the mapping phase is done, it will release the second mission vehicle, the aeroshell and then perform an inclination change. The aeroshell will deorbit and enter the Venusian atmosphere. Once the parachute has been deployed and the aeroshell has decelerated to subsonic speeds, it will release the third mission vehicle, the reference lander, and the fourth mission vehicle, the aircraft. The reference lander will descend to the ground and transmit the scientific data to the spacecraft. The aircraft will fly on Venus and from time to time dip beneath the clouds to find a suitable landing location to deploy the fifth mission vehicle, the objective lander. The objective lander will land on or near the volcano and transmit the scientific data to the spacecraft.

Chapter 2 gives a general introduction, showing the Venusian atmosphere, mission objectives and design description. Chapter 3 discusses the astrodynamics of the mission. The detailed design of the different vehicles are treated, starting with the lander in Chapter 4, since it has the least dependencies. The aircraft is described in Chapter 5, followed by the entry aeroshell in Chapter 6. Chapter 7 covers the spacecraft design.

With the different detailed designs completed, a sensitivity analysis is performed in Chapter 8 on the individual vehicles and the mission in general. The operations and logistics of the project are covered in Chapter 9. The Reliability, Availability, Maintainability and Safety (RAMS) and risk analyses are performed in Chapters 10 and 11, respectively. Chapter 12 describes the verification and validation procedures. Chapter 13 and Chapter 14 discuss the sustainability and the project development logic with detailed cost breakdown of the entire project, respectively. A compliance matrix is created in Chapter 15 to show that the design has met all of the top-level requirements. Chapter 16 treats possible follow-up research that would further improve the design. Chapter 17 draws conclusions from the complete report.

# 2

## MISSION OVERVIEW

This chapter serves to provide a general description of the mission to Venus being designed. To do so, first, Section 2.1 discusses the mission goals. After this, the Venusian environment is described in Section 2.2. Next, Section 2.4 gives a global description of the design. Finally, Section 2.5 shows the functional analysis of the complete mission.

### 2.1. MISSION GOALS

The mission goals mainly consist of two different types of objectives, namely the primary objectives, which are discussed in Section 2.1.1, and secondary objectives, which are discussed in Section 2.1.2.

#### 2.1.1. PRIMARY OBJECTIVES

The primary objective of the project is to identify an active Venusian volcano. Once found, the eruption products should be analysed to identify possible sources and sinks of sulphur. Active volcanoes are defined as volcanoes that are currently erupting or have erupted in the past 1,000 years [1]. In order to perform this objective there are two main steps. The first is to locate the potential active volcanoes on the surface of Venus.

This will be done by using an instrument to map heights and temperatures of the surface of Venus, as was also done by the Venus Express mission. A comparison of the data can then be used to look for changes in landscape, which can be indicators of recent volcanic activity. Once the most likely location for active volcanoes is determined, it is still required to perform an in-situ analysis of eruption products or to take pictures to prove that there are indeed active volcanoes on Venus. As the Venusian atmosphere is very thick with dense clouds, this in-situ measurement will rely on the deployment of a lander on the Venusian surface.

#### 2.1.2. MARKET ANALYSIS AND SECONDARY OBJECTIVES

The mission to Venus offers the possibility to perform more scientific objectives than the primary ones alone. These can help increase the understanding of Venus. The Venus Exploration Analysis Group (VEXAG) was established by NASA in July 2005 to identify scientific priorities and set up a strategy for the exploration of Venus. From the VEXAG technical report [2], the goals, objectives, and investigations for Venus exploration, as well as elaboration on those topics, can be deduced. The chosen secondary objectives for this mission and how they can be accomplished will be discussed in this section.

#### MAPPING VENUS

In order to complete the primary objective, it will be necessary to map the surface of Venus. The data from this mapping surface mapping can also be used for other purposes. For example, by combining it with the data from the Magellan mission (1994) that was generated using a Synthetic Aperture Radar (SAR)<sup>1</sup>, the accuracy of the surface maps can be improved and changes with respect to past data can be found. Such changes can indicate processes on Venus that can be of interest to the scientific community and help gain further knowledge of Venus.

#### IMAGES OF VENUS

In order to complete the primary objectives, the spacecraft, aircraft and landers will each take images of Venus from different positions. However, these images can also be used for a large range of other scientific objectives. An example of this is the use of the images of the Venusian surface created by the aircraft and landers to get a better understanding of the surface geology.

<sup>1</sup><http://nssdc.gsfc.nasa.gov/planetary/magellan.html>

### VENUSIAN LIGHTNING

For a long time there have been discussions on whether there is lightning on Venus<sup>2,3</sup>. To resolve this discussion, the aircraft can be used to detect Venusian lightning, because it is possible that the aircraft is struck during its mission lifetime. Once struck, the currents in the lightning protection system that is explained in Section 5.5.1 will change. These changes can be measured by implementing simple sensors throughout that system. This way they can not only detect the currents generated by the lightning, but also narrow down the location of the impact. Should there be lightning, then it will also be possible to determine the frequency at which the aircraft is hit. All this data can help prove the existence of Venusian lightning and thereby help increase knowledge of Venus. Note that if the aircraft is not struck by lightning, this does not disprove Venusian lightning. Also, the lightning itself can not be characterised by the equipment. This should be performed by any future missions, in case the aircraft provides proof of Venusian lightning.

### VENUSIAN ATMOSPHERE DATA

With the aircraft operating inside the Venusian atmosphere for a relatively long period of time while also oscillating between altitude levels, it will be able to measure the atmospheric properties such as temperature, pressure and wind speeds over a large area of the planet. This will provide the scientific community with more data on the Venusian atmosphere that can help improve the accuracy of the Venus International Reference Atmosphere (VIRA). It should, however, be noted that the aircraft will only operate in regions within  $\pm 20^\circ$  latitude, so outside that region, no atmospheric data will be generated.

Furthermore, the spacecraft can accurately measure the wind speeds in the upper cloud levels during its mapping phase by making use of a Doppler Wind Lidar (DWL). The instrument will also be able to determine cloud properties such as height, thickness, and opacity. The specifications of this instrument are mentioned in Section 7.1.2.

### 2.1.3. CLIMATE MODELS AND PUBLIC AWARENESS

One of the UN Sustainable Development Goals (SDGs) to be achieved by 2030 is to "take urgent action to combat climate change and its impacts"<sup>4</sup>. Getting a better understanding of the Venusian atmosphere will contribute to achieving that goal. While not having an immediate effect on Earth sustainability, it is expected that in the long term significant contributions can be made to sustainability. Therefore, it is still considered in this report. Venus is the perfect research location as it is considered to be the sister planet of Earth because of the numerous similarities [3] between them, namely:

- Approximately the same age.
- Relatively similar size in terms of both mass and volume.
- Comparable gravity and bulk composition.
- Closer, yet comparable position with respect to the Sun.
- Common effective temperature and pressure at cloud level.

However, there are also major differences between the two planets. The Venusian atmosphere mostly consists of carbon dioxide, is extremely dry, has sulfuric acid clouds and hurricane-force winds. Thus, better understanding the Venusian atmosphere and geology could provide potential clues about the future of Earth. Since 1990, global emissions of carbon dioxide on Earth have increased by nearly 50 percent<sup>4</sup>, hence, better understanding of the strong greenhouse effect on Venus would facilitate the creation of climate models to better predict Earth's atmospheric evolution.

Furthermore, this mission will make the effects of global warming more relatable to the general public by showing the extreme case of a greenhouse gas warming the atmosphere. This can be done by taking images of the Venusian surface to show to the public, as this is expected to have more effect than just numbers. As a result, green education might improve and there will be an awareness-raising effect. It will sensibilise humans and institutions on the need for climate change mitigation, adaptation, impact reduction, and early warning.

By using a Spectropolarimeter for Planetary EXploration (SPEX), an instrument for detecting and characterising aerosols, essential information to better understand the weather and climate of Venus can be found [4]. The specifications of this instrument are further explained in Section 5.1.4.

<sup>2</sup><http://www.jpl.nasa.gov/releases/2001/cassinivenus010119.html>

<sup>3</sup><http://www.nasa.gov/vision/universe/solarsystem/venus-20071128.html>

<sup>4</sup><http://www.un.org/sustainabledevelopment/climate-change-2/>

## 2.2. VENUSIAN ATMOSPHERE

Venus is a very hostile planet compared to Earth. It has a thick atmosphere consisting out for 96%  $CO_2$ , 4%  $N_2$  and a number of trace elements [5]. At the surface, the density is approximately  $65 \text{ kg/m}^3$ , the pressure is  $9.2 \text{ MPa}$  and the temperature is  $464 \text{ }^\circ\text{C}$ . The values are the result of a large atmospheric mass and an extreme greenhouse effect.

Several missions to Venus have performed remote and in-situ measurements, showing that for a given solar longitude  $\lambda_S$  and latitude  $\phi$  the Venusian atmosphere shows fairly constant temporal characteristics. These characteristics are embodied by the Venus International Reference Atmosphere (VIRA) [6] [7]. The variations of the aforementioned atmospheric properties according to this model are shown in Fig. 2.1.

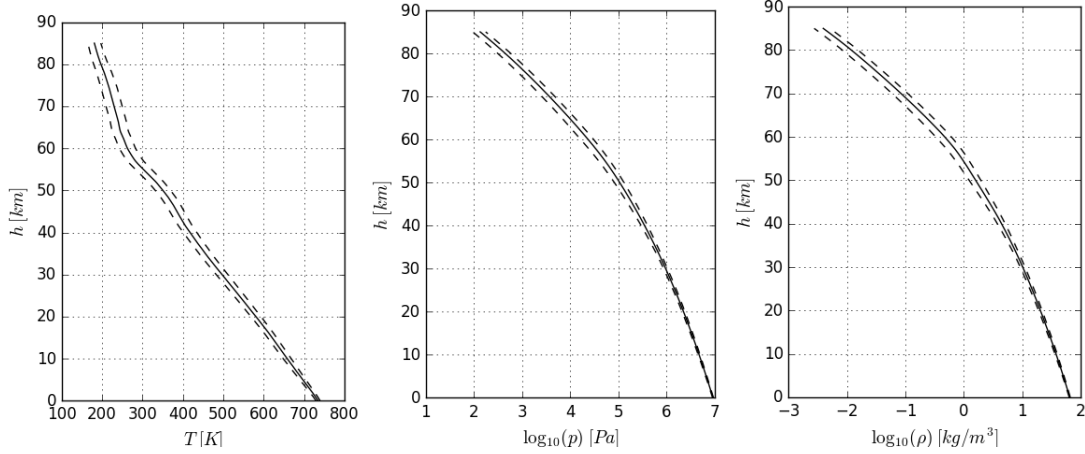


Figure 2.1: The temperature, pressure and density of the Venusian atmosphere at  $\lambda_S = 0^\circ$ ,  $\phi = 0^\circ$  according to VIRA with dashed error bounds.

As can be seen around an altitude of  $50 \text{ km}$  the values reach what one might consider Earthlike: a density  $\rho$  of  $1.59 \text{ kg/m}^3$ , a pressure  $p$  of  $106.6 \text{ KPa}$  and a high temperature of  $86.9 \text{ }^\circ\text{C}$ .

Aside from these properties, Venus also features an extraordinarily thick cloud layer spanning the entire planet. The clouds are composed of sulphuric acid and are situated between  $45 \text{ km}$  and  $70 \text{ km}$  height. Variations in this range are mainly influenced by latitude and solar longitude. These clouds are surrounded by a sulfuric acid haze ranging from  $30 \text{ km}$  to  $100 \text{ km}$ .

The entire planet is enveloped in a large Hadley cell: There is a larger vertical wind component at the equator, albeit still small, due to the large incident solar flux, causing air to rise to the upper atmosphere. From here the meridional winds moves towards the poles, where it drops and returns to the equator again. The zonal winds are very large and generally reach a maximum at a height of approximately  $70 \text{ km}$  with a mean value of  $90 \text{ m/s}$ . At the ground the thick atmosphere causes the wind speeds to approach  $0 \text{ m/s}$  [8]. The variation of zonal wind speed at the equator with height is shown in Fig. 2.2. At a northern and southern latitude  $\phi$  of around  $50^\circ$  there are midlatitude jets: regions of larger zonal wind speeds at a varying altitude of around  $68 \text{ km}$ . The vertical wind speeds were measured by the Venera balloons and determined to be very small, ranging from  $0 \text{ m/s}$  to  $2 \text{ m/s}$  [5].

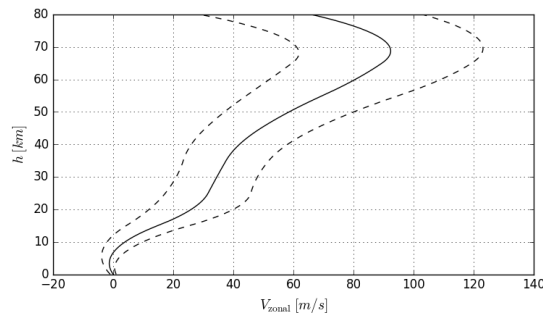


Figure 2.2: Variations of zonal wind speed in the Venusian atmosphere at  $\lambda_S = 0^\circ$ ,  $\phi = 0^\circ$  according to VIRA with dashed error bounds

## 2.3. VENUSIAN GEOLOGY

Understanding the geology of Venus is key to determining the sort of vehicles that can be deployed, as well as what to expect when searching for active volcanoes. The evolution of the planet has yielded many different surface features, including thousands of potentially active volcanoes.

### 2.3.1. HISTORY OF THE SURFACE

Unlike Earth, Venus' surface is a single global lithospheric plate [9]. It may be around 200 km thick [10]. Although there is no plate tectonic activity, the elastic lithosphere can still expand and contract, resulting in mountain ridges and wrinkle ridges.

The lack of impact craters on the surface of Venus lead us to believe that the surface is relatively young, only 300 to 500 million years old [11], which is 20% of the planet's age. This is most likely caused by a rapid volcanic resurfacing that covered over 70% of the planet's surface. However, structures due to local tectonic activity are measured to predate and postdate the resurfacing. There is still some debate as to whether the surface was catastrophically or gradually resurfaced, though the evidence supports the catastrophic process. This would suggest that Venus was much more volcanically active in the beginning of its geological history, 0.5-1 billion years ago [11].

### 2.3.2. SURFACE FEATURES

The Venusian surface can be split into three main domains [11]:

- 80% Volcanic plains
  - 70% Regional plains with wrinkle ridges
  - 10% Shield plains with wrinkle ridges
- 8% Deformed Tessera (raised 'continents', mainly Aphrodite Terra and Ishtar Terra) with criss-crossing ridges making a very rough surface
- 8% Broad topographic rises (e.g. Beta and Atla Regio)

There are over 1600 recorded large volcanoes on Venus. Additionally, there are hundreds of thousands of smaller volcanoes, which seem to be randomly distributed across the surface. The volcanic plains are considered to be quite smooth, although there are also rocks scattered throughout the surface. These scattered rocks are considered to be quite rough and some areas may have a few centimetres of soil or dust. There is also practically no water on the the surface. This lack of water, low wind speeds (although the wind has contributed to aeolian activity) and absence of thermal cycles has limited the weathering of the surface [10]. There are less impact craters than other planets as the thick atmosphere ensures that only large meteorites make it through intact, so no craters are really smaller than three kilometres. They have also been smoothed by volcanic flows and the corrosive atmosphere <sup>5</sup>.

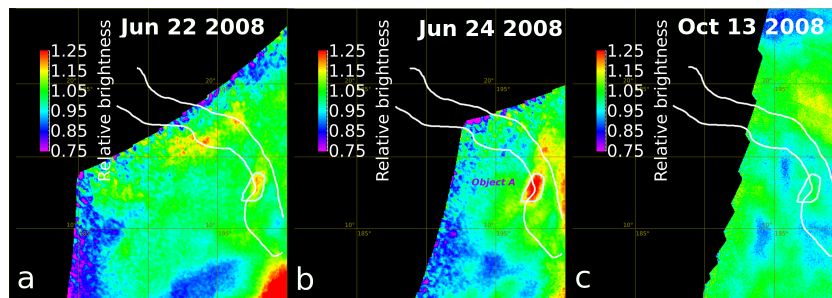
Most of the volcanoes are of the shield variety. There are hundreds of large ones, the largest being Maat Mons, 8 km above the mean planetary radius [10]. Additionally, there are thousands of smaller ones being on average 50 to 400 km wide and one to two km high. Comparing to Earth, the high amount of shield volcanoes indicate that most of the magma on Venus is of the basaltic low silica, low gas composition. The high surface pressure could limit the eruptive nature, ensuring that the lava smoothly flows out. Furthermore, the high temperature on the surface would lead to a slower solidification of the lava, allowing it to travel for longer time. This is likely a characteristic which helped form the vast flood basalts which cover the surface [11]. Another reason why the volcanoes might be larger than on Earth is due to the absence of plate tectonics, where there are no separations through which internal heat can escape. Therefore all volcanoes are considered hotspots, which stay fixed in one location and develop or grow over time. Additional geological features which must be taken into account are:

- Pancake domes (broad flat solidified lava structures)
- Coronae (large oval-shaped features)
- Arachnoids (concentric ovals connected by network of fractures)
- Ticks (domes with deposited debris forming 'legs')
- Novae (radial network of dikes or graben)
- Rift Valleys

### 2.3.3. POTENTIAL VOLCANIC ACTIVITY

It is strongly believed, though not absolutely certain, that there is currently active volcanism on Venus [9]. All the evidence thus far comes from measurements from orbiting satellites or flybys. The Venera and Vega

<sup>5</sup><http://csep10.phys.utk.edu/astr161/lect/venus/surface.html>

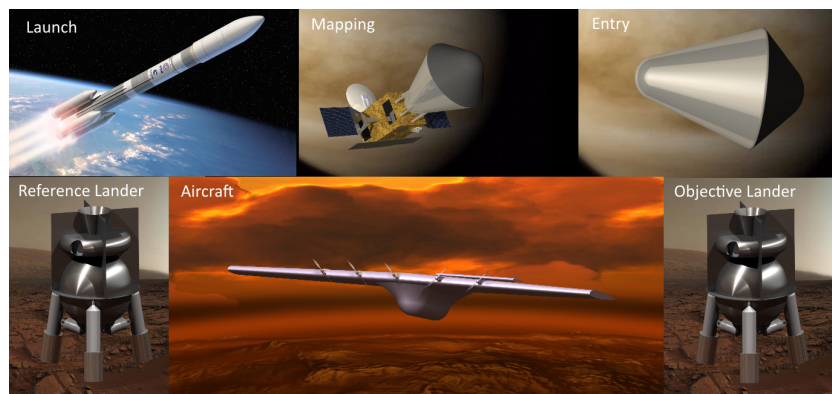
Figure 2.3: Potential hotspot activity<sup>6</sup>

landers only managed to take images and perform stationary spectrometry tests. There are always uncertainties, because the atmosphere is so thick and not yet fully understood. The atmosphere may therefore be interfering with measurements, which may be producing results mistaken for surface activity.

ESA's Venus Express has created images of four 'transient bright spots' which may represent active hot spots [9]. They were observed by the Visible and Infrared Thermal Imaging Spectrometer (near Infrared channel of the Venus Monitoring Camera) in 2008. Localised changes in surface brightness in the Ganiki Chasma rift zone changed between images taken only a few days apart, as is depicted in Fig. 2.3. Due to blurring by clouds, the perceived emission spreads out over hundreds of kilometres, but post-calculations find that they correspond to an area of one square km. The temperature was 350 K higher than the global average. Furthermore, recent analysis of Idunn Mons shows a volcanic structure with an emissivity anomaly, suggesting the surface was only formed 25 million years ago<sup>7</sup>. This is considered a rather recent event over the planet's morphological record.

## 2.4. DESIGN DESCRIPTION

The concept that was selected consists of five different vehicles that will together be able to complete the mission objectives. The five vehicles are a spacecraft, aeroshell, aircraft and two landers. One lander will be stored inside the aircraft, and the aircraft will be stored in the aeroshell together with the second lander. The aeroshell in turn will be connected to the satellite by six struts. Finally, the spacecraft and aeroshell will be stored inside the launcher fairing.

Figure 2.4: Concept of operations of Project Matryoshka<sup>8</sup>

The general mission profile, shown in Fig. 2.4, is as follows: after launch the spacecraft with the aeroshell will be separated from the launcher fairing. Once in orbit around Earth, the spacecraft will wait for the transfer window to initiate the kick stage that will allow it to go into the transfer orbit to Venus. During that transfer

<sup>7</sup>[http://www.esa.int/Our\\_Activities/Space\\_Science/Venus\\_Express/Hot\\_lava\\_flows\\_discovered\\_on\\_Venus](http://www.esa.int/Our_Activities/Space_Science/Venus_Express/Hot_lava_flows_discovered_on_Venus)

<sup>8</sup><sup>1</sup> <http://spaceflightnow.com/wp-content/uploads/2015/06/ariane64.png>

<sup>2</sup> <http://www.universetoday.com/wp-content/uploads/2009/08/surfaceofvenus.jpg>

<sup>3</sup> [http://www.esa.int/var/esa/storage/images/esa\\_multimedia/images/2012/02/animation\\_of\\_venus/9610238-4-eng-GB/Animation\\_of\\_Venus\\_large.jpg](http://www.esa.int/var/esa/storage/images/esa_multimedia/images/2012/02/animation_of_venus/9610238-4-eng-GB/Animation_of_Venus_large.jpg)

<sup>4</sup> <http://i.imgur.com/TcVUMLM.jpg>

the spacecraft will separate from the kick stage and deploy its solar panels. Upon arrival at Venus after about nine months of travel, the kick stage will detach from the spacecraft. After this, the spacecraft will initiate a deceleration manoeuvre to get into a stable mapping orbit around Venus, where it will start up all other systems. The spacecraft will stay in this orbit for some time to generate an altitude map of the Venusian surface. By comparing this map to that created by the past Magellan mission (1994), it will be possible to locate potential volcanic activities that can indicate active volcanoes.

Once this mapping is completed and the most promising region has been located, the aeroshell will detach from the spacecraft and enter the Venusian atmosphere. After this, the spacecraft will initiate a new thrust to change the orbit to one that allows for good communication time with the aircraft and landers. Upon entry into the Venusian atmosphere, the heat shield will protect the aeroshell as the atmospheric drag decelerates the vehicle. Once an altitude of 143 km is reached, a parachute is deployed that further decelerates the aeroshell. Next, the heat shield is dropped from the aeroshell. After this the first lander will be deployed to the surface when the speed of the aeroshell has decreased sufficiently. This lander will act as a reference for the lander on board of the aircraft and has the exact same design. A while after the lander is dropped, the aircraft will be deployed from the aeroshell, which will continue its descent to the surface. After deploying its wings the aircraft will start following its oscillatory flight trajectory in which it charges its batteries and cools down at high altitudes and takes measurements at lower altitudes below the clouds. With those measurements the most promising location for volcanic activity is further narrowed down. During its operations, the aircraft will relay all its data to the spacecraft.

The lander inside the aircraft will be deployed from the aircraft above a location where an active volcano is most likely. This way, the lander can be dropped from a relatively low altitude compared to a spaceborne deployment. As a result of the low altitude, it is expected that the lander will land close to the target. During descent and after landing, the lander will take measurements of the ambient environment. Its data will be transmitted to the spacecraft and as the lander has a lifetime of only about two hours, care has to be taken that the spacecraft is in range when the lander is deployed. After the lander is deployed, the aircraft will continue its operations until it suffers a critical failure. Once the aircraft fails, the spacecraft will still continue taking measurements until it reaches the point at which its propellant is almost depleted. At this point, a decaying orbit will be initiated to have the spacecraft burn up in the atmosphere. After the spacecraft becomes unresponsive, the mission ends.

## 2.5. FUNCTIONAL ANALYSIS

In this section the upper level functions of the three mission vehicles will be analysed. The resulting functional flow diagrams and breakdown structures are shown in Sections 2.5.1 and 2.5.2, respectively.

### 2.5.1. FUNCTIONAL FLOW

Functional flow diagrams show the order of functions that each vehicle has to perform. To reduce the amount of detail the focus is on top-level functions. A list that provides the major steps taken within each block is given after each diagram. The first functional flow diagram is that of the spacecraft and can be seen in Fig. 2.5. It should be noted that until step 3.4 of the functional flow of the spacecraft, it also contains the aeroshell in which the aircraft and landers are stored.

#### Spacecraft:

- 1.1 Vehicle inspection: Inspect structure, inspect systems, determine severity of problems (if any), repair and possibly delay launch, put into launcher.
- 1.2 Launch preparation: Roll out, add propellant, pre-launch check, if problems occur abort and reschedule launch.
- 1.3 Launch: Lift off, stage separation(s), Earth orbit insertion, burnout, main launcher separation.
- 2.1 Transfer orbit insertion: Orient spacecraft, wait for transfer window, initiate kick stage to enter transfer orbit, kick stage burnout, separate kick stage.
- 2.2 Transfer housekeeping: Detumble, deploy solar panels, initiate continuous Earth communication, continuously check and possibly correct orbit transfer.
- 2.3 Arrival at Venus: Orient spacecraft, decelerate, insert into stable Venusian orbit for mapping.

The functional flow for the aircraft begins once the aeroshell is deployed from the spacecraft. Also, because the aircraft deploys the lander to the Venusian surface, it was decided to include the functional flow of the lander at the bottom of the aircraft flow diagram. The diagram is shown in Fig. 2.6.

#### Aircraft:

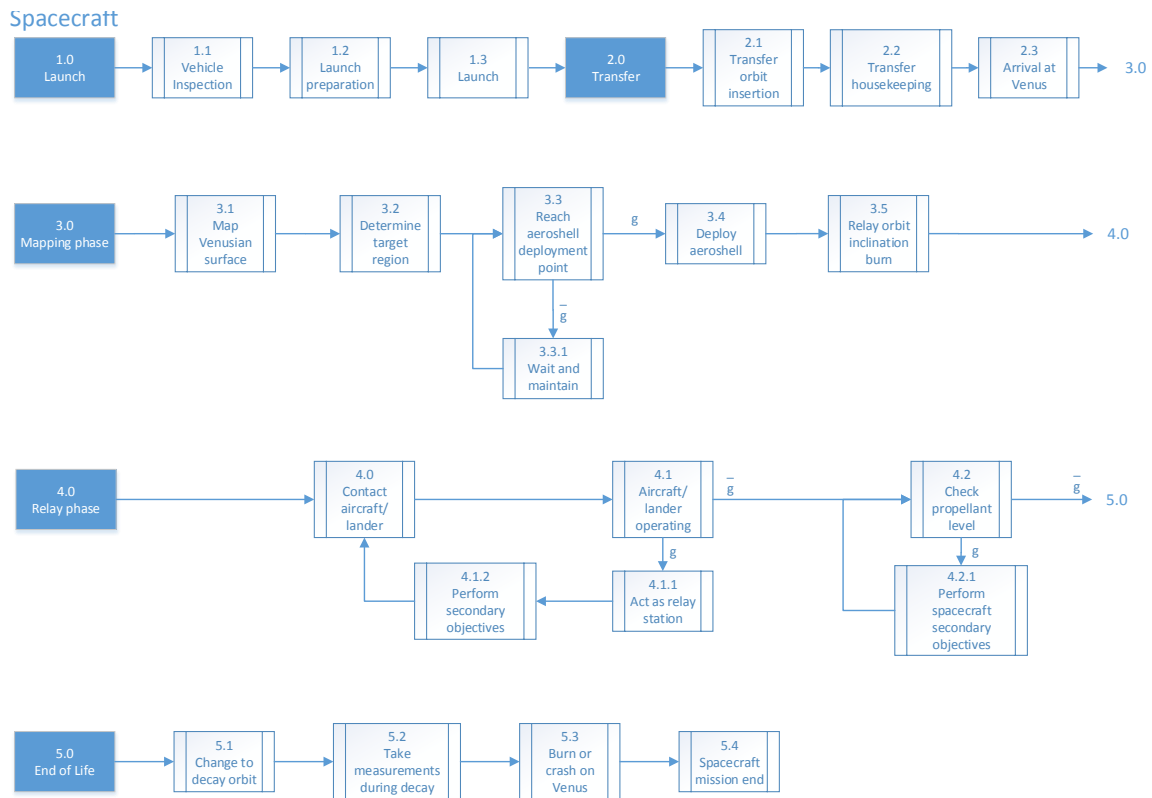


Figure 2.5: Spacecraft functional flow diagram

- 1.1 Entry phase: Separation from spacecraft, orient, lower periapsis, atmospheric entry, decelerate.
  - 1.2 Deployment: Deploy parachute, decelerate, separate heat shield, start up lander systems (see L.1), release aeroshell lander for reference (Continues with L.2), release aircraft.
  - 1.3 Stabilisation: Deploy horizontal stabiliser, deploy main wings, flip upright, start engines, level out to upper track altitude.
  - 2.0 Aircraft Operations: The different mission profiles of the aircraft can be found in Section 5.2.
  - 2.1 Nominal wind speeds: Check if wind speeds allow nominal flight profile.
  - 2.1.1 High winds speeds: Check if the wind speeds are too high for nominal flight profile.
  - 2.1.2 High altitude safe profile: If wind speeds too high, climb to higher altitude and perform high speed mission profile until wind speeds decrease.
  - 2.1.3 Low altitude safe profile: If wind speeds too low, descend to lower altitude and perform low speed mission profile until wind speeds increase.
  - 2.2 Normal flight profile: Initiate dive, dive down to required altitude, flare, stay shortly and perform measurements, deploy lander if above interesting region, climb up to higher altitude and recharge.
  - 2.3 End of life: If a critical failure has occurs, descend down to Venusian surface.
  - 2.4 Aircraft mission end: Aircraft mission ends upon crash with surface.
- Lander:** Note that this diagram applies to both the first lander in the aeroshell that acts as a reference and the lander inside the aircraft.
- L.1 System check: Start up lander systems, perform self diagnostics.
  - L.2 Deployment: Detach from carrier, establish communication to spacecraft.
  - L.3 Descend and land: Take measurements during descend, touch down with possible crushing of legs.
  - L.4 Analyse volcanoes: Start transmitting data, take pictures, measure temperature, perform spectrometry and complete secondary objectives.
  - L.5 Lander mission end: Temperature of spacecraft electronics too high to continue operations, end of lander mission.

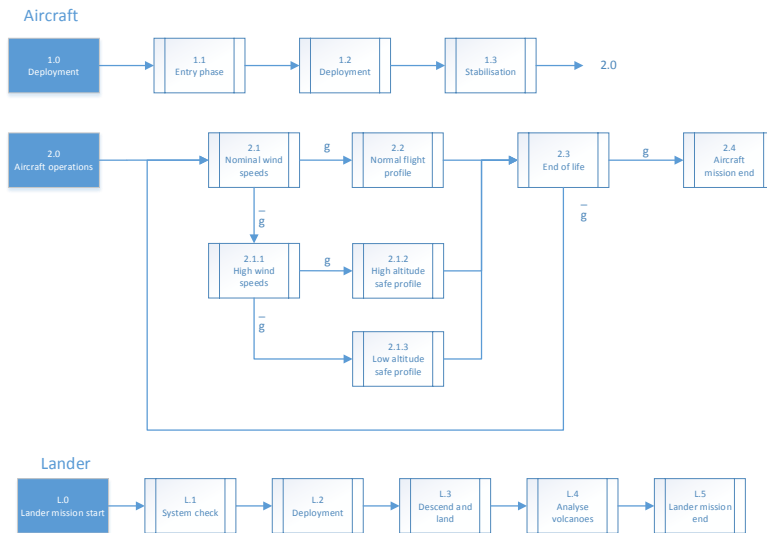


Figure 2.6: Aircraft and lander functional flow diagram

**2.5.2. FUNCTIONAL BREAKDOWN**

For the functional breakdown the functions from the functional flow diagrams are structured differently. Instead of showing the order in which the functions are performed, they are grouped under the different sub-systems performing them. A functional breakdown is performed for the three mission vehicles. Firstly, the spacecraft functional breakdown is shown in Figs. 2.7 and 2.8. Secondly, aircraft functional breakdown can be found in Figs. 2.9 and 2.10. Finally, the lander functional breakdown is shown in Fig. 2.11.

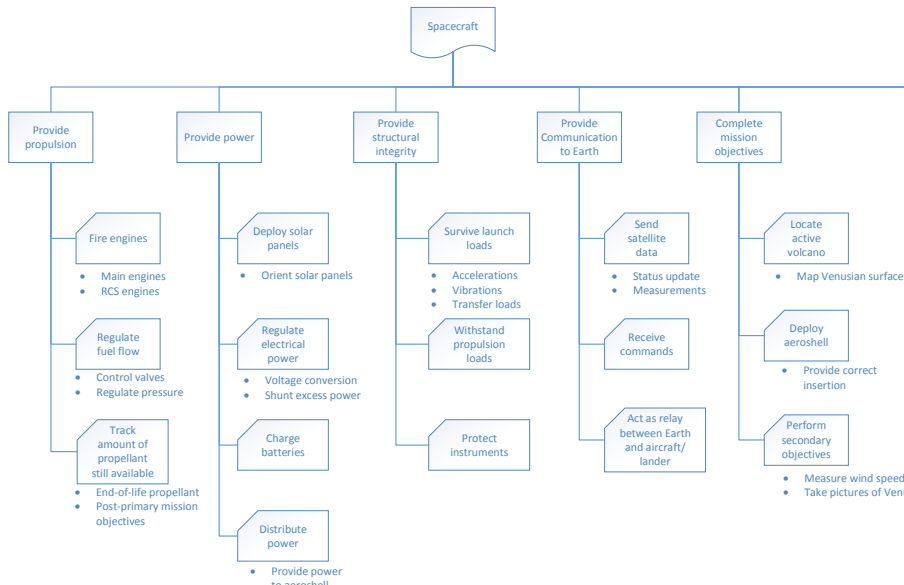


Figure 2.7: Spacecraft Functional Breakdown part 1

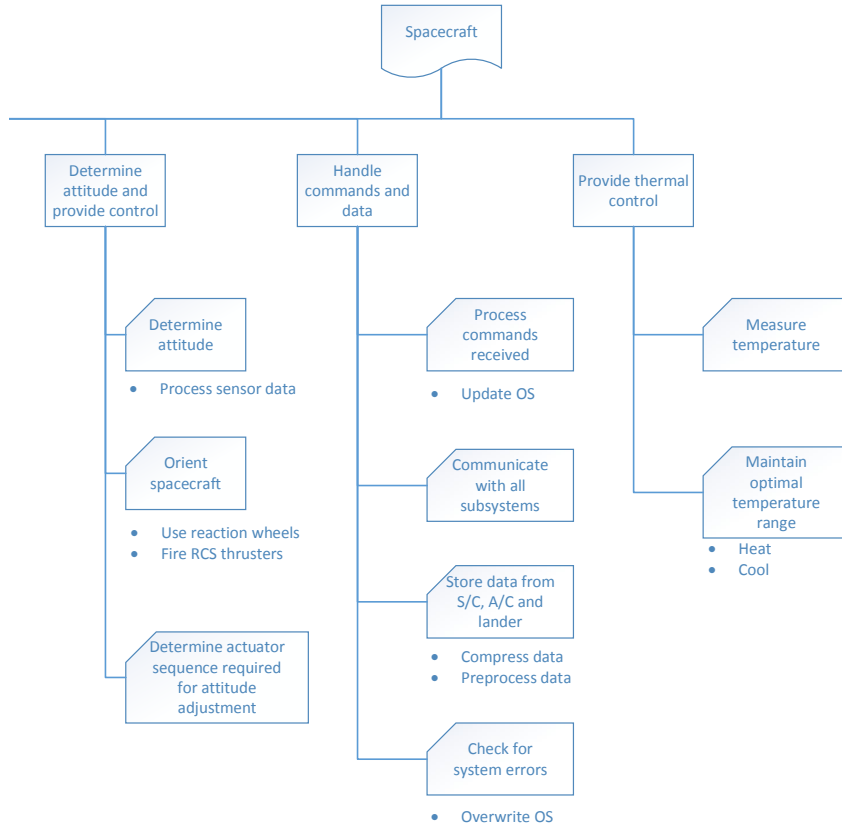


Figure 2.8: Spacecraft Functional Breakdown part 2

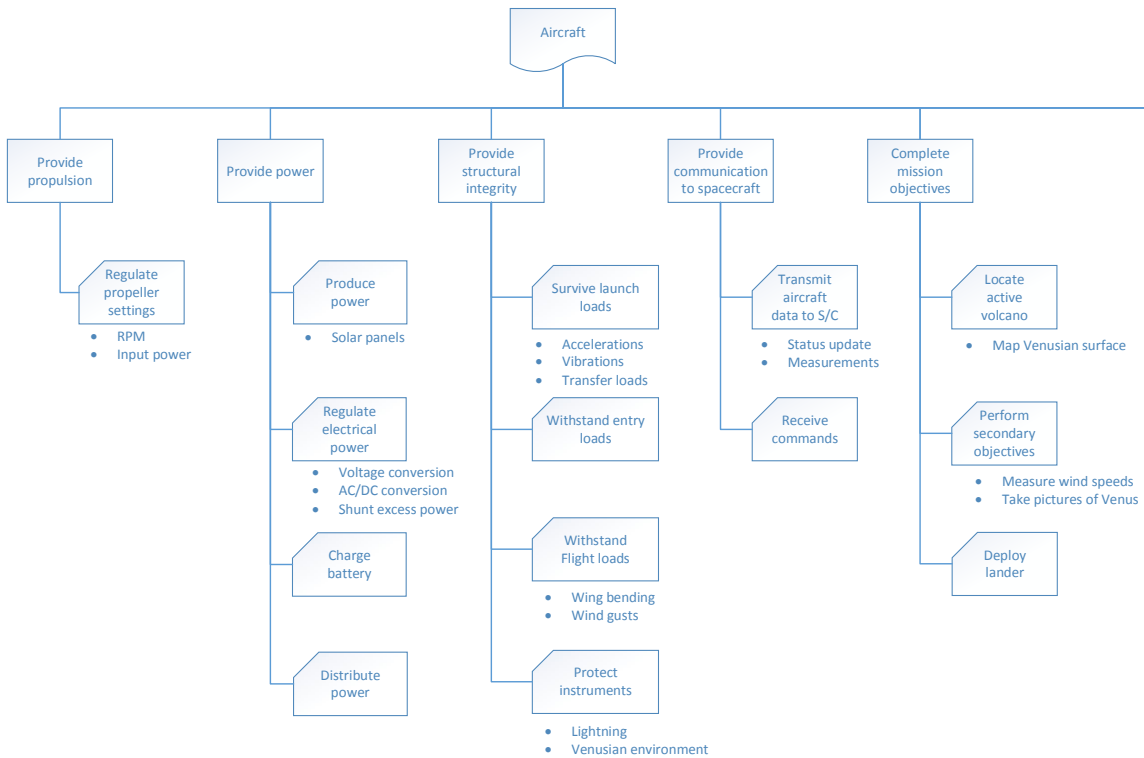


Figure 2.9: Aircraft Functional Breakdown part 1

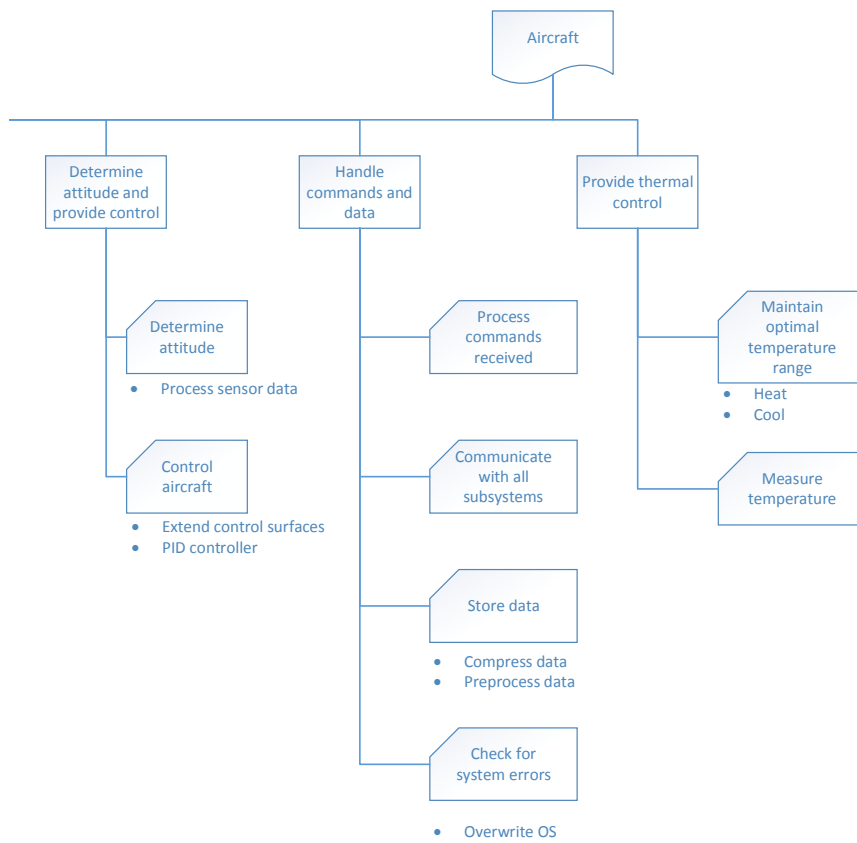


Figure 2.10: Aircraft Functional Breakdown part 2

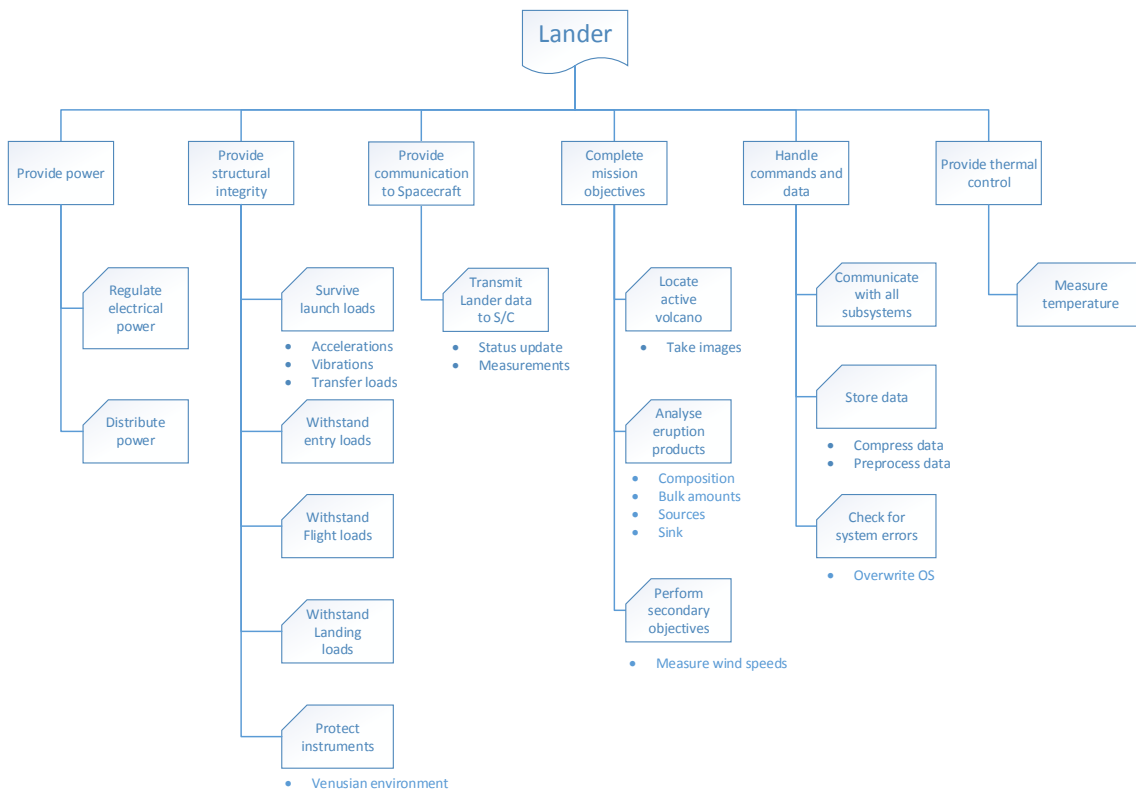


Figure 2.11: Lander Functional Breakdown

# 3

## ASTRODYNAMICS

In this chapter, the astrodynamical characteristics of the mission including the trajectory trade-off with possible launch windows, Venusian orbit trade-off,  $\Delta V$ -budget, coverage and visibility, and launch vehicle selection are presented.

### 3.1. PLANETARY AND ORBITAL CHARACTERISTICS

The general planetary parameters of Venus are summarised in Table 3.1 and are compared to that of the Earth and Sun.

Table 3.1: General features of Venus compared to the Earth and Sun<sup>9 10</sup>

	Venus	Earth	Sun
Mass [ $10^{24}$ kg]	4.8675	5.9724	1,988,500
Radius [km]	6051.8	6378.1	695,700
Surface gravity [ $m/s^2$ ]	8.87	9.80	274.0
$\mu = GM$ [ $10^6 km^3/s^2$ ]	0.32486	0.39860	132,712
Escape velocity [km/s]	10.36	11.19	617.6
Semi-major axis [ $10^{26}$ km]	108.21	149.60	-

The orbital characteristics of Venus are summarised in Table 3.2. It has the longest rotational period compared to any other planet in the solar system. It also has a retrograde spin which can be seen in Table 3.2 with the negative sidereal rotational period.

Table 3.2: Orbital characteristics of Venus (J2000)<sup>11</sup>

Aphelion	$108.94 \cdot 10^{26}$ km
Perihelion	$107.48 \cdot 10^{26}$ km
Semi-major axis	0.72333199 AU
Sidereal orbit period	224.701 days
Tropical orbit period	224.695 days
Synodic period	583.92 days
Sidereal rotation period	-5832.6 hrs
Length of day	2802.0 hrs
Obliquity of rotation axis	$177.36^\circ$
Inclination of equator	$2.64^\circ$
Mean orbital velocity	35.02 km/s
Max. orbital velocity	35.26 km/s
Min. orbital velocity	34.79 km/s
Orbital eccentricity	0.00677323
Orbital inclination	$3.39471^\circ$

The parameters presented here will be used in the following subsections to calculate the relevant transfer and orbit characteristics.

<sup>9</sup><http://nssdc.gsfc.nasa.gov/planetary/factsheet/venusfact.html>

<sup>10</sup><http://nssdc.gsfc.nasa.gov/planetary/factsheet/sunfact.html>

<sup>11</sup><http://nssdc.gsfc.nasa.gov/planetary/factsheet/venusfact.html>

### 3.2. ORBITAL TRANSFER

Three types of transfer trajectories were considered: bi-elliptical transfer, fast trajectory transfer, and Hohmann transfer. Gravity assist was not considered as Venus is the closest planet to Earth, hence gravity assist would be ineffective in this case. A preliminary investigation was carried out to see if aerobraking is feasible. However, it was turned down for three main reasons. Firstly, since the Venusian atmosphere is still not properly understood, the aerobraking manoeuvre would have too many uncertainties. Secondly, aerobraking would potentially induce damaging stresses to the solar panels and the scientific instruments such as the Synthetic Aperture Radar (SAR). Lastly, if aerobraking is implemented, approximately 5 to 7 months would be needed to circularise the orbit. In this amount of time, the risk of failure for the stowed aircraft and landers would increase.

When calculating the Hohmann and fast trajectory transfer to reach Venus, it is assumed that the orbits of Earth and Venus are circular and co-planar. Also, any change in momentum is assumed to be instantaneous. The first assumption is considered valid as both Venus and Earth have a very low orbital eccentricity, 0.0068 and 0.0167 respectively. Moreover, the Hohmann transfer has the additional assumption that the transfer orbit touches tangentially.

The data from Table 3.1 are used to make the computations. The values summarised in Table 3.3 are used to compute both the Hohmann and fast trajectory transfer.  $r_3$  is obtained after the orbit trade-off. The calculations made are based on the AE2230-I Flight & Orbital Mechanics course. It should be noted that the values obtained are for a circular insertion around Venus.

Table 3.3: General interplanetary transfer parameters

Parameter	Value
$r_0$ [km]	185
$r_3$ [km]	385
$r_{SOI,Earth}$ [km]	924,658
$r_{SOI,Venus}$ [km]	616,282
$V_{Earth}$ [km/s]	29.78
$V_{Venus}$ [km/s]	35.02
$V_{c0}$ [km/s]	7.79
$V_{c3}$ [km/s]	7.10

#### 3.2.1. BI-ELLIPTICAL TRANSFER

The effectiveness of using a bi-elliptical transfer was also investigated. In terms of  $\Delta V$ , a bi-elliptical transfer is more efficient than a Hohmann transfer if the ratio of the final to initial semi-major axis is equal or greater than 11.94 even though a bi-elliptical transfer requires one more engine burn than the Hohmann transfer.

$$a = \frac{a_{Venus}}{a_{Earth}} = \frac{0.72333199 AU}{1.0 AU} = 0.72333199 \quad (3.1)$$

It can be observed from Eq. (3.1), that it is more efficient to use a Hohmann transfer since  $a < 11.94$ .

#### 3.2.2. FAST TRAJECTORY TRANSFER

Using the information from Table 3.3, the  $\Delta V$  required to perform a fast trajectory is explored here. Taking the  $V_{\infty,1}$  as  $10 km/s$ , and the parking orbit altitude at Earth is 185 km and at Venus is 385 km, the results are summarised in Table 3.4 and Table 3.5.

It can be observed from Table 3.4 that the transfer time is about 94 days whilst having the  $V_{\infty,1}$  restricted to  $10 km/s$ . This in turn restricts the characteristic energy  $C_3$  to  $100 km^2/s^2$ , which is an estimate of what future launchers might be able to provide.

#### 3.2.3. HOHMANN TRANSFER

Using the information from Table 3.3, the  $\Delta V$  required to perform a Hohmann transfer is explored here.

It can be observed from Table 3.6 that the transfer time is about 146 days with a characteristic energy  $C_3$  of  $6.23 km^2/s^2$ .

Table 3.4: General characteristics of fast trajectory transfer

$a_{tr}$ [km]	$0.9597 \cdot 10^8$
$e_{tr}$ [-]	0.5588
$r_p$ [km]	$42.3 \cdot 10^6$
$r_a$ [km]	$149.6 \cdot 10^6$
$T_{tr}$ [yrs]	0.2561
$C_3$ [ $km^2/s^2$ ]	100
$H$ [ $km^2/s$ ]	$2.9598 \cdot 10^9$
$\theta_1$ [deg]	180
$\theta_2$ [deg]	2.3433
$E_1$ [rad]	$\pi$
$E_2$ [rad]	0.0218
$M_1$ [rad]	$\pi$
$M_2$ [rad]	0.0096
$\gamma_2$ [rad]	0.5810

Table 3.5:  $\Delta V$  characteristics of fast trajectory transfer

	[km/s]
$V_{\infty,1}$	10.00
$V_1$	19.78
$V_2$	32.71
$V_{2,trans}$	27.35
$V_{2,rad}$	17.92
$V_{\infty,2}$	19.51
$V_0$	14.88
$V_3$	21.98
$\Delta V_0$	7.09
$\Delta V_3$	14.83
$\Delta V_{tot}$	21.92

### 3.2.4. ORBITAL TRANSFER - METHOD SELECTED

When considering the transfer for this mission, two main criteria were identified that can drive the design of the mission: the transfer time, and the amount of fuel needed for the transfer to take place.

However, to remain aligned with the sustainable development strategy, fuel consumption is selected to be the design driver. Furthermore, placing transfer time as a secondary concern, the propellant mass needed and cost of using such a system are more likely to be lowered since it requires less powerful rocket engines. Additionally, there are no time constraints for the arrival of the spacecraft, just a launch time constraint.

Using a Hohmann transfer in this situation would result in a low fuel consumption and maximising energy efficiency as it only requires two-impulsive manoeuvres. Moreover, it can be observed that the Hohmann transfer takes approximately 4.8 months for a  $C_3$  of  $6.23 km^2/s^2$  while the fast trajectory transfer takes about 3.1 months for a  $C_3$  of  $100 km^2/s^2$ . Choosing a fast trajectory would only save 52 days but require 16 times more characteristic energy. For the above mentioned reasons, a Hohmann transfer is selected.

Moreover, to get an idea of what transfer method previous missions used, the transfer times of previous Venus missions are summarised in Table 3.7.

Table 3.6: Summary of parameters for Hohmann transfer

$a_{tr}$ [km]	$1.2890 \cdot 10^8$
$e_{tr}$ [-]	0.1605
$T_{tr}$ [yrs]	0.40
$C_3$ [ $km^2/s^2$ ]	6.23
$V_1$ [ $km/s$ ]	27.29
$V_2$ [ $km/s$ ]	37.73
$V_{\infty,1}$ [ $km/s$ ]	2.50
$V_{\infty,2}$ [ $km/s$ ]	2.71
$V_0$ [ $km/s$ ]	11.30
$V_3$ [ $km/s$ ]	10.47
$\Delta V_0$ [ $km/s$ ]	3.51
$\Delta V_3$ [ $km/s$ ]	3.30
$\Delta V_{tot}$ [ $km/s$ ]	6.81

Table 3.7: Previous mission transfer time. Value in bracket represents actual transfer time.

Mission	Transfer time [months]
Venera 9	4.5
Venera 10	4.5
Pioneer Venus 1	6.5
Venera 15	5.3
Venera 16	5.1
Magellan	15.2
Venus Express	5.1
Akatsuki	6.5 (66.6)

It can be observed from Table 3.7 that most missions had a transfer time of about 5 months, and thus supports the decision to make a Hohmann transfer. It should be noted that the Magellan had a 15 months transfer time as the spacecraft performed a type-IV heliocentric orbit where it would circle the Sun 1.5 times. This was done because the spacecraft was initially planned to be launched with a Centaur-G upper-stage booster from a Space Shuttle with a 6 months transfer time but due to the Challenger disaster, another method was used which had a less powerful upper stage. Moreover, the Akatsuki had an initial planned transfer time of 6.5 months but as the main engine failed to put the orbiter into a Venusian orbit, it continued onto a heliocentric

orbit. After a couple of years, when the window was opened again, it used its attitude control thrusters to finally put the orbiter into a Venus orbit.

### 3.2.5. LAUNCH WINDOW

From now on, only a Hohmann transfer will be considered. The required phase angle,  $\theta_{e,v}$ , is calculated using Eq. (3.2):

$$\theta_{e,v} = \left[ 1 - \left( \frac{1 + \left( \frac{a_{Earth}}{a_{Venus}} \right)}{2} \right)^{1.5} \right] \pi = -54.03^\circ \quad (3.2)$$

The spacecraft should perform its initial engine burn when Venus is 54.03 degrees behind Earth. Every 583.92 days, or 19 months, the synodic period of Venus is completed. During such an event near optimal paths exist between Earth and Venus. Using this information, launch windows can be computed. The dates presented in Table 3.8 are the most efficient time to launch the spacecraft.

Table 3.8: Potential Hohmann transfer launch windows

Window	Departure date	Arrival date
1	16/05/2023	10/10/2023
2	22/12/2024	16/05/2025
3	27/07/2026	21/12/2026

Launch window 3 is illustrated in Fig. 3.1.

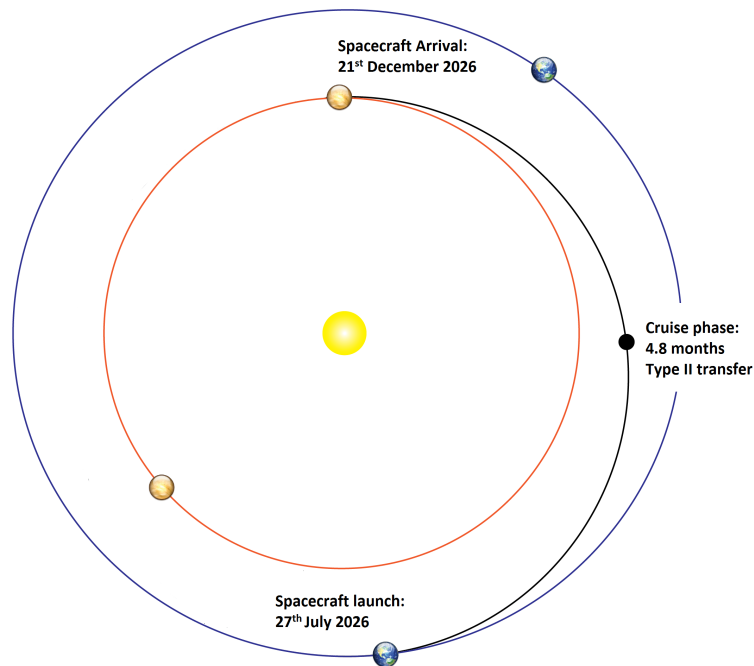


Figure 3.1: Type II Hohmann transfer of spacecraft using launch window 3

However, to take into account potential adverse weather conditions and technical launch problems, the window is extended to  $\pm 7$  days. In Fig. 3.2, window 1 is extended to a 15 day window where the required characteristic energy is also given.

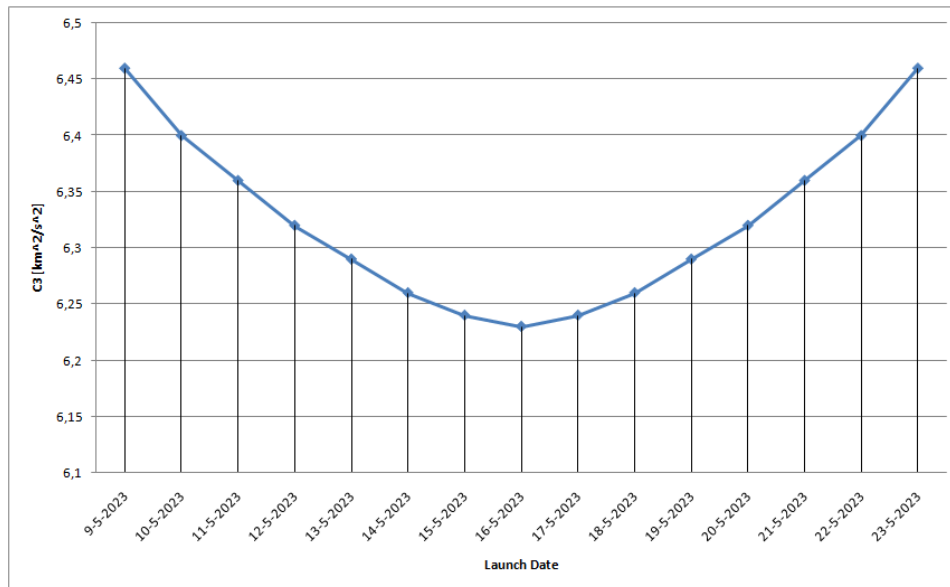


Figure 3.2: Characteristic energy versus launch dates for window 1 type-II Hohmann transfer

### 3.3. ORBIT TRADE-OFF

When selecting a specific type of orbit, different mission requirements need to be taken into account. Hence, the general requirements of the orbits are as follows:

1. The orbit shall provide enough sunlight for the solar cells for power generation purposes.
2. The orbit shall not be too low to be affected by atmospheric drag.
3. The orbit shall provide enough contact time with Earth communication.
4. The orbit shall minimise the required  $\Delta V$  as much as possible, given the lower the  $\Delta V$ , the lower the propellant mass.

Since the mission will be divided into two distinct operational phases, they will have different mission requirements. The mapping phase demands the following primary requirements:

1. The orbit shall have an orbit altitude that provides adequate precision for the imaging instruments on-board to map the surface for hotspots.
2. The orbit shall provide sufficient coverage for a near-global mapping of Venus.

The telecommunication relay phase demands the following primary requirements:

1. The orbit shall cover an area where the lander and aircraft are in view.
2. The orbit shall have enough contact time with the aircraft and lander for telecommunications purposes.

Therefore, two orbits need to be designed that take in account their mission-specific requirements and the general requirements.

#### 3.3.1. MAPPING PHASE: ALTITUDE & INCLINATION DETERMINATION

The main driving requirement for orbit selection are the restrictions imposed by the Synthetic Aperture Radar (SAR) and the Venus Emissivity Mapper (VEM). This is represented by mapping requirement 1 from Section 3.3. Furthermore, as the SAR images will be compared to that of the Magellan, having a ground resolution of 75m or better is the requirement imposed. Hence, when designing for the resolution, the SAR is leading compared to the VEM. This is discussed in more detailed in Chapter 7, but the ground resolution, which is limited by the bandwidth, determines the swath width.

It can be observed from Fig. 3.3<sup>12</sup> and Fig. 3.4<sup>13</sup>, that the swath width mainly depends on the look angle of the instrument ( $\beta$ ), the offset angle from the nadir direction ( $\theta$ ) and the altitude of the orbit ( $h$ ). However, only the altitude and offset angle can be varied to some extent. Through iteration, an altitude of 385 km would

<sup>12</sup><http://slideplayer.com/slide/4674399/>

<sup>13</sup><http://slideplayer.com/slide/4674399/>

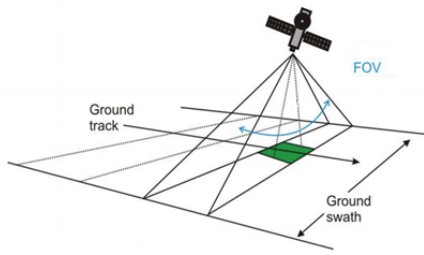


Figure 3.3: Field of view and swath width of Orbiter

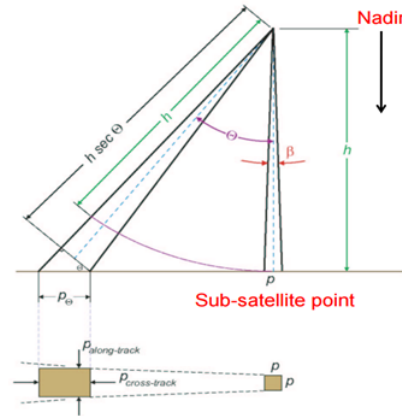


Figure 3.4: Orbiter viewing geometry

provide the 100 km swath width for the SAR and a 288 km swath width for the VEM. This corresponds to a ground resolution of 60 m for the SAR and 43.65 km for the VEM. However, the SAR will require an nadir offset angle of  $36.07^\circ$  and the VEM will require  $16.07^\circ$ . This can be done by placing the instrument at an angle on the spacecraft or make the whole spacecraft rotate by the required offset.

Table 3.9: Specifications for mapping instruments

Instrument	Look angle, $\beta[^\circ]$	Nadir-offset angle, $\theta[^\circ]$	Swath width [km]
SAR	10	36.07	100
VEM	30	16.07	288

Moreover, the mapping orbit would greatly benefit from being circular as it would provide a constant resolution for the images. However, a circular orbit would put an extremely large demand on the Venusian Orbit Insertion (VOI) burn which would greatly increase the propellant mass and volume needed and in turn increase the launch mass. This would harmfully restrict the launch vehicle selection. This issue is discussed in greater detail in Section 3.6

Now, an inclination needs to be selected. This depends on which parts of the surface needs to be mapped. To answer mapping requirement 2 and unambiguously prove the existence of active volcanoes on Venus, the orbital inclination of the spacecraft must be polar to obtain a full coverage. On the other hand, having a purely polar orbit of  $90^\circ$  means there will be no overlap (except at the poles) which would be undesirable since it will not provide topographical relief for the SAR. Thus, a compromise is selected. Since the mapping data is going to be compared to that of the Magellan, it would be sensible to select the same inclination of  $85.5^\circ$  to cover the same area as the Magellan. This inclination would create two 'blind spots', one at each pole. The surface area that would not be mapped is about  $1.42 \cdot 10^6 \text{ km}^2$  which corresponds to about 0.31% of the total Venusian face area. Moreover, the revolution-to-revolution shift of spacecraft ground track is about 78 km at the equator, which is smaller than the SAR and VEM swath width. This means that there will be a 22 km overlap for the SAR and a 210 km overlap for the VEM.

### 3.3.2. TELECOMMUNICATION PHASE: ALTITUDE & INCLINATION DETERMINATION

Altitude determination is mainly governed by the amount of contact time required with the lander and aircraft. As the lander is more critical than the aircraft, it shall be used to size the orbit. The total lander operation time is 100 minutes including descent. However, a 1.5 safety factor is applied which requires the contact time to be at least 2.5 hours just in case the lander might survive longer. Now, the elevation needs to be taken into account. The minimum elevation angle is usually selected to be around  $5^\circ$  to  $10^\circ$  when there are no obstructions, but since the lander will be placed near lava fields, rift zones, chasma, and elevated mass forms, the elevation angle needs to be selected appropriately.

Since a landing site cannot be decided at this stage of the design, two worst case scenarios are chosen. Firstly, the lander might be placed in the Ganis Chasma where transient hotspots were identified by Venus

Express. This chasma is approximately 2.3 km deep and 150 km wide. The other worst case scenario is if the lander is placed also in the Atla Regio but near the highest landmass, Maat Mons. It has a height of 8 km above the mean surface but 5 km above the surrounding terrain <sup>14</sup>. It should be noted that placing the lander near Maat Mons is more constricting than placing it in the Imdr Regio near Idunn Mons which only rises 2.5 km above the surrounding fields <sup>15</sup>.

In Table 3.10, the maximum possible distance to Maat Mons and the edge of the Ganis Chasma are computed with respect to different elevations angles.

Table 3.10: Maximum possible horizontal distances with respective to elevation angles

Elevation angle [°]	Maat Mons Horizontal distance [km]	Ganis Chasma Horizontal distance [km]
0	5.00	2.3
5	4.98	2.29
10	4.92	2.27
15	4.83	2.22
20	4.70	2.16
25	4.53	2.08
30	4.33	1.99
35	4.10	1.88
40	3.83	1.76
45	3.54	1.63
50	3.21	1.48
55	2.87	1.32
60	2.50	1.15
65	2.11	0.97
70	1.71	0.79
75	1.29	0.60
80	0.87	0.40
85	0.43	0.20
90	0.00	0.00

Through calculations, it turned out that selecting an elevation angle larger than 65° would severely restrict the contact time with the lander. Thus, choosing 65° as elevation angle, the lander will be able to be 2.11 km away from Maat Mons and 0.97 km away from the edge of the Ganis Chasma.

Now, the inclination needs to be determined. Through the literature study documented in Section 2.3.3, the most likely places to find hotspots are in the Atla Regio and the Imdr Regio, where evidence was found in the Ganis Chasma and at Idunn Mons respectively <sup>16</sup>. The Atla Regio also contains the highest volcano, Maat Mons. From Fig. 3.5, it can be observed that both regions of interest lie in between  $\pm 50^\circ$  latitude. Ishtar Terra does not contain any interesting assets pertaining to this mission. This data is also co-related to the locations of large volcanoes as can be observed from Fig. 3.6, where it can be seen that most of the volcanoes also lie in between  $\pm 50^\circ$  latitude. Hence, the inclination for the telecommunications relay phase is selected to have 55° inclination to be able to cover the potential places of interest which also includes the Beta Regio, Phoebe Regio and Aphrodite Terra with a 5° margin.

With an inclination and elevation selected, an orbit can be determined. Since elliptical orbit would provide more contact time than a circular one, the former is chosen. Since the  $\Delta V$  needs to be minimised due to the general requirement 4, the periapsis is fixed to 385 km. To be able to have at least 2.5 hours of contact time with the lander, an apoapsis of at least 37,105 km is needed. The contact times are summarised in Table 3.11. Moreover, it is also interesting to consider where the previous missions have landed or crashed their landers. The previous landing or crashing sites of previous landers are summarised in Fig. 3.7. It should be noted that *V#* stands for the Russian Venera lander missions, and *PV* for the American Pioneer Venus probes. The potential area of interest, Ganis Chasma, located in the Northern part of the Atla Regio has been marginally investigated by Russian Vega landers.

<sup>14</sup><http://photojournal.jpl.nasa.gov/catalog/PIA00106>

<sup>15</sup>[http://www.dlr.de/en/DesktopDefault.aspx/tabid-726/1206\\_read-23529/gallery-1/gallery\\_read-Image.1.13994/](http://www.dlr.de/en/DesktopDefault.aspx/tabid-726/1206_read-23529/gallery-1/gallery_read-Image.1.13994/)

<sup>16</sup>[http://www.esa.int/Our\\_Activities/Space\\_Science/Venus\\_Express/Hot\\_lava\\_flows\\_discovered\\_on\\_Venus](http://www.esa.int/Our_Activities/Space_Science/Venus_Express/Hot_lava_flows_discovered_on_Venus)

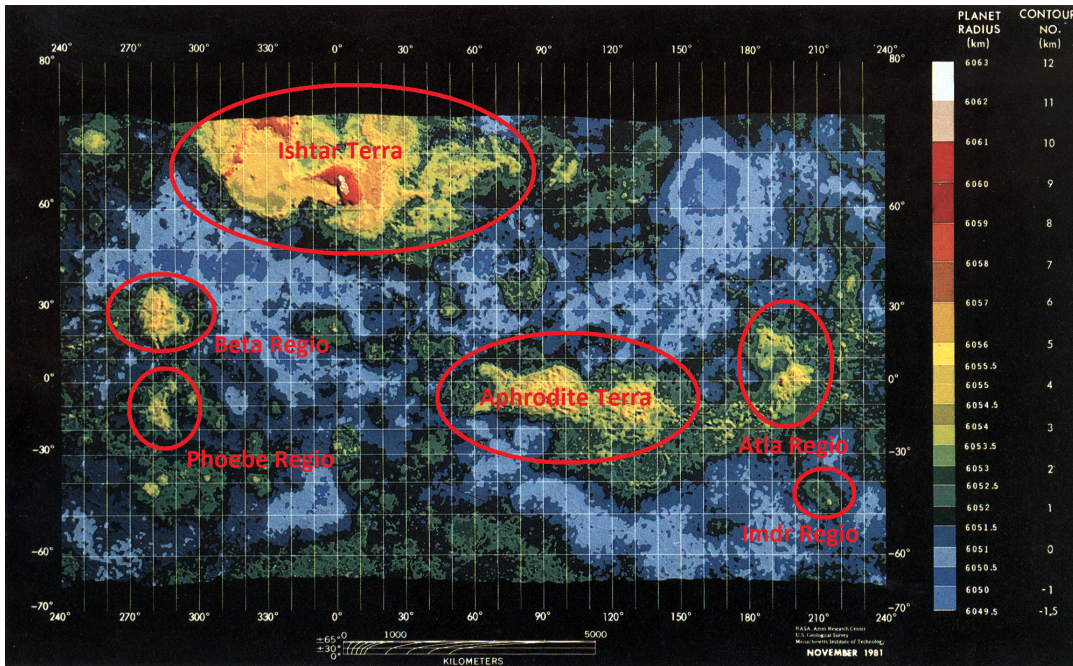


Figure 3.5: Relief map of Venus <sup>17</sup>

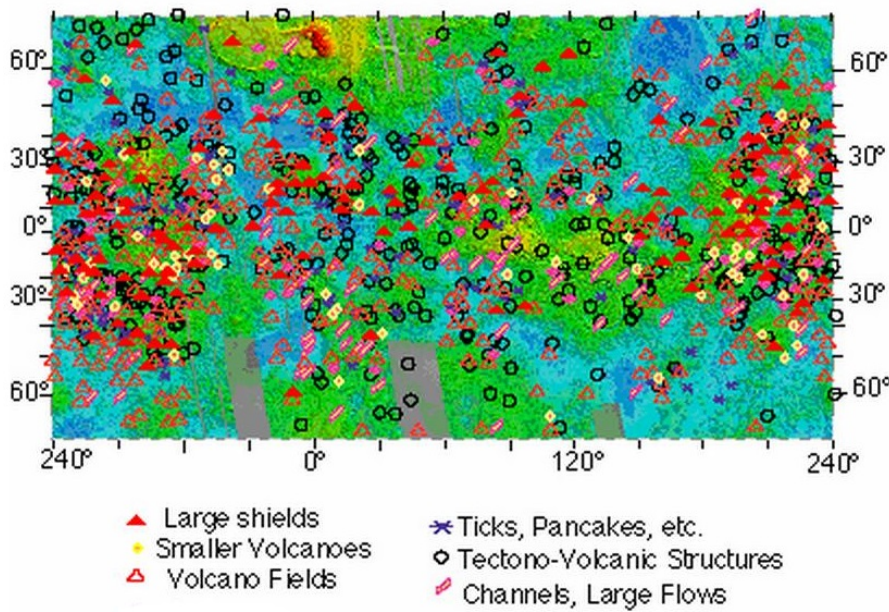
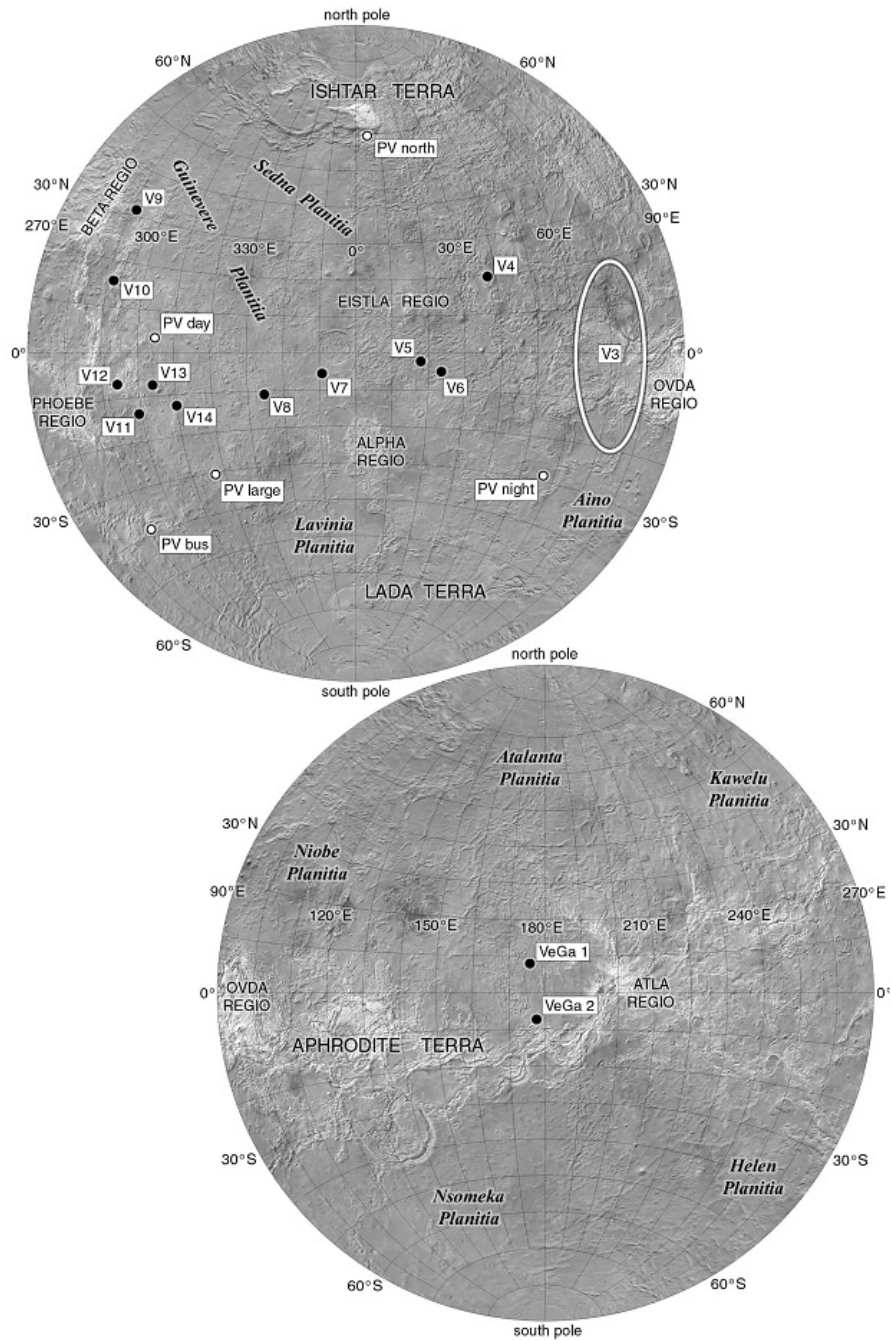


Figure 3.6: Volcano locations <sup>18</sup>

Table 3.11: Contact time with lander and aircraft

Vehicle	Contact time [hrs]	Non-contact times [hrs]
Lander	2.50	9.46
Aircraft	9.47	2.48

To have an idea of what types of orbit were selected by previous missions, the orbital characteristics of all the orbiters used in previous Venesian missions are summarised in Table 3.12. The unit RV represents the Venesian radius which is equal to 6,052 km. The year corresponds to launch year of the mission.

Figure 3.7: Previous landing sites<sup>19</sup>

From Table 3.12, it can be observed that all orbits are highly elliptical except that of the Magellan which had a low elliptical polar orbit. The Magellan mission was solely an orbiter used for the near-global mapping of the Venusian surface using an SAR. Venera 9 and 10 were orbiter missions to act as a communications relay for the lander and to explore cloud layers and atmospheric parameters. However, Venera 15 and 16 were just orbiters designed to use 8 cm band side-looking radar mappers to study the surface properties of Venus. Pioneer Venus 1 was the first of a two-spacecraft orbiter-probe combination designed to conduct a comprehensive investigation of the atmosphere of Venus. Venus Express was an orbiter to study the atmosphere and plasma environment of Venus from orbit. Finally, the Akatsuki is an orbiter to study the dynamics of the atmosphere

<sup>20</sup><http://nssdc.gsfc.nasa.gov>

<sup>21</sup>[http://global.jaxa.jp/projects/sat/planet\\_c/](http://global.jaxa.jp/projects/sat/planet_c/)

<sup>22</sup>[http://www.esa.int/Our\\_Activities/Operations/Venus\\_Express](http://www.esa.int/Our_Activities/Operations/Venus_Express)

Table 3.12: Orbital characteristics of past mission orbiters<sup>20 21 22</sup>

Year	Mission	Periapsis [RV]	Apoapsis [RV]	Period [hrs]	Inclination [°]	Eccentricity [-]
1975	Venera 9	1.26	19.51	48.3	29.5	0.89002
1975	Venera 10	1.27	19.82	49.4	29.5	0.87980
1978	PV 1	1.03	12.01	24.0	105.0	0.84200
1983	Venera 15	1.17	11.91	24.0	92.5	0.82110
1983	Venera 16	1.17	11.91	24.0	92.5	0.82110
1989	Magellan	1.05	2.40	3.26	85.5	0.39177
2005	Venus Exp.	1.04	11.91	24.0	90.0	0.83938
2010	Akatsuki	1.05	14.22	30.0	172.0	0.86248

of Venus from orbit, particularly the upper atmosphere super-rotation and the three-dimensional motion in the lower part of the atmosphere, using multi-wavelength imaging.

The characteristics of both mission phases are summarised in Table 3.13. Such an orbit would have a solar eclipse time of 0.34 hours.

Table 3.13: Orbital characteristics of mapping and telecommunications phases

Mission phase	Periapsis altitude [km]	Apoapsis altitude [km]	Period [hrs]	Inclination [°]	Eccentricity [-]
Mapping	385	37,105	11.96	85.5	0.74
Telecom relay	385	37,105	11.96	55	0.74

If the mapping phase is circular, it will have 1.58 hours as orbital period and an eccentricity of zero, naturally.

### 3.3.3. MAPPING PHASE

If a circular insertion is selected, in Fig. 3.8, the sub-satellite point of the orbiter during the mapping phase is shown.

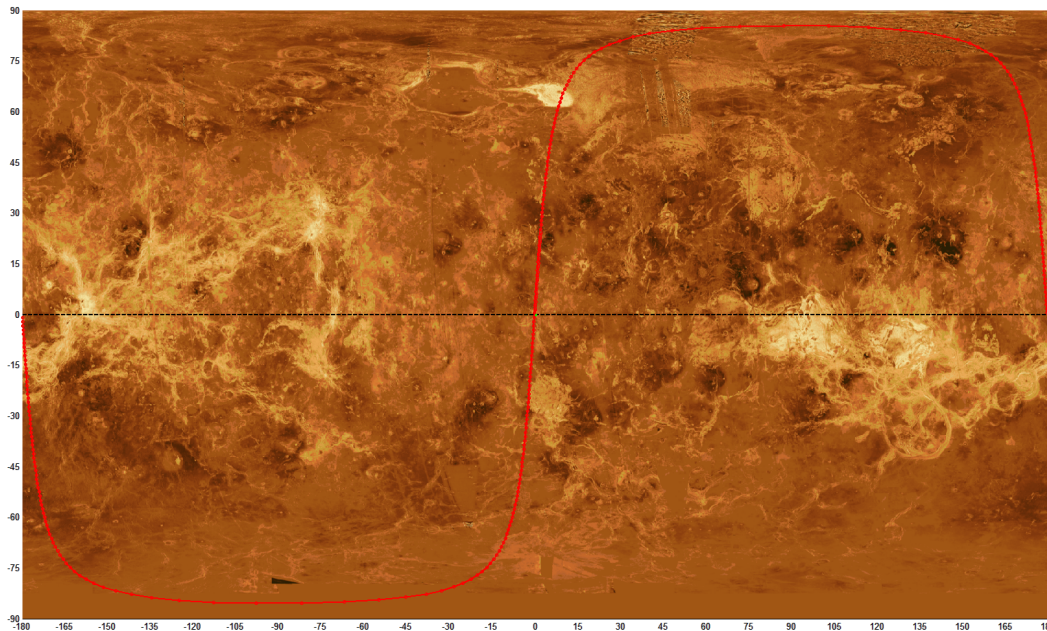


Figure 3.8: Ground track for circular mapping phase (single orbit)

If an elliptical insertion is selected, in Fig. 3.10, the sub-satellite point of the orbiter during the mapping phase is shown.

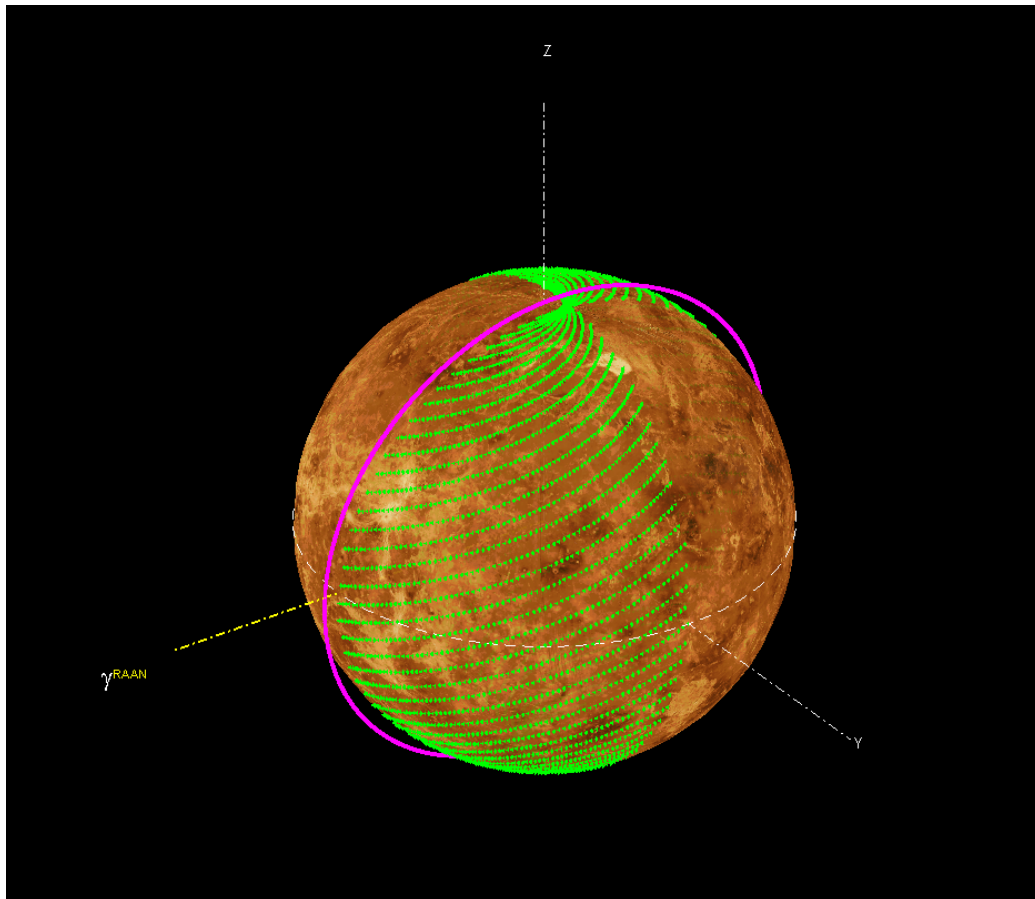


Figure 3.9: Orbit geometry for half a cycle of circular mapping phase

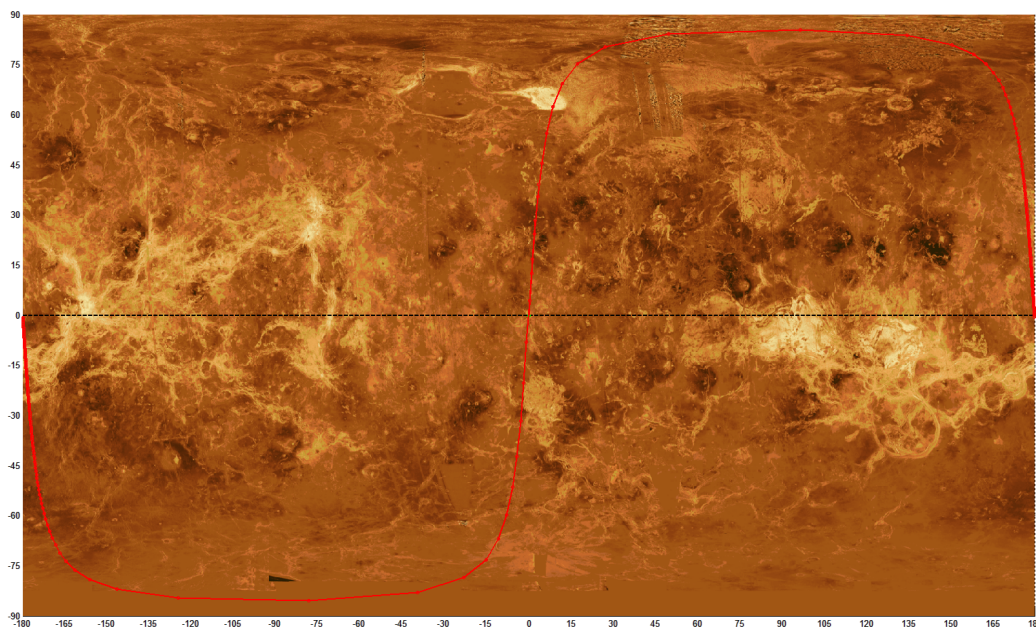


Figure 3.10: Ground track for elliptical mapping phase (single orbit)

It can be observed that there is not much difference in ground track between Fig. 3.8 and Fig. 3.10 as the inclination is still the same for both orbits but the dwell time is different which is represented by the concen-

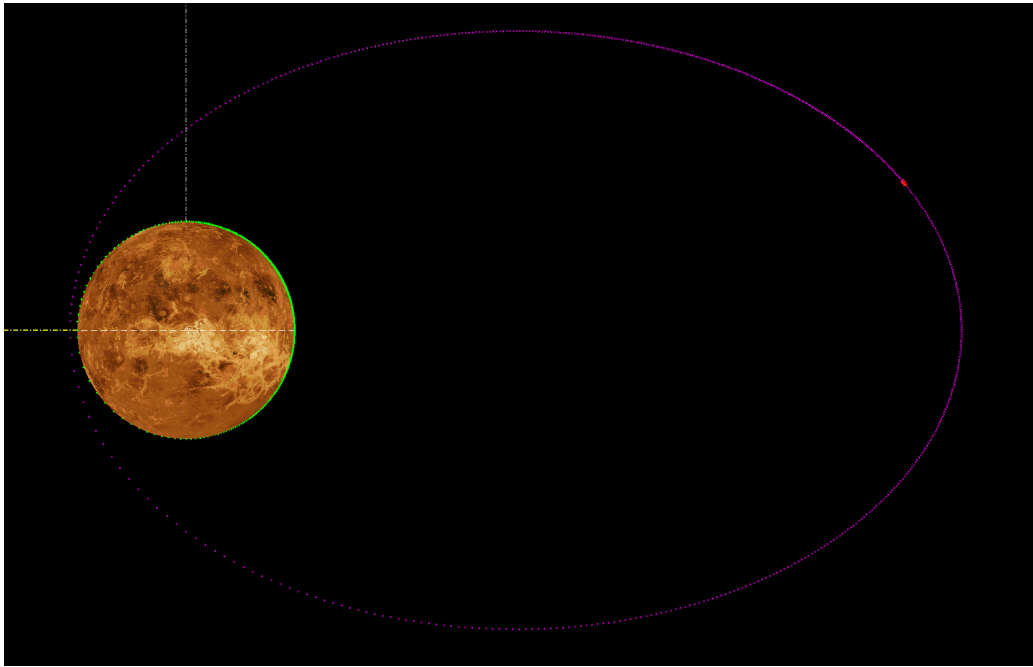


Figure 3.11: Orbit geometry for elliptical mapping phase

tration of red dots.

#### 3.3.4. TELECOMMUNICATION RELAY PHASE

In Fig. 3.8, the sub-satellite point of the orbiter during the telecommunication relay phase is shown.

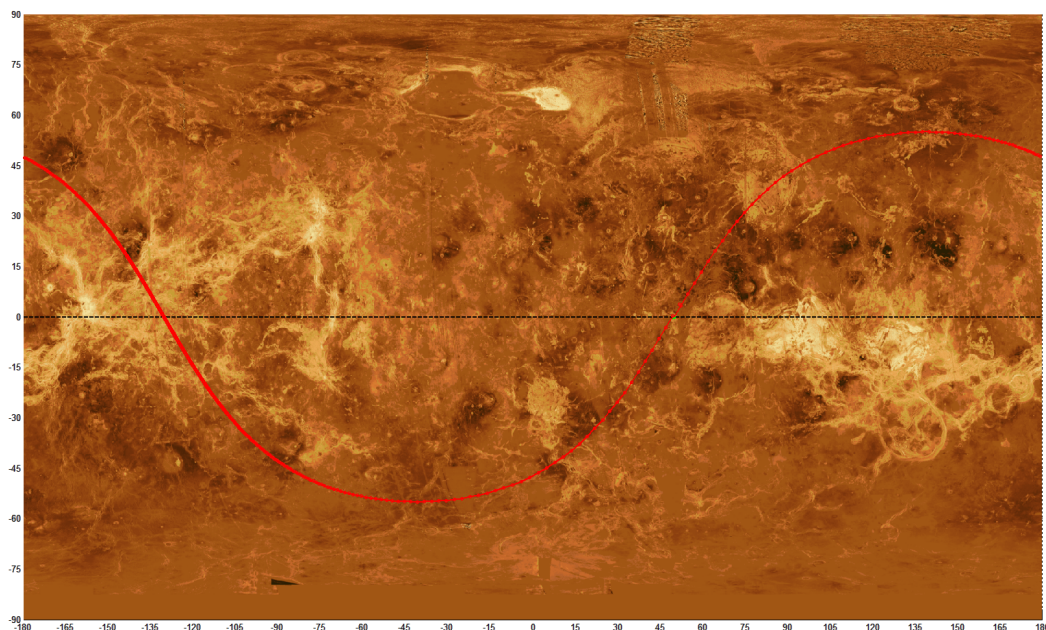


Figure 3.12: Orbit geometry for telecommunication phase (single orbit)

From Fig. 3.12, it can be observed that the dwell time of the spacecraft is longer on the Ganis Chasma region (left side of picture). This is seen by the concentration of red dots. To obtain such a dwell time, the spacecraft must perform its orbit inclination when it is at  $50^\circ$  East from the prime meridian of Venus.

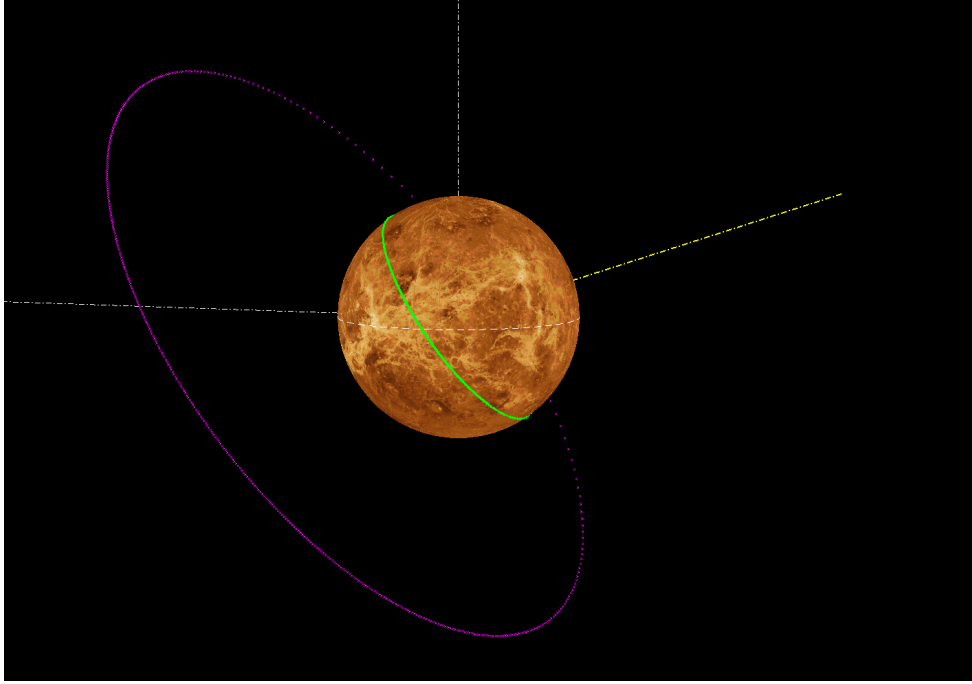


Figure 3.13: Ground track of telecommunication relay phase

### 3.3.5. UNFEASIBLE ORBITS

A Sun-synchronous orbit was also considered since it would have the advantage of passing over the same region at roughly the same local solar time. This would be enormously advantageous since the lander and aircraft would necessitate lower telecommunication re-orientation requirements. The only way to obtain a Sun-synchronous orbit is for there to be a torque applied to the orbit to rotate the angular momentum vector of the orbit in the correct direction once per year. The gravity field of an oblate planet provides just such a torque, but only at the right orbit altitude and inclination. The rotation rate of the ascending node is given by Eq. (3.3).

$$\dot{\Omega} = -\frac{3}{2} \cdot J_2 \left( \frac{r_V}{a(1-e^2)} \right)^2 \sqrt{\frac{\mu}{a^3}} \cdot \cos(i) \quad (3.3)$$

The first coefficient of the spherical harmonic expansion of a non-spherical gravity field is called  $J_2$ , and results from the oblateness of the planet.  $r_V$  is the equatorial radius of the planet. If  $J_2$  is large enough, it is possible to select  $a$ ,  $e$ , and  $i$  to get a rotation rate that matches the inertial rotation of a Sun-centered frame, about a degree a day. However, a Sun-synchronous orbit is not feasible since Venus is not oblate enough. This can be characterised by the low  $J_2$  value of Venus,  $4.458 \cdot 10^{-6}$  compared to that of Earth,  $1082.6 \cdot 10^{-6}$ . There is not sufficient torque to rotate the orbit fast enough.

A geostationary Venus orbit (GVO) was also considered. Such an orbit would be beneficial since it would constantly cover a wide area where the lander and aircraft would operate. However, in the case of Venus, to obtain a GVO, the orbiter will lie outside the Hill Sphere of the planet. The required distance needed from Venus for a GVO is given by Eq. (3.4).

$$R_{GVO} = \sqrt[3]{\frac{G \cdot M_V \cdot T_{rot,V}^2}{4 \cdot \pi^2}} \quad (3.4) \quad R_{Hill} \approx a \cdot \sqrt[3]{\frac{m}{3 \cdot M}} \quad (3.5)$$

An orbit radius of 1,536,581.759 km would be required. However, the radius of the Hill sphere is only 1,011,161 km given by Eq. (3.5), making a geo-synchronous orbit unfeasible.

## 3.4. COVERAGE

The specifications from Table 3.9 are used here to compute the coverage of each instrument, that is, the SAR, VEM, and telecom antenna. The coverage geometry is illustrated in Fig. 3.14. All calculations here are based on an elliptical orbit for the mapping phase.

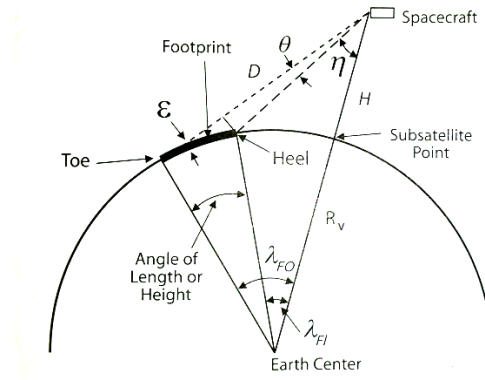


Figure 3.14: Computational geometry for footprint parameters [12]

The footprint area is the area that the instrument or antenna is viewing at any instant. It can also be understood as the field of view (FOV) of the instrument. All three instruments used the same equation which is given by:

$$FA = \left( \frac{\pi \cdot D \cdot K_L}{4} \right) \cdot \sin \theta \cdot (\lambda_{FO} - \lambda_{FI}) \approx \left( \frac{\pi \cdot D^2}{4} \right) \cdot \frac{\sin^2 \theta}{\sin \epsilon} \cdot (\lambda_{FO} - \lambda_{FI}) \quad (3.6)$$

It should be noted that the approximation for the footprint area is invalid when  $\epsilon \approx 0$ . Also,  $K_L = 1$  for length in degrees and  $K_L = 111.319543$  for length in kilometres.

The instantaneous access area or length is all the area or length that the instrument could potentially see at any instant as given by Eq. (3.7) to Eq. (3.9). The area coverage rate is the rate at which the instrument or antenna is sensing or accessing new land. It is given by Eq. (3.10) to Eq. (3.12). The area access rate is the rate at which new land is coming into the spacecraft's access area as shown in Eq. (3.13) to Eq. (3.15).

$$IAL_{SAR} = 2 \cdot K_L \cdot (\lambda_1 - \lambda_2) \approx 2 \cdot K_L \cdot D \cdot \frac{\sin \theta}{\sin \epsilon} \quad (3.7)$$

$$IAL_{VEM} = K_L \cdot (\lambda_1 + \lambda_2) \quad (3.8) \quad IAA_{telecom} = K_A \cdot (1 - \cos(\lambda)) \quad (3.9)$$

$$ACR_{SAR} = \frac{2 \cdot K_A \cdot (\sin \lambda_1 - \sin \lambda_2)}{P} \quad (3.10) \quad ACR_{VEM} = \frac{K_A \cdot (\sin \lambda_1 - \sin \lambda_2)}{P} \quad (3.11)$$

$$ACR_{telecom} = \frac{F_A \cdot (1 - O_{avg}) \cdot DC}{T} \quad (3.12) \quad AAR_{SAR} = \frac{2 \cdot K_A \cdot (\sin \lambda_1 + \sin \lambda_2)}{P} \quad (3.13)$$

$$AAR_{VEM} = \frac{K_A \cdot (\sin \lambda_1 + \sin \lambda_2)}{P} \quad (3.14) \quad AAR_{telecom} = \frac{2 \cdot K_A \cdot (\sin(\lambda))}{P} \quad (3.15)$$

T is the time in view. P is the orbit period.  $K_A = 20626.4806$  for area in  $deg^2$  or  $K_A = 2.55604187 \cdot 10^8$  for area in  $km^2$ . It should be noted that a typical value of 20% [12] is selected for the  $O_{avg}$  and a typical value of 50% [12] is taken for the duty cycle of the telecom antenna.

The access area of the SAR, VEM and telecom antenna are illustrated in Fig. 3.15, Fig. 3.16, and Fig. 3.17 respectively. The results for all three instruments are summarised in Table 3.14 and Table 3.15.

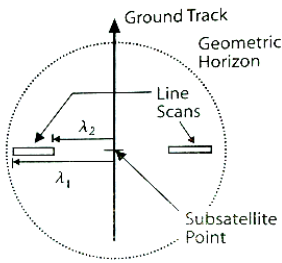


Figure 3.15: SAR access area [12]

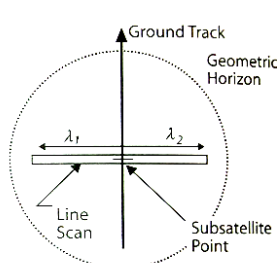


Figure 3.16: VEM access area [12]

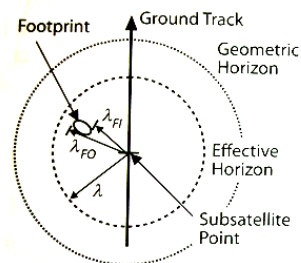


Figure 3.17: Telecom antenna access area [12]

Table 3.14: Mapping and telecommunication coverage characteristics

Instrument	FA [ $km^2$ ]	IAA/IAL [ $km^2$ or $km$ ]	ACR [ $km^2/s$ ]	AAR [ $km^2/s$ ]
SAR	10,695	5	3830	20,768
VEM	72,320	554	4499	7800
Telecom antenna	18,252,616	219,761,272	485	11,759

Table 3.15: Mapping and telecommunication coverage attributes

Phase	$\lambda_{FO}$ [ $^\circ$ ]	$\lambda_{FI}$ [ $^\circ$ ]	$\lambda_1$ [ $^\circ$ ]	$\lambda_2$ [ $^\circ$ ]	Footprint length [km]	Footprint width [km]
SAR	n/a	n/a	3.93	2.70	136.27	99.93
VEM	n/a	n/a	3.93	1.05	319.91	287.83
Telecom antenna	72.06	18.50	n/a	n/a	5962.54	3897.66

### 3.5. VISITING FREQUENCY

The visiting frequency is the time it takes for the orbiter to be in sight of the same reference point again. It is useful as it gives an approximate indication of how long it takes for the orbiter to be in sight that can be used for telecommunications purposes. The data used for the computations are taken from Table 3.13.

The visiting frequency for the orbiter when communicating with the lander is given by the orbital period, which is:

$$P_{S/C,lander} = 2 \cdot \pi \sqrt{\frac{a_{S/C,telecom}^3}{\mu_{Venus}}} = 11.96 \text{ hrs} \quad (3.16)$$

The visiting frequency for the orbiter when communicating with the aircraft is given through an iterative process:

$$P_{S/C,A/C} = (2 \cdot \pi + P_i \cdot \kappa_{A/C}) \sqrt{\frac{a_{S/C,telecom}^3}{\mu_{Venus}}} = 12.39 \text{ hrs} \quad (3.17)$$

Where  $\kappa$  is the rotational rate of the aircraft.

### 3.6. $\Delta V$ BUDGET

The  $\Delta V$  budget takes in account the plane changes, inclination changes, orbit maintenance, end-of-life manoeuvre, and a margin. The orbit maintenance for both phases takes into account the atmospheric drag, the solar pressure, and the third body perturbations. The time frame for the mapping orbit maintenance is 243 days which is the time it takes for Venus to make a complete revolution. The time frame for the telecom orbit maintenance is 90 days which is the mission lifetime of the aircraft. It should be noted that the initial Earth-orbit escape stage will be provided by the kick-stage of the launcher. The required  $\Delta V$  for this manoeuvre is 3.51 km/s. In addition, the launch will be executed at an inclination of  $85.5^\circ$  to save approximately 10 km/s on the  $\Delta V$  required by the spacecraft.

If a circular orbit of 385 km altitude is selected for the mapping phase, the necessary  $\Delta V$  requirements are summarised in Table 3.16.

Table 3.16:  $\Delta V$  Budget if circular mapping orbit selected

Sequence of manoeuvres	$\Delta V$ required [ $\frac{km}{s}$ ]	Percentage of total $\Delta V$ [%]
Venus Orbit Insertion	3.30	41.8
Apoapsis change	2.27	28.8
Inclination change	1.44	18.3
Mapping orbit maintenance	0.01	0.13
Telecom orbit maintenance	0.03	0.38
De-orbit	0.05	0.63
Margin	0.79	10.0
<b>Total</b>	<b>7.89</b>	<b>100</b>

As the spacecraft already enters the Venusian orbit at an inclination of  $85.5^\circ$ , it can directly start its mapping phase after the Venus Orbit Insertion (VOI) burn. The apoapsis change refers to the manoeuvre where the

spacecraft would increase its apoapsis from 385 km to 37,105 km to increase its contact time with the lander and aircraft. The inclination change refers to the manoeuvre where the spacecraft will have to decrease its inclination from 85.5° to 55° to start its telecommunication relay phase. The de-orbit manoeuvre refers to when the periapsis will be lowered from 385 km to 200 km for the spacecraft to burn up in the Venusian atmosphere. Finally, a 10% margin is also included in the budget which is the typical amount in most interplanetary missions [12]. This margin can be used for unforeseen correction manoeuvres or performing secondary objectives. It should be noted that the only launcher that can deliver that much  $\Delta V$  and mass (launch mass of spacecraft is 17,890 kg) is the SLS.

If a 385 km by 37,105 km elliptical orbit is selected for the mapping phase, the necessary  $\Delta V$  requirements are summarised in Table 3.17.

Table 3.17:  $\Delta V$  Budget if elliptical mapping orbit selected

Sequence of manoeuvres	$\Delta V$ required [ $\frac{km}{s}$ ]	Percentage of total $\Delta V$ [%]
Venus Orbit Insertion	1.03	35.4
Inclination change	1.44	49.5
Mapping orbit maintenance	0.07	2.4
Telecom orbit maintenance	0.03	1.0
De-orbit	0.05	1.7
Margin	0.29	10.0
<b>Total</b>	<b>2.91</b>	<b>100</b>

The mission sequence is basically the same as the previous one except that the VOI has a smaller  $\Delta V$  of 1.03 km/s as the spacecraft enters into an ellipse which requires less energy. Any launcher presented in Section 3.7 can provide the required  $\Delta V$  of 2.91 km/s with a spacecraft launch mass of 5533 kg (excluding launch adapter).

No relevant data was available to compare it with previous missions but since most previous missions had similar transfer times, that means they probably had approximately the same  $\Delta V$  requirements.

### 3.7. LAUNCHER SELECTION

A launcher needs to be selected that can deliver the spacecraft plus aeroshell to Venus. Based on our mission scenario, this launcher will need to satisfy the following requirements:

- It shall be able to deliver at least 6,000 kg into a transfer orbit to Venus.
- It shall have a fairing inner diameter of at least 4.6 meter.
- It shall be operational by 2026.

According to the following sources<sup>23, 24, 25, 26</sup> [13], the mission could be launched using any of the following launchers:

- Atlas-V 551
- Delta-IV heavy
- Space Launch System
- Falcon heavy
- Ariane 64

Table 3.18: Launcher specifications

Launcher	Payload mass possible [kg]	Launch cost [Million \$]
Atlas-V 551	~6000	85-110
Delta-IV Heavy	~8500	130-150
Falcon Heavy	~13000	100-120
Space Launch System	~32000	>500
Ariane 64	~7000	126.4

As all launchers are capable of bringing the spacecraft to Venus, if an elliptical insertion orbit is selected. If a circular insertion is selected, only the SLS can be used. The final selection of a launcher will have to be selected based on client's preference.

<sup>23</sup><http://www.ulalaunch.com/uploads/docs/AtlasVUsersGuide2010.pdf>

<sup>24</sup>[http://www.ulalaunch.com/uploads/docs/Launch\\_Vehicles/Delta\\_IV\\_Users\\_Guide\\_June\\_2013.pdf](http://www.ulalaunch.com/uploads/docs/Launch_Vehicles/Delta_IV_Users_Guide_June_2013.pdf)

<sup>25</sup><http://ntrs.nasa.gov/archive/nasa/casi.ntrs.nasa.gov/20140008794.pdf>

<sup>26</sup><http://www.spacex.com/falcon-heavy>

# 4

## LANDER

This section discusses the lander in detail. The instruments are elaborated on and the layout is described and shown, accompanied by the necessary design calculations. Furthermore, several block diagrams and budgets are given at the end of this chapter.

### 4.1. SCIENTIFIC PAYLOAD

This section deals with the instruments on board of the lander. The lander has two main instruments, a camera capable of taking images in the visual and infrared spectra and a Laser-Induced Breakdown Spectroscopy similar to the ChemCam instrument on the Mars Science Laboratory. These are discussed in Sections 4.1.1 and 4.1.2, respectively.

#### 4.1.1. VNIR CAMERA

The lander will be equipped with a camera capable of taking pictures in the visible and infrared-spectrum. This camera will be mounted in a unit on top of the lander pressure sphere which is capable of rotating 360 degrees. The images in the visual spectrum will help give context to the measurements taken by the Laser-Induced Breakdown Spectroscopy detailed in Section 4.1.2. The infrared capability will give final confirmation of any hot-spots detected from orbit or from the aircraft.

#### 4.1.2. LASER INDUCED BREAKDOWN SPECTROSCOPE

The Laser Induced Breakdown Spectroscopy (LIBS) is based on the ChemCam instrument of NASA's Mars Science Laboratory and is capable of analysing the composition of rocks from a distance of up to seven meters. This makes it a perfect tool for a lander, as it gives it a bigger area of operations than would be allowed with more traditional means.

A LIBS functions by targeting a specimen with a high-powered laser, causing part of it to turn into a plasma. The instrument will then detect the colour of the plasma, which will be analysed by a spectrometer. The data from the spectrometer can then be used to determine the composition of the plasma and thereby the composition of the target.

The instrument has two laser and detection modules for redundancy, both linked to a single spectrometer by fibre optic cables. Both of these are located within the head occupied by the camera. The instrument will be able to shift down to target the ground. It will take measurements in a pre-programmed pattern. This approach was chosen over a more deliberate manual targeting based on the camera pictures because of the severe time-constraints imposed by the Venusian environment. This pattern will then be overlaid on data gathered by the landers cameras, allowing researchers to correlate the LIBS data with specific geological features.

#### 4.1.3. CAMERA HOUSING

The camera housing will be a titanium wheel with pyrogel insulation surrounding the instruments. For the instruments to do measurements, a cutout is made, closed by a diamond lens. This lens will be protected by a cap while the lander is inactive and this cap will pop off during landing. The housing is connected to a mast reaching into the pressure vessels around the horn antenna. This mast is connected to an electric motor rotating the mast so the camera can do measurements all around the lander.

### 4.2. LAYOUT

The lander is shown in Fig. 4.1. It will consist of two shells, an externally pressurised Polymer Matrix Composite (PMC) inner shell and an internally pressurised titanium outer shell, as further explained in Section 4.2.1. A ring will be connecting the four semi-spheres to form the two pressure shells and internal struts will add additional structural strength between the pressure shells. The lander will be supported by three landing

gear legs attached to the ring and have a mast unit consisting of two cameras and a horn antenna. Furthermore, it will have four fins to ensure the correct orientation during the landing. Both the antenna and the fins are made from aluminium as they do not have to carry high loads and therefore weight can be saved. The properties of the materials used can be found in Table 4.1 [14].

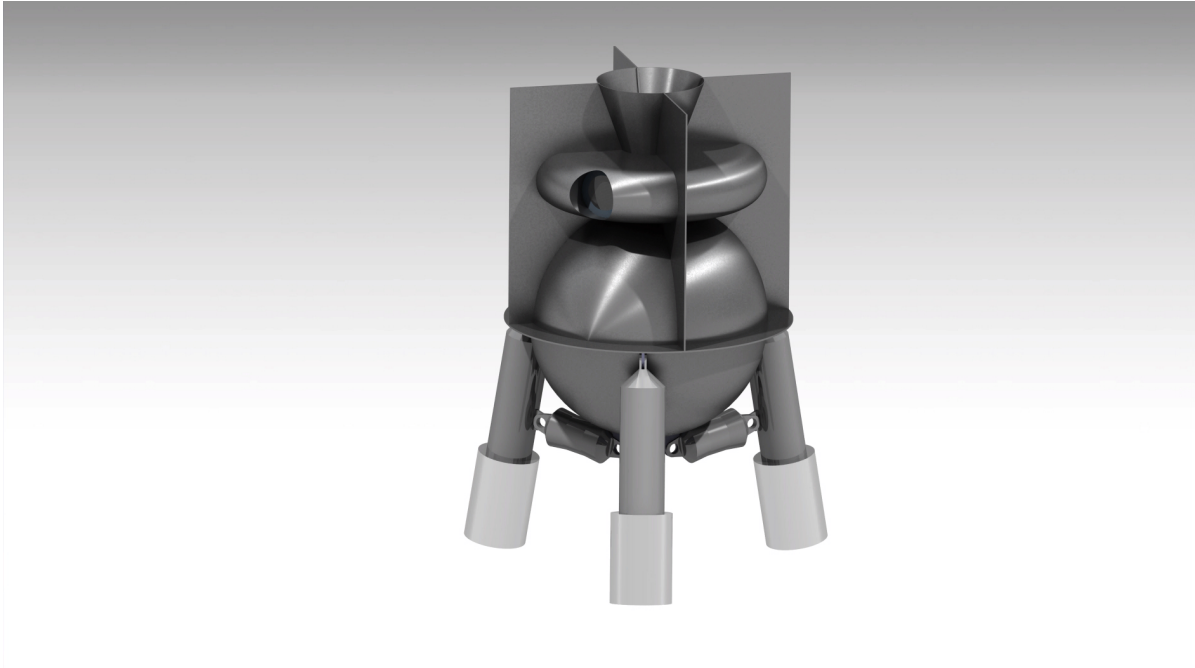


Figure 4.1: Lander

Table 4.1: Material properties of the lander

Property	PMC	Titanium Ti-6Al-4V	Aluminium 6061-T6
$\nu$ [-]	0.29	0.31	0.33
$E$ [GPa]	127	116	69
$\rho$ [ $\frac{kg}{m^3}$ ]	1450	4510	2700

#### 4.2.1. PRESSURE SHELLS

A concept has been implemented replacing an externally pressurised single titanium shell by two shells pressurised in between [14]. This means that the inner shell material does not have to withstand extremely high temperatures, thus titanium can be replaced by a lighter material. Furthermore, the outer shell can be sized for internal pressure, also resulting in a reduction in weight.

An inner shell with an outer radius of 0.17 m and will provide sufficient space for the internal instruments and battery and an outer shell of 0.33 m radius ensures enough insulation gas for sufficient surface lifetime of an hour. The pressure in between the shells will be 150 bar to ensure that it is greater than the outside pressure and the gas is a xenon krypton mixture, a gas with a high molecular mass of approximately 120 g/mol that acts as insulation, as further described in Section 4.3.

The critical buckling load of an externally pressurised shell can be calculated using Eq. (4.1), where  $\phi$  is a knockdown factor of 0.14 [14],  $E$  is the Young's modulus,  $t$  is the thickness,  $r$  is the radius, and  $\nu$  is the Poisson's ratio. From this equation the inner shell required thickness is calculated using Eq. (4.2), where  $P_{CR}$  is the critical buckling load. The yield strength of a thin spherical shell is calculated using Eq. (4.3), which can be rewritten to Eq. (4.4) to calculate the required thickness for the outer shell, where  $P_F$  is the fill pressure and  $f$  is a safety factor of 1.5. This results in a thickness of 4.5 mm for both the inner shell as the outer shell.

$$P_{CR} = \phi \frac{2Et^2}{r^2 \sqrt{3(1-\nu^2)}} \quad (4.1)$$

$$F_{TY} = f P_F \frac{r}{2t} \quad (4.3)$$

$$t_{in} = \sqrt{\frac{P_{CR} r_{in}^2 \sqrt{3(1-\nu_{in}^2)}}{2\phi E_{in}}} \quad (4.2)$$

$$t_{out} = \frac{f P_F r_{out}}{2F_{TY}} \quad (4.4)$$

#### 4.2.2. LANDING GEAR

The landing gear is responsible for handling the shock and stress of touch-down of the lander. To do this, it needs to be both strong and capable of absorbing the shock of touchdown.

For the structure of the landing gear, titanium will be used. This alloy retains good mechanical properties under the extreme heat of the Venusian atmosphere and has very limited thermal expansion<sup>27</sup>.

The landing gear consists of three legs, each has been designed to be able to endure the entire landing force. This is necessary because, if the lander lands on a slope or is not oriented completely vertical on touch-down, one landing leg will hit the ground first, taking on all loads.

Since the lander is deployed from the aircraft at an altitude of 38 km, it will take a while before it reaches the surface. During descent, the lander temperature will already start increase, so a lower descent time would increase surface lifetime. On the other hand, a faster descent also results in a larger impact, meaning stronger and therefore heavier landing gear. A trade-off was made between longer lifetime and lower landing gear weight. Deploying a parachute near the surface was discarded due to the chance of the parachute covering the lander on the surface.

To calculate the velocity of the lander during the descent, the drag is calculated using Eq. (4.5). Combined with the gravitational acceleration and mass at every time step, the acceleration per time step can be calculated from which the velocity can be calculated by Eq. (4.6). Using a conservative 0.45 for  $C_D$ , the vertical velocity during touchdown will be no more than 10 m/s with a descend time of approximately 38 minutes, graphically shown in Fig. 4.2. The horizontal velocity was also taken into account, since the lander will have a initial horizontal velocity similar to the aircraft, but due to the dense atmosphere, this velocity reaches zero within the first minutes, long before landing.

$$D = C_D \frac{1}{2} \rho V^2 S \quad (4.5) \quad V_{i+1} = V_i + \frac{F_{g,i} - D_i}{m} * t_{step} \quad (4.6)$$

The landing gear consists of a main strut and a perpendicular secondary strut. The purpose of the secondary strut is to carry and absorb lateral forces. These have been sized to resist buckling and yielding due to the touch-down forces. The final lander design lander can be seen in Fig. 4.1.

The vertical and horizontal speeds have been used to optimise the inclination of the landing gear. The landing gear angle with respect to the ground is 80 degrees. This is based on a desire to limit the maximum speed of the ground with respect to the secondary landing gear. Landing slope angles from 0 to 20 degrees where analysed to determine the most optimal inclination.

Based on the payload and structural concerns, it was decided that the maximum vertical deceleration would be 30g, while the tip-over criteria also played a role in the decision to limit the maximum horizontal deceleration to 5g. These maximum accelerations, when combined with the lander weight, determine the maximum force that will be applied to the landing gear. The landing gear is then sized to resist these forces. Both the direct compression strength of the material and the buckling criteria have been used to determine the final dimensions of the landing gear.

Shock absorption is provided by an aluminium hexagonal honeycomb structure [15]. During landing, the structure is crushed, thereby reducing the shock on the structure as a whole.

This simple but irreversible solution was chosen over other options due to the challenges posed by the Venusian and space environment.

The secondary struts have a small pad of 6 cm thick of the honeycomb material. The main landing gear has a thicker column of 24 cm. The thickness of the honeycomb materials was based on the reduction in landing gear length needed to result in the stipulated maximum deceleration, as detailed in Eq. (4.7). Here, L is the length of the crushable region, a is the acceleration and V is the speed during touchdown.

$$L = \frac{1}{2} \frac{V^2}{a} \quad (4.7)$$

<sup>27</sup><http://cartech.ides.com/datasheet.aspx?i=101&E=269>

### 4.2.3. FINS

It is crucial for the mission to ensure that the lander will land with the correct orientation. Adding a parachute or drag plate on top would result in descent times too long for survival, and thus fins were added instead. Fins ensure that the Centre of Pressure (CP) is behind the Centre of Gravity (CG), resulting in dynamic stability and landing feet down. The CG is computed in CATIA with the ring as reference height. Determining the exact location of the CP is beyond the scope of this research, therefore, since the CG is approximately at the height of the ring i.e. at 3 cm, it is assumed that the CP will be above the CG when the surface above the ring is larger than that underneath the ring. The surface underneath the ring is estimated to be  $0.25 \text{ m}^2$ , so applying a safety factor of 2, adding the fins results in an upper surface over  $0.5 \text{ m}^2$ .

## 4.3. THERMAL CONTROL

The Venusian surface temperature shall overheat the processor of the lander over time, rendering the lander useless. It is important to design the lander such that it has enough time to do its measurements and send back the data. To satisfy the primary mission objectives, it is assumed the lander can satisfy them if it has a surface lifetime of 30 minutes.

The thermal resistance of the lander is calculated as the sum of the thermal resistance of three spherical shells, the inner shell, insulation gas, and the outer shell. The conductance of a sphere is calculated using Eq. (4.8), where  $k$  is the thermal conductivity of the material. To determine the thermal conductivity of a gas, Eq. (4.9) is used [14], where  $M$  is the molar mass. The thermal flow can then be found with Eq. (4.10), where  $f$  is a safety factor and  $\dot{Q}_{eq}$  the heat flow produced by the equipment. Eq. (4.11) gives the new equipment temperature, where  $c$  is the specific heat of the instruments.

Applying these equations and setting the failure temperature at  $125^\circ \text{ Celsius}$ <sup>28</sup>,  $\dot{Q}_{equip}$  at 20 W and a safety factor of 1.5, and a specific heat similar to aluminium of  $910 \text{ J/kgK}$ , the total lifetime of the lander is 102 minutes and the surface lifetime is 64 minutes, as shown in Fig. 4.3. Similarly, the lifetime of the cameras is estimated. Note that during descent, the temperature of the lander increases exponentially due to the fact that the the outside temperature increases with decreasing altitude, this effect stops when the lander reaches the surface, explaining the bump in Fig. 4.3. The instruments are simulated as a cylinder of 5 cm radius with an pyrogel insulation of 2 cm thick around it. The conductance of a cylinder is calculated using Eq. (4.12), resulting in 58 minutes surface life time.

The surface lifetime for both the internal instruments as the external cameras of approximately an hour should suffice to fulfil the primary mission objectives, including a safety factor.

$$G_{sphere} = \frac{4\pi k R_{out} R_{in}}{R_{out} - R_{in}} \quad (4.8) \quad k = 1.6 \times 10^{-2} \left( \frac{M^{-0.35}}{40} + 1.6 \times 10^{-5} T_{avg} \right) \quad (4.9)$$

$$\dot{Q} = \Delta T \cdot Gf + \dot{Q}_{eq} \quad (4.10) \quad T_{eq_{i+1}} = T_{eq_i} + \frac{\dot{Q} dt}{m_{eq} c} \quad (4.11) \quad G_{cylinder} = \frac{2\pi k L}{\log\left(\frac{R_{out}}{R_{in}}\right)} \quad (4.12)$$

## 4.4. POWER SYSTEM

A primary battery will be the power source for the lander because of the short lifetime, the lack of sufficient charging methods on the surface, and the higher specific energy compared to secondary batteries. Lithium thionyl chloride batteries ( $\text{Li/SOCl}_2$ ) have the highest energy density operating at high temperatures [16]. At the moment, batteries with a  $375 \text{ Wh/kg}$  specific energy are available<sup>29</sup>. When the lander operates at full capacity, it consumes 110 W, since the laser and electric motor will never be active at the same time. Combined with the surface lifetime of approximately 60 minutes and a large safety factor, the battery should be sized to provide 200 Wh. Using a conservative  $250 \text{ Wh/kg}$  and aiming for for  $200 \text{ Wh/kg}$ , only 0.8 kg of batteries are necessary. This safety factor compensates for the self-discharge rate of 0.08% per month [17] over the 13 month period prior to deployment as well as other efficiency losses.

## 4.5. COMMUNICATIONS

The data that is gathered by the scientific instruments and housekeeping sensors on the lander has to be transmitted to the satellite. For this, a communications subsystem is necessary. In this section first the Com-

<sup>28</sup>[https://www.altera.com/products/common/temperature/ind-temp.html#temp\\_grades](https://www.altera.com/products/common/temperature/ind-temp.html#temp_grades)

<sup>29</sup><http://www.powerstream.com/lip.htm>

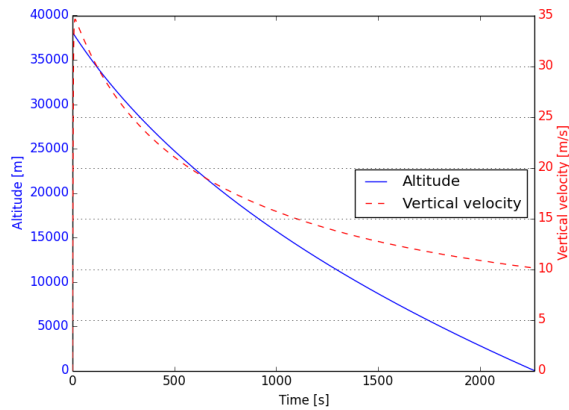


Figure 4.2: The altitude and vertical velocity of the lander over time during the descent

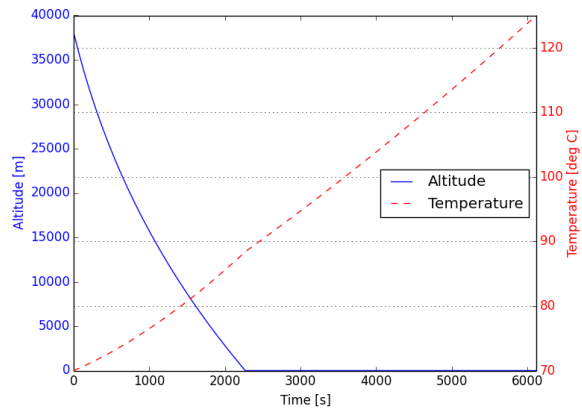


Figure 4.3: The altitude and equipment temperature of the lander over time

mand and Data Handling System (CDHS) will be treated followed by the method of communicating with the satellite.

#### 4.5.1. CDHS

The CDHS collects, stores and prepares all data for transmission. It also receives the incoming commands from Earth and distributes the commands over the appropriate subsystems. The lander will almost instantly transmit any data it generates to the spacecraft because of its short lifetime so only 2 Gbit of storage capacity is included to account for possible data overflow. The data rate generation of the lander that needs to be sent to the spacecraft is 283 kbit/s. Before the data can be transmitted or even stored, it needs to be compressed. This compression will be performed by a processor, which will not only be reserved for compressing data but also act as the central brain of the lander. Therefore, it needs to be a rather powerful processor. Furthermore, the processor will also interpret the commands coming from Earth and distribute them over the subsystems.

To fulfil these objectives the CDHS is made out of the components listed below. For redundancy each of the components will be used twice. The specific models mentioned at each part are examples that would fulfil the specification. However, the specific model might change in the final product due to a cheaper or better alternative.

- Airbus DS solid state recorder<sup>30</sup>: This solid state recorder based on new flash memory will provide the 2 Gbit storage space necessary. Two of these solid state recorders will be used for redundancy.
- The BAE RAD 5545<sup>31</sup>: Will provide the computational power necessary. The processor is radiation hardened to reduce the risk of bit flipping due to radiation. The RAD 5545 is currently one of the fastest radiation hardened processors with four physical cores running at 2.2 GHz. For redundancy two of these processors will be used in the design.

#### 4.5.2. TT&C

The Telemetry Tracking and Command (TT&C) system is responsible for the transmitting of data and receiving of commands. The lander will only communicate with the spacecraft. The lander will therefore only have one antenna. The sizing of the antenna and the power required is determined by the need to close the link budget. To close the link budget, the antenna specifications listed in Table 4.2 are required.

For the communications the required Bit Error Rate (BER) is  $10^{-6}$  as this will provide enough data clarity to process the data [12]. To close the link budget a certain Signal to Noise Ratio (SNR) is necessary to actually distinguish the data at the receiver. To reduce the required SNR, the data can be coded by using so called forward error correcting codes. By using these codes one reduces the necessary SNR by sending extra, redundant bits. For the communication of the lander QPSK 1/4 code was selected. With the selected forward error correcting code, QPSK 1/4, a SNR of 2.31 dB is necessary to achieve the BER of  $10^{-6}$  [12]. It should be noted that an additional safety factor is applied in the link budget by increasing the atmospheric loss to 3 dB

<sup>30</sup>[http://www.space-airbusds.com/media/document/ens\\_5\\_ssr\\_2014\\_bd.pdf](http://www.space-airbusds.com/media/document/ens_5_ssr_2014_bd.pdf)

<sup>31</sup><http://www.baesystems.com/en-us/download-en-us/20151124120253/1434571328901.pdf>

to account for the thicker Venusian atmosphere.

With the system as described above the link budget between lander and spacecraft can be closed as is shown in Table 4.3. For the uplink from the spacecraft a data rate of 10 kbit/s is assumed. The table shows that this uplink budget also closes by a very large margin, meaning that the data rate can be increased if necessary.

Table 4.3: Linkbudget Lander-Spacecraft

Parameter [dB]	Downlink	Uplink
Lander antenna gain	24.39	
Lander pointing loss	-0.03	
Lander power	11.14	N/A
Lander loss factor	-0.97	
S/C antenna gain	34.15	
S/C pointing loss	-0.05	
S/C power	N/A	6.99
S/C loss factor	-0.97	
Space loss	-211.92	
Atmospheric loss	-3.00	
System noise temperature	-21.30	
Boltzmann	228.60	
Data rate	-54.52	-40.0
QPSK 1/4 required margin	2.31	
Required margin to close	3.00	
<b>Total required <math>E_b/N_0</math></b>	<b>5.31</b>	
<b>Total <math>E_b/N_0</math></b>	5.52	15.89
<b>Total margin</b>	<b>0.21</b>	<b>10.58</b>

Table 4.2: Specifications of spacecraft telemetry system

Specifications	Lander-Spacecraft
Antenna type	Conical horn
Antenna size/diameter [m]	0.26
Transmitter power [W]	13
Data transmission band	X-band [8.0-8.4 GHz]

## 4.6. BLOCK DIAGRAMS

This section shows a number of block diagrams for the lander that help better visualise the interactions between the different components used in the design. This includes, the hardware, software, data handling and electrical diagram, which are treated in Section 4.6.1 through Section 4.6.4.

### 4.6.1. HARDWARE

The hardware diagram shown in Fig. 4.4 indicates the different systems present in the lander and their interactions with each other. All the heat flowing to the inside flows through the thermal control system and is spread evenly over the systems on the inside. The scientific payload will be rotated by the rotary engine. There is also a connection from the lander to the aircraft which will be used to provide the lander with some power to keep some systems running and to transfer housekeeping data of the lander. This connection is cut when the lander is deployed from the aircraft.

### 4.6.2. SOFTWARE

The software diagram in Fig. 4.5 indicates how the different software on board of the lander communicate with each other, to provide scientific data. As the lander has a lifetime of only a few hours, and in that time simply generates scientific data, the software diagram is not very complex. The key software are those that process the inputs to the payload sensors. All data generated will be added to a carrier signal, the so-called modulation, before it is transmitted to the spacecraft.

### 4.6.3. DATA HANDLING

The lander scientific equipment and other on board equipment will be generating data from the point at which it is deployed from the carrier. To visualise how this data is handled, the data handling diagram in Fig. 4.6 is created. As the lander will almost instantly transmit any data it has generated, because of its short lifetime, it will have to be in range of the satellite during its deployment. All data generated by the instruments is sent to the processor that compresses the data, and either sends it to the flash storage, or directly to the

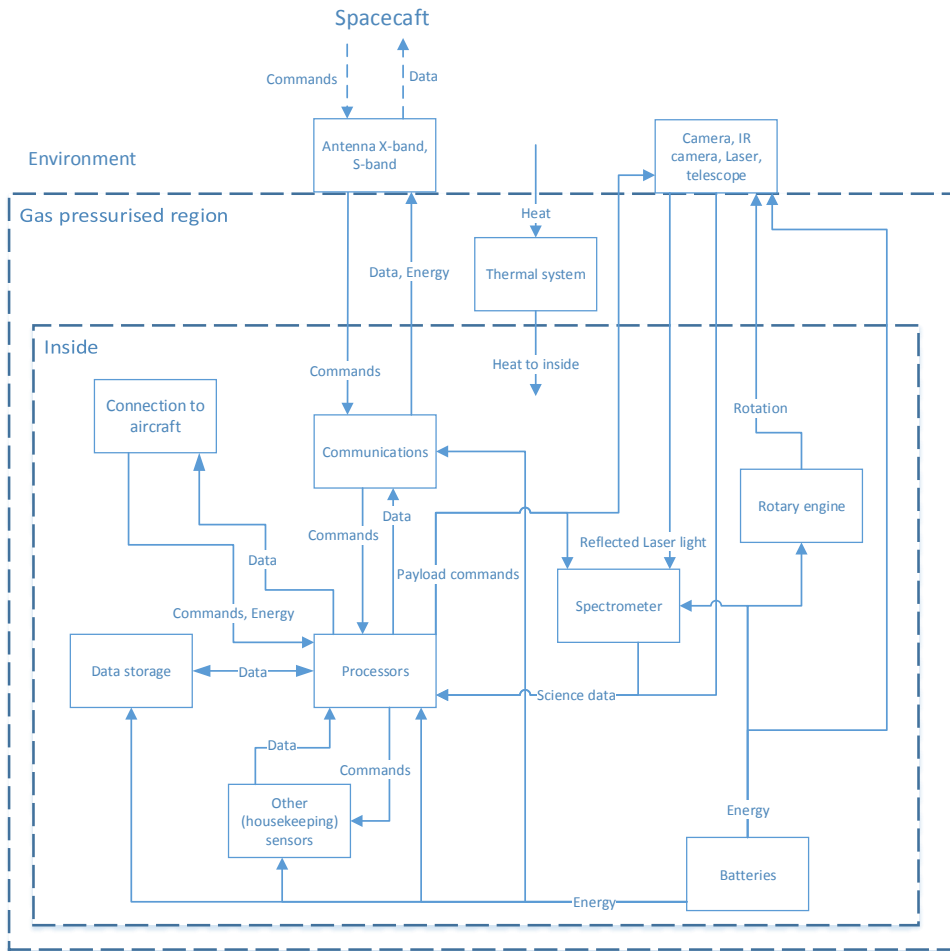


Figure 4.4: Lander H/W diagram

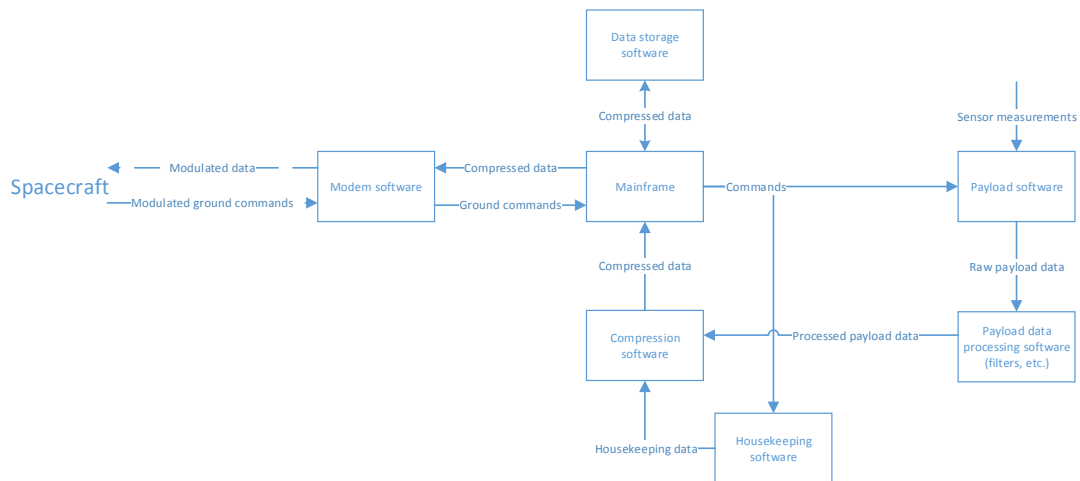


Figure 4.5: Lander S/W diagram

modem. The modem then modulates the signal for the antenna, which transmits the data to the spacecraft.

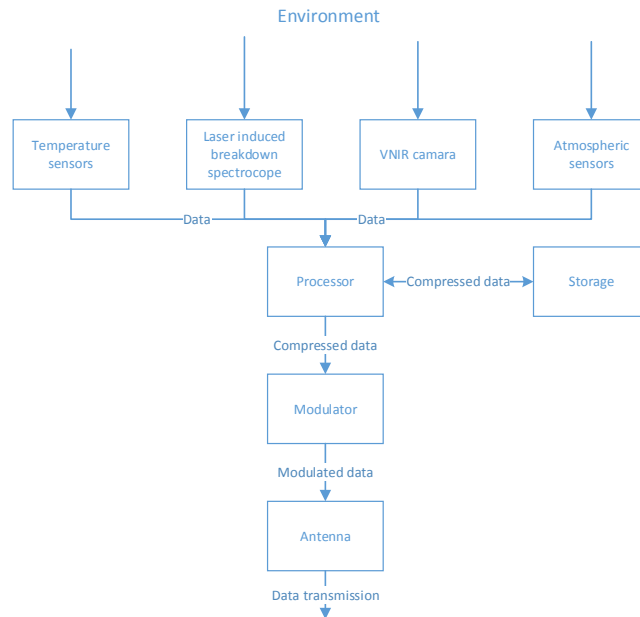


Figure 4.6: Lander data handling block diagram

#### 4.6.4. ELECTRICAL

The electric block diagram of the lander can be seen in Fig. 4.7. In this diagram, PDU stands for Power Distribution Unit. This unit contains all the switches of the different loads. In front of the loads, power converters and a fuse is used. Fuses can be used to prevent the circuit from overcurrent. It will separate circuit from the load after the fuse, which means this load can not be used any longer. They are only used for non-critical loads. Fuses for critical loads are left out for simplicity of the system. Power converters are needed because the different loads require different input voltages and currents. In the block diagram, wire redundancy was not taken into account. However, the most critical wires will have redundancy in the final design.

In general, a power system can be fully regulated or Sun-regulated. In case of a fully regulated system, a power regulated unit assure a constant circuit voltage. This unit is needed because battery output voltages depends on if its fully charged or not. In case of a sun-regulated system, the voltage depends on the power available from the solar panels. Because the lander does not use solar energy, the second option does not exist and the first option is chosen. The lander will use a direct current. Power converters are more efficient for an alternating current. However, power converters for direct current are becoming more efficient and the payload requires a direct current.

#### 4.7. BUDGETS

The mass, power, and cost budget of the lander are shown in Table 4.4. The mass was estimated by making the lander in CATIA to get accurate volumes of the components and multiplying those by the material density. Furthermore, information mass and power consumption of the instruments were found from [18] [19]. An unforeseen cost category of 10 million euros is added as a margin to account for costs underestimations.

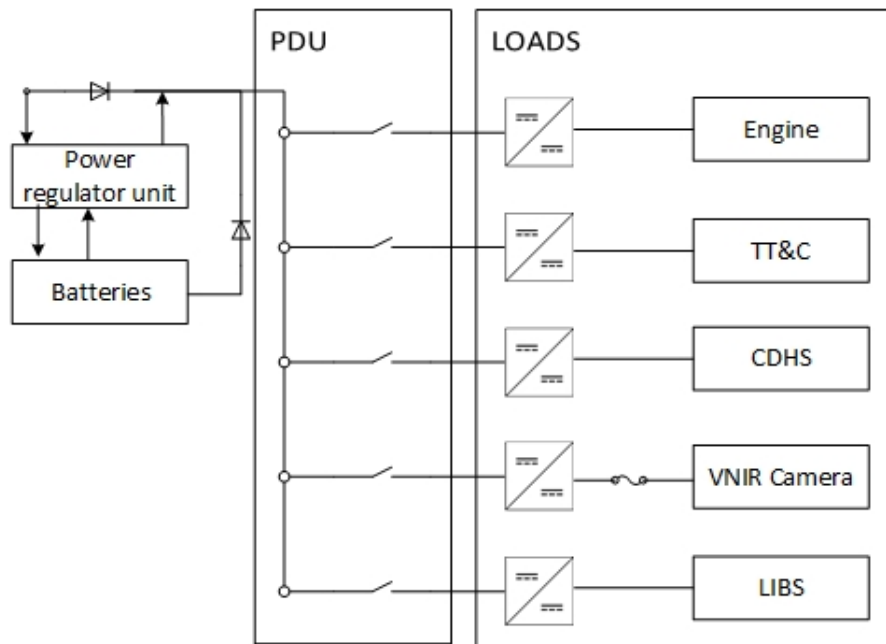


Figure 4.7: Lander electrical block diagram

Table 4.4: Mass, power, and cost budget of the lander

Component	Mass [kg]	Power [W]	Cost [k€]
Payload	9.11	149.7	30,610
LIBS	5.01	64.7	30,000
VNIR Camera	2.50	5	200
CDHS and TT&C	0.30	40	300
Electric motor	0.50	40	10
Battery	0.80		100
Structural components	83.01		5,000
Inner tank	2.08		
Outer tank	27.20		
Ring	9.19		
Camera housing	20.33		
Mast	0.93		
Structural reinforcements	5.51		
Landing gear	16.69		
Antenna	1.08		
Insulation	1.10		130
Pressurised gas	0.65		30
Pyrogel	0.45		100
Unforeseen			10,000
<b>Total</b>	<b>93.22</b>	<b>149.7</b>	<b>45,740</b>

# 5

## AIRCRAFT

This chapter will discuss all of the key features of the aircraft that will be operating on Venus. This ranges from the scientific payload in Section 5.1 to the different budgets in Section 5.11.

### 5.1. SCIENTIFIC PAYLOAD

In order to perform the mission objectives the aircraft has to carry four scientific instruments. These instruments are detailed in Sections 5.1.1 to 5.1.4 below. In addition to these instruments, the aircraft also carries a lander. The lander was already described in Chapter 4.

#### 5.1.1. SYNTHETIC APERTURE RADAR

The Synthetic Aperture Radar (SAR) was included due to the necessity of the aircraft being able to determine its ground speed. It will have a very rough resolution, comparable to that obtained by the SAR on the spacecraft, with a smaller swath width.

#### 5.1.2. VENUS EMISSIVITY MAPPER

The Venus Emissivity Mapper (VEM) is designed to map the surface emissivity of Venus. This would allow it to detect 'hot-spots' on the surface which would indicate volcanic activity. It would also allow for the characterisation of the surface geology due to the different infrared spectra of various kinds of rocks.

The VEM observes 13 different spectral bands with bandwidths of less than 20 nm. These bands are located within the 800-1800 nm wavelength region. These wavelengths are located in an 'atmospheric window', which is a wavelength region in which minimal absorption by the Venus atmosphere occurs. This means that the light received by the instrument has not been interfered with by the atmosphere

#### 5.1.3. CAMERA

A camera will be used to take aerial pictures of the Venusian surface when the aircraft is in the lower part of its track below most of the clouds. These pictures will be used for locating volcanoes and suitable landing zones for the lander, but also for other scientific objectives that can be completed by making use of the images.

Table 5.1: The aircraft SAR specifications. The parameters of the SlimSAR<sup>a</sup> where used as a basis, though the design will have to be modified somewhat to work at longer range. Table 5.2: Main parameters of the VEM [20].

Synthetic Aperture Radar		Venus Emissivity Mapper	
Power consumption [W]	150	Power consumption [W]	18.5
Mass [kg]	2.8	Mass [kg]	5.4
Swath width [km]	10	Swath width [km]	330
Ground resolution [m]	60	Ground resolution [km]	50

<sup>a</sup><https://directory.eoportal.org/web/eoportal/airborne-sensors/microasar>

Table 5.3: Specifications of the camera. Its parameters are based on terrestrial aerial cameras such as [21]

Aerial Camera	
Power consumption [W]	7.5
Mass [kg]	0.4
Resolution	3840x2160
Viewing angle [degrees]	variable

The camera will be a relatively standard Charge-Coupled Device (CCD) digital camera with a lens that will allow for the field of view to be varied. This allows for close examination of possible lander landing sites or other interesting features, while a wider angle allows for larger areas to be captured in one picture.

#### 5.1.4. SPECTROPOLARIMETER FOR PLANETARY EXPLORATION

The Spectropolarimeter for Planetary EXploration (SPEX) will gather data on the composition, size and shape of aerosol particles within the atmosphere. This information will improve the understanding of the Venusian

atmosphere and its composition. The instrument consists of three sets of optics pointing in different directions. These are connected to a single sensor that processes the light. This means that measurements can only be taken with one set of optics at a time, but it also reduces the weight and power consumption of the complete unit.

Electromagnetic radiation can be portrayed as a wave oscillating in a plane. Normal light consists of light oscillating in a wide variety of different planes. Many substances can force light to adhere to only one plane when light passes through or is reflected by it. A polarimeter can detect the amount by which the light has been rotated, or polarized. Based on this data, scientists can determine the properties of the polarising medium and thereby determine the composition.

## 5.2. MISSION PROFILE

The desire to fly at lower altitudes to perform more accurate measurements coupled with the extreme Venusian atmosphere imposes challenges on the aircraft that can only be resolved when limiting the speeds, altitudes and cruising times that the aircraft will fly at in the Venusian atmosphere. In order to gauge where and how flight is possible this section will first perform a basic aircraft-oriented investigation into the Venusian atmosphere in Section 5.2.1, after which the method by which the tracks the aircraft will fly through the Venusian atmosphere are determined will be present in Section 5.2.2. When tracks can be determined the limits to flight are established in Section 5.2.3. The required solar panel area and battery capacity required to fly at any given generated flightpath will be analysed in Section 5.2.4.

### 5.2.1. INFLUENCES OF THE VENUSIAN ATMOSPHERE ON AIRCRAFT DESIGN

General aircraft design for Earthbound aircraft usually does not take wind speeds into account in the initial design phases. However, as the zonal wind speeds are extremely large on Venus they must be taken into account first hand [6] [22]. Hence it makes sense to distinguish the aerodynamic freestream velocity  $V_\infty$  from the wind speeds  $V_W$  and an inertial velocity  $V_I$ , these are related by the simple relation shown in Eq. (5.1). The inertial velocity  $V_I$  is measured compared to a fixed point, continuously above the same spot on the surface of Venus, at the same height as the aircraft is flying at any given moment.

For a given inertial velocity  $V_I$  at a given height  $h$  VIRA predicts a corresponding density  $\rho$  and zonal wind-speed  $V_W$  [6] [7]. Neglecting the meridional and vertical windspeed components this allows calculating the dynamic pressure  $q_\infty$  experienced by the aircraft. The zonal windspeed will be influenced by the severity of the weather. In order to deal with these variations in a systematic manner a weather severity parameter  $\zeta$  is introduced and defined for any given atmospheric parameter  $c$  (density, temperature, etc.) as shown in Eq. (5.2) (e.g. a value for  $\zeta$  of 0.0 implies average atmospheric conditions, a  $\zeta$  of 1.0 implies more severe weather: higher wind speeds, densities and temperatures). The dynamic pressure  $q_\infty$  for various values of atmospheric severity  $\zeta$  are shown in figure Fig. 5.1.

$$V_\infty = V_W + V_I \quad (5.1)$$

$$c = \begin{cases} \bar{c} + \zeta \cdot (c_{\max} - \bar{c}) & \text{if } \zeta \geq 0 \\ \bar{c} + \zeta \cdot (\bar{c} - c_{\min}) & \text{if } \zeta < 0 \end{cases} \quad (5.2)$$

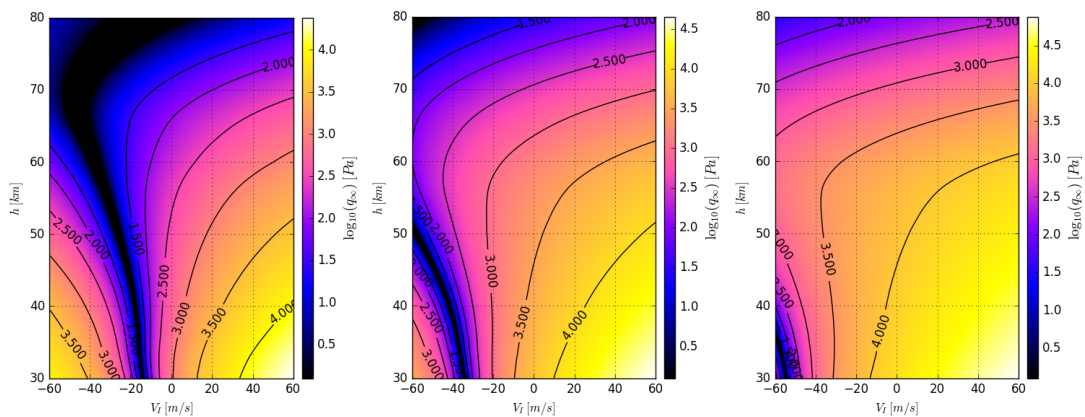


Figure 5.1: The variation of dynamic pressure  $q_\infty$  with inertial speed  $V_I$ , altitude  $h$  and the atmospheric severity  $\zeta$ . From left to right  $\zeta = -1.5$ ,  $\zeta = 0.0$  and  $\zeta = 1.5$ .

Comparing Fig. 5.1 to Fig. 2.1 one can see that at the lower altitudes the influence of the wind speed is predominantly influencing the dynamic pressure  $q_\infty$ . At higher altitudes the main influencing parameter is the density  $\rho$ . The flight envelope is now determined as dictated by the dynamic pressures through the items listed below. Other limitations will be investigated later.

- The aircraft cannot experience too large a range of dynamic pressures. For a given chosen planform without high lift devices the aircraft must be able to fly without stalling at low dynamic pressures and must be able to fly in a controllable fashion at high dynamic pressures (small changes in angle of attack may not cause large variations in aerodynamic forces and moments).
- The aircraft must stay, on average, at the same solar longitude close to the subsolar point to satisfy power generation requirements. This implies flying at a inertial speed  $V_I$  such that the ground speed is equal to the rotational rate of Venus with respect to the sun (an almost constant value of  $1.81 \text{ m/s}$  at the considered flying altitudes). Alternatively the inertial speeds must consist of a section where  $V_I > 0 \text{ m/s}$  to move prograde, followed by a section where  $V_I < 0 \text{ m/s}$  to move in retrograde fashion back to the same solar longitudinal position.
- In case of prolonged extreme weather there must be a point where the aircraft can fly at a constant cruising velocity at a given latitude and solar longitude until the weather calms down.

Initially requiring that the ratio of maximum to minimum dynamic pressure  $q_\infty$  stays within a reasonable factor of 25 then from Fig. 5.1 it can be seen that the aircraft must fly against the wind ( $V_I > 0$ ) at upper altitudes and must fly with the wind ( $V_I < 0$ ) at lower altitudes. In order to keep the analysis relatively simple large banking manoeuvres are not considered and the freestream speed  $V_\infty$  is assumed to always be pointed prograde.

Apart from aerodynamic considerations the aircraft must also remain cool enough for the electronics to remain operational. Active cooling, considering the temperatures shown in Section 2.2 will be very power consuming, hence the choice for passive cooling: remaining long enough in the upper atmosphere to cool down and using the aircraft's thermal mass and insulation to survive the higher temperatures at lower altitudes.

Lastly the thick clouds on Venus have their upside and downside. On one hand quite a lot of solar flux is scattered and reflected in the upper atmosphere. Causing approximately an equivalent 70 – 80% of the incident solar flux at the top of the aircraft to arrive at the bottom of the aircraft [23]. This allows using the bottom of the aircraft to generate electricity using solar panels.

However, due to the thick clouds, the solar efficiency drops rapidly below  $55 \text{ km}$ . Hence, when residing in the lower atmosphere enough battery capacity must be available to perform measurements and climb out again. In the upper atmosphere enough solar panel area must be available in order to recharge the batteries.

### 5.2.2. DETERMINING THE FLIGHTPATH THROUGH THE VENUSIAN ATMOSPHERE

For a given aircraft with defined wing planform and relations between lift coefficient  $C_L$ , drag coefficient  $C_D$ , and angle of attack  $\alpha$  its flightpath under specified flight conditions can be simulated by solving a simplified set of equations of motion. In order to perform these calculations and optimise the aircraft's path throughout the atmosphere three methods are required. Firstly, the aircraft's angle of attack under a given set of flight conditions and assumptions must be determined. Secondly, given the initial aircraft orientation and some control input, a timestep in the aircraft's motion must be solvable. Lastly these timesteps must be repeated in order to generate time series of the aircraft's flight parameters.

#### DETERMINING THE ANGLE OF ATTACK UNDER SPECIFIED FLIGHT CONDITIONS

During the various flight phases of the aircraft a recurring requirement is to figure out the angle of attack (and thrust, in some cases) in order to facilitate certain flight conditions. For climbing flight there is the case where there is a given thrust and where the angle of attack should be determined in order to allow for a constant climb angle  $\gamma$ . The other climbing case is the one where the angle of attack and the thrust are determined to produce a constant climb angle  $\gamma$  flight path without accelerating. Lastly there is the case where the angle of attack and thrust have to be determined to result in steady cruising flight.

The forces associated with climbing are shown in Fig. 5.2. The equations of motion are given by Eq. (5.3).

$$\frac{W}{g} a_{\text{hor}} = T \cos(\gamma + \alpha + \epsilon) - L \sin(\gamma) - D \cos(\gamma) \quad \frac{W}{g} a_{\text{ver}} = T \sin(\gamma + \alpha + \epsilon) + L \cos(\gamma) - D \sin(\gamma) - W \quad (5.3)$$

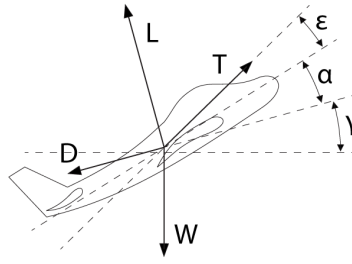


Figure 5.2: Overview of flight forces and geometry during climbing

Where  $W$  is the aircraft weight in  $N$ ,  $g$  is the local gravitational acceleration in  $m/s^2$ ,  $a_{\text{hor}}$  and  $a_{\text{ver}}$  are the aircraft's horizontal and vertical acceleration in  $m/s^2$ .  $T$ ,  $L$  and  $D$  are the thrust, lift and drag forces in  $N$  and  $\gamma$ ,  $\alpha$  and  $\epsilon$  are the flight path angle, angle of attack and the propeller incidence angle in rad, respectively. Requiring that the aircraft's acceleration is in the direction of the current flight path yields Eq. (5.4).

$$a_{\text{ver}} = a_{\text{hor}} \tan(\gamma) \quad (5.4)$$

Combining Eq. (5.3) and Eq. (5.4) yields equation Eq. (5.5).

$$T \left( \frac{\cos(\gamma + \alpha + \epsilon)}{\cos \gamma} - \frac{\sin(\gamma + \alpha + \epsilon)}{\sin \gamma} \right) - q_{\infty} S C_L \left( \frac{1}{\sin \gamma \cos \gamma} \right) + \frac{W}{\cos \gamma} = 0 \quad (5.5)$$

This equation cannot be easily solved analytically as  $C_L$  depends on  $\alpha$  and differs with each wing planform design iteration. By implementing the relation between the lift coefficient  $C_L$  and the angle of attack  $\alpha$  and Reynolds number  $Re$  by a lookup table programmatically the equation can be solved numerically. The lookup table is implemented by performing bisectional lookup on both the  $\alpha$  and the  $Re$  axis [24]. Taking the derivative of Eq. (5.5) with respect to the angle of attack  $\alpha$  yields Eq. (5.6).

$$-T \left( \frac{\sin(\gamma + \alpha + \epsilon)}{\cos \gamma} + \frac{\cos(\gamma + \alpha + \epsilon)}{\sin \gamma} \right) - q_{\infty} S \frac{dC_L}{d\alpha} \frac{1}{\sin \gamma \cos \gamma} = 0 \quad (5.6)$$

Applying a Newton-Rhapson method to Eq. (5.5) and Eq. (5.6) allows estimating the angle of attack  $\alpha$  [24]. Differentiation of  $C_L$  is performed by a 5-point central difference algorithm. At the edge the 1 point forward/backward method and at the point next to it a 3 point central difference method is used. Given the linearly increasing  $C_L$  graph and the quadratic  $C_D$  graph a safe initial estimate is an angle of attack  $\alpha$  of  $0^\circ$ .

Another considered flight condition is climbing flight where both the velocity  $V_I$  and the flight path angle  $\gamma$  remain constant. Using the same forces as shown in Fig. 5.2, the required thrust  $T$  and angle of attack  $\alpha$  can be obtained by using Eq. (5.3) but now requiring the accelerations  $a_{\text{hor}}$  and  $a_{\text{ver}}$  to be 0. This yields Eq. (5.7), taking its derivative with respect to the angle of attack  $\alpha$  results in equation Eq. (5.8).

$$q_{\infty} S [C_L (\sin \gamma \tan(\gamma + \alpha + \epsilon) + \cos \gamma) + C_D (\cos \gamma \tan(\gamma + \alpha + \epsilon) - \sin \gamma)] - W = 0 \quad (5.7)$$

$$q_{\infty} S \left( \frac{dC_L}{d\alpha} (\sin \gamma \tan(\gamma + \alpha + \epsilon) + \cos \gamma) + C_L \frac{2 \sin \gamma}{\cos(2(\gamma + \alpha + \epsilon)) + 1} + \frac{dC_D}{d\alpha} (\cos \gamma \tan(\gamma + \alpha + \epsilon) + \sin \gamma) - C_D \frac{2 \cos \gamma}{\cos(2(\gamma + \alpha + \epsilon)) + 1} \right) = 0 \quad (5.8)$$

The Newton-Rhapson method can now be applied on the two equations above to yield the angle of attack. Using a similar argument as before the initial angle of attack  $\alpha$  is set to  $0^\circ$ . Once the final angle of attack is obtained the thrust can be calculated using Eq. (5.9).

$$T = \frac{q_{\infty} S C_L \sin \gamma + q_{\infty} S C_D \cos \gamma}{\cos(\gamma + \alpha + \epsilon)} \quad (5.9)$$

The equations for non-accelerating climbing flight cannot be applied to steady cruising flight due to a  $\sin \gamma$  term appearing in a denominator. Using the geometrical situation and forces as shown in Fig. 5.3 and deriving the equations of motion yields Eq. (5.10).

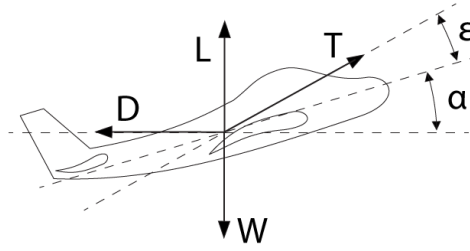


Figure 5.3: Overview of flight forces and geometry during cruise

$$T \cos(\alpha + \epsilon) - D = 0, \quad T \sin(\alpha + \epsilon) + L - W = 0 \quad (5.10)$$

Combining the two equations and solving for the angle of attack  $\alpha$  yields Eq. (5.11), taking the derivative with respect to the angle of attack yields Eq. (5.12). These two equations facilitate estimating the angle of attack  $\alpha$ . Once obtained the thrust can be calculated using Eq. (5.13).

$$q_{\infty} S (C_L + C_D \tan(\alpha + \epsilon)) - W = 0 \quad (5.11)$$

$$q_{\infty} S \left( \frac{dC_L}{d\alpha} + \frac{dC_D}{d\alpha} \tan(\alpha + \epsilon) + C_D \frac{2}{\cos(2(\alpha + \epsilon)) + 1} \right) = 0 \quad (5.12)$$

$$T = -\frac{q_{\infty} S C_D}{\cos(\alpha + \epsilon)} \quad (5.13)$$

#### PERFORMING SIMULATION STEPS FOR VARIOUS FLIGHT PHASES

Given that the aircraft will be flying at different altitudes three distinct flight phases, enumerated below, can be distinguished which can be stitched together to form any desired flightpath.

1. Diving flight: A phase where the aircraft will dive without using propulsion. This phase commences from a given horizontal steady flight condition down to a new lower altitude. The aircraft will arrive at this new flight condition ready to perform an accelerating flight phase by making sure its final flight path angle  $\gamma$  is close to zero.
2. Accelerating flight: A phase where the aircraft maintains altitude but accelerates or decelerates from a given initial speed to an intended final speed.
3. Climbing flight: A phase where the aircraft will climb from a given horizontal steady flight condition up to a new higher altitude. As with diving the aircraft will arrive at the new height ready to perform an accelerating flight phase.

The forces the aircraft experiences in diving flight is shown in Fig. 5.4. The associated equations of motion are shown in Eq. (5.14) and the relation between the inertial velocity  $V_I$ , windspeed  $V_W$ , and the flight path angle  $\gamma$  is shown in Eq. (5.15).

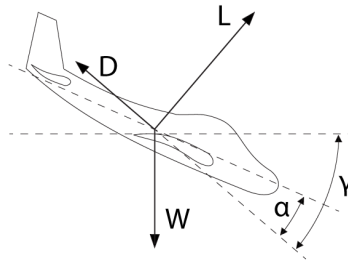


Figure 5.4: Overview of flight forces and geometry during diving

$$L \sin \gamma - D \cos \gamma = \frac{W}{g} a_{\text{hor}}, \quad L \cos \gamma + D \sin \gamma - W = \frac{W}{g} a_{\text{ver}} \quad (5.14)$$

$$\tan \gamma = -\frac{V_{W,\text{ver}} + V_{I,\text{ver}}}{V_{W,\text{hor}} + V_{I,\text{hor}}} \quad (5.15)$$

For a given initial flight state and a given angle of attack these equations allow calculating the acceleration. By discretising the number of points at which these equations are evaluated and applying trapezoidal integration new flight velocities  $V_{I,\text{hor}}$  and  $V_{I,\text{ver}}$  can be calculated according to Eq. (5.16).

$$V_{I,\text{ver},i+1} = V_{I,\text{ver},i} + \frac{1}{2} (a_{\text{ver},i} + a_{\text{ver},i+1}) \Delta t, \quad V_{I,\text{hor},i+1} = V_{I,\text{hor},i} + \frac{1}{2} (a_{\text{hor},i} + a_{\text{hor},i+1}) \Delta t \quad (5.16)$$

Combining Eq. (5.14) and Eq. (5.15) yields Eq. (5.17) and Eq. (5.18).

$$V_{I,\text{ver},i+1} - V_{I,\text{ver},i} = \frac{1}{2} \left( \frac{g_i q_{\infty,i} S}{W} (C_{L,i} \cos \gamma_i + C_{D,i} \sin \gamma_i) - g_i + \frac{g_{i+1} q_{\infty,i+1} S}{W} (C_{L,i+1} \cos \gamma_{i+1} + C_{D,i+1} \sin \gamma_{i+1}) - g_{i+1} \right) \Delta t \quad (5.17)$$

$$V_{I,\text{hor},i+1} - V_{I,\text{hor},i} = \frac{1}{2} \left( \frac{g_i q_{\infty,i} S}{W} (C_{L,i} \sin \gamma_i - C_{D,i} \cos \gamma_i) + \frac{g_{i+1} q_{\infty,i+1} S}{W} (C_{L,i+1} \sin \gamma_{i+1} - C_{D,i+1} \cos \gamma_{i+1}) \right) \Delta t \quad (5.18)$$

These equations allows estimating the next flight speed. Initially the atmospheric and graviational properties at the next timestep are not known as the change in height is not yet known. By defining an auxilliary parameter  $K_i = g_i q_{\infty,i} S / W$  and a relaxation factor  $\kappa$ , the new flight parameters can be calculated as following: Given a small enough timestep it is assumed that that the new flight conditions are exactly the same as the old flight conditions and that the new angle of attack  $\alpha$  is known. Eq. (5.19) and Eq. (5.20) are used to initially estimate the new velocities.

$$\Delta \tilde{V}_{I,\text{ver},0} = \frac{1}{2} (K_0 [(C_{L,0} + C_{L,1}) \cos \gamma_0 + (C_{D,0} + C_{D,1}) \sin \gamma_0] - 2g_0) \Delta t \quad (5.19)$$

$$\Delta \tilde{V}_{I,\text{hor},0} = \frac{1}{2} (K_0 [(C_{L,0} + C_{L,1}) \sin \gamma_0 - (C_{D,0} + C_{D,1}) \cos \gamma_0]) \Delta t \quad (5.20)$$

The new velocities provide the change in height. The new height will provide new atmospheric properties using the atmospheric model based on VIRA. This provides the new flight path angle  $\gamma$  in turn. The calculations are shown in (5.21) and (5.22).

$$\Delta \tilde{h}_1 = \frac{1}{2} (V_{I,\text{ver},0} (1 + \kappa) + \kappa \Delta \tilde{V}_{I,\text{ver},0}) \Delta t \quad (5.21)$$

$$\tilde{\gamma}_1 = -\tan^{-1} \left( \frac{V_{W,\text{ver},1} + V_{I,\text{ver},0} (1 + \kappa) + \kappa \Delta \tilde{V}_{I,\text{ver},0}}{V_{W,\text{hor},1} + V_{I,\text{hor},0} (1 + \kappa) + \kappa \Delta \tilde{V}_{I,\text{hor},0}} \right) \quad (5.22)$$

With the initial estimates obtained an iterative method can be applied until the solution stabilises. The iterative calculations are very similar to above: first the new velocity estimates are obtained with Eq. (5.23) and Eq. (5.24), after which the new change in height and flight path angle are calculated using Eq. (5.25) and Eq. (5.26). With the new estimates the velocity is recalculated. These calculations are repeated until the relative difference between both the old and new velocities  $V_{I,\text{hor}}$  and  $V_{I,\text{ver}}$  are smaller than  $1 \cdot 10^{-8}$ .

$$\Delta \tilde{V}_{I,\text{ver},i} = \frac{1}{2} [K_i (C_{L,i} \cos \gamma_i + C_{D,i} \sin \gamma_i) + K_{i+1} (C_{L,i+1} \sin \gamma_{i+1} - C_{D,i+1} \cos \gamma_{i+1}) - (g_i + g_{i+1})] \Delta t \quad (5.23)$$

$$\Delta \tilde{V}_{I,\text{hor},i} = \frac{1}{2} [K_i (C_{L,i} \sin \gamma_i - C_{D,i} \cos \gamma_i) + K_{i+1} (C_{L,i+1} \sin \gamma_{i+1} - C_{D,i+1} \cos \gamma_{i+1})] \Delta t \quad (5.24)$$

$$\Delta \tilde{h}_{i+1} = \frac{1}{2} (V_{I,\text{ver},0} (1 + \kappa) + \kappa \Delta \tilde{V}_{I,\text{ver},i}) \quad (5.25)$$

$$\tilde{\gamma}_{i+1} = -\tan^{-1} \left( \frac{V_{W,ver,i+1} + V_{I,ver,0}(1 + \kappa) + \kappa \Delta \tilde{V}_{I,ver,i}}{V_{W,hor,i+1} + V_{I,hor,0}(1 + \kappa) + \kappa \Delta \tilde{V}_{I,hor,i}} \right) \quad (5.26)$$

For climbing flight the procedure is largely the same, except that some of the equations are different. Given the forces and the flight geometry as shown in Fig. 5.2 the equations of motion are as shown in Eq. (5.27) and the flight path angle  $\gamma$  can be calculated using Eq. (5.28).

$$T \cos(\gamma + \alpha + \epsilon) - L \sin \gamma - D \cos \gamma = \frac{W}{g} a_{hor}, \quad T \sin(\gamma + \alpha + \epsilon) + L \cos \gamma - D \sin \gamma - W = \frac{W}{g} a_{ver} \quad (5.27)$$

$$\tan \gamma = \frac{V_{W,ver} + V_{I,ver}}{V_{W,hor} + V_{I,hor}} \quad (5.28)$$

Given these two equations the new velocities are derived in the same way as they were for diving flight. Initial estimates for the new height and therefrom obtained atmospheric properties are chosen by assuming conditions similar to the starting conditions. Because the derivations for climbing flight are similar to those in diving flight, complete derivations are omitted. An initial propeller sizing equation is used to relate the power available to generate thrust  $P_A$  in  $W$  to the freestream velocity  $V_\infty$  in  $m/s$  and the produced thrust  $T$  in  $N$ . This equation, alongside the definition of two auxiliary parameters reducing the verbosity of the mathematics are shown in Eq. (5.29).

$$P_A = V_\infty T, \quad K_{A,i} = \frac{g_i P_A}{W V_{\infty,i}}, \quad K_{B,i} = \frac{g_i q_{\infty,i} S}{W}, \quad (5.29)$$

$$\text{where } V_{\infty,i} = \sqrt{(V_{I,hor,i} + V_{W,hor,i})^2 + (V_{I,ver,i} + V_{W,ver,i})^2}$$

The equations used to iterate to a stable new velocity after a given timestep  $\Delta t$  are shown in Eq. (5.30) through Eq. (5.33).

$$\Delta \tilde{V}_{I,hor,i} = \frac{1}{2} [ K_{A,i} \cos(\gamma_i + \alpha_i + \epsilon) + K_{A,i+1} \cos(\gamma_{i+1} + \alpha_{i+1} + \epsilon) - K_{B,i} (C_{L,i} \sin \gamma_i + C_{D,i} \cos \gamma_i) - K_{B,i+1} (C_{L,i+1} \sin \gamma_{i+1} + C_{D,i+1} \cos \gamma_{i+1}) ] \Delta t \quad (5.30)$$

$$\Delta \tilde{V}_{I,ver,i} = \frac{1}{2} [ K_{A,i} \sin(\gamma_i + \alpha_i + \epsilon) + K_{A,i+1} \sin(\gamma_{i+1} + \alpha_{i+1} + \epsilon) + K_{B,i} (C_{L,i} \cos \gamma_i - C_{D,i} \sin \gamma_i) + K_{B,i+1} (C_{L,i+1} \cos \gamma_{i+1} - C_{D,i+1} \sin \gamma_{i+1}) - (g_i + g_{i+1}) ] \Delta t \quad (5.31)$$

$$\Delta \tilde{h}_{i+1} = \frac{1}{2} (V_{I,ver,i} (1 + \kappa) + \kappa \Delta \tilde{V}_{I,ver,i}) \quad (5.32)$$

$$\tilde{\gamma}_{i+1} = \tan^{-1} \left( \frac{V_{W,ver,i+1} + V_{I,ver,i} (1 + \kappa) + \kappa \Delta \tilde{V}_{I,ver,i}}{V_{W,hor,i+1} + V_{I,hor,i} (1 + \kappa) + \kappa \Delta \tilde{V}_{I,hor,i}} \right) \quad (5.33)$$

Lastly, there is the phase in flight where the aircraft is levelled and flying at a certain velocity but must accelerate to a different velocity in order to commence a different flight phase (e.g. accelerating to upper segment cruise speed after climbing out of the lower atmospheric regions). Considering the flight geometry and forces as shown in Fig. 5.3 the equations of motion can be derived to be as shown in Eq. (5.34).

$$L + T \sin(\alpha + \epsilon) - W = 0, \quad T \cos(\alpha + \epsilon) - D = \frac{W}{g} a_{hor} \quad (5.34)$$

For a given thrust  $T$  the angle of attack  $\alpha$  to maintain level flight can be calculated. Using those two values the horizontal acceleration  $a_{hor}$  can be calculated which allows calculating the new flight velocity. Solving for the angle of attack proceeds in a manner similar to that outlined in Section 5.2.2. Taking the derivative of the leftmost equation in Eq. (5.34) with respect to the angle of attack  $\alpha$ , as shown in Eq. (5.35), and using the Newton-Raphson method with an initial guess for  $\alpha$  of  $0^\circ$  will provide the angle of attack.

$$\frac{d}{d\alpha} \left( q_{\infty} S C_L + \frac{P_A}{V_{\infty}} \sin(\alpha + \epsilon) - W \right) = q_{\infty} S \frac{dC_L}{d\alpha} + \frac{P_A}{V_{\infty}} \cos(\alpha + \epsilon) \quad (5.35)$$

By using the rightmost equation in Eq. (5.34) the new horizontal acceleration  $a_{\text{hor}}$  is determined. Using a trapezoidal integration method this acceleration results in a new horizontal velocity  $V_{I,\text{hor},i+1}$ . The associated calculations are shown in Eq. (5.36). Again an iterative method is used as the new velocity will influence the dynamic pressure, in turn influencing the new angle of attack and the drag experienced by the aircraft.

$$a_{\text{hor},i} = \frac{g_i}{W} (T \cos(\alpha_i + \epsilon) - q_{\infty,i} S C_{D,i}), \quad V_{I,\text{hor},i+1} = V_{I,\text{hor},i} (1 + \kappa) + \kappa \frac{1}{2} (a_{\text{hor},i} + a_{\text{hor},i+1}) \Delta t \quad (5.36)$$

#### GENERATING FLIGHTPATHS THROUGHOUT THE ATMOSPHERE

The sets of equations developed in the previous section estimates the differences in flight conditions after a single timestep  $\Delta t$ . Generating a flightpath through the atmosphere requires choosing the most efficient track. The chosen method consists of generating a large set of simulation outcomes by varying the inputs within certain limits and generating a metric to determine which of the outcomes is preferred over the other ones. The metric that is minimised is a summation of values which can be subdivided into two categories:

- **Base metric:** This is a value that becomes smaller as the solution approaches the optimum solution and increases whenever the solution moves away from it. An example would be, when diving as quick as possible, to maximise the vertical speed.
- **Penalty metrics:** Metrics that are based on a certain flight parameter not allowed to violate a given requirement. These are not always incorporated into the summed metric, only when the aircraft is close to violating a requirement. An example would be to not go faster than a preset percentage of the local speed of sound.

All contributions by any of the metric categories to the main metric are normalised by using some known maximum value of the considered quantity. An example is to divide all speeds by the maximum allowable speed such that the final value is in the order of [0, 1].

Metrics can also be categorised based on what they are trying to accomplish with regards to choosing the best solution. The possibilities are enumerated below.

- **Approaching metrics:** This is a metric that tends to try to make a certain quantity approach a desirable value. For any general quantity  $c$  that has a known maximum  $c_{\text{max}}$  and a desired value of  $c_{\text{target}}$  such a metric  $m$  will generally be calculated as shown in Eq. (5.37).

$$m = \left( \frac{c - c_{\text{target}}}{c_{\text{max}}} \right)^2 \quad (5.37)$$

- **Minimization metrics:** These metrics try to minimise a given quantity and tend to take a form as shown in Eq. (5.38).

$$m = \left( \frac{c}{c_{\text{max}}} \right)^2 \quad (5.38)$$

- **Maximization metrics:** These metrics try to maximise a given quantity and usually look as shown in Eq. (5.39).

$$m = \left( \frac{c_{\text{max}} - c}{c_{\text{max}}} \right)^2 \quad (5.39)$$

- **Avoidance metrics:** These metrics try to avoid a given target  $c_{\text{target}}$  imposed on the considered quantity. These will only be taken into account after a certain boundary quantity  $c_{\text{bound}}$  is surpassed by the quantity. These metrics assume the form of Eq. (5.40).

$$m = \left( \frac{c - c_{\text{bound}}}{c_{\text{target}} - c_{\text{bound}}} \right)^2 \quad (5.40)$$

As stated earlier metrics are not always added to the total metric. Only when a certain boundary value is surpassed will the contribution of some metrics be added to the total metric. It would make no sense to take a metric into account if the current flight condition is not close to violating the underlying restrictions. On the other hand only taking it into account when very close to violating the requirement might cause none of the

generated timestep solutions to satisfy the requirement.

Considering this issue an adaptive method was devised where the boundary quantity is changed whenever no valid solutions at a certain flight state exist, after which the simulation is restarted. This solution is referred to as bias mapping and is best explained with an example: A bias map for the speed of sound limit would be a height-dependent discrete function  $f_{V_\infty/a}(h_i)$  that is initially set at a constant value  $f_{V_\infty/a,0}$  that is close to 1.0. The speed of sound metric is an avoidance metric which is only taken into account when  $V_{\infty,i}/a_i > f_{V_\infty/a}(h_i) \cdot a_{\text{limit}}$ . Imagine diving from a very large height optimised for as fast a descent as possible. This would cause the flight path angle  $\gamma$  to quickly increase to  $90^\circ$  while the speeds are still reasonable low. At some height  $h_v$  at time  $t_v$  all the considered solutions by inputting a range of angles of attack  $\alpha$  in the diving step equations Eq. (5.23) through Eq. (5.26) will cause the speed of sound limit to be violated. At this point the bias map will be adjusted according to Eq. (5.41).

$$f_{V_\infty/a}(h_i)_{\text{new}} = f_{V_\infty/a}(h_i)_{\text{old}} - C_{\text{step}} \left[ 1 - \left( \text{erf} \left( \frac{h_i - h_v}{0.5 C_{\text{width}}} \right) \right)^2 \right] \quad (5.41)$$

Where  $C_{\text{step}}$  is an arbitrary value, set to 0.15 in all simulations, by which the bias map is reduced at the height  $h_v$  at which the requirement was violated.  $\text{erf}$  is the error function and  $C_{\text{width}}$  is the approximate range of altitudes around  $h_v$  which will be adjusted. In the current simulations this width value is set to 5 km.

Once the bias map is adjusted the simulation is ran again. These adjustments are performed for all possible metrics until one of the bias map values becomes negative. If this occurs then the considered simulation is marked as invalid.

The bias mapping method was created in order to compensate for failing simulations due to a complete input set resulting in outputs all violating a given requirement. The method by no means guarantees reaching a local optimum, but was employed anyway due to time constraints. It is reasonably accurate when estimating the time it takes to perform a certain manoeuvre and under which flight parameters these manoeuvres take place, but exhibits issues reminiscent of unoptimised linear control systems.

The diving simulations feature a maximisation base metric which attempts to maximise the negative vertical speed as to arrive at the lower height as fast as possible. This base metric is supplemented by several penalty metrics:

- **$\dot{\gamma}$  avoidance metric:** The rate at which the flightpath changes cannot exceed a maximum value of  $2.5^\circ/s$ . The speed at which the flightpath changes is related to the load factor experienced by the aircraft and hence should be minimized.
- **Speed of sound avoidance metric:** The freestream velocity  $V_\infty$  should never exceed 60% of the local speed of sound  $a$ .
- **$\gamma$  avoidance metric:** The maximum allowed flight path angle  $\gamma$  shall not be smaller than  $-90^\circ$  and shall not be larger than  $90^\circ$ .
- **Retrograde avoidance metric:** The velocity shall always be such that the aircraft is pointing its nose prograde with respect to the wind.

Once the diving simulation arrives at the target height a bisectional algorithm is applied to simulate attaining steady flight conditions. Initially the diveout height is set halfway between the initial and final diving height. The metrics during diveout are formulated such that the aircraft will try to attain a flight path angle  $\gamma$  of  $0^\circ$ . If this value is attained before reaching the target height then the diveout height is lowered. If the target height is reached but the flight path angle  $\gamma$  is not yet  $0^\circ$  then the diveout height is increased. This process is repeated until both the final height is within 250 m of the final height and the final flight path angle  $\gamma$  is within  $1.5^\circ$  of  $0^\circ$ . The base metric is a  $\gamma$  approach metric set to  $0^\circ$  as target. The penalty metrics are the same as the ones formulated above.

The climbing simulations are based on expending the least amount of energy while climbing a certain vertical distance. The derivation for this metric is shown in Eq. (5.42).

$$\frac{dh}{dE} = \frac{V_{I,\text{ver}} dt}{(P_A + P_{a/c}) dt} = \frac{V_{I,\text{ver}}}{P_A/\eta_{\text{prop}} + P_{a/c}} = \frac{V_{I,\text{ver}}}{T \cdot V_\infty/\eta_{\text{prop}} + P_{a/c}} \approx \frac{\eta_{\text{prop}} \sin \gamma}{T} \quad (5.42)$$

In the equation above  $E$  is the expended energy in  $J$ ,  $\eta_{\text{prop}}$  is the total propeller efficiency and  $P_{a/c}$  is the energy required by the aircraft, aside from the power required by the propellers, in  $W$ . The approximation at the end of Eq. (5.42) is based on initial calculations showing that much more energy is required for the

propellers than is required for the other aircraft systems. Instead of an analytical investigation, a numerical investigation into how the quantity in Eq. (5.42) is maximised, is performed by calculating at a given height  $h$  and inertial forward velocity  $V_{I,\text{hor}}$  the maximum climbing efficiency for a reasonable range of vertical velocities (between  $0.1 \text{ m/s}$  and  $20 \text{ m/s}$ ). The thrust  $T$  (and thereby the propeller power  $P_A$ ) is calculated using Eq. (5.7) through Eq. (5.9). Imposing a reasonable upper limit to the propeller power  $P_A$  of between  $20 \text{ kW}$  and  $50 \text{ kW}$  results in the same trend each time: minimising the horizontal velocity  $V_{I,\text{hor}}$  and using the available propeller power  $P_A$  at its maximum will maximise the climbing efficiency as defined in Eq. (5.42). These values and the associated vertical velocities are shown in Fig. 5.5.

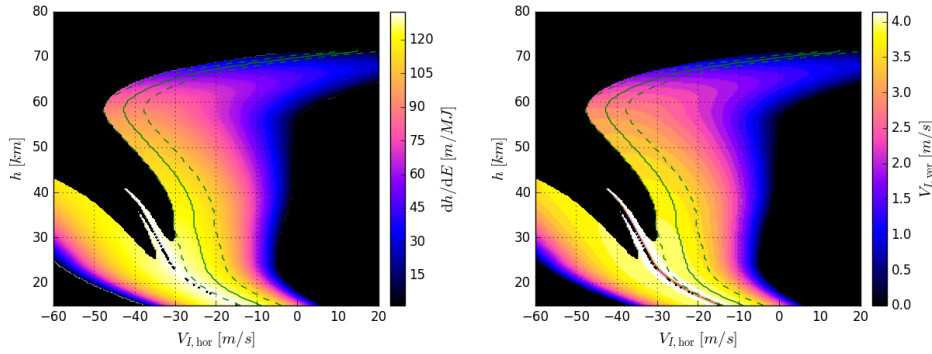


Figure 5.5: Results of a numerical climbing efficiency analysis at a maximum propeller power  $P_A$  of  $32 \text{ kW}$  at a latitude  $\phi$  of  $0^\circ$ , a solar longitude  $\lambda_S$  of  $0^\circ$  and a weather severity factor  $\zeta$  of  $0.0$ . Displayed are the climbing efficiency on the left and the vertical velocity on the right. The green lines indicate the optimum ascent path to any given height.

The climbing penalty metrics are the same as the diving penalty metrics.

Once the climbing simulation arrives at the target height a similar bisectional algorithm is applied to simulate attaining steady flight conditions at climbout as during diving: Choosing the flight path angle  $\gamma$  as a base metric to approach  $0^\circ$  within a range of  $1.5^\circ$  while the final height must be within  $250 \text{ m}$  of the target height. The penalty metrics are the same as during climbing.

The acceleration simulations attempt to reach the target velocity as quickly as possible. The earlier mentioned issues using the least-squares approach is most severely felt here: without intervention the solution's velocities tends to oscillate around the target velocity for extended periods of time. This is currently circumvented by applying Eq. (5.11) through Eq. (5.13) to determine the final required thrust and to attempt to match the thrust to that final value as the final velocity is being approached. Hence the base metric is twofold: one approach metric attempting to approach the intended final horizontal velocity  $V_{I,\text{hor}}$ , and one approach metric to reduce velocity oscillations around the target velocity. The accelerating penalty metrics are as following:

- **$\alpha$  avoidance metric:** A metric which avoids angles of attack that are too extreme. As the software used to generate aerodynamic data cannot estimate stalling these angles are forced to remain within conservative estimates of  $-8^\circ$  and  $8^\circ$ .
- **Speed of sound avoidance metric:** The freestream velocity  $V_\infty$  should never exceed  $60\%$  of the local speed of sound  $a$ .
- **$\dot{\alpha}$  avoidance metric:** The rate at which the angle of attack changes is limited to  $1.5^\circ/\text{s}$  as to reduce requirements posed on the control surfaces and their actuators.
- **Retrograde avoidance metric:** The velocity shall always be such that the aircraft's nose is pointing prograde with respect to the wind.

### 5.2.3. INVESTIGATING THE LIMITS OF FLIGHT

The heights and speeds at which the aircraft operates cannot be chosen at will. At low horizontal speeds  $V_{I,\text{hor}}$  the angle of attack to sustain flight will become too high (or, similarly, the dynamic pressure will become very low) and at high horizontal speeds the drag will become so large that an enormous amount of energy is required to fly at cruising speeds.

For a given wing planform with determined aerodynamic characteristics Eq. (5.11) through Eq. (5.13) can be used to estimate the required angle of attack  $\alpha$  and propeller power  $P_A$  in order to perform sustained cruising flight. For this initial investigation a wing planform area  $S$  of  $36 \text{ m}^2$  consisting solely out of the NACA15012

airfoil was used. This estimate resulted from the sizing performed during the feasibility study. The characteristics of the wing are shown in Table 5.4. Aerodynamic characteristics arising from this configuration were provided by the software XFRLR5.

Table 5.4: Aircraft properties determined in the initial feasibility study

Symbol	Unit	Value	Description
$m$	$kg$	700	Aircraft mass
$S$	$m^2$	35	Wing planform area
$c_r$	$m$	3.5	Root chord
$c_t$	$m$	1.93	Tip chord
$\eta_{prop}$		0.80	Total propeller efficiency
$\alpha_{min}$	$^\circ$	-8.0	Minimum angle of attack
$\alpha_{max}$	$^\circ$	8.0	Maximum angle of attack

Plotting the required power to facilitate cruising at the given height  $h$  and inertial horizontal velocity  $V_{I,hor}$  for various atmospheric severity values  $\zeta$  and overlaying a contour in which conditions imposed on the angles of attack are satisfied for varying propeller power  $P_A$  levels results in figure 5.6.

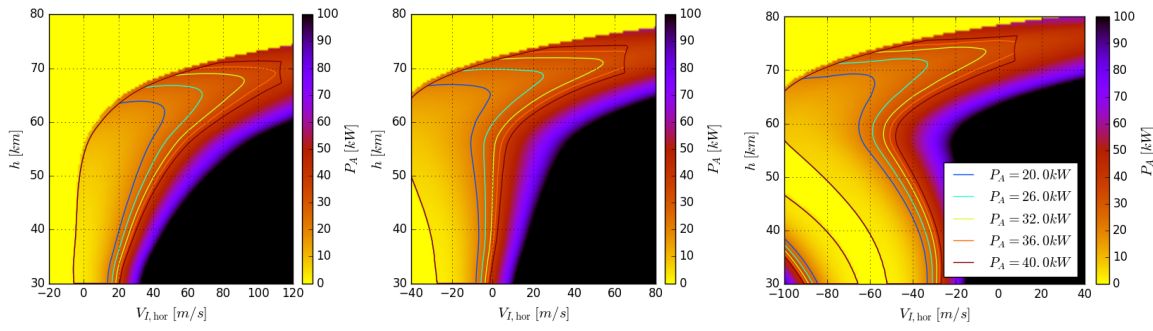


Figure 5.6: Maps of the power required for atmospheric severity factors  $\zeta$  of, from left to right,  $-1.55$ ,  $0.0$  and  $1.8$ . In each plot a contour is drawn in which all flight parameters are within the required bounds for a given available propeller power.

From this figure it is clear that requiring the propellers to output more than  $36 kW$  under the initial sizing conditions does not make sense for cruising as this will result in the aircraft exceeding the speed of sound limits at the higher achievable velocities. The upper height limit to the cruising capabilities is caused by the thin atmosphere and the resulting lack of dynamic pressure  $q_\infty$ . Considering the temperatures of the Venusian atmosphere, the lower atmospheric severity  $\zeta$  that the aircraft can fly at is  $-1.55$ . Any lower and the only operational cruising point that will allow the aircraft to stay beneath the subsolar point continuously will be below  $53 km$ . At this height at the atmospheric temperature can reach values up to  $70^\circ C$ , the upper limit for most of the electronics. The upper limit for atmospheric severity  $\zeta$  of  $1.55$  can be higher, but the value of  $1.55$  already allows constant sub-solar cruising at a height of  $70 km$  with allowable wind speeds of  $147.8 m/s$  at temperatures between  $-63.4^\circ C$  and  $-23.35^\circ C$  when designing the propellers such that they produce a thrust power of  $32 kW$ .

Based on the results provided in Fig. 5.5 and Fig. 5.6 the limits of speeds and altitudes at which the aircraft can fly at are roughly established. Note that during each iteration of the aircraft's design these limits are investigated once more. The propeller power in the track analysis is assumed to produce  $32 kW$  of power.

Having picked a particular upper cruising height  $h_u$ , lower cruising height  $h_l$ , upper cruising speed  $V_{I,hor,u}$  and lower cruising speed  $V_{I,hor,l}$  then the methods outlined in Section 5.2.2 makes generating tracks possible in regions within the flight envelope. An example of a diving and a climbing phase is shown in Fig. 5.7. The oscillations in the diving velocity are caused by the optimisation algorithm attempting to limit the velocity of the aircraft such that it remains below the speed of sound.

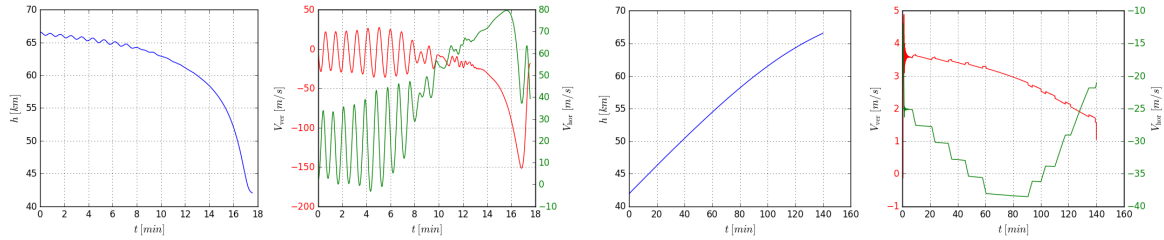


Figure 5.7: Example of flight parameters generated by simulating a diving maneuver (on the left) and a climbing maneuver (on the right)

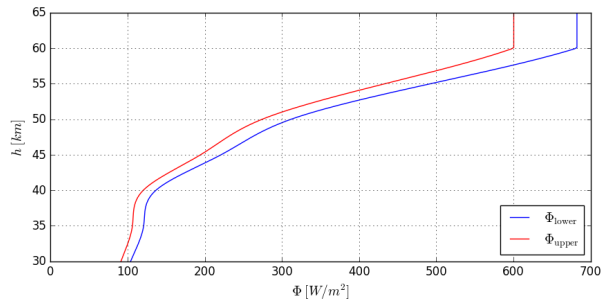


Figure 5.8: Available upward and downward power produced by solar panels due to available solar flux and considered efficiencies. The sharp corner at 60 km height is there because above that point the influence of the atmosphere is considered negligible.

#### 5.2.4. THE INFLUENCES OF THE POWER SUBSYSTEM DESIGN ON MISSION PROFILE

With the methods outlined in Section 5.2.1 through Section 5.2.3 a dataset can be generated containing all flight parameters of interest for a certain combination of upper and lower cruising speed and altitude. These datasets, however, do not yet contain the time spent in the cruising phases of the flight track. In this section the influences of the solar panels and the battery capacity will be determined.

##### ESTIMATING AVAILABLE SOLAR POWER

Solar panels will provide the aircraft with the power throughout its mission life. The aircraft will make use of Gallium-Arsenide (GaAs) triple junction solar cells. To size the solar panels, data from [25] was used as this provided the power generated for a range of altitudes in the Venusian atmosphere that is traversed in the flight profile. In the coming years the efficiency of the solar panels is expected to increase further. The new CPV Point Focus Solar Cells created by Spectrolab will have an efficiency of 40%<sup>32</sup>, compared to the 29% efficiency of those applied in the experiment<sup>33</sup>. It is expected that by the time of launch, these solar cells will be available. However, as they should be used on Venus, the expected increase in overall efficiency is set to a conservative value of 5%.

During design one can place solar panels on the bottom of the aircraft at the cost of a small loss in solar flux. This loss in flux is estimated by using a measured ratio between the upward flux and the downward flux for all wavelengths between  $0.4\mu\text{m}$  and  $1.8\mu\text{m}$  as a function of height. This is considered accurate, even though the solar cells of choice feature three junctions, as their conversion efficiency is fairly constant through the considered passbands [23]. This upward flux function is implemented in a lookup table in a piecewise linear fashion. The available power, taking all efficiencies into account except for the packing factor, is shown in Fig. 5.8.

##### LIMITING THE LOWER CRUISING TIME BY BATTERY CAPACITY

A complete flight path can be subdivided into two sets consisting of multiple segments. One set consists of segments where the available generated power is larger than the required power. The excess can be used to charge a battery. This region will be indicated by the subscript 'ch'. The other set consists of segments where the required power is larger than the available power and is indicated by the subscript 'dis'. The deficit should be taken care of by a certain required battery capacity.

<sup>32</sup>[http://www.spectrolab.com/DataSheets/PV/CPV/C4MJ\\_40\\_Percent\\_Solar\\_Cell.pdf](http://www.spectrolab.com/DataSheets/PV/CPV/C4MJ_40_Percent_Solar_Cell.pdf)

<sup>33</sup><http://www.spectrolab.com/DataSheets/cells/2015%20XTJ%20CIC%20Datsheet.pdf>

Requiring the capacity to be larger than the total energy deficit results in Eq. (5.43). The last term between brackets is intentionally not incorporated into the integral and represents the contribution due to cruising at the lower flight path segment.

$$C \geq \frac{1}{\eta_{\text{dis}}\eta_P} \left( \int_{\text{dis}} P_R dt - \eta_P A \int_{\text{dis}} \frac{P}{A} dt + t_l \left( P_{R,l} - \eta_P A \frac{P}{A} \Big|_l \right) \right) \quad (5.43)$$

In this equation  $C$  is the battery capacity in  $J$ ,  $\eta_{\text{dis}}$  is the discharge efficiency of the battery and assumed to be 0.95,  $\eta_P$  is the overall power efficiency of the aircraft and assumed to be 0.92,  $P_R$  is the required battery at a given point in time in  $W$ ,  $P/A$  is the available power per unit of solar cell area in  $W/m^2$  and  $t_l$  is the time spent in the lower flight path segment.

By setting  $t_l$  in Eq. (5.43) to 0  $s$  and solving for  $C$  yields the minimum required battery capacity for diving and climbing. Note that the equation is not linearly related to the solar cell area  $A$  as increasing its size results in more available power in the lower regions of the atmosphere thereby decreasing the span of the discharging integrals.

The equation can be rewritten to solve for  $t_l$  using a given designed solar cell area  $A$  and battery capacity  $C$  as shown in equation (5.44).

$$t_{l,\text{max}} = \frac{\eta_{\text{dis}}\eta_P C + \eta_P A \int_{\text{dis}} \frac{P}{A} dt - \int_{\text{dis}} P_R dt}{P_{R,l} - \eta_P A \frac{P}{A} \Big|_l} \quad (5.44)$$

This equation should be interpreted carefully. The maximum lower cruising time  $t_{l,\text{max}}$  can exceed the time allowed in the lower atmosphere before the aircraft's internal temperature exceeds the imposed limits. Furthermore, if the lower cruising segment results in a net energy production then  $t_{l,\text{max}}$  will become negative. In both cases  $t_l$  will be set to the maximum allowed cruising time before overheating. Because the generated flight tracks are discrete datasets all integrals will be evaluated numerically using Simpson's method [24].

In order to realise a given required capacity, batteries will be used. The aircraft will operate in regions of the Venusian atmosphere with temperatures ranging from 0° to 200° Celsius. Regular rechargeable batteries can only be used if they are properly insulated. The reason for this is that the liquid electrolyte used in the batteries becomes unstable at temperatures above 80° Celsius [26]. Although solid-electrolyte batteries capable of operating at higher temperatures, such as sodium-sulphur batteries, are being researched, their readiness for the launch in 2026 is questionable. Also, no commercial companies providing solid electrolyte battery datasheets were found to allow for proper comparison. Therefore, no solid-electrolyte batteries are considered for the design. This does mean however, that for the batteries to operate, they should be insulated so that they do not overheat.

To minimise the weight of the batteries and thereby help reduce aircraft weight, the OXIS Energy Ultra Light Lithium Sulphur cells will be used<sup>34</sup>. Though still in development, these cells show the best energy storage to weight ratio currently (June 2016) available and have high cycle life. According to company planning the batteries should be available by 2019, so even if problems are encountered, they are expected to be ready in time for launch. The key characteristics of the cells are shown in Table 5.5.

Table 5.5: OXIS Energy Ultra Light Lithium Sulphur Cells characteristics for 2019<sup>34</sup>

Parameter	Value	Parameter	Value
Gravimetric Specific Energy [Wh/kg]	450	Cycle Life [cycles]	1,500 <sup>35</sup>
Volumetric Energy [Wh/L]	500	Operating temperature [°C]	-30 to 70

Using this data and the battery capacity found in the mission analysis, the required battery mass can be calculated using Eq. (5.45) [12].

$$m_{\text{battery}} = \frac{Cap}{SCap \cdot DOD \cdot TL \cdot RF} \cdot (1 + SF) \quad (5.45)$$

In order to determine the volume of the batteries, the only thing that has to be changed is the  $SCap$ , which will become the volumetric specific energy, rather than the gravimetric specific energy. All inputs used for this equation and the results are shown in Table 5.6.

<sup>34</sup><http://www.oxisenergy.com/technology/product/>

<sup>35</sup>At DOD of 80%<sup>34</sup>

Table 5.6: Aircraft battery sizing parameters<sup>34</sup>

Parameter	Definition	Mass	Volume
Cap	Required capacity	141 MJ	
SCap	Gravimetric/volumetric specific energy	450 Wh/kg	500 Wh/L
DOD	Depth Of Discharge	0.8 (80%)	
TL	Time Loss during transfer and orbiting (15% loss assumed)	0.85 (85%)	
RF	Reduction Factor to indicate energy fraction remaining at cycle life	0.8 (80%)	
SF	Safety Factor	1.25	
Result		<b>200 kg</b>	<b>0.18 m<sup>3</sup></b>

### ESTIMATING MINIMUM REQUIRED UPPER CRUISE SPEED TO RECHARGE BATTERIES

If a given battery capacity  $C > C_{\min}$  (as stipulated by Eq. (5.43)) and solar panel area  $A$  result in a positive  $t_l$  then the upper cruise segment can be designed such that the batteries are fully charged. The basis for this is Eq. (5.46), stating that the total energy produced in the sets of segments that produce net power is equal to the minimum required capacity.

$$\eta_P \eta_{ch} \left( A \int_{ch} \frac{P}{A} dt - \frac{1}{\eta_P} \int_{ch} P_R dt \right) + \eta_P \eta_{ch} t_u \left( A \frac{P}{A} \Big|_u - \frac{1}{\eta_P} P_R \Big|_u \right) \geq \frac{1}{\eta_{dis} \eta_P} \left( \int_{dis} P_R dt - \eta_P A \int_{dis} \frac{P}{A} dt \right) + \frac{t_l}{\eta_{dis} \eta_P} \left( P_R \Big|_l - \eta_P A \frac{P}{A} \Big|_l \right) \quad (5.46)$$

In this equation  $t_u$  is the time spent cruising in the upper segment of the flight path in  $s$  and  $\eta_{ch}$  is the charging efficiency and assumed to be 0.95. Rewriting this equation to solve for the minimum upper cruise segment time required to recharge the battery up until the point where the aircraft can start performing a second cycle of the flight track yields Eq. (5.47).

$$t_u = \frac{1}{\eta_P \eta_{ch} \left( A \frac{P}{A} \Big|_u - \frac{1}{\eta_P} P_R \Big|_u \right)} \left[ \frac{1}{\eta_{dis} \eta_P} \left( \int_{dis} P_R dt - \eta_P A \int_{dis} \frac{P}{A} dt + t_l \left( P_R \Big|_l - \eta_P A \frac{P}{A} \Big|_l \right) \right) - \eta_P \eta_{ch} \left( A \int_{ch} \frac{P}{A} dt - \frac{1}{\eta_P} \int_{ch} P_R dt \right) \right] \quad (5.47)$$

If the upper segment cruising time  $t_u$  becomes negative then this is indicative of enough energy being generated as to not have to spend any time cruising in the upper atmosphere to recharge the batteries. As this is impossible  $t_u$  will be assumed to be 0 in the case this happens. One can see that for a given solar cell area  $A$ , battery capacity  $C$  and flight path increasing  $t_l$  will linearly increase  $t_u$ .

### 5.2.5. COMPARING DIFFERENT GENERATED FLIGHT PATHS

The time spent performing a single flight path is not of direct importance as long as the aircraft is capable of staying within a certain range of a given latitude and solar longitude. What matters is the time spent analysing the surface for the main mission goals and the time spent analysing the atmosphere for the secondary mission goals. To be able to compare differing flight paths four performance metrics will be defined. The first is the main mission ratio  $f_m$ : the ratio of time spent cruising and accelerating in the lower flight path segment to the total flight path time  $t_{lower} / t_{total}$ , indicative of how much time is spent mapping the surface at the highest accuracy and certainty (due to less atmospheric influences for which measurements have to be compensated). The second metric is secondary mission ratio  $f_s$ : the ratio of time spent during climbing to the total flight path time  $t_{climb} / t_{total}$ , indicating how much time is available during main mission life to determine atmospheric properties.

The third metric is the overlap factor  $f_o$ , related to how quickly the aircraft advances over the Venusian ground with respect to the lower segment ground track and is defined as is shown in Eq. (5.48).

$$f_o = \left( \int_{total} \frac{V_{I,hor}}{R+h} R dt \right) / \left| \int_{post\ dive}^{pre\ climb} \frac{V_{I,hor}}{R+h} R dt \right| \quad (5.48)$$

An overlap factor that is smaller than 0 implies the aircraft is moving retrograde faster than the ground is moving. If it is smaller than 0 but larger than  $-1$ , then the aircraft is covering a part of the lower ground track

of the previous flight path in the new one. Conversely, an overlap factor larger than 0 implies prograde motion with respect to the ground and if it remains smaller than 1 then a part of the previous flight path lower ground track is covered once more. In case of values smaller than  $-1$  or larger than  $1.0$  then the aircraft can perform a sustained cruise at a high or respectively low velocity to end up at the same solar longitude, but the available mission life is more effectively used if the resulting overlap factor is close to 0.

The last metric is the cyclic time ratio  $f_c$ , of importance when  $f_o$  is much smaller than 0.0, indicating the main mission time ratio but taking cruising back to the same solar longitude into account in the total mission time.

### 5.2.6. RESULTS

Requiring that the aircraft is able to perform a sustained cruise at severe weather conditions in emergency conditions severely influences the required solar cell area. Requiring the aircraft to produce enough power to perform a sustained cruise at a required power  $P_R$  of  $32\text{ kW}$  at a propeller efficiency of 67% (as will be detailed in Section 5.4, maximum effective solar cell efficiency of 26%, packing factor of 0.92<sup>32</sup> and a conservative degradation value of 0.97 requires a solar cell area  $A$  of  $53.53\text{ m}^2$  when flying at a latitude  $\phi$  of  $12.5^\circ$  and solar longitude  $\lambda_S$  of  $5^\circ$  employing a safety factor of 1.25. The given area  $A$  is assumed to be installed once on the top side of the aircraft and once on the bottom side, resulting in a total solar cell area of  $107.1\text{ m}^2$ . The given latitude of  $12.5^\circ$  implies that the aircraft, when registering elevated wind speeds, should move to the equator as fast as possible. Requiring more solar panel area to be fitted to the aircraft to increase the reachable range of latitudes while experiencing extreme weather conditions, then the design becomes impossible due to constraints on the size of the vehicle due to the enveloping aeroshell and launcher fairing.

Using this solar cell area  $A$  the process of selecting flight tracks was performed by first generating a set of upper height  $h_u$  and upper segment cruise speeds  $V_{I,\text{hor},u}$  and a set of lower heights  $h_l$  and lower segment cruise speeds  $V_{I,\text{hor},l}$ . For each permutation formed by selecting one operating point from each set a simulation was performed for the accelerating, climbing and diving phases. If the chosen solution was possible for the given design solar cell area  $A$  and battery capacity  $C$  then the lower segment cruising time  $t_l$  was varied to see what its effects were on the mission parameters. The resulting set of valid solutions were filtered manually for flight tracks applicable to the mission. This process was repeated for varying latitudes and battery capacities manually in order to gauge the limits of the flight envelope.

Due to the large computational costs involved the tracks could not be designed and investigated with the same degree of accuracy as other optimisations in this report. It is likely that some efficiency can be gained by performing an analysis with a finer selection of operating points. At the very least it will provide better insight into the exact operating regions in the Venusian atmosphere. The considered battery masses, from which the battery capacity is determined, are  $100\text{ kg}$ ,  $150\text{ kg}$ ,  $200\text{ kg}$  and  $250\text{ kg}$ . The considered lower altitudes range from  $32\text{ km}$  to  $52\text{ km}$  in steps of  $5\text{ km}$ . The latitudes are varied up until a value of  $45^\circ$ .

To dive to an altitude of  $37\text{ km}$  and climb out again the required battery capacity is  $190\text{ MJ}$  at a latitude  $\phi$  of  $15^\circ$  and a capacity of  $208\text{ MJ}$  at  $25^\circ$ . These correspond to battery weights of  $269\text{ kg}$  and  $295\text{ kg}$ , respectively. These values, although attainable, require a complete redesign of all developed vehicles and are, as a result, not used.

Instead a battery mass of  $200\text{ kg}$ , corresponding to a capacity of  $141\text{ MJ}$ , is used in the final aircraft. This allows flying at tracks at various latitudes as indicated in Table 5.7 while adhering to the developed vehicle estimates so far.

Table 5.7: Designed flight tracks for a range of latitudes at mean atmospheric weather intensity.

$\phi [^\circ]$	$h_u [km]$	$V_{I,\text{hor},u} [m/s]$	$h_l [km]$	$V_{I,\text{hor},l} [m/s]$	$f_m [\%]$	$f_s [\%]$	$f_o$	$f_c [\%]$	$t_l [\text{min}]$
35.0	66.7	2.6	47.0	-23.1	4.22	49.0	-14.3	0.82	3
35.0	67.6	18.4	47.0	-17.7	41.4	24.9	-1.2	27.7	200
35.0	69.6	34.2	47.0	-12.3	1.93	28.6	18	N/A	20
25.0	66.7	2.6	42.0	-23.8	4.35	54	-15.6	0.7	7.65
25.0	69.6	34.2	42.0	-23.8	31.2	45.7	-1.77	22.6	119
25.0	69.6	34.2	47.0	-12.3	35.3	34.6	-1.14	30.8	153
15.0	69.6	34.2	42.0	-7.2	6.34	65.0	-17.2	4.47	10.7
15.0	69.6	34.2	42.0	-18.3	36.7	46.9	-2.25	25.4	136
15.0	67.7	18.4	47.0	-12.3	51.8	30.0	-1.89	31.1	212

Each set of three consecutive flight tracks is associated with flying at a single latitude. The first track in each group is a track that is used to move retrograde quickly, the second track is used as the general flight track to perform the main scientific mission. The last flight track in each group of three is used to move prograde more quickly while still spending a decent amount of time taking measurements. The nominal flight track considered throughout the rest of the report is the general main mission flight track at a latitude  $\phi$  of  $15^\circ$  as this covers the main regions of interest in the Atla region. The flight track for the lower segment time  $t_l$  of 136 min, as indicated in Table 5.7, is shown in Fig. 5.9 as a curve relating flying altitude  $h$  to the covered ground track  $d_G$ . Apart from this figure the variation of the various flight track metrics as a function of the lower segment time  $t_l$  are shown as well. As can be seen much more mission time can be allocated to secondary mission objectives by reducing the lower segment time.

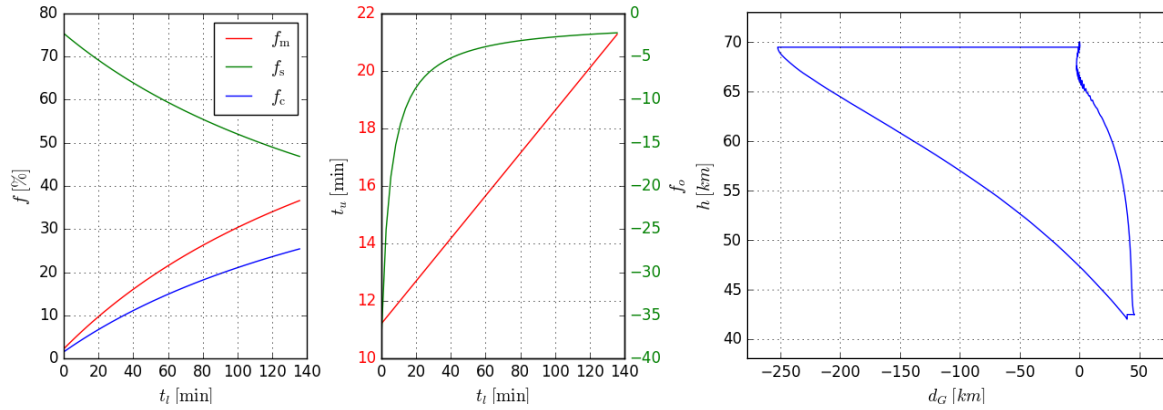


Figure 5.9: The flight track parameters as a function of lower segment cruising time  $t_l$  in the left two figures and ground track geometry in the right figure.

The aircraft can probably fly lower than the indicated 42 km height, but this requires a new investigation into the flight tracks with finer mesh of considered flying altitudes and velocities for which the computational resources were not available. Furthermore, some of the sizing methods used for the other vehicles still depend on an earlier iteration's lower segment height of 37 km. The altitude of 42 km, although still in the sulphuric acid haze, is below the reported lower cloud height of 45 km. This will allow for a relatively unobscured view of the surface for remote sensing as compared to the satellite.

## 5.3. AERODYNAMICS

### 5.3.1. ENCOUNTERED RANGES OF ATMOSPHERIC PROPERTIES

Given the mission profile as determined in Section 5.2 the aircraft has a limited range of dynamic pressures and Reynolds numbers it will encounter. The dynamic pressure is estimated for cruising conditions as described in Section 5.2.1. The Reynolds number is defined as shown in Eq. (5.49).

$$\text{Re} = \frac{\rho (V_W + V_{I,\text{hor}}) L}{\mu} = \frac{(V_W + V_{I,\text{hor}}) L}{\nu} \quad (5.49)$$

Where  $L$  is a characteristic length in  $m$ , the root chord in this case,  $\mu$  is the dynamic viscosity in  $Pa \cdot s$  and  $\nu$  is the kinematic viscosity in  $m^2/s$ . The kinematic viscosity is estimated by using Sutherland's law combined with VIRA [6] [7].

Overlaying a contour describing the operating ranges of the aircraft over a map displaying the Reynolds number  $\text{Re}$  and the freestream dynamic pressure  $q_\infty$  for the minimum and maximum atmospheric severity values of  $\zeta = -1.55$  and  $1.55$  yields Fig. 5.10. Analysing these figures for the operating conditions during lower cruise, climbing and upper cruise yields values as shown in Table 5.8

### 5.3.2. WING PLANFORM DESIGN

Section 5.2.4 indicated the requirement to have a total of  $107.06 m^2$  of solar panels installed on the aircraft. Putting solar panels on the main wing and the horizontal stabiliser ensure a solar incidence angle that is nearly normal to the solar cell surface. Mutually designed with the control surface sizing method described in Section 5.7,  $79.06 m^2$  of solar cells should fit on the top and the bottom of the main wing. As this is already a very large surface area, the main wing should have a planform area  $S$  of no larger than approximately  $40 m^2$ .

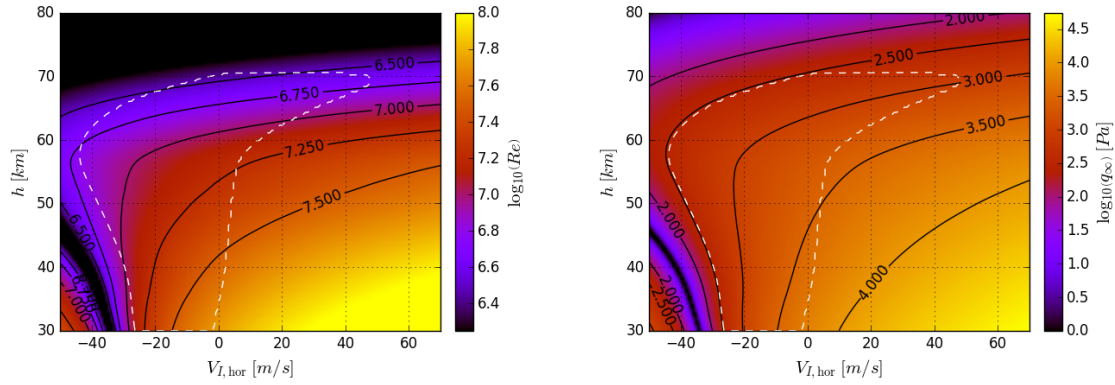


Figure 5.10: The variation of the Reynolds number  $Re$  and freestream dynamic pressure  $q_\infty$  with height  $h$  and velocity  $V_{I,hor}$  for the atmospheric severity values  $\zeta$  of 0 at a solar longitude  $\lambda_S$  of  $0^\circ$  and a latitude  $\phi$  of  $0^\circ$

Table 5.8: Ranges of Reynolds numbers  $Re$  and dynamic pressures  $q_\infty$  most commonly experienced by the aircraft during the three powered flight phases

Flight phase	$Re_{min}$	$Re_{max}$	$q_{\infty,min}$ [Pa]	$q_{\infty,max}$ [Pa]
Lower cruise	$1.22 \cdot 10^7$	$2.63 \cdot 10^7$	447.7	1995
Climbing	$7.08 \cdot 10^6$	$1.17 \cdot 10^7$	354.8	446.7
Upper cruise	$3.98 \cdot 10^6$	$5.29 \cdot 10^6$	398.1	1000

Another requirement is imposed by the maximum available diameter within an aeroshell of  $4.6m$  and a maximum height of  $7.0m$ , as the folded aircraft will have to fit within the launcher fairing together with a spacecraft. For a given aeroshell height  $h_{ae}$  and intermediate chord  $c_i$ , the section spans  $b_1$  and  $b_2$  can be calculated using Eq. (5.50).

$$tc_i + b_1 = \sqrt{r_{ae,b}^2 - c_i^2} \rightarrow b_1 = -tc_i + \frac{1}{2} \sqrt{(2tc_i)^2 - \left(t^2c_i^2 + \frac{1}{4}c_i^2 - r_{ae,b}^2\right)} \quad (5.50)$$

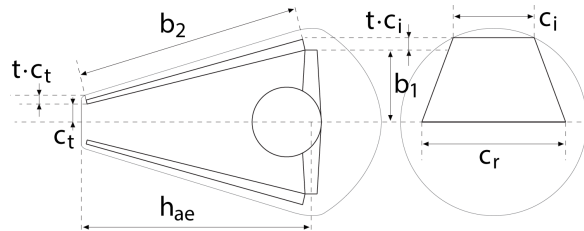


Figure 5.11: Geometrical parameters associated with the aeroshell and the wing planform

All parameters in this equation are geometric parameters as shown in Fig. 5.11 in  $m$ . Requiring that the total wing area equals the planned planform area  $S$  imposes a requirement on the tip chord  $t_i$ , which in turn determines the top aeroshell radius  $r_{ae,t}$ . These requirements are given by Eq. (5.51).

$$S = b_1(c_r + c_i) + b_2(c_t + c_i) \rightarrow c_t = \frac{S}{b_2} - \frac{b_1}{b_2}(c_r + c_i) - c_i \quad (5.51)$$

These calculations are performed with the aeroshell height  $h_{ae}$  varied between  $1m$  and  $7m$ , the intermediate chord  $c_i$  varied between  $0.1m$  and  $4.75m$  and fixing the root chord  $c_r$  to  $4.0m$  to leave some extra space for a possible bulging fuselage. A design space is formulated by restricting  $b_1$  to values of  $1.4m$  and  $3.0m$  to leave room for a folding tail,  $c_t$  to values between  $0m$  and  $c_r$  and  $r_{ae,t}$  to values between  $0m$  and  $1.1m$  to result in some form of conical shape for the aeroshell. The resulting design space is very small, essentially fixing the design to root chord  $c_r$ , intermediate chord  $c_i$  and tip chord  $c_t$  of  $4.0m$ ,  $3.04m$  and  $1.45m$ , respectively with spans  $b_1$  and  $b_2$  of  $1.41m$  and  $6.70m$ . This produces a wing planform area  $S$  of  $40m^2$ .

By assuming an elliptical lift distribution and using the determined wing planform together with the freestream dynamic pressures  $q_\infty$  as given in Table 5.8, design lift coefficients of 0.35, 0.58 and 0.30 are determined for lower cruise, climbing and upper cruise, respectively [27]. Investigating the NACA 6-series airfoils using trial and error with XFOIL and XFLR5 yielded the NACA 64<sub>2</sub>-110 and NACA 64<sub>2</sub>-210 as possible candidates for reasons listed below.

- Airfoils that were thinner than 9% tended to stall very quickly at the lower Reynolds numbers which was deemed dangerous when accelerating to upper segment cruise speed after climbout.
- Airfoils producing less lift than the chosen ones (being essentially symmetrical) performed well during cruise but performed worse while climbing.
- Airfoils with more camber caused the cruising angle to become very small. As a result small changes in angle of attack would cause large changes in aerodynamic forces. For this reason these airfoils were considered dangerous.

Airfoils with larger thicknesses were compared to the chosen ones but were found to be less efficient. The NACA 64<sub>2</sub>-210 airfoil performs well at low Reynolds numbers but performs bad at the higher Reynolds numbers. The NACA 64<sub>2</sub>-110 airfoil exhibits the opposite behaviour. By combining the two airfoils in a single design the aerodynamic performance in the low Reynolds and high Reynolds regions take a performance hit but a decent overall performance is achieved. With the chosen airfoils the lift distribution was adjusted by introducing a small amount of washin. This yielded further increases in overall aerodynamic performance at the cost of having to keep the angle of attack relatively low, but within operational angles of attack, to reduce the risk of tip stalling.

The wing planform design parameters per spanwise station can be reviewed in table Table 5.9. A graphical depiction of the wing, as rendered by XFLR5, is shown in Fig. 5.12.

Table 5.9: Geometrical parameters associated with the designed wing planform

Root distance [m]	Local span [m]	Local taper ratio [m]	Chord [m]	Twist [°]	Airfoil
0	0	0	4.00	-0.81	NACA 64 <sub>2</sub> -210
1.41	1.41	0.76	3.04	-0.73	NACA 64 <sub>2</sub> -210
8.11	6.70	0.48	1.45	0.99	NACA 64 <sub>2</sub> -110

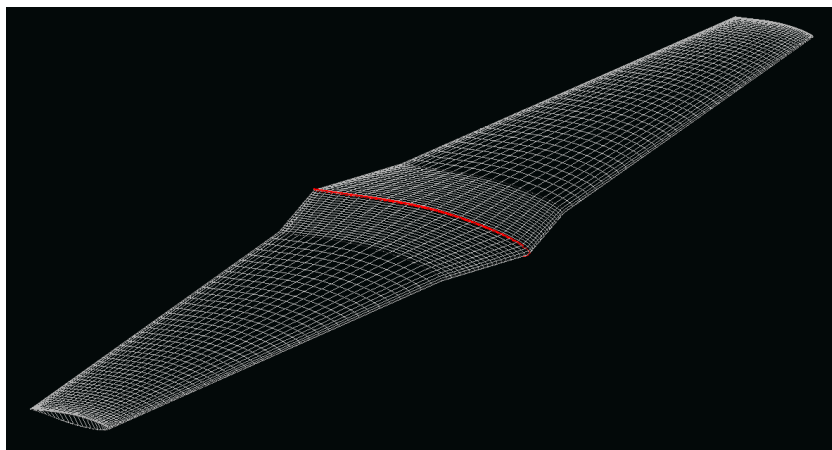


Figure 5.12: Graphical depiction of the wing planform design

## 5.4. PROPULSION

The propulsion of the aircraft is provided by electric propellers. Since no fuel is required, this increases the lifetime of the aircraft. In this section, the design choices are elaborated upon. With the choices in place, the mass and efficiency of the system are calculated.

### 5.4.1. PROPELLER DESIGN

The design choices for the propellers are discussed in order of: number and size of propellers, number of blades, pitch, rotational speed and airfoil. The main driving factor is required thrust.

### PROPELLER SIZING

The main limiting factors of the propeller sizing are the space in the aeroshell and along the wing. Considering the inter-propeller interference it is required to optimise for the effective propulsive area. The resulting minimum distance between any two propellers is 1 m. The distance between the end of the wing and the last propeller is 20 cm.

With these spacings, 5 propellers will fit on the aircraft: A propeller in the center with a diameter of 2.8 m and two propellers at each side of the fuselage with diameters of 2.3 m. From these five propellers, three will be used at the lower altitudes (including the large one) and two at the higher altitudes. Designing the propeller blades just for one altitude would decrease the amount of available thrust for the other altitudes to below the required thrust.

The number of propeller blades is another design choice. On one hand, the efficiency of the propellers decreases with the increasing number of blades, on the other, the maximum thrust increases. The differences in efficiency and thrust are small, however since available power is limited and therefore efficiency is driving two blade propellers are used.

### PITCH AND ROTATION SPEED

The pitch and the rotational speed as well as the aircraft velocity define the advance ratio, which defines the propeller efficiency. Since the aircraft velocity varies greatly, the pitch and rotational speed must change as well, otherwise the efficiency will drop by an unacceptable amount.

The rotation speed is limited to 3000 RPM because of structural reasons. A higher rotational speed would require an increase in the mass of the blades. A high rotational speed will also cause local velocities to reach the speed of sound and therefore increase drag and decrease the efficiency.

### BLADE TWIST

Another aspect which effects the propeller efficiency is the blade twist. Since the aircraft velocity, density, pitch and rotational speed vary greatly with altitude, a variable twist propeller is preferred. However, since these do not exist, different twists are used for the 5 propellers to emulate the variable pitch and have reasonable efficiencies along a range of altitudes.

The first design point is the high altitude cruise flight since the aircraft flies in this region for a major part of the track. The required thrust is relatively low, 351 N, two out of the five propellers will be used for the upper track. The other design point chosen was at the highest required thrust, 3107 N. This occurs at the lowest altitude, where the power required is the same, but the velocity is 10.3 m/s.

The blade twist was optimised such that the blade angle of attack along the blade is equal to 4° at the design point. This angle of attack has the highest L/D for the used propeller airfoil. As the direction of the incoming flow differs along the blade, this will give a twist in the blade.

### AIRFOIL

In principle the airfoil of propeller blades can differ along the blade length. However, the airfoil was set constant to reduce the running time of the programme and to allow for verification. For the airfoil selection and chord variation along the length of the blades, the program JavaProp was used. This program takes into account the following parameters: Density, kinematic viscosity, velocity, required thrust, diameter, speed of sound, RPM, number of blades and spinner diameter (set to 5 cm). The selected airfoil is mh114, 13% because of its high L/D. This airfoil is used as input for the program XFLR5 to calculate the Cl and Cd for a range of angle of attacks. The polar graphs can be seen in Fig. 5.14. The Reynolds number used for the Cl- $\alpha$  and Cd- $\alpha$  graphs is 300,000. Although the Reynolds number changes along the blade length, this has a limited effect on the Cl and Cd.

#### 5.4.2. EFFICIENCY CALCULATION

The efficiency was calculated using Eq. (5.52) for each type of propeller. In this equation Q is the required torque in Nm and  $\omega$  the rotational speed in rad/s. A factor 1.15 is used because in reality, the actual required power is 15% more than the required power that follows from this equation<sup>36</sup>.

$$\eta = \frac{TV_{\infty}}{1.15Q\omega} \quad (5.52)$$

For the calculation of the thrust and torque, the blades were divided into small sections dr. Where r is the distance from the center to the position on the blade. The thrust and torque contributions per blade section

<sup>36</sup><http://web.mit.edu/16.unified/www/FALL/thermodynamics/notes/node86.html>

are calculated using Eq. (5.53) and Eq. (5.54). In this equation  $\phi$  stands for the angle between the velocity in the plane of the propeller and the axial velocity. In the calculation of these velocities, axial and angular inflow factors are used<sup>37</sup> to take into account the swirl and the increase of the axial velocity in front of the propeller. The  $C_l$  and  $C_d$  of the airfoil are calculated using the local angle of attack, the  $C_l$  and  $C_d$  plots generated by XFLR5 and Prandtl-Glauert corrections for the local Mach number. The velocity  $V$  is in this case the local velocity over the blade section and  $c$  the local chord.

$$dT = [C_l \cos(\phi) - C_d \sin(\phi)] \frac{1}{2} \rho V^2 c dr \quad (5.53)$$

$$dQ = [C_l \sin(\phi) + C_d \cos(\phi)] \frac{1}{2} \rho V^2 c dr \quad (5.54)$$

In the efficiency calculations the rotational speed and pitch were optimised for each time step. This was done using an RPM step of 50 and a pitch angle step of  $\pi/25$ . Furthermore a safety factor of 1.2 was used on the required thrust to take into account unexpected atmospheric properties such as densities.

The weighted average propulsive efficiency was calculated from the three propellers used at the lower altitudes. At a certain moment during climb, the efficiency of the other two propellers will become larger and those propellers will take over. In this way a graph is made with the propulsive efficiency along the whole track. Next to the propulsive efficiency, the electrical engines of the propellers have an efficiency. Based on [28] the engine efficiency is estimated at 0.8. With the propulsive efficiency and the engine efficiency, the total efficiency was calculated followed by the required power. Both efficiencies can be seen in Fig. 5.13.

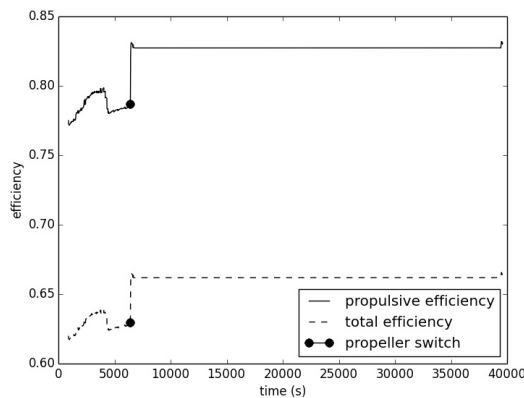


Figure 5.13: Propeller efficiency

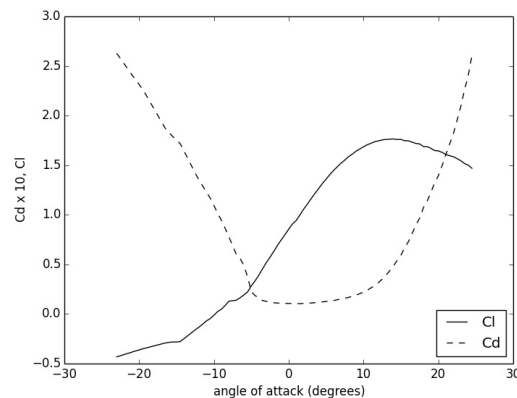


Figure 5.14: Airfoil polar

### 5.4.3. MASS ESTIMATION

The mass estimation of the propulsion system is based on existing large scale solar aircraft like Helios[29]. The mass depends on the input power of the electric engines and is estimated as 0.00042 kg/W. Using the highest input power for each engine the different propeller sets (blades, spinner and engine) will have a mass of: 11.4 kg for the large propeller, 8.0 kg the smaller propellers at low altitude and 11.3 kg for the propellers at high altitude. This will give a total weight of the propulsion system of 50.0 kg.

## 5.5. MATERIALS

Since the aircraft is relying on solar panels to power the propulsion, it would greatly benefit from being as lightweight as possible. However, this lightweight structure must also be able to withstand temperatures up to 200°C during the lower track phase. Furthermore, it must also be able to resist corrosion while flying through the acidic clouds, as well as survive potential lightning strikes. The requirements on the materials are summarised below:

- High Specific Strength
- High Specific Stiffness
- Stable mechanical properties at temperatures between 0-200°C
- Low thermal conductivity
- Resistance to acid corrosion
- Resistance to damage from lightning strikes
- Low absolute Coefficient of Thermal Expansion (CTE)

<sup>37</sup>[http://www-mdp.eng.cam.ac.uk/web/library/enginfo/aerothermal\\_dvd\\_only/aero/propeller/prop1.html](http://www-mdp.eng.cam.ac.uk/web/library/enginfo/aerothermal_dvd_only/aero/propeller/prop1.html)

In order to adhere to this variety of requirements, the aircraft skin will consist of multiple layers. This section will explain the structural composite, acid-resistant coating, lightning protection, and production strategy of the aircraft.

### 5.5.1. STRUCTURAL MATERIAL

Achieving a lightweight, stiff design can most appropriately be achieved by using composites. Continuous fibre reinforced composites are considered to be the most suitable for structural applications [30]. They generally exhibit high specific strength and stiffness, as well as a good dimensional stability. Furthermore, polymer composites are generally more resistant to acid corrosion than metals, which is a useful redundancy in case the coating becomes damaged. Although metals are generally favoured for damage tolerance and maintainability on Earth, this aircraft will not be maintainable and will have a shorter service life than commercial aircraft.

The main challenge is finding a composite material that can withstand the high temperatures, while still being structurally applicable. Most common thermoplastic polymers are not suitable for high temperatures, since they will melt at these temperatures. Although raising the curing temperature of the resin typically raises the maximum operating temperature of the composite, most common thermoset polymers cannot exceed 200°C before decomposing. Furthermore, the thermoset adhesives that hold parts together would also start degrading at a similar temperature. For both, the matrix material is the limiting factor for operating temperature since the fibres will start decomposing at much higher temperatures[30]. The potential materials which were explored are listed below:

- Polyimides
- Liquid Crystal Polymers (LCP)
- Polyaryletherketones (PAEK)
- Metal Matrix Composites (MMC)
- Ceramic Matrix Composites (CMC)
- Phenylethynyl Terminated Imides (PETI)

After studying the characteristics and specifications of these materials, **PETI-330** is chosen as the composite matrix material. It is a low molecular weight imide oligomer developed by NASA Langley Research Centre particularly for creating composites with resin transfer moulding and resin infusion processing [31]. It is able to be readily processed into a composite without the use of an autoclave or complex cure cycles [32]. What is special is that it can be heat processed like a thermoplastic, but then post-cured for heightened mechanical properties and a glass transition temperature of 330°C.

While it is unlikely that the aircraft will experience temperatures higher than 220°C, having a glass transition temperature well beyond this will ensure a more reliable structural performance. It is therefore chosen due to its retention of mechanical properties at high temperatures, and its processability. It can be used as a resin in a composite with a variety of specific carbon fibres, such as Toray. It is commercially available from UBE Industries Ltd. as a resin, with main specifications given in Table 5.10 below [31] [33]:

Table 5.10: Specifications of PETI-330 Composite

Composite	PETI-330, 59% T300-3K plain woven carbon fibre
Tg	330 °C
E-modulus	64 GPa
Density	1300 kg/m <sup>3</sup>
Tensile Strength (room temp)	558 MPa
Tensile Strength retention (232 °C)	80 %

It is also important to consider the failure modes of the chosen structural material. In composites, impact compressive strength typically becomes the design allowable and is therefore more important than fatigue [34]. However, it is assumed that there is nothing in the Venusian atmosphere that can impact the aircraft, and so it is primarily designed for fatigue. Furthermore, since the loading is considered to be cyclic due to changing flight altitudes, creep is not explored.

Fatigue strength is dominated by the fibre type, and not the length of the fibre or the matrix [35]. Since fatigue performance of composites is generally superior to metals, and carbon fibres have particularly outstanding fatigue (and creep) properties [34], this aircraft is at an inherent advantage in this regard. Therefore, it is beneficial to orient the fibres in the direction of principle stresses of the structure.

Final fatigue failure is still a complex combination of matrix and fibre failure. Microcracks can occur early and be present for most of the aircraft's lifetime [34]. Therefore, it is very important to ensure that the composite is sufficiently sealed from the acidic environment. Furthermore, hot environments and thermal cycling

most negatively impact fatigue strength. While it would be useful to predict the fatigue life, limited characterisation data and physics-based theories are not easily applied at a composite level [36]. Relevant experimental data could not be found for the composite matrix nor the fibres, and so it is best to mitigate the risk of fatigue by implementing multiple load paths for a fail safe design [34].

#### ACID RESISTANT COATING

The coating must be able to effectively protect the structural material and solar panels from sulfuric acid corrosion, as well as not degrade under the lower track temperatures. Ideally, if the coating could be self healing, then protection could be ensured even if damage occurs. However, no self healing materials were found that could function at such a high temperature.

**Teflon PTFE resin**, a fluoropolymer, is therefore chosen as the aircraft coating for its excellent corrosion and chemical resistance at operating temperatures up to 315°C. Furthermore, it also exhibits an extremely low coefficient of friction as well as a low electrical conductivity<sup>38</sup>. The VEGA balloons were also made of Teflon, proving its functionality in the Venusian atmosphere [37]. Furthermore, having been applied extensively and commercially in many different industries, it is a well developed product that has proven its reliability.

From exploring the variety of Teflon products on the DuPont website, Teflon PTFE DISP 30 is considered to be a suitable variety for the application of the aircraft. It is often preferred for coating woven composites. It can be sprayed on or dip coated and baked to a tough finish [38].

A Teflon thickness of 0.0508 mm (2 mils) is typical for an industrial coating<sup>39</sup>. With a density of 2160 kg/m<sup>3</sup> [39], applying this coating over the whole surface area yields a total weight of 14.26 kg for one coat.

#### LIGHTNING PROTECTION

Faint luminosities, traditionally known as the Ashen light, have already been observed on the night side of Venus for over 300 years [40]. Despite observations that could be considered as evidence, to this day there is still an unresolved discussion as to whether there are occurrences of lightning in the clouds of Venus. Although it is an uncertainty, it will still be treated as a possible risk. If it is left untreated and a lightning strike does occur, it could lead to failure of the aircraft and consequently failure of the mission.

Unless protected, composite structures can suffer more damage from lightning strikes than metals. Furthermore, electronics can suffer from the electromagnetic waves emitted by the lightning [34]. Ideally, the entire outer surface should be highly conductive and electrically continuous. In this way, the charge can either be directed to a ground point, or be redirected back into the air. Although carbon fibre laminates are very conductive, they still pose a puncture threat for skin thicknesses less than 4 mm [34]. Furthermore, since the outermost layer of the aircraft will be coated with electrically insulating Teflon, it is in danger of confining strikes to a local area, intensifying the damage. The required protection against the acidic environment is therefore a complication which aircraft on Earth are not concerned with.

Several mechanisms were explored in order to provide a lightweight protection against potential lightning strikes. Aluminium is often applied as either a wire mesh, arc spray, interwoven fibres, conductive paint or bar diverters [34]. However, aluminium is considered incompatible with carbon based fibres due to the risk of galvanic corrosion [41]. Furthermore, any outer aluminium layers will be in danger of acid corrosion. This could be countered by using another metal, such as copper, which is very conductive and also unreactive with sulfuric acid, although it will be heavier. A lightweight expanded copper foil is available from Dexmet, called MicroGrid. Its application to the aircraft for a preliminary weight estimation is summarised in Table 5.11 below:

Table 5.11: Lightning prevention: copper mesh weight estimation

Type	% Surface Area	Surface Area [m <sup>2</sup> ]	Mass [kg]
Lightweight	75	97.5	4.76
Zone 1A	20	26	5.07
Heavy	5	6.5	10.38
			20.21

Conductive polymers have recently been developed which allow significant weight savings compared to metals. In an effort to minimise the added weight, LORD UltraConductive Coating is chosen, which advertises

<sup>38</sup><http://www.metcoat.com/chemical-resistant-coatings.htm>

<sup>39</sup><http://www.metcoat.com/chemical-resistant-coatings.htm>

the equivalent conductivity of one millimetre of aluminium, while being 55% lighter than copper mesh counterparts [42]. The apparent weight saving percentage is applied to the weight estimation of Table 5.11. Taking advantage of this yields a total protection of weight of a mere 11.11 kg.

It is important that the polymer layer is connected to the structural composite at several locations, so that the charge can also flow through the carbon fibres. Furthermore, any metal bolts need to be capped with plastic to prevent arcing. Finally, as described in Section 2.1.2 it is useful to connect the system to a unit which can detect a surge in electrical charge, which can unambiguously confirm the presence of lightning for the scientific community.

#### ASSEMBLY

Since the PETI-330 composite is not commercially available as a prepreg, the main components of the aircraft must be manufactured using either resin transfer moulding, or resin infusion. While there are numerous advantages to using a prepreg for production [34], it can be beneficial to be able to lay the carbon fibres in the chosen directions and locations which will ensure the strongest structure for the lightest weight.

One significant advantage of using PETI-330 is that since it behaves like a thermoplastic before it is post-cured, separate parts can be welded together during this stage. This eliminates the need to use adhesives, and limits the number of mechanical joints needed. Weight can therefore be reduced. Although a variety of welding processes can be used on the aircraft, induction welding will be the main method. Its advantages are improved efficiency, effectiveness for curved or complex parts, and the possibility of single side access [34]. The risk of insufficient quality welds is higher than other techniques, but given that only one aircraft will be produced, more time can be invested in ensuring a consistent quality.

In certain areas of the aircraft, such as the folding points, it is useful to use mechanical joints. Although it is a mature technology with an assured reliability, the strength loss from the laminate notched effect must be compensated with extra material reinforcement. Only 20-50% of the basic laminate tensile strength is retained in a mechanical joint [34]. The calculations concerning the required reinforcement around mechanical joints are complex, depending on the orientation of the fibres and specific layup. For accurate results, the open hole compression strengths of the composite datasheet and the following guidelines [34] are implemented:

- Reinforce plies at 90° and 45° (quasi-isotropic) in order to prevent shear out failure at the hole.
- Use two joint rows if possible.
- Use fasteners with diameters approximately equal to the laminate thickness
- Use double lap joints

The fasteners and bolts will be manufactured from Grade 5 Titanium alloy. This is not only important because of titanium's strength, but also because it can acceptably be used together with the composite without risk of galvanic corrosion with the carbon fibres. It is typically beneficial to also reinforce the laminate by replacing a few plies with titanium sheeting [34], however this can pose delamination risks due to the differences in CTE values.

One of the most important parameters to consider is the CTE of each material in the layup of the aircraft skin. During the thermal cycling at different altitudes, the materials will expand and contract at different rates which may cause additional stresses or delaminations if they are too different. The CTE values for the various materials are given in Table 5.12. PETI-330 composite will expand at a faster rate than the coating. However, Teflon also has an elongation of 400% before failure, which will ensure that it will stretch rather than fracture under the extra stress. Furthermore, titanium has a significantly higher CTE than the other materials, meaning that it must not be placed in between composite plies or in sections where its expansion may crush laminates. Unfortunately, detailed specifications of the UltraConductive coating is unavailable, creating an uncertainty about how it will expand across different temperatures. The entire structure layup should be experimentally tested to ensure that it will stay coherent under thermal cycling.

Table 5.12: CTE values

Material	CTE [ppm/K]
PETI-330 composite	4.6
Teflon PTFE	1.0
Grade 5 Titanium	9.2

The layup of the aircraft skin will start with the aerogel insulation interior, followed by the PETI-330 composite, UltraConductive coating, and Teflon PTFE coating. It is essential that the Teflon coating be the last layer for acid protection, however this has implications for the lightning protection. If lightning strikes, it will have to damage the Teflon before being conducted by the UltraConductive. This would leave an area exposed to acid corrosion. Since it is unknown what the intensity or frequency of the lightning strikes may be, it is also unknown to what extent the aircraft can sustain damage. Minimising the unknown risk will require more and thicker coatings which can greatly increase mass and complicate the power/propulsion requirements. Therefore, the design will be considered sufficient as thus.

## 5.6. STRUCTURE

In this section, the various load cases experienced by the aircraft during the whole mission lifetime are analysed. Once the loads are know, it is possible to size the internal structure to withstand the encountered loads.

### 5.6.1. LOAD CASES

During the mission, there are five load cases to be considered, namely launch load, cruise load, ascent load, descent load, entry load. They are analysed individually in this section. The base value of lift and weight of the aircraft and the wing are 8330 N, 850 kg, 185 kg respectively.

#### LAUNCH LOAD

Figs. 5.15 and 5.16 show the Free Body Diagrams of the launch vehicle and the wing during launch. Fig. 5.17 indicates the corresponding loading and moment diagrams along the wing span.

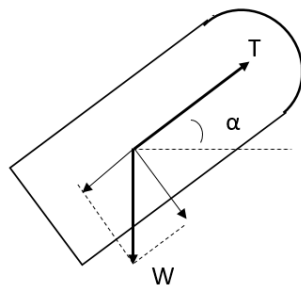


Figure 5.15: FBD: launch vehicle during launch

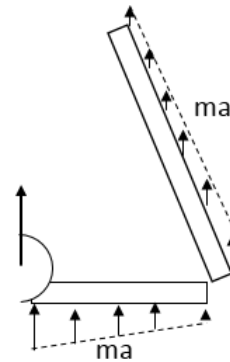


Figure 5.16: FBD: wing during launch

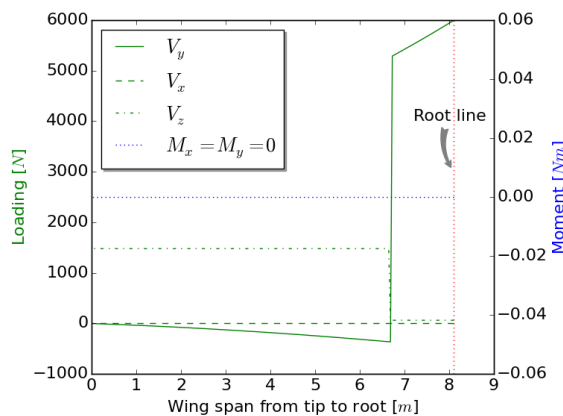


Figure 5.17: Loading and moment diagram of the wing during launch

During launch, the spacecraft will experience acceleration generated by the launch vehicle. Using the SLS

Block 1 as a reference, the maximal acceleration of 3.5g occurs during the second stage burn-out<sup>40</sup>. To find out the acceleration of the axial and lateral direction at that moment, the angle of attack at that moment has to be determined. Due to the lack of data including  $C_L$ ,  $C_D$  and flight path angle, these values are assumed to be 0 in this simulation. The simplified equation to calculate angle of attack of where 3.5g occurs is thereby in Eq. (5.55). The result shows an angle of attack of 79 deg, an  $a_{axial}$  of 3.44g and  $a_{lateral}$  of 0.67g.

$$(T - M \cdot \sin(\alpha))g = M \cdot a \cdot \sin(\alpha) \tag{5.55}$$

**CRUISING LOAD**

Figs. 5.18 and 5.19 are the FBD of the front view and top view of the wing during cruising. Figs. 5.20 and 5.21 indicate the loading and moment diagram in vertical and horizontal directions respectively.

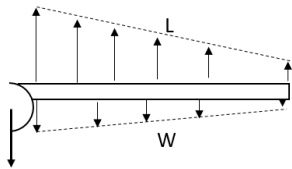


Figure 5.18: FBD: Wing loading during cruising, front view

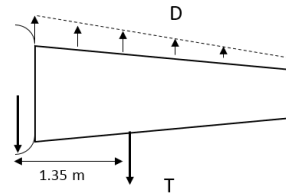


Figure 5.19: FBD: Wing loading during cruising, top view

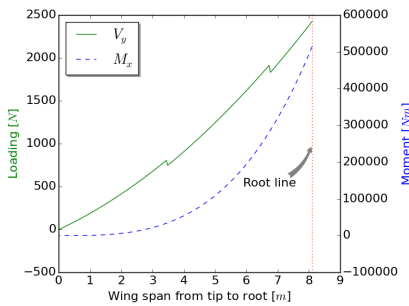


Figure 5.20: Vertical loading and moment diagram of the wing during cruise

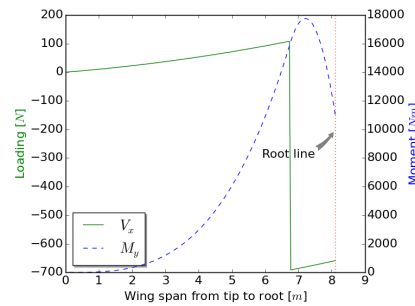


Figure 5.21: Horizontal loading and moment diagram of the wing during cruise

Cruising is achieved on both the higher and lower tracks. The lower track cruising is considered due to the fact that the propellers generate more thrust at lower track, making it more crucial for the load case analysis. During cruising, the vertical forces acting on the wingbox will be dominant. The angle of attack and flight path angle are assumed to be zero degree.

**ASCENT LOAD**

Ascent has the same FBD as cruising load, provided that the angle of attack during ascent is close to 0°. The aircraft will experience a 1.1 g of acceleration during this phase. The flight path angle is also as low as 8°. Figs. 5.22 and 5.23 indicate the loading and moment diagram in the vertical and horizontal direction respectively, using the FBD in Figs. 5.18 and 5.19.

**CLIMB-OUT LOAD DURING DESCENT**

Figs. 5.24 and 5.25 are the FBD for climb-out during descent. Figs. 5.26 and 5.27 indicate the loading and moment diagram during the climb-out in descent phase in both vertical and horizontal directions. The aircraft will experience the largest load during the end phase of the descent, where the aircraft will be climbing out from a whopping -85° flight path angle. The load factor during the climb-out goes up to 1.5.

<sup>40</sup>SLS Mission Planners Guide (MPG) Overview, 02/2014

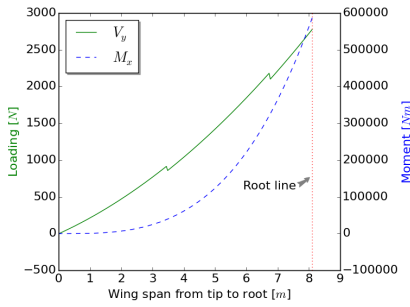


Figure 5.22: Vertical loading and moment diagram of the wing during ascent

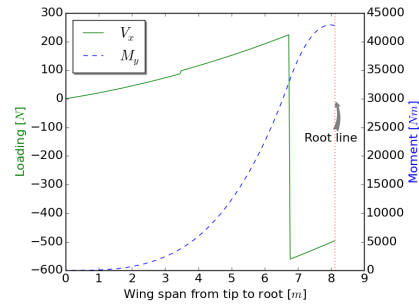


Figure 5.23: Horizontal loading and moment diagram of the wing during ascent

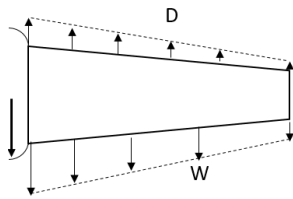


Figure 5.24: FBD: Wing loading during climb-out in the descent phase, top view

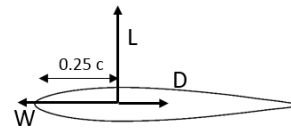


Figure 5.25: FBD: Wing loading during climb-out in the descent phase, side view

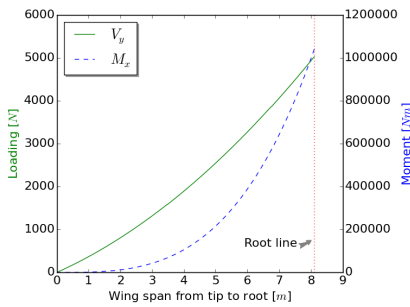


Figure 5.26: Vertical loading and moment diagram of the wing during the climb-out of descent phase

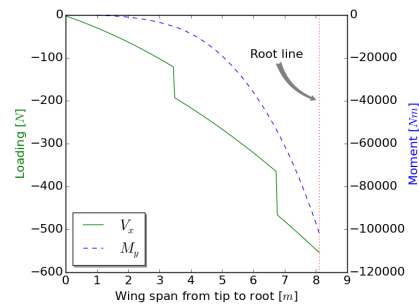


Figure 5.27: Horizontal loading and moment diagram of the wing during the climb-out of descent phase

**ENTRY LOAD**

During the entry to Venus’ atmosphere, the aircraft that is still in the aeroshell can experience an acceleration as much as 26.1g due to aerobraking and parachute drag at an angle of attack of about  $-10^\circ$ . The FBD of the wing during this phase is the same as launch load in Fig. 5.16. Fig. 5.28 shows the loading and moment diagram along the wing span during entry.

**TURNING LOAD**

Figs. 5.29 and 5.30 are the FBD for turning load case. The loading and moment diagrams are indicated in Figs. 5.31 and 5.32.

Lastly, the turning load is analysed. The load factor during turning is as high as 1.7. The turning during the lower track taking into account the lower-track propellers are at higher power output.

**FUSELAGE SPECIFIC**

During entry, the fuselage is assumed to be supported with two pairs of struts. The location of these struts in the length of the fuselage are optimised such that the maximum moment in the fuselage is as low as possible. These locations are at 6% and 88% of the fuselage. The contribution of the wing has not been taken into account because they have supports themselves. The structural mass of the fuselage, was considered as an equally distributed mass, and the other parts inside the fuselage are considered to be point loads. A free body diagram of this situation fuselage is shown in Fig. 5.33. In Fig. 5.35, a free body diagram (FBD) of the fuselage

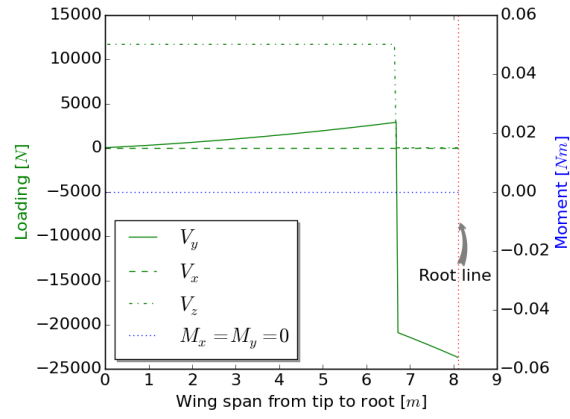


Figure 5.28: Loading and moment diagram of the wing during entry. Note that this is identical to that of the launch case.

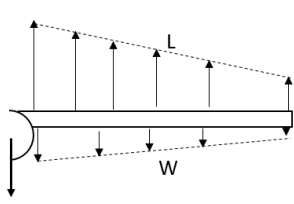


Figure 5.29: FBD: Wing loading during turning, front view

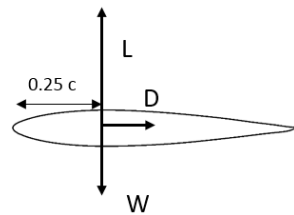


Figure 5.30: FBD: Wing loading during turning, side view

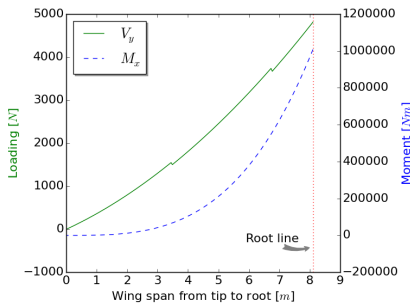


Figure 5.31: Vertical loading and moment diagram of the wing during turning

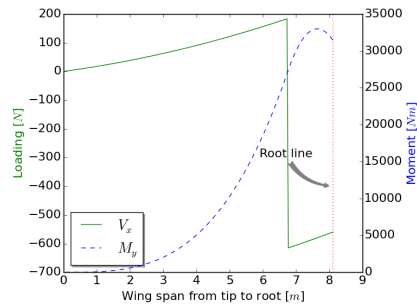


Figure 5.32: Horizontal loading and moment diagram of the wing during turning

cross section at a location of a pair of struts is shown. The moment and shear force diagram can be seen in Fig. 5.34.

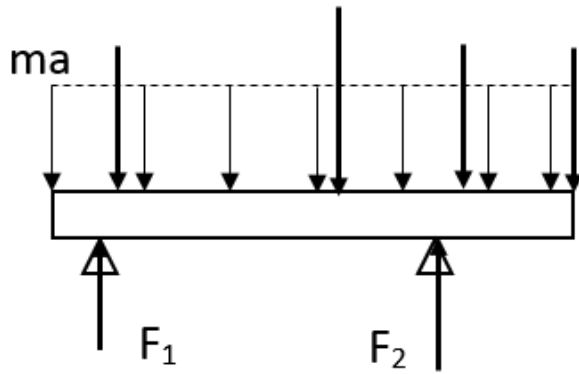


Figure 5.33: FBD Fuselage,  $F_1$  and  $F_2$  are supported loads, the other forces represent acceleration forces

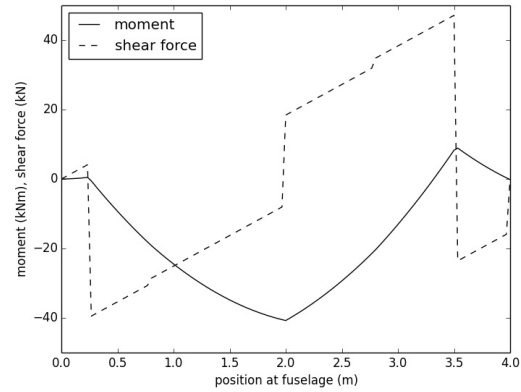


Figure 5.34: Fuselage moment and shear load diagram

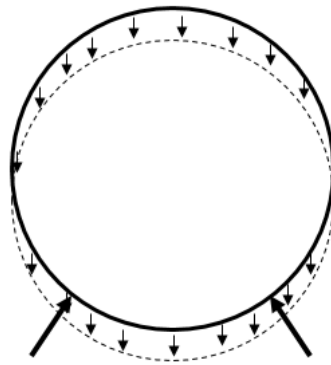


Figure 5.35: FBD Fuselage cross section

### 5.6.2. WING

#### DESIGN METHOD

Comparing the six load cases, it was determined that some are similar. Thus by taking the most critical case out of the similar ones, it will improve efficiency for structural design. First, the launch and entry load case have a similar loading case (just in opposite directions) where during entry, the aircraft will experience a load factor of 26.1g, comparing to launch load's 3.44g. The entry load is therefore a more critical case of the two. Entry load stresses has been analysed as a result. Second, cruise, ascent, and turning load have an identical loading case, amongst which turning load has a load factor of 1.7 comparing to cruise load's 1 and ascent load's 1.1. Turning load case has been analysed thereafter. Last, the climb-out during descent has a unique load case with a load factor of 1.5, hence also a candidate for structural analysis.

The airfoil NACA 64110 has been used during the structural analysis. A wingbox consisting stringers, flanges, spars, and ribs has been designed to reinforce the structure. The location of the front spar of the wingbox is based on [43], at  $0.120c$ . While the end spar of the wingbox is chosen to be smaller than  $0.6c$  to leave room for ailerons, at  $0.592c$ , where  $c$  represents the chord. Note that the location accuracy also depends on the accuracy of the airfoil data interpolation. The number of data points used in this analysis is 302. The word 'spar' used later in this section refers to the spars inside the wingbox, unless specified otherwise. The position of the first spar, is decided to locate at the  $0.255c$  along the airfoil since the load is assumed to act on the aerodynamic center of the wing. The first step in designing the wingbox is set an initial equal spacing for the stringers, or 'booms'. This is to avoid missing airfoil coordinate when the airfoil data points are limited even with an interpolation process. Furthermore, the upper boom spacing is chosen to be the same as lower booms. Once the spacing of booms are defined, the number of booms in the wingbox can be defined. Apart from the analysis of boom number, the effect of a second spar is also discussed. In total, 10 different configurations of wingbox are evaluated, as shown in Fig. 5.37. The rules for the configuration layout is as

follows:

- The configuration nomenclature indicates 'the number of booms on top panel' / 'the number of spars'.
- The alteration of the position and size of the wingbox was not considered in this analysis.
- The baseline is '8/2', each other configuration simplifies in terms of number of booms one by one.
- Once a boom is removed, the rest of the booms remain the same coordinate. This is to keep the load path continuous through booms/spars.
- The first spar is always located at  $0.25c$ .
- The second spar is chosen to be located at the sixth boom in configuration '8/2' to accommodate the later much simplified configuration '4/2'. The location along the chord is  $0.46c$  that is in the range of optimal spar location tested in [43].
- The boom reduction in general follows 'c to 0' and '0.25c concentration'. This means the booms around  $0.25c$  are favourable since it is believed the wing pressure distribution is highest around the  $0.25c$ .

Other design variables that have been considered are: the thickness of the skin, the thickness of the spar, the area of the stringer, last but not least, the spacing and corresponding number of ribs. In total, four structural characteristics were evaluated, namely bending stress, shear stress, rate of twist, and buckling load. Fig. 5.37 illustrates the configuration layouts in a wingbox cross-section.

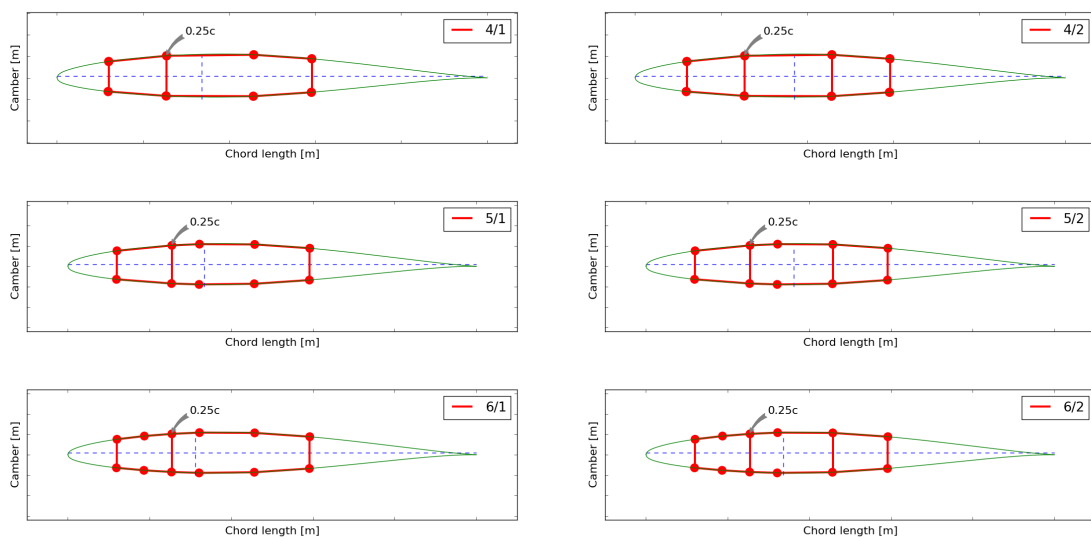


Figure 5.36: Configurations, 8 booms to 12 booms

#### ASSUMPTIONS

- Load case specific:
  - The thrust angle of the propeller is assumed to be  $0^\circ$ .
  - The angle of attack of the aircraft during cruise is ignored.
  - During entry, both the folded and unfolded wing are assumed to be consistently supported so the internal moment is 0.
- The lift and weight is assumed to be a point force acting on the quarter chord, from side view.
- The lift and drag is assumed to be linearly distributed as a function of chord length along the wing span, ignoring finite wing limitation since the shape of lift distribution is unknown.
- The drag is assumed to be a point force acting on the intersection between  $0.25c$  and x neutral axis, from side view.
- Stringers/flanges and skin are combined into 'booms', an idealisation.
- Wingbox skin takes shear only when evaluating shear flow/stress.
- $t_{skin}$  is thereafter assumed to be 0 when calculating shear flow.
- The shear flow between booms is constant.
- Booms take both bending stress and shear stress.

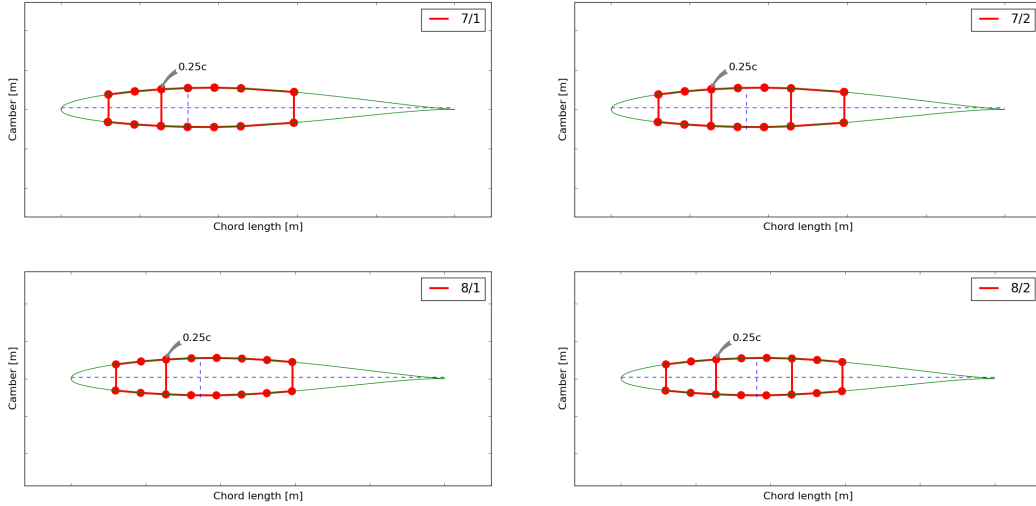


Figure 5.37: Configurations (continued), 14 booms to 16 booms

- There is no distortion in the wingbox.

#### DESIGN CRITERIA

Tsai-Hill failure criteria has been applied for judging the structural integrity due to the fact the aircraft is using PETI-330 composite that is anisotropic. For a panel in tension in x direction:

$$\frac{\sigma_x^2}{X_t^2} - \frac{\sigma_x \sigma_y}{X_t^2} + \frac{\sigma_y^2}{Y_c^2} + \frac{\tau_{xy}^2}{S^2} \leq 1 \quad (5.56)$$

Where the stresses at the numerator are the values retrieved from the simulation and the stresses at the denominator are the material properties. This requires finding out bending stress and shear stress.

The shear flow is calculated using the following procedure that can be found in [44]. To analyse the shear flow, Eq. (5.57) calculates the shear flow of a closed section.

$$q_s = -\frac{I_{xx}S_x - I_{xy}S_y}{I_{xx}I_{yy} - I_{xy}^2} \sum_{r=1}^n B_r x_r - \frac{I_{yy}S_y - I_{xy}S_x}{I_{xx}I_{yy} - I_{xy}^2} \sum_{r=1}^n B_r y_r + q_{s0} \quad (5.57)$$

The open section shear flow is first calculated. Then by equating the rate of twist in the left and right cell of the wingbox,  $G \frac{d\theta_1}{dz} = G \frac{d\theta_2}{dz}$ , and applying the moment equilibrium,  $0 = \sum_{R=1}^n \int p q_{bR} ds + \sum_{R=1}^n 2A_R q_{s0R}$ , the constant shear flow  $q_{s0R}$  in the left and right cell is calculated. The resulting shear flow  $q_s$  is thus adding  $q_{s0}$  to the open section shear flow.

To calculate buckling force and the corresponding critical buckling load, the wing is divided into  $n_{rib} - 1$  boxes. Each part represents a beam. The buckling criteria of a clamp-clamp scenario is used given that the ends of each box are non-deflectable, thus equivalent to a clamp-clamp beam buckling case. An exception is made to the tip, in which the tip box is free to deflect at the tip end. Eq. (5.58) calculates the critical buckling load for a beam, where  $L_{eff} = 2L_{beam}$  for clamp-clamp beams and  $L_{eff} = 0.5L_{beam}$  for clamp-free beams.

$$P_{crit} = \frac{\pi^2 \cdot EI}{L_{eff}^2} \quad (5.58)$$

The structural design process follows the flow chart in Fig. 5.38.

As shown in Figs. 5.39 and 5.40, the change of thickness of the skin is most sensitive to Tsai-Hill criteria, with the thickness of the spar being the least. This is kept in mind during the optimisation to select the appropriate range for each parameters.

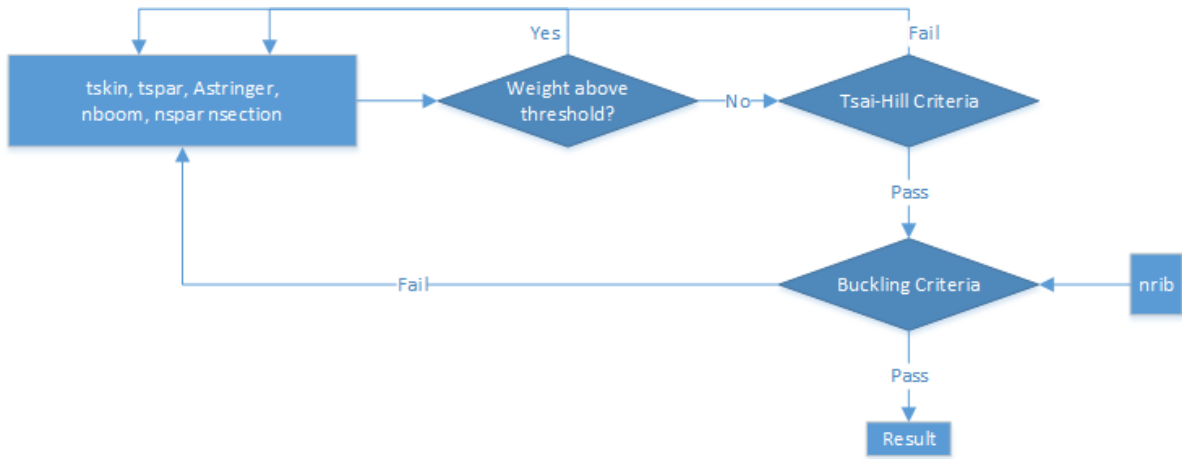


Figure 5.38: The flow chart of the structural design of the wing. Meaningful results of the wingbox dimensions are only generated if the current wingbox characteristic passes three criteria, namely light weight, Tsai-Hill, and lastly, critical buckling.

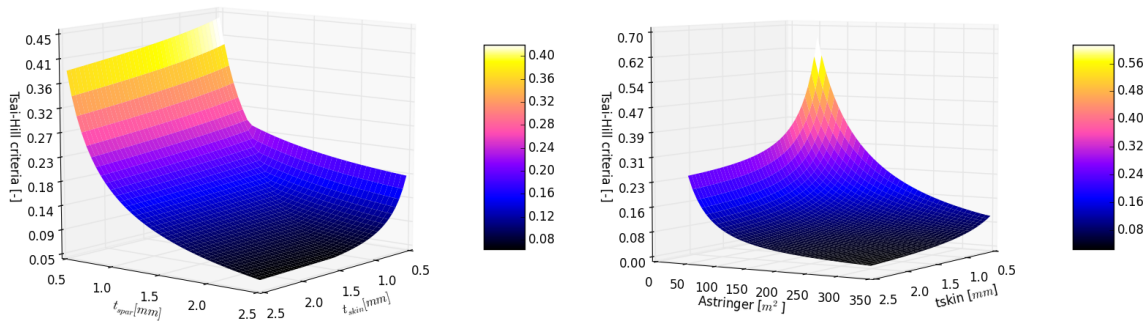


Figure 5.39: Tsai-Hill value sensitivity analysis,  $t_{spar}$  vs.  $t_{skin}$ . The Figure 5.40: Tsai-Hill value sensitivity analysis,  $A_{stringer}$  vs.  $t_{skin}$ . The Tsai-Hill value the lower the better.

**OPTIMISATION**

The wing has been split into 3 sections. The first section is from the root to the hinge line, which corresponds to 1.4 m. The second and the third section have equal length, splitting the rest of the wing, which corresponds to 3.35 m. The following is the changeable parameters for the wing structural optimisation.

Parameter	Value range
$t_{skin}$	0.5 mm - 1.5 mm
$t_{spar}$	0.5 mm - 1.5 mm
$A_{stringer}$	100 mm <sup>2</sup> - 250 mm <sup>2</sup>
$n_{rib}$	3 - 9
$n_{boom}$	12 - 18
$n_{spar}$	1 - 2

Table 5.13: Variable parameters to experiment with the wingbox

**Effect of A Second Spar**

Out of 10 configurations, half are 2-spar configurations. It is believed a second spar can help share the shear flow in the wingbox and reduce stress concentration. To illustrate this, Figs. 5.42 and 5.43 plot the shear stress and flow of two identical configuration – with spar being the only difference. The order of the numbers

at each span-wise location is using the rule that follows clockwise direction in each cell in the wingbox as can be seen in Fig. 5.41:

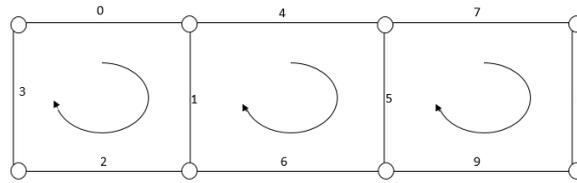


Figure 5.41: Illustration of the ordering of the shear stress and shear flow results, taking configuration '4/2' as an example.

An extra kink can be seen at boom section number 9 in Fig. 5.43. This is where the second spar is located in '8/2' following the rule of shear flow ordering in Fig. 5.41. This means a second spar reduces stress concentration.

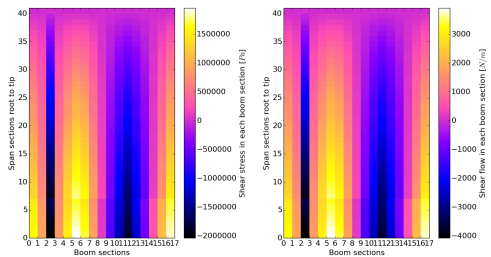


Figure 5.42: Shear stress and flow with 1-spar configuration, the configuration used is '8/1'. The load case used is 'turning'.  
 $t_{skin} = t_{spar} = 2mm, A_{flange} = 150mm^2$

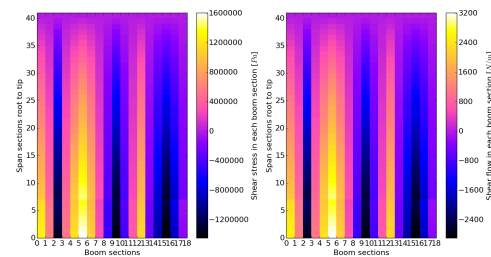


Figure 5.43: Shear stress and flow with 2-spar configuration, the configuration used is '8/2'. The load case used is 'turning'.  
 $t_{skin} = t_{spar} = 2mm, A_{flange} = 150mm^2$

**RESULTS**

Analysis was done for the three chosen load cases, namely climb-out during descent, turning, and entry. Moreover, since the wingbox has been split into 3 sections, the stresses are simulated separately from section to section for better clarification. A safety factor of 1.2 for stresses was used, while 1.1 was used for critical buckling load. Table 5.14 provides an overview of the wingbox parameter specifications.

Section	Configuration	$t_{skin}$ [mm]	$t_{spar}$ [mm]	$A_{stringer}$ [mm <sup>2</sup> ]	$n_{rib}$	Weight [kg] [kg]
Root to hinge line	7/1	1	1	100	6	32.47
Hinge line to second cut	7/2	0.5	1	150	8	51.20
Second cut to tip	4/1	0.5	0.5	100	5	16.23
<b>Total</b>	-	-	-	-	-	<b>99.9</b>

Table 5.14: Specification of each section in the wingbox along the span

For the bending stress, the shear stress and shear flow results, plots are generated for each load cases in the order of 'climb-out during descent', 'turning', 'entry'. In each load case, the plots are split into 3 sections as the wing intended to have, namely 'second cut to tip', 'hinge line to second cut', and 'root to hinge line'.

**Climb-out During Descent**

The bending stress of the three wing sections from tip to root is shown in Figs. 5.44, 5.46 and 5.48. The shear stress and flow of the three wing sections from tip to root is shown in Figs. 5.45, 5.47 and 5.49.

**Turning**

The bending stress of the three wing sections from tip to root is shown in Figs. 5.50, 5.52 and 5.54. The shear stress and flow of the three wing sections from tip to root is shown in Figs. 5.51, 5.53 and 5.55.

**Entry**

In the entry phase, as previously mentioned, the support to the wing are designed so that no internal moment

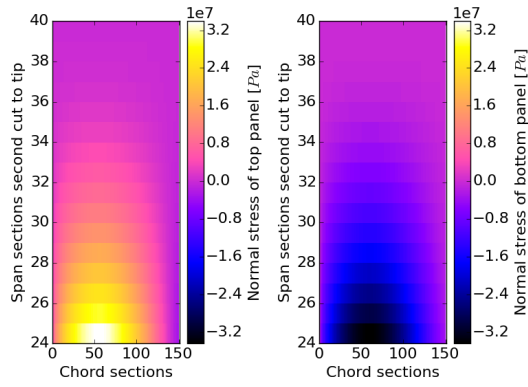


Figure 5.44: Bending stress from second cut to tip during climb-out in the descent phase

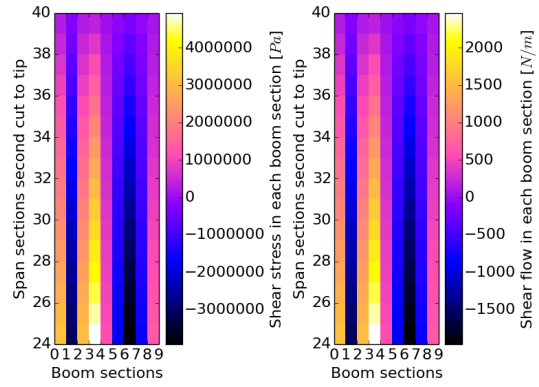


Figure 5.45: Shear stress (left) and flow (right) from second cut to tip during climb-out in the descent phase

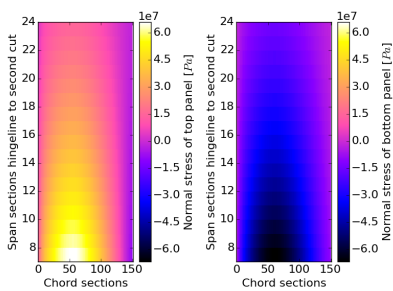


Figure 5.46: Bending stress from hinge line to second cut during climb-out in the descent phase

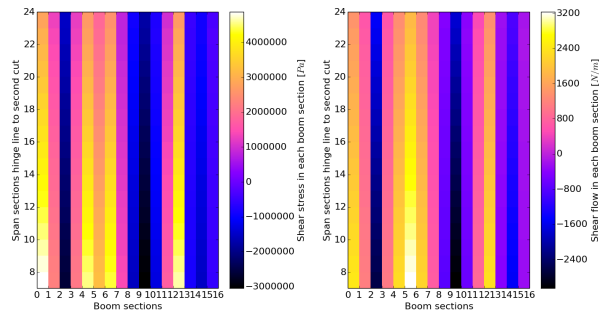


Figure 5.47: Shear stress (left) and flow (right) from second cut to tip during climb-out in the descent phase

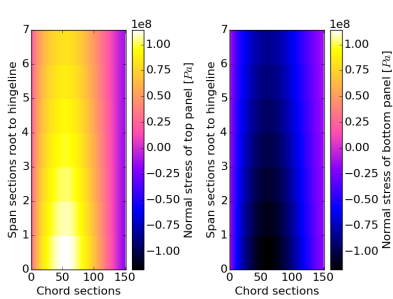


Figure 5.48: Bending stress from root to hinge line during climb-out in the descent phase

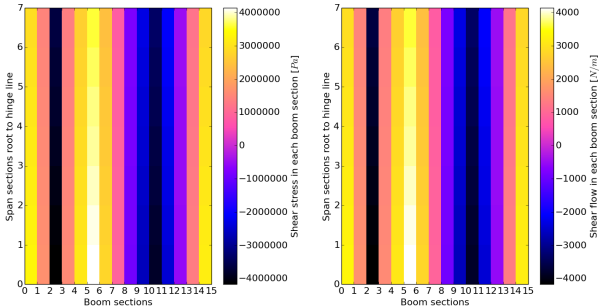


Figure 5.49: Shear stress (left) and flow (right) from second cut to tip during climb-out in the descent phase

present in the wing. Therefore the bending stress is 0. The shear stress and flow of the three wing sections from tip to root is shown in Figs. 5.56 to 5.58.

Fig. 5.59 shows the layout of the wing design.

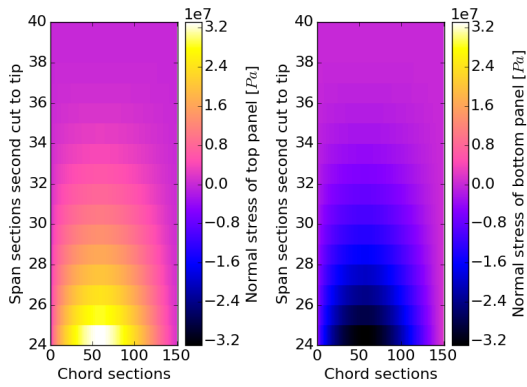


Figure 5.50: Bending stress form second cut to tip during turning

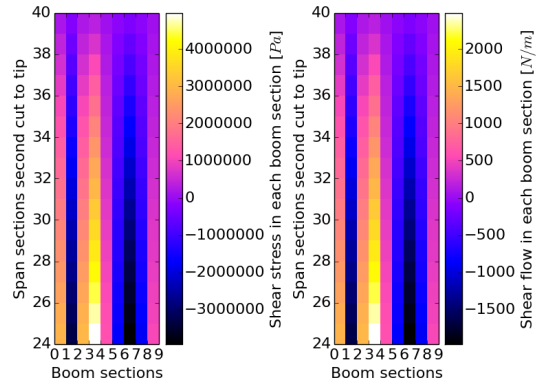


Figure 5.51: Shear stress (left) and flow (right) form second cut to tip during turning

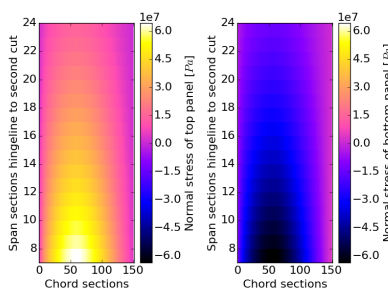


Figure 5.52: Bending stress form hinge line to second cut during turning

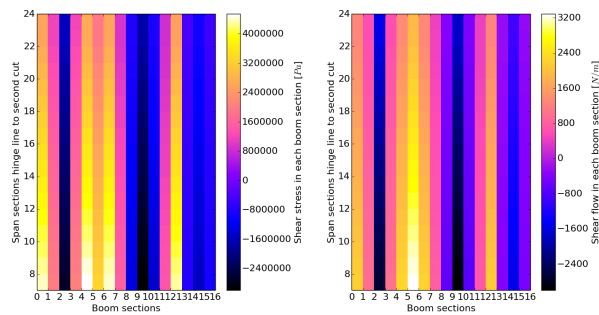


Figure 5.53: Shear stress (left) and flow (right) form hinge line second cut during turning

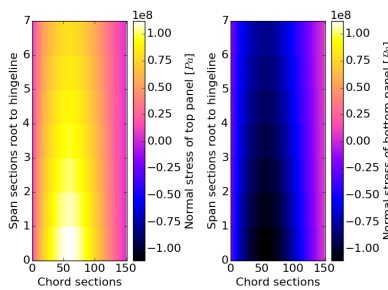


Figure 5.54: Bending stress form root to hinge line during turning

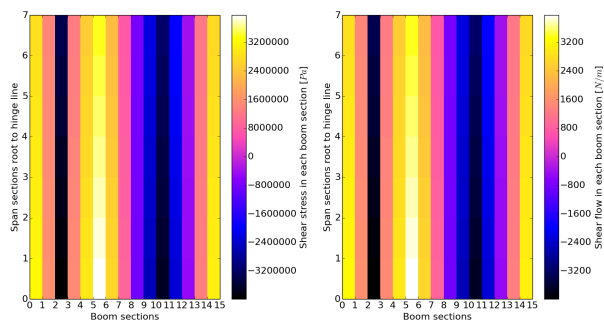


Figure 5.55: Shear stress (left) and flow (right) form root to hinge line during turning

**RECOMMENDATION**

After some algorithm tweaks and debugging, and newest iteration suggest an even more promising wingbox, pertaining the specifications shown in Table 5.15. This means quite a few wingbox parameters can be further optimised.

Furthermore, a comprehensive verification is required to perform. A Nastran finite element analysis is in progress to verify the structural analysis program. Lastly, the range and parameters can be considered to expand for more design freedom, such as spar location, wingbox length, stringer shapes, etc. Lastly, the stress concentration of rivets and bolts needs to be looked into.

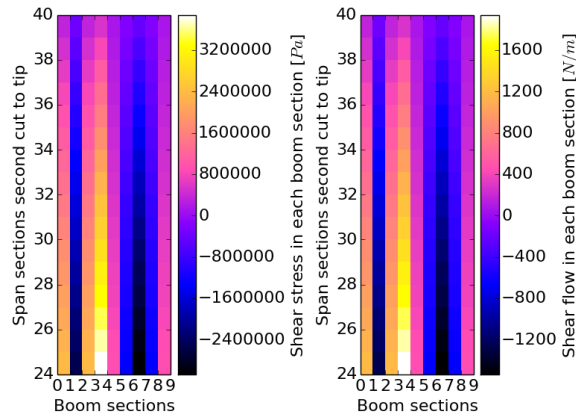


Figure 5.56: Shear stress (left) and flow (right) form second cut to tip during entry

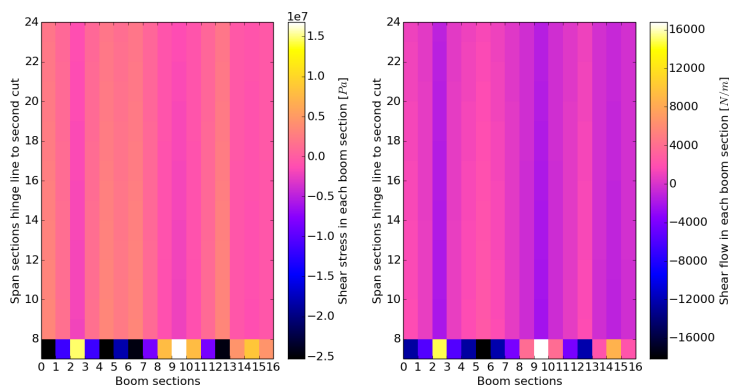


Figure 5.57: Shear stress (left) and flow (right) form hinge line second cut during entry

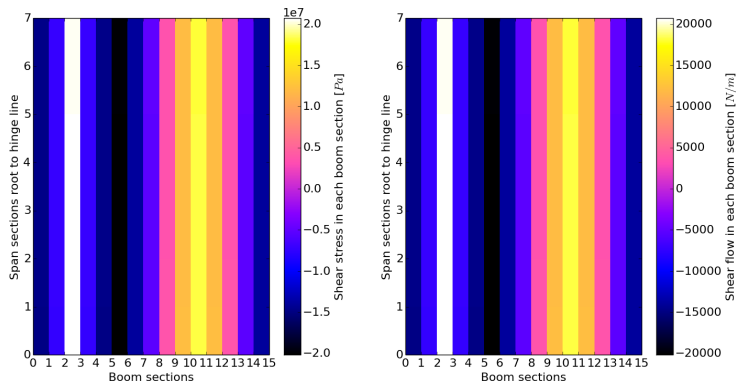


Figure 5.58: Shear stress (left) and flow (right) form root to hinge line during entry

### 5.6.3. FUSELAGE

For the stress calculation it is assumed that the shear force shown in the loading diagram, acts in the center of the fuselage. However, this is not the case in reality. The struts do not act in the center and neither do the masses in the fuselage. However, the further away from the struts, the better the assumption of a shear force acting in the center of the fuselage. As this is also the place where the largest moments are, this assumption seems reasonable. Nevertheless, a safety factor of two is used to deal with the inaccuracies caused by this assumption.

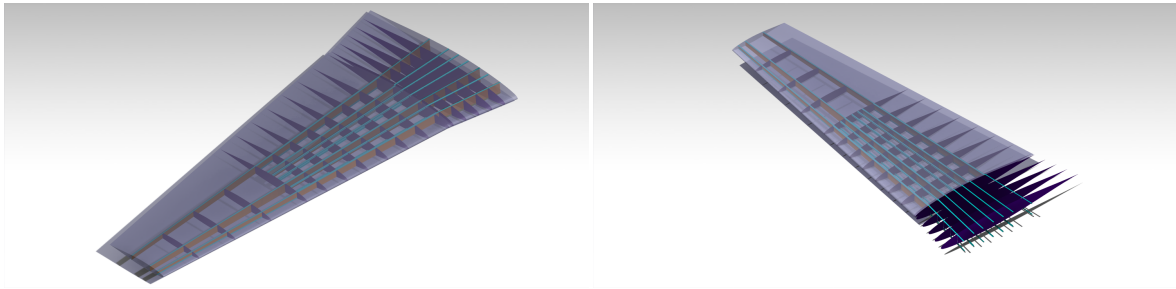


Figure 5.59: Schematic of the wing. Skin of the root torn off for clearance (right)

Section	Configuration	$t_{skin}$ [mm]	$t_{spar}$ [mm]	$A_{stringer}$ [mm <sup>2</sup> ]	$n_{rib}$	Weight [kg] [kg]
Root to hinge line	6/2	0.5	0.5	100	9	21.75
Hinge line to second cut	4/1	0.5	1	250	9	47.77
Second cut to tip	4/1	0.5	0.5	100	5	16.24
<b>Total</b>	-	-	-	-	-	<b>85.76</b>

Table 5.15: Specification of each section in the wingbox along the span, extracted from the newest iteration.

In the fuselage, the hatch will be considered as a filled cut-out during entry. This means that for a large part of the fuselage, stress concentrations occur. Therefore the stress concentration factor two for filled cut-outs is used in the stress calculations.

Because a non-isotropic material is used, the Von Mises stress cannot be used as a maximum stress criteria. Instead the Tsai-Hill criteria<sup>41</sup> will be used, taking into account the material properties. To verify the program and to have an idea where the high stresses are, it is still useful to plot the von Mises stress. This plot can be seen in Fig. 5.60.

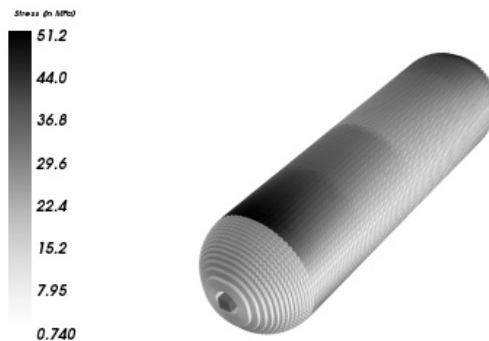


Figure 5.60: Fuselage moment and shear load diagram

Stiffeners can be used to prevent buckling and increase the moment of inertia. As the forces during entry are in vertical direction only, stiffener area should preferably be concentrated at the top and bottom of the fuselage to have a maximum increase in moment of inertia. However, several stiffeners with a spacing in between will give better properties against buckling. Buckling could occur during entry when a compression force exists within the cross section.

To prevent the fuselage from buckling, frames will be used. For the buckling calculation, the maximum normal stresses in the fuselage are used. This means that the frame spacing can be made larger at other parts

<sup>41</sup>[http://www.doitpoms.ac.uk/tlplib/fibre\\_composites/laminate\\_failure.php](http://www.doitpoms.ac.uk/tlplib/fibre_composites/laminate_failure.php)

of the fuselage. Optimising for mass[45] the optimum frame spacing for maximum internal moment is 0.3 m.

## 5.7. STABILITY AND CONTROL

The aircraft must be able to perform manoeuvres on Venus, and should also be stable during flight. In order to check that this is true, static and dynamic stability analyses have to be performed. This involves the determination of the controllability and stability of the aircraft, by using the shift in Center of Gravity (CG). Based on the outcome of these analyses, the horizontal and vertical tail, but also the ailerons, elevator and rudder, will be sized and positioned. All these items will be discussed in Section 5.7.1 through Section 5.7.7.

### 5.7.1. CONTROL METHOD

For the control of the aircraft, it is necessary to select a type control method. As the aircraft is technically an Unmanned Aerial Vehicle (UAV), but also located on Venus, manually controlling the aircraft from Earth is not possible, as the response time is at least 4.6 minutes. However, the aircraft can not be fully automated either as there may always be unforeseen circumstances that have not been included in the control algorithm. Therefore the aircraft will use the exception control method. This means that the aircraft is autonomous, and will ask for advice if it encounters an unforeseen situation [46].

### 5.7.2. STATIC STABILITY

The static stability of an aircraft usually determines the required size of horizontal stabiliser as well as the available range of center of gravity shift. The static stability is limited by the stability and controllability of the aircraft. Eq. (5.59) shows the stability equation modified for canard and tail, while Eq. (5.60) is for the controllability [47, 48]. The stability margin,  $M_{stability}$ , is the fractional distance relative to the mean aerodynamic chord (MAC) from the CG to the neutral point. It is assumed to be 0.1 since commercial aircraft having a stability margin of 0.05 [47] and then applying a safety factor of 2. The equations will result in three unknowns,  $x_{cg}$ ,  $S_c$  and  $S_t$  but that can be reduced to two by using a defined canard to tail ratio  $R_H = \frac{S_c}{S_t}$ .

The aerodynamic center (AC) is assumed to be at the quarter chord line and the velocity fraction of the tail is assumed to be 0.95 due to having a fin mounted tail [47, 48]. The  $C_{L\alpha_{A-H}}$  of the main wing is 0.0753 and for the tail the airfoil NACA 6 series 64-011 gives a  $C_{L\alpha_t}$  of 0.0945.

$$\bar{x}_{cg} \leq \bar{x}_{ac} - \frac{S_c l_c}{S_{A-H} \bar{c}} \left( \frac{V_c}{V_{A-H}} \right)^2 \frac{C_{L\alpha_c}}{C_{L\alpha_{A-H}}} \left( 1 - \frac{\delta \epsilon_c}{\delta \alpha_{A_H}} \right) + \frac{S_t l_t}{S_{A-H} \bar{c}} \left( \frac{V_t}{V_{A-H}} \right)^2 \frac{C_{L\alpha_t}}{C_{L\alpha_{A-H}}} \left( 1 - \frac{\delta \epsilon_t}{\delta \alpha_{A_H}} \right) - M_{stability} \quad (5.59)$$

$$\bar{x}_{cg} \geq \bar{x}_{ac} - \frac{C_{m_{ac}}}{C_{L_{A-H}}} + \frac{C_{L_h}}{C_{L_{A-H}}} \frac{S_t l_t}{S_{A-H} \bar{c}} \left( \frac{V_t}{V} \right)^2 - \frac{C_{L_c}}{C_{L_{A-H}}} \frac{S_c l_c}{S_{A-H} \bar{c}} \left( \frac{V_c}{V} \right)^2 \quad (5.60)$$

#### HORIZONTAL TAIL

During the mission lifetime of the aircraft, it will experience one big CG shift, which happens when the lander is deployed. Therefore it is necessary to calculate where the CG of the aircraft is with and without lander.

For the estimation of the CG the following parts are considered: wings, canard, tail, lander, battery, propellers and engines, scientific equipments and CDHS. The mass and X-locations can be found in Table 5.16. The leading edge at the root is the reference point to which all the X-locations are relative to as can be seen in Fig. 5.61. Using Eq. (5.61) it is possible to determine the center of gravity with and without the lander.

$$x_{cg} = \frac{\sum_i^N M_i x_i}{\sum_i^N M_i} \quad (5.61)$$

Since the mass and location of the tail and canard is unknown, an estimation was performed to determine these relative to the wing.  $l_c$  and  $l_t$  are the maximum distances from the aerodynamic center (AC) of the canard / tail relative to the wing's AC and are limited by the aeroshell size.

It is assumed that the mass of the canard and tail scales linearly with the surface area of the main wing. This assumption allows us to write the relations  $M_t = \frac{M_w}{S_w} S_t$  and  $M_c = \frac{M_w}{S_w} S_c$ . This gives a first order estimation from which it is possible to determine the ideal configuration. Once the configuration is determined, it is possible to determine a more accurate mass estimation.

As can be seen from Fig. 5.62, the lowest expected mass is with a ratio of zero, so a pure tail configuration without canard. At a ratio of one, due to the aft CG location, the stability will require a near infinite large horizontal tail and canard as can be seen in Fig. 5.63. The aft CG will not allow a bigger  $R_H$  ratio since it will

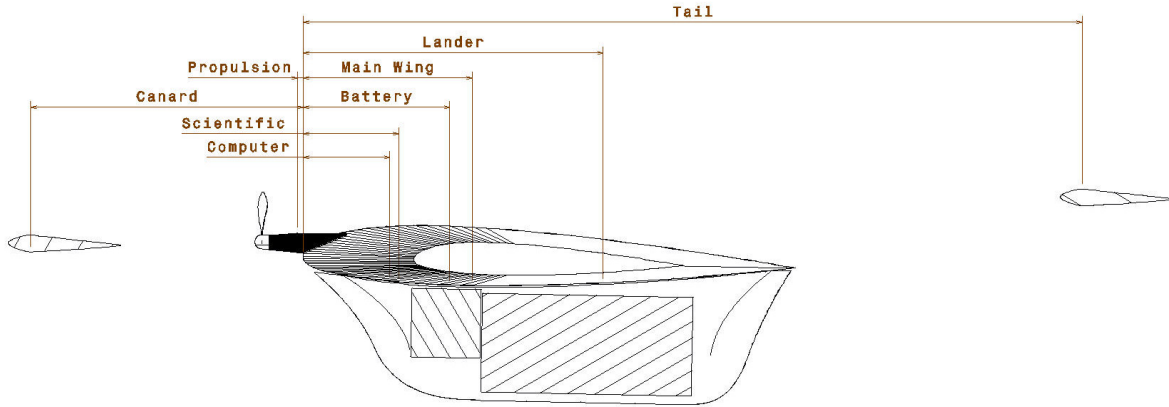


Figure 5.61: First order mass distributing estimation of the aircraft

Table 5.16: Main system mass and their CG with respect to the leading edge

Component	Mass [kg]	X-location [m]
Wing	171	1.33
Canard	$\frac{M_w}{S_w} S_c$	$l_c + \frac{c_w}{4}$
Tail	$\frac{M_w}{S_w} S_t$	$l_t + \frac{c_w}{4}$
Lander	93	2.4
Propulsion	50	-0.04
Scientific equipment	20	0.8
Battery	200	1.2
Flight computer	10	0.7

become unstable. Fig. 5.64 shows the optimum configuration, and it can be seen that the minimum surface area of the tail must be  $9.7m^2$ . Since, the required solar panel surface area cannot be reached by only placing solar panels on the main wing, the tail also needs to be covered by solar panels. The minimum surface area due to solar panel area requirement is  $14m^2$ . A bigger tail does not limit the stability or controllability. Instead it is beneficial since it allows for bigger CG shifts.

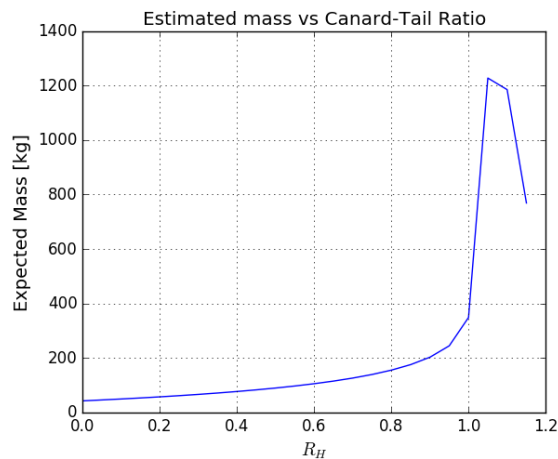
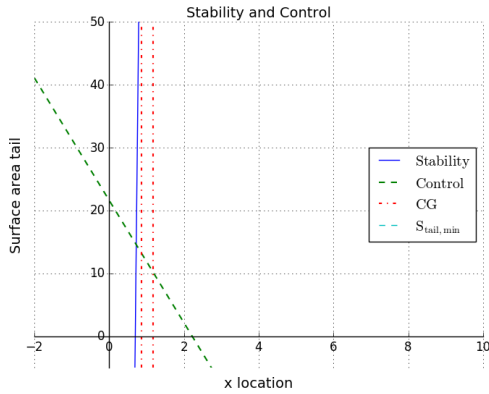
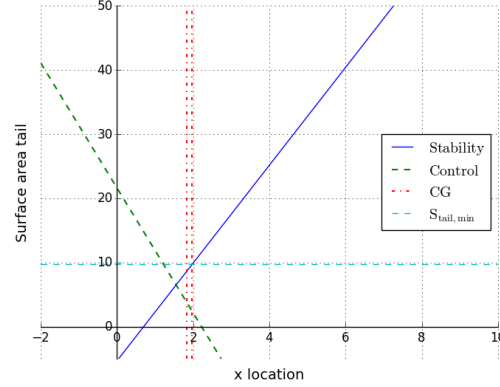


Figure 5.62: Expected mass with varying tail to canard ratio  $R_H$

Figure 5.63: Aircraft scissor plot  $R_H = 1$ , limited by the aft CGFigure 5.64: Aircraft scissor plot  $R_H = 0$ , a pure tail configuration without canard

### VERTICAL TAIL

The vertical tail is there to provide lateral dynamic stability and in case of an engine failure, produce a counter torque and force. For conventional aircraft the surface area of the vertical tail is between 0.1 and 0.15 of the main wing [49]. In case the outermost engine fails, the moment  $M_e = l_e F_e$  needs to be countered by the moment produced by the vertical stabiliser,  $M_v = l_v 0.5 \rho V^2 S C_L$ . From this an initial estimate for the vertical surface area can be taken as seen in Eq. (5.62).

$$S_{vert} = \frac{l_e F_e}{l_v 0.5 \rho V^2 C_L} = \frac{6.75 \cdot 500}{5.5 \cdot 0.5 \cdot 0.121 \cdot 112^2 \cdot 0.2} = 4.04 m^2 \quad (5.62)$$

### 5.7.3. TAIL CONFIGURATION

The configuration of the vertical and horizontal tails are depicted in Fig. 5.65. The vertical tails each vertically protrude from the booms which connect to the aircraft main wing. The horizontal tail is then attached to the top of the two vertical tails, so that its elevation can positively benefit from the downwash induced by the main wing. The horizontal tail also has hinges at the lines of the vertical tails. The tips will fold downwards, and then the booms will also fold downwards at the main wing for stowing in the aeroshell. It is stowed as such that the tail configuration and the folded horizontal tail will aerodynamically be pushed into place during the deployment.

### 5.7.4. AILERON SIZING

For the sizing of the control surfaces, the aircraft is considered to be a Class I aircraft as its weight is less than 6,000 kg. The flight phase category is B as this encompasses climb, cruise, loiter, descend and aerial delivery. Finally, the level of acceptability is assumed to be 1 because flying qualities need to be adequate for completing the mission [49]. From [49] it is then found that the ailerons have to be capable of providing the aircraft with a roll angle of  $45^\circ$  in 1.7 seconds. Also, a maximum deflection of the ailerons is selected to be  $\pm 20^\circ$  which is a value similar to that of small aircraft [49].

Using the method from section 12.4 in [49] and values in Table 5.17 for a range of flight conditions, multiple roll time plots are created. It should be noted that the value of the mass moment of inertia,  $I_{xx}$  is approximated using data from the Cessna Citation and scaled down as the Venus aircraft is lighter. However, as it is expected to be smaller than this approximation, it introduces a safety factor.

Table 5.17: General inputs aileron sizing

Parameter	Value	Parameter	Value
$\lambda$ [-]	0.3807	$\bar{c}$ [m]	2.64
$b$ [m]	16.212	$I_{xx}$ [kg·m <sup>2</sup> ]	3,500
$c_r$ [m]	4.0	$S_{vt}$ [m <sup>2</sup> ]	6.06
$S$ [m <sup>2</sup> ]	40.0	$S_{ht}$ [m <sup>2</sup> ]	14.0
$C_{l_{\alpha_w}}$ [1/rad]	4.314	$\delta_{e,max}$	$\pm 20^\circ$

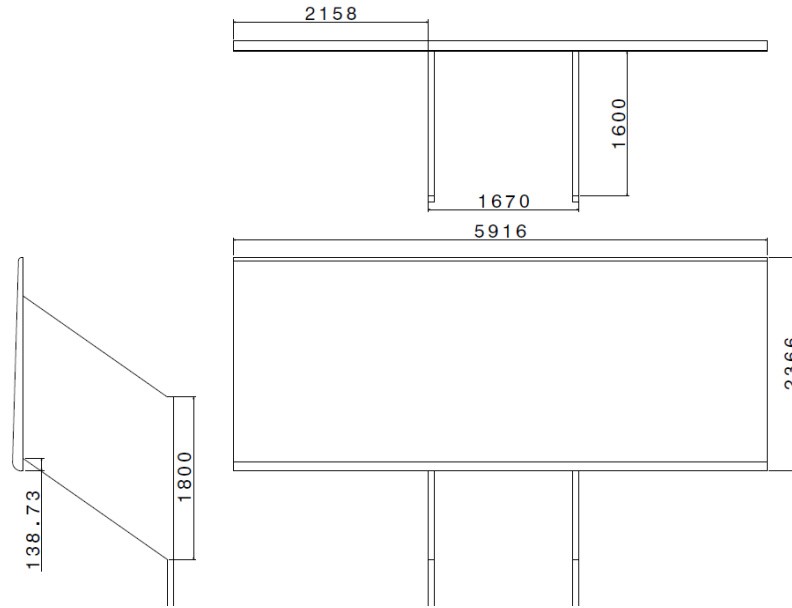


Figure 5.65: Horizontal Tail Configuration

From the initial plots it is found that the critical situation, at which the required elevator deflection is maximal, occurs for the highest altitude under the highest wind speeds, and without the lander on board the aircraft. The roll time plots for the three wind scenarios as defined in Section 2.2, high, nominal and low, without a lander are shown in Fig. 5.66.

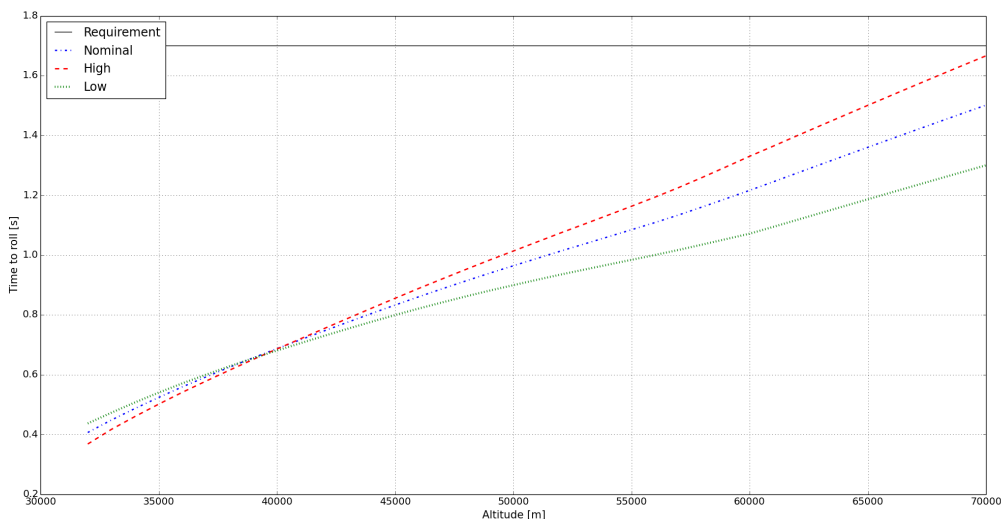


Figure 5.66: Roll time plot

This figure also indicates that for the high winds, the roll time is just below the requirement for the upper altitude of 70 km, meaning that the ailerons are properly sized.

The aileron dimensions that satisfy the rolling requirement for all conditions are shown in Table 5.18. Here, the inside position is the fraction of the location along the wing semi-span where the aileron starts, and outside position the one where it ends. So, in this situation, the inside starts at 67% of the semi-span, or  $0.67 \cdot 0.5 \cdot 16.212 = 5.43$  m from the fuselage centerline. The aileron-to-chord ratio indicates what part of the wing chord is used for the aileron. In this case, from 67 to 90% of the wing semi-span, 30% of the wing is occupied by the aileron. As the rear spar of the wing is located at 59.1% of the chord, the aileron does not

intersect with it, meaning that the aileron can be easily integrated.

Table 5.18: Aileron characteristics

Parameter	Value
Inside position [-]	0.67 b/2
Outside position [-]	0.9 b/2
Aileron-to-chord ratio [-]	0.30
$\tau_a$	0.52
Aileron area [m <sup>2</sup> ]	2.30
$C_{l_{\delta_a}}$ [1/rad]	0.1676

### 5.7.5. ELEVATOR SIZING

For the sizing of the elevator there are two situations that typically need to be taken into account, namely take-off and longitudinal stability during flight. As the aircraft will not have any take-off, the elevators are only sized for longitudinal stability. For the sizing of the elevators, the last part of the method explained in section 12.5 in [49] is used. From this source Eq. (5.63) through Eq. (5.66) are found, and applied.

$$C_{m_{\delta_e}} = -C_{L_{\alpha_w}} \cdot \eta_h \cdot \bar{V}_h \cdot \frac{b_e}{b_h} \cdot \tau_e \quad (5.63) \quad C_{L_{\delta_e}} = C_{L_{\alpha_h}} \cdot \eta_h \cdot \frac{S_h}{S} \cdot \frac{b_e}{b_h} \cdot \tau_e \quad (5.64)$$

$$C_{L_{h_{\delta_e}}} = C_{L_{\alpha_h}} \cdot \tau_e \quad (5.65)$$

$$\delta_e = \frac{\left(\frac{T \cdot z_T}{q \cdot S \cdot \bar{c}} + C_{m_0}\right) \cdot C_{L_{\alpha}} + (C_{L_1} - C_{L_0}) \cdot C_{m_{\alpha}}}{C_{L_{\alpha}} \cdot C_{m_{\delta_e}} - C_{m_{\alpha}} \cdot C_{L_{\delta_e}}} \quad (5.66)$$

This last equation is then used to determine the elevator deflection for a velocity ranging from the stall speed to the maximum speed. Because the stall speed depends on the weight of the aircraft, it will differ for the situation with and without the lander on board. Also, the thrust force will not be constant but varying with flight speed. The stall speeds, maximum speeds, and thrust are all generated in the flight track determination procedure as shown in Sections 5.2 and 5.2.4. Apart from these values, the different input variables used are shown in Table 5.19.

Table 5.19: Elevator sizing input values

Parameter	Value	Parameter	Value
$C_{L_{\alpha_h}}$ [-]	5.414	$\eta_h$ [-]	0.9
$\bar{V}_H$ [-]	0.6981	S [m <sup>2</sup> ]	40
$W_{FW}$ [kg]	722	$\bar{c}$ [m]	2.64
$W_{Aft}$ [kg]	815	$C_{L_{\alpha_w}}$ [-]	4.314
$x_{ac_w}$ [m]	1.0	$z_T$ [m]	-1.0
$C_{L_0}$ [-]	0.084	$C_{m_0}$ [-]	-0.035
$x_{cg_{aft}}$ [m]	1.9552	$x_{cg_{FW}}$ [m]	1.7956
$\frac{d\epsilon}{d\alpha}$ [-]	0.0395	$S_{ht}$ [m <sup>2</sup> ]	14.0

Applying these values plots as the one shown in Fig. 5.67 are created for the three different wind speed situations and the most forward and most aft center of gravity location, at a range of altitudes from 32 to 70 km. The shape of these graphs show similar behaviour to examples in [49].

Using this plot it can be checked that the maximum elevator deflection does not exceed the maximum elevator design deflection of  $\pm 20^\circ$ . During the analysis it was found that the most critical case for elevator sizing is that of the lowest altitude at the lowest stall speed, under the highest wind conditions. The final characteristics of the elevator that meets the requirement for all flight conditions are shown in Table 5.20.

### 5.7.6. RUDDER SIZING

The rudder is the last of the three key control surfaces to be sized for the aircraft and primarily provides the aircraft with yaw control. Assuming that the aircraft is a multi-engine transport with wing mounted engines,

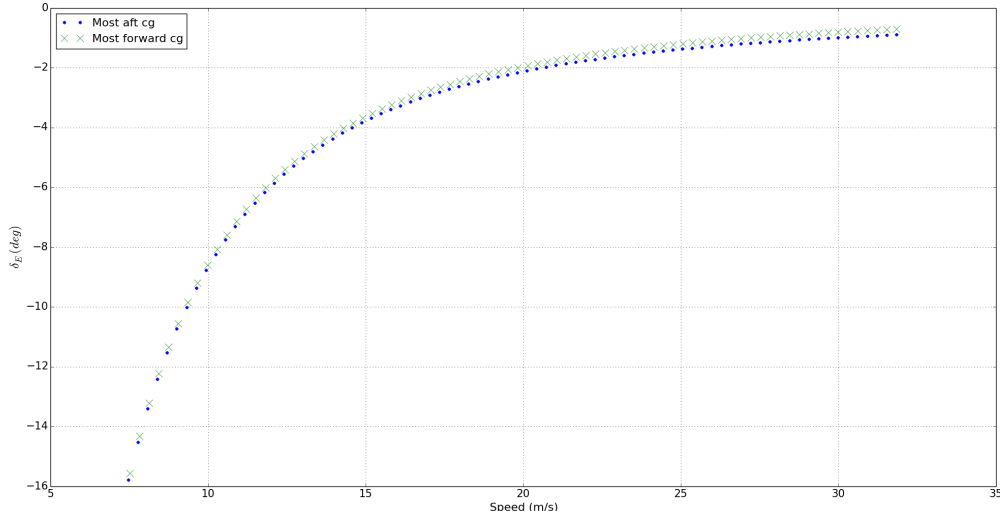


Figure 5.67: Elevator sizing plot example

Table 5.20: Elevator characteristics

Parameter	Value
Elevator-to-horizontal tail chord ratio [-]	0.25
Elevator-to-horizontal tail span ratio [-]	0.8
$\tau_e$	0.47
Elevator area [m <sup>2</sup> ]	2.80
$C_{m_{\delta_e}}$ [1/rad]	-1.2792
$C_{L_{\delta_e}}$ [1/rad]	-0.6413

the asymmetric thrust situation is critical for the rudder sizing [49]. This means that the rudder has to be sized to counter the failure of the engine(s) on one of the wings.

For normal aircraft, the minimal speed at which this has to be possible is 80% of the stall speed to allow for take-off. To include a safety factor, the rudder is still sized for this flight speed, despite not having a take-off operation in the mission profile. It is also assumed that the maximum rudder deflection is  $\pm 20^\circ$  [49]. The most critical situation is with the most aft center of gravity as the arm of the rudder will then be smallest, making it least effective. To check the size of the rudder, the situation of both engines failing on one wing is considered for multiple altitudes. It is also assumed that once the two engines fail, the remaining three will have to provide the same amount of thrust as the five combined originally produced. This adds a further safety factor to the rudder sizing.

For the range of altitudes it is then checked that the rudder deflection does not exceed the maximum of  $20^\circ$  in either of those cases. The equation used is (5.67). Note that this equation assumes that the aircraft is symmetric, has zero sideslip and that the ailerons are not deflected [49].

$$\delta_r = \frac{-\sum T \cdot y}{q \cdot S \cdot b \cdot C_{n_{\delta_r}}} \quad \text{where} \quad C_{n_{\delta_r}} = -C_{L_{\alpha_v}} \cdot \bar{V}_V \cdot \eta_V \cdot \tau_R \cdot \frac{b_R}{b_V} \quad (5.67)$$

More information about the procedure can be found in section 12.6 in [49]. Using the inputs in Table 5.21 and varying the dynamic pressure and thrust for a range of altitudes, the plot in Fig. 5.68 is created. Note that in the table, the matrix for  $y_T$  indicates the arms of the five engines around the center of gravity, which is their position along the wing semispan with respect to the fuselage centerline.

This plot indicates that the most critical situation is for the highest wind speeds, and at the lowest altitude, without the lander on board as  $\delta_r$  is close to  $20^\circ$  for that situation. Furthermore, this plot shows that the aircraft rudder has been properly sized as none of the situations considered leads to a rudder deflection of more than  $\pm 20^\circ$ , and even introduces an additional safety margin. The characteristics of this rudder are

Table 5.21: Rudder sizing input values

Parameter	Value	Parameter	Value
$\frac{S_v}{S}$ [-]	0.1515	$\eta_v$ [-]	0.9
$\bar{V}_V$ [-]	0.3022	$S$ [m <sup>2</sup> ]	40
$b$ [m]	16.212	$\bar{c}$ [m]	2.64
$W_{Aft}$ [kg]	815	$C_{L_{\alpha_v}}$ [-]	5.4145
$V$ [m]	$0.8 \cdot V_{stall}$	$y_T$ [m]	[6.85, 3.55, 0, -3.55, -6.85]

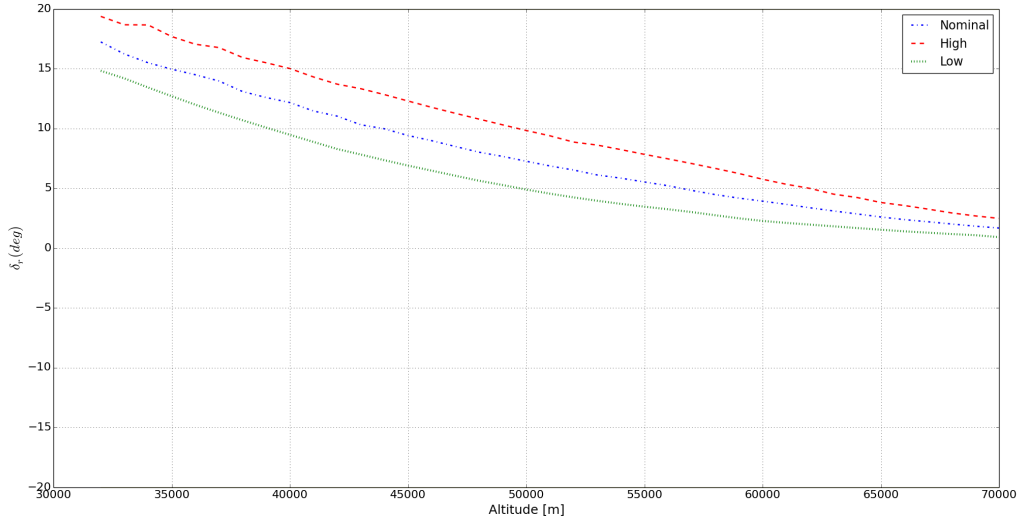


Figure 5.68: Rudder sizing plot

shown in Table 5.22. Note that the rudder is split equally over the two vertical tails. Also, if the engines on the other side of the aircraft would fail, the plots will be mirrored with respect to  $\delta_r$  of zero degree.

Table 5.22: Rudder characteristics

Parameter	Value
Rudder-to-vertical tail chord ratio [-]	0.30
Rudder-to-vertical tail span ratio [-]	0.88
$\tau_r$	0.52
Rudder area [m <sup>2</sup> ]	1.5872
$C_{n_{\delta_r}}$ [1/rad]	-0.6739

### 5.7.7. DYNAMIC STABILITY

Throughout the operation of the aircraft disturbances will act on the aircraft. These can be either from outside or inside sources such as control surface deflections. To ensure that the aircraft is stable and will return to the initial neutral point, a dynamic stability analysis needs to be performed. The aircraft motion can be split into longitudinal and lateral motions and are therefore separately analysed in the sections below. A linear state space system was developed using the Flight Dynamics Lecture Notes [50]. From the lecture notes it was possible to calculate most stability coefficients. Some were missing and taken from [49]. The stability coefficients do not take into account the propeller nor the fuselage, only the main wing and the tail. A better analysis of the derivatives need to be performed in a wind tunnel.

#### LONGITUDINAL STABILITY

The longitudinal stability has the following state space variables: unit less velocity  $u$ , angle of attack  $\alpha$ , pitch  $\theta$  and unit less pitch moment  $q$ . The input variable is the elevator  $\delta_e$ . The stability derivatives coefficients are

recorded in Table 5.24.

Table 5.23: Aircraft parameters assumed for the simulation

Parameter	Value
$I_{xx}$	3500 kg m <sup>2</sup>
$I_{yy}$	6000 kg m <sup>2</sup>
$I_{zz}$	9000 kg m <sup>2</sup>
$I_{xz}$	200 kg m <sup>2</sup>
M	850 kg
$C_L$	0.23 -
$C_D$	0.033 -
$V_0$	140 m s <sup>-1</sup>
$\rho_0$	0.45 kg m <sup>-3</sup>
$\alpha_0$	1 deg

Table 5.24: Longitudinal stability derivatives for the aircraft [49]

$C_{X_0}$	0.00	$C_{Z_0}$	-0.046	$C_{m_0}$	0.00
$C_{X_u}$	-0.099	$C_{Z_u}$	-0.46	$C_{m_u}$	0.0
$C_{X_\alpha}$	-0.019	$C_{Z_\alpha}$	-0.13	$C_{m_\alpha}$	-0.03
$C_{X_{\dot{\alpha}}}$	0	$C_{Z_{\dot{\alpha}}}$	0	$C_{m_{\dot{\alpha}}}$	0
$C_{X_q}$	0	$C_{Z_q}$	0	$C_{m_q}$	0
$C_{X_{\delta_e}}$	0	$C_{Z_{\delta_e}}$	0	$C_{m_{\delta_e}}$	-1.09

From the poles in the Bode plot analysis, it is determined that the two pairs of eigenvalues are:  $-0.0855 - 1.56i$  for the phugoid and  $-0.0668 + 0.188i$  for the short period. For stability reasons, the damping ratio for the phugoid needs to be above 0.04 and the short period damping ratio should be in between 0.3 and 2.0 [49]. The damping ratio for the phugoid is 0.05, which is in the acceptable range and the damping ratio for the short period is 0.335, which is also in the acceptable range. Therefore the aircraft is dynamically stable.

Another aspect to analyse is the gust stability of the aircraft. Since on Venus the aircraft will fly in a region of high wind speeds of  $140 \frac{m}{s}$ , the aircraft should be able to take a 10% wind speed gust from any direction. The longitudinal stability will consider front gusts and up gusts. A front gust will change the velocity, while an up gust will induce an angle of attack. The dynamic responses are simulated in Fig. 5.69 and Fig. 5.70. From these simulations, it is possible to determine that for a 10% windspeed gust, the aircraft is dynamically stable and will not stall since the angle of attack is within negative and positive 8 degrees.

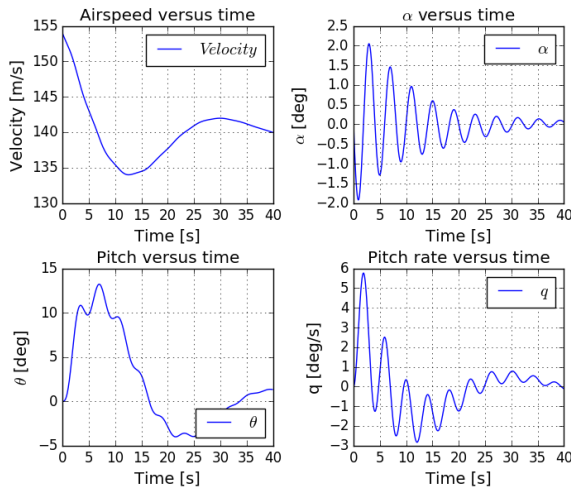


Figure 5.69: Dynamic response to frontal gust of  $14 \frac{m}{s}$

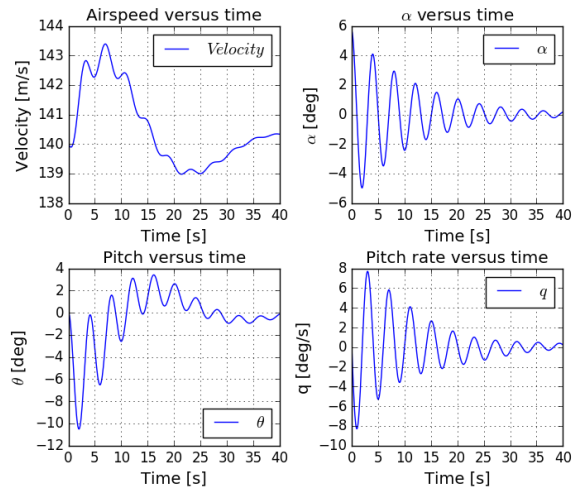


Figure 5.70: Dynamic response to up gust of  $14 \frac{m}{s}$

### LATERAL STABILITY

The lateral stability has the following state space variables: yaw angle  $\beta$ , roll angle  $\phi$ , yaw rate  $r$  and roll rate  $p$ . The input variable is the aileron  $\delta_a$  and rudder  $\delta_r$ . Through iterations for the dynamic stability, it was determined that the aircraft is unstable. The solution to this problem was to increase the vertical stabiliser to  $6m^2$ . The stability derivatives coefficients with the larger vertical stabiliser are recorded in Table 5.25.

From the poles in the Bode plot analysis, it is determined that the two single and one pair of eigenvalues are:  $-8.53 + 0i$ ,  $-0.0074 + 0i$  and  $-0.013 + 1.3i$  respectively.

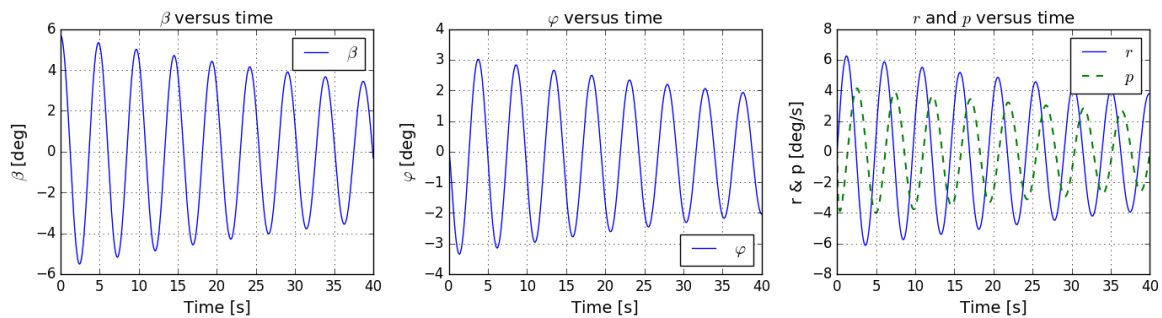
For stability reasons, the damping ratio for the spiral needs to be around 0.08 [49]. The damping ratio for the spiral is 0.01, which is not acceptable. A possible explanation for this is that the coefficients do not

Table 5.25: Lateral stability derivatives for the aircraft [49]

$C_{Y\beta}$	-0.015	$C_{l\beta}$	-0.011	$C_{n\beta}$	0.0064
$C_{Y\dot{\beta}}$	0	$C_{l\dot{\beta}}$	0	$C_{n\dot{\beta}}$	-0.0024
$C_{Yp}$	-0.0024	$C_{lp}$	-0.32	$C_{np}$	-0.0010
$C_{Yr}$	0.013	$C_{lr}$	0.00092	$C_{nr}$	-0.0056
$C_{Y\delta_a}$	0	$C_{l\delta_a}$	0.20	$C_{n\delta_a}$	0
$C_{Y\delta_r}$	0.13	$C_{l\delta_r}$	0.0096	$C_{n\delta_r}$	-0.058

account for the fuselage and propellers which have a large impact on the stability. In addition, the moments of inertia have a large impact on the response of the aircraft and currently only estimations are used.

Using the lateral stability, it is possible to simulate the dynamic response to a side gust, which will induce a side slip angle. The dynamic responses are simulated in Fig. 5.71. While the damping is not very high, it does converge. In addition, the dutch roll is also stable and can be seen in the third plot.

Figure 5.71: Dynamic response to side gust of  $14 \frac{m}{s}$ 

## 5.8. THERMAL CONTROL

During operations on Venus, the aircraft will experience a vast range of temperatures, against which it needs to be protected from. The temperature ranges from  $-30^{\circ}\text{C}$  at the high track altitude up to  $160^{\circ}\text{C}$  at the low track altitude. The maximum sustainable temperature of the aircraft is  $80^{\circ}\text{C}$  and minimum is  $0^{\circ}\text{C}$ .

It is assumed that the aircraft can be simulated thermally as a cylinder with a length of three meters and a diameter of one meter closed with two spherical end caps. In addition, the internal heat produced by the aircraft is assumed to be mainly from the batteries. A discharge efficiency of 95% is assumed, therefore 5% of the total power needed is converted to heat. The power draw from the batteries is provided by the given flight track. Peak internal heat production is 2070 W.

For the aircraft heat capacity, the aircraft is calculated to have a internal mass of 1,050 kg, which includes the atmosphere inside the aircraft that does not contribute to the actual mass of the aircraft. An internal specific heat capacity of  $600 \frac{\text{J}}{\text{kgK}}$ <sup>42 43 44</sup> was assumed taken from the lowest of the main components in the aircraft which is  $\text{CO}_2$  for the space and LiS for the batteries. This results in a heat capacity of  $630000 \frac{\text{J}}{\text{K}}$ .

To regulate the heat, a layer of aerogel, Pyrogel 6650, is applied to the inside of the aircraft. The layer is 5 mm thick and has a thermal conductivity of  $0.03 \frac{\text{W}}{\text{mK}}$ <sup>45</sup>. The structural layer of PETI-330 is 2 mm thick with a thermal conductivity of  $0.53 \frac{\text{W}}{\text{mK}}$  [33] and finally the Teflon layer is 0.05 mm thick with a conductivity of  $0.238 \frac{\text{W}}{\text{mK}}$  [39]. A safety margin of 1.2 was applied on the heat flow.

Using the heat capacity, integral heat production, thermal conductivity and track flight information, it is possible to simulate the internal temperature using the method as in Section 4.3. From this simulation Fig. 5.72 was generated. It can be seen that the steady state maximum temperature reached is  $60^{\circ}\text{C}$  and steady state minimum temperature is  $15^{\circ}\text{C}$ . This temperature range is acceptable and the aircraft can operate with this track. This is also used in the track design to calculate the time the aircraft can stay at the lower altitude.

<sup>42</sup>[https://www.ohio.edu/mechanical/thermo/property\\_tables/gas/idealGas.html](https://www.ohio.edu/mechanical/thermo/property_tables/gas/idealGas.html)

<sup>43</sup>[http://www.engineeringtoolbox.com/specific-heat-capacity-gases-d\\_159.html](http://www.engineeringtoolbox.com/specific-heat-capacity-gases-d_159.html)

<sup>44</sup><https://www.doria.fi/bitstream/handle/10024/118685/Kirill%20Murashko%20A4.pdf?sequence=2>

<sup>45</sup><http://www.insulationfabricators.com/downloads/data-sheets/aspens-aerogel-pyrogel-6650-ds.pdf>

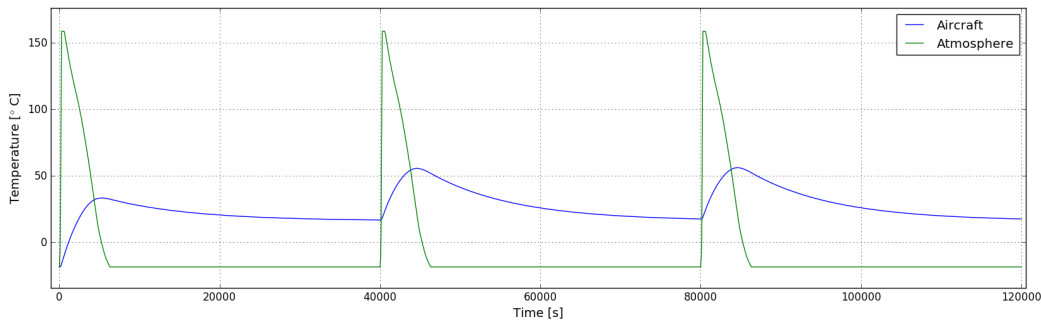


Figure 5.72: Thermal simulation of aircraft for nominal track

## 5.9. COMMUNICATIONS

The data that is gathered by the scientific instruments and housekeeping sensors on the aircraft has to be transmitted to the satellite. For this, a communications subsystem is necessary. In this section first the Command and Data Handling System (CDHS) will be treated followed by the method of communicating with the satellite.

### 5.9.1. CDHS

The CDHS collects, stores and prepares all data for transmission. It also receives the incoming commands from Earth and distributes the commands over the appropriate subsystems. The aircraft will not be able to continuously transmit data to the spacecraft because the spacecraft will not be in range all the time. This means that a form of data storage is required. The data rate generation of the aircraft sensors is 396 kbit/s on average. To properly store this data, 28.6 Gbit of storage capacity needs to be available. This includes a safety factor of two to account for possible missed communications during a single spacecraft orbit.

Before the data can be transmitted or even stored, it needs to be compressed. This compression will be performed by a processor, which will not only be reserved for compressing data but also act as the central brain of the aircraft. Therefore, it needs to be a rather powerful processor. Furthermore, the processor will also interpret the commands coming from Earth and distribute them over the subsystems.

To fulfil these objectives the CDHS is made out of the components listed below. The specific models mentioned at each part are examples that would fulfil the specification. However, the specific model might change in the final product due to a cheaper or better alternative.

- Airbus DS solid state recorder<sup>46</sup>: This solid state recorder based on new flash memory will provide the 14.3 Gbit storage space necessary. Two of these solid state recorders will be used for redundancy and provide the total necessary capacity of 28.6 Gbit.
- The BAE RAD 5545<sup>47</sup>: Will provide the computational power necessary. The processor is radiation hardened to reduce the risk of bit flipping due to radiation. The RAD 5545 is currently one of the fastest radiation hardened processors with four physical cores running at 2.2 GHz. For redundancy three of these processors will be used in the aircraft.

### 5.9.2. TT&C

The Telemetry Tracking and Command (TT&C) system is responsible for the transmitting of data and receiving of commands. The aircraft will only communicate with the spacecraft and therefore only has only one antenna. The sizing of the antenna and the power required is determined by the need to close the link budget. To close the link budget, the antenna specifications listed in Table 5.26 are required.

As with the lander in Section 4.5.2, the required BER is  $10^{-6}$  as this will provide enough data clarity to process the data [12]. Also, for the communication of the aircraft QPSK 1/4 code was selected. With the selected forward error correcting code, QPSK 1/4, a SNR of 2.31 dB is necessary to achieve the BER of  $10^{-6}$  [12]. It should be noted that an additional safety factor is applied in the link budget by increasing the atmospheric loss to 3 dB to account for the thicker Venusian atmosphere.

With the system as described above the link budget between lander and spacecraft can be closed as is shown in Table 4.3. For the downlink to the spacecraft, a data rate of 300.3 kbit/s is applied. For the uplink

<sup>46</sup>[http://www.space-airbusds.com/media/document/ens\\_5\\_ssr\\_2014\\_bd.pdf](http://www.space-airbusds.com/media/document/ens_5_ssr_2014_bd.pdf)

<sup>47</sup><http://www.baesystems.com/en-us/download-en-us/20151124120253/1434571328901.pdf>

Table 5.26: Specifications of spacecraft telemetry system

Specifications	Lander to spacecraft
Antenna type	Parabolic dish
Antenna size/diameter [m]	0.28
Transmitter power [W]	11
Data transmission band	X-band [8.0-8.4 GHz]

from the spacecraft a data rate of 10 kbit/s is assumed. The table shows that this uplink budget also closes by a very large margin, meaning that the data rate can be increased if necessary.

Table 5.27: Linkbudget Aircraft-Spacecraft

Parameter [dB]	Downlink	Uplink
A/C antenna gain	25.23	
A/C pointing loss	-0.04	
A/C power	10.41	N/A
A/C loss factor	-0.97	
S/C antenna gain	34.15	
S/C pointing loss	-0.04	
S/C power	N/A	6.99
S/C loss factor	-0.97	
Space loss	-211.92	
Atmospheric loss	-3.00	
System noise temperature	-21.30	
Boltzmann	228.60	
Data rate	-54.78	-40.0
QPSK 1/4 required margin	2.31	
Required margin to close	3.00	
<b>Total required <math>E_b/N_0</math></b>	5.31	
<b>Total <math>E_b/N_0</math></b>	5.37	15.72
<b>Total margin</b>	<b>0.06</b>	<b>10.41</b>

## 5.10. AIRCRAFT BLOCK DIAGRAMS

In this section, the interactions between components of several aircraft systems will be explained with the help of block diagrams. The hardware system shows the computational electronics in more detail and the software complements the hardware diagram as it shows what software is used by the hardware. The data handling explains what type of data the software has to handle and where they come from. Last, the electrical system details the important electronic circuits

### 5.10.1. HARDWARE

The hardware diagram of the aircraft shown in Fig. 5.73 indicates the interactions between the different systems that comprise the aircraft. The diagram shows the barrier between the inside and outside of the aircraft core that is formed by the insulating layer, with the heat flow going through that system. It should be noted that the heat inflow is spread over all systems on the inside, as well as the outflow. The solar panels are all located on the outside. Also, the lander will only be stored in the aircraft for the first part of the mission. Furthermore, part of the control system, such as the control surface are located outside the insulated layer, but this is not shown in the diagram.

### 5.10.2. SOFTWARE

The software block diagram for the aircraft Fig. 5.74 is similar to the software block diagram for the lander in Fig. 4.5, except that the aircraft flight state and aircraft control have been added. The flight state consists of: velocity, position, angular velocities, angular positions, battery levels, pressure, temperature and density.

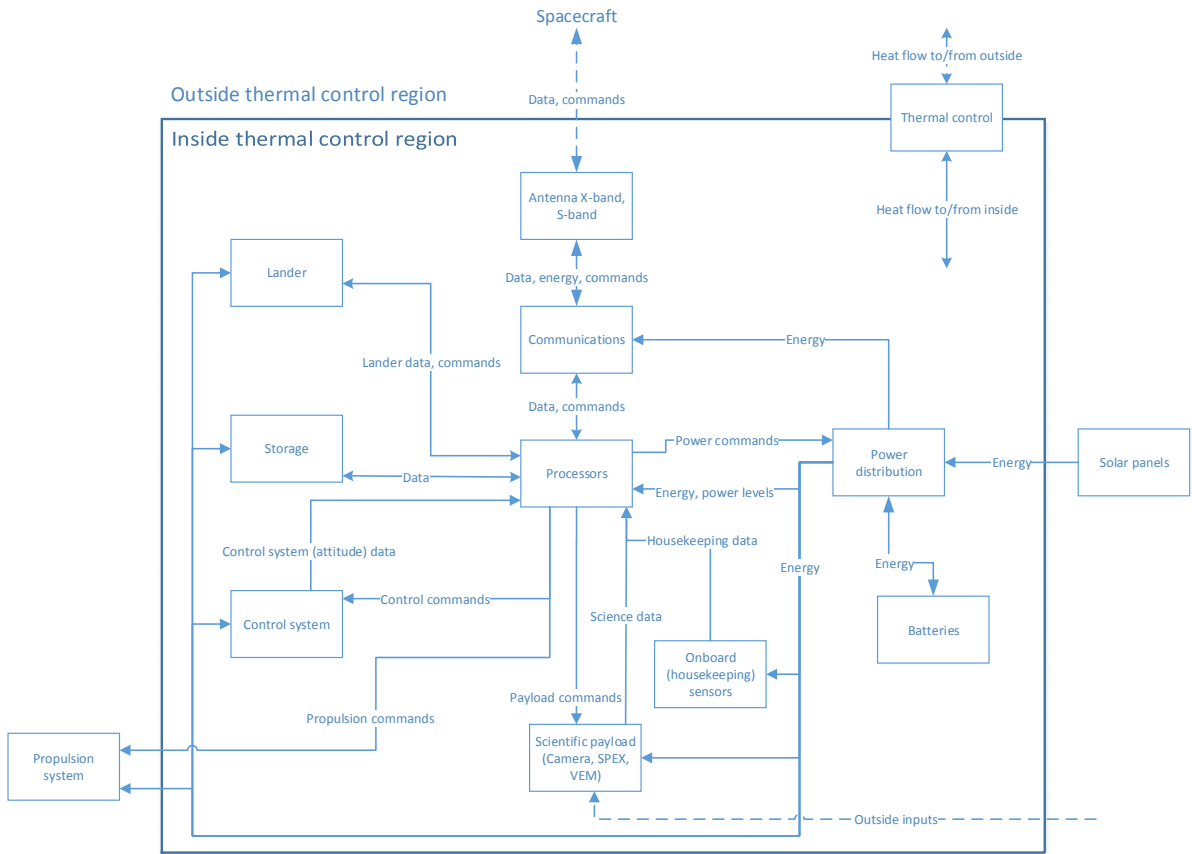


Figure 5.73: Aircraft H/W diagram

These values are compressed, stored and transmitted to Earth for analysis. The aircraft control software is the auto pilot and accepts commands from Earth in form of flight tracks, as well as the feedback from the aircraft flight state to determine the required deflection of the control surfaces to get in the required position.

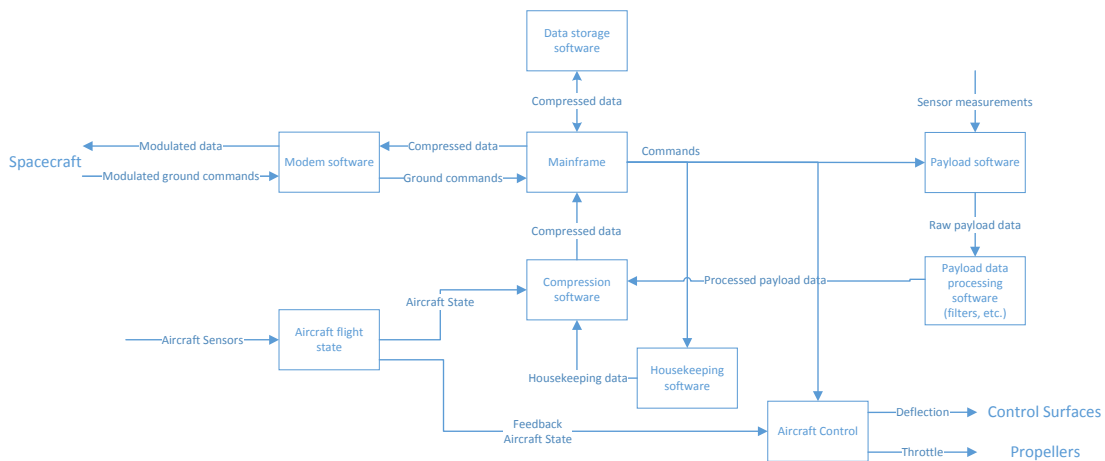


Figure 5.74: Aircraft software block diagram

### 5.10.3. DATA HANDLING

The aircraft scientific equipment and other on board equipment will be generating data from the point at which it is deployed from the aeroshell until it crashes on Venus. To visualise how this data is handled, the data handling diagram in Fig. 5.75 is created. All data generated by the instruments is sent to the processor that compresses the data, and either sends it to the data storage, or directly to the modem. This depends on whether the spacecraft is in communications range or not. Once the spacecraft is in range, the data in the storage is also sent to the modem. The modem then modulates the data into a signal for the antenna, which transmits it to the spacecraft.

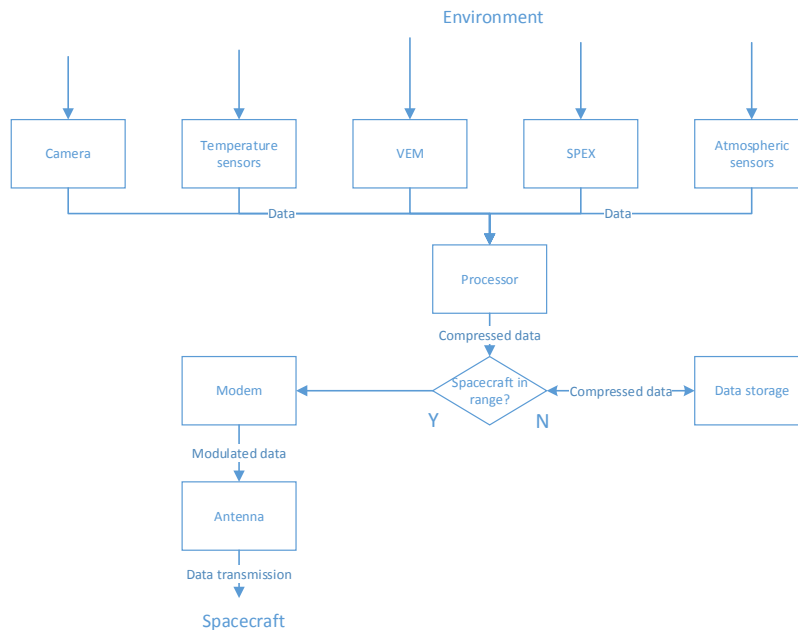


Figure 5.75: Aircraft data handling block diagram

### 5.10.4. ELECTRICAL

The electric block diagram of the aircraft can be seen in Fig. 5.76. Like the lander, a direct current is used and a power distribution unit (PDU) and a power regulator unit is needed. As in Section 4.6.4, fuses will only be used for non-critical loads and the most critical wires will have redundancy. For the aircraft and spacecraft, shunts are required when the voltage in the circuit gets to high and the batteries are fully recharged. This is possible because of the variable solar flux. A mode controller in the aircraft and spacecraft will decide to use the shunts or to use batteries, using the required circuit voltage as reference. The solar panel area is divided into separate sections. Next to the non-critical loads, fuses will also be used for these individual solar panels. In this way, a defect in one of the solar panels will still allow the aircraft to operate using the remaining ones.

The aircraft electricity can be fully regulated or sun-regulated. In case of a sun-regulated system, the voltage will depend on the power available from the solar panels. Although an estimation has been made on the solar flux at different heights, the accuracy should be improved. Because of the uncertainty on a approximately constant input power, the electricity will be fully regulated.

## 5.11. BUDGETS

In this section the mass and power budgets are shown. The values shown are based on calculations and datasheets of individual components. The costs for the aircraft are based on the equations from [51]. A safety factor of five has been applied to account for the fact that this is a highly unusual and experimental design. The Development support costs pertain to all the costs involved in developing and making tools, molds and other necessary components that are not directly part of the aircraft.

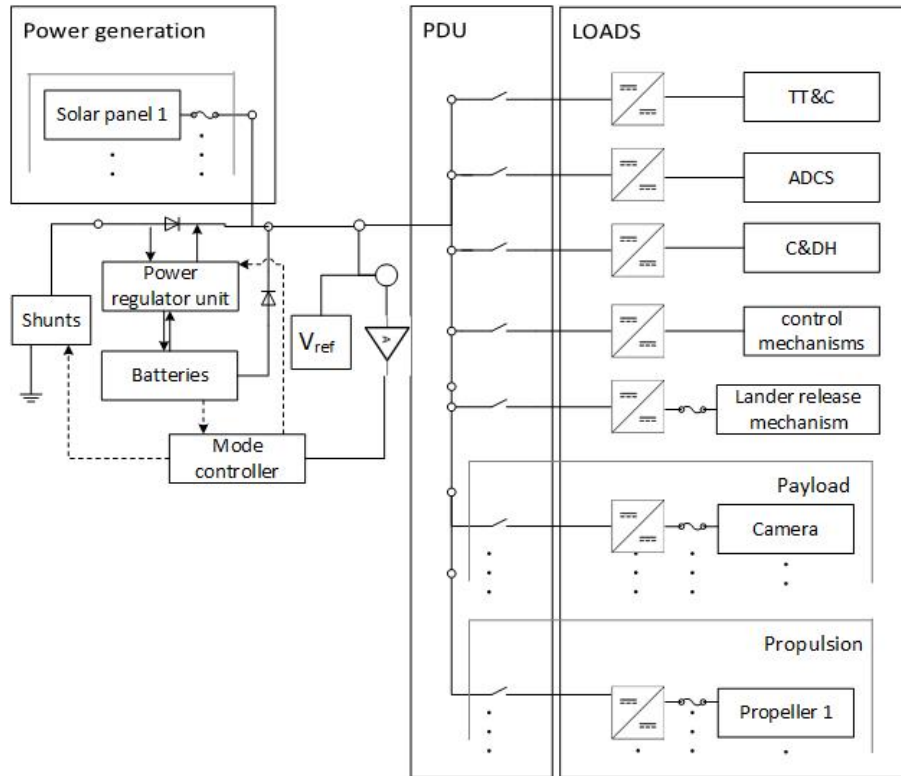


Figure 5.76: Aircraft electrical block diagram

Table 5.29: Aircraft mass and power budgets

Element	Allocated [kg]	Allocated [W]
1.0 Payload	100.02	81
1.1 VEM	5.4	18.5
1.2 Camera	0.4	7.5
1.3 SPEX	1.0	5
1.4 Lander	93.22	50
2.0 Structural	190.0	0
2.1 Fuselage	15.0	0
2.2 Wings	172.0	0
2.3 Stabilisers	50.0	0
3.0 Subsystems	425.3	54619.7
3.1 Flight instruments	2.8	150
3.2 Control surfaces	9.6	1000
3.3 Propulsion	50.0	53333
3.4 TT&C	1.2	11
3.5 CDHS	9.0	50
3.6 Thermal	6.6	0
3.7 Coatings	25.7	25.7
3.8 Power	373.0	50
<b>Total</b>	<b>814.9</b>	<b>54700.7</b>

Table 5.28: Costs for aircraft

Item	Cost [M€]
Development support costs	146.3
Material costs	6.7
Engine costs	5.5
<b>Total</b>	<b>158.5</b>

# 6

## ENTRY

It is necessary to analyse the entry and decent of the aeroshell to ensure that the aircraft will arrive safely in the high altitudes of Venus. This chapter will focus on the aeroshell design and entry simulation in Sections 6.1 and 6.2 respectively. Finally, Section 6.3 shows the deployment sequence once the aeroshell has entered the atmosphere.

### 6.1. AEROSHELL DESIGN

For the aircraft and lander to arrive safely in the Venusian atmosphere, it is important to design the aeroshell properly. Firstly, the aeroshell needs to accommodate all the payloads. In addition, during entry, the aeroshell should not burn up in the atmosphere and also be stable during decent.

#### 6.1.1. SHAPE

The shape of an entry vehicle significantly affects the thermal environment it creates during entry [52]. The primary requirements of the chosen shape are stability of flight and rate of deceleration. The shape that reasonably fulfils these requirements is a blunted cone with a half-cone angle, Fig. 6.1. When both convective and radiative heating are considered, the optimum angle lies somewhere between 45 en 60 degrees [53] [54]. Optimising the heat shield shape is beyond the scope of this research, therefore a similar shape to the Pioneer Venus probes is used with a halve-cone angle of 45 degrees, as all four probes successfully entered the atmosphere [16]. Maximising the heat shield diameter in the launcher results in a radius of 2.3 m, resulting in a 1.15 nose radius using the same  $R/R_N$  ratio of 2 as the Pioneer Venus probes.

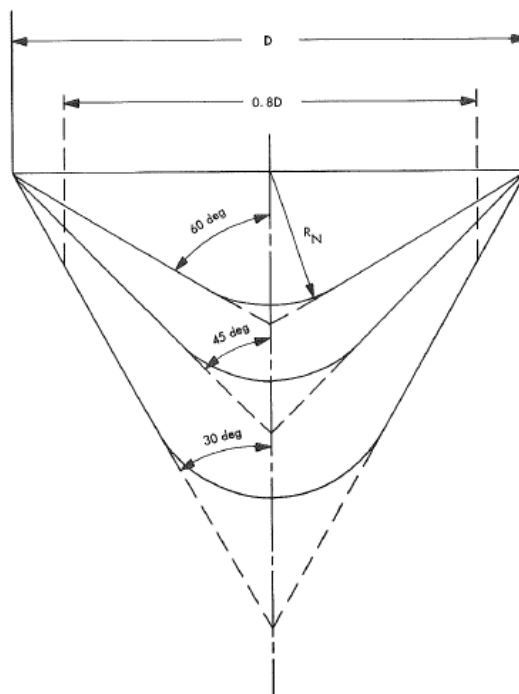


Figure 6.1: Comparison of blunted-cone shapes [52]

### 6.1.2. HEAT FLUX

The maximum heat flux during entry can be computed using Eq. (6.1) [55] [56]. In this equation,  $V_E$  is the entry velocity,  $\beta$  the inverted scale height of Venus,  $\gamma$  the entry angle. Furthermore,  $c_1$  is a constant calculated as shown in Eq. (6.2), where  $c^*$  and  $M$  are planet dependent empirical constants,  $\rho_0$  the air density at sea-level, and  $V_C$  the circular velocity.  $M$  was assumed 3 for this research [57]. Lastly,  $K$  is the ballistic parameter. Using known data from the pioneer Venus probes, [58], and combining and rewriting Eq. (6.2) and Eq. (6.1),  $c^*$  for Pioneer Venus probes was estimated to be between  $4.3 \times 10^8$  and  $6.6 \times 10^8$ . There is a large uncertainty in these values due to simplifications made to obtain the heat flux equations, therefore a  $c^*$  of  $1 \times 10^9$  is used for further calculations including a safety factor. The ballistic parameter is calculated as shown in Eq. (6.3), where  $C_D$  is the drag coefficient of the heat shield, 1.23, and  $S$  is the exposed surface.

Using all these equations, and a safety factor of 2 to compensate for the simplifications, the computed maximum heat flux during entry is  $7.6 \text{ MW/m}^2$ , which is lower than the Pioneer Venus probes experienced. This is due to the large nose radius, low entry velocity of 7.2 km/s and entry angle of -10 degrees. A 1 cm thick layer of carbon phenolic would suffice in resisting the heat [58]. Other materials were also considered that can sustain the calculated heat flux, such as phenolic impregnated carbon ablator (PICA), used on the curiosity Mars entry vehicle [59]. The problem, however, is that these materials would fail if the calculated maximum heat flux would turn out higher [60]. That risk was deemed not worth the weight reduction.

$$q_{c,max} = c_1 V_E^M \sqrt{\frac{-K\beta \sin \gamma}{3eR_{NG}}} \quad (6.1) \quad c_1 = \frac{c^*}{\rho_0^n V_C^M} \quad (6.2) \quad K = \frac{mg}{C_D S} \quad (6.3)$$

## 6.2. ENTRY SIMULATION

Using the linear state space system from the course Flight Dynamics [50] and Re-entry Systems [55] it is possible to get an estimation of the entry dynamics. The simulation requires an estimate of the aeroshell aerodynamic properties, which is achieved with the Modified Newtonian Flow (MNF) method. Newtonian Flow (NF) is only valid at hypersonic Mach numbers, while MNF adapts the NF to approximate supersonic flows. In NF analysis, any arbitrary shape can be split into multiple sharp cones and then analysed to calculate the coefficients as is explained in Dynamics of Atmospheric Entry [61]. The equations for sharp cones from NF were adapted to MNF by replacing the constant 2 by  $C_{p,max}$ , resulting in equations Eq. (6.4) and Eq. (6.5), while equation, Eq. (6.6) remained unchanged [62].

$$C_A = C_{p,max} \sin^2 \theta_c + \sin^2 \alpha (1 - 3 \sin^2 \theta_c) \quad (6.4)$$

$$C_N = \frac{C_{p,max}}{2} \cos^2 \theta_c \sin 2\alpha \quad (6.5)$$

$$C_M = -\frac{2}{3} \left( C_N \frac{1}{\tan(\theta_c) \cos^2(\theta)} \right) \quad (6.6)$$

where  $C_{p,max}$  is <sup>48</sup>

$$C_{p,max} = \frac{p_{0_2} - p_\infty}{q_\infty} = \frac{p_{0_2}/p_\infty - 1}{\gamma/2 M_\infty^2} \quad (6.7)$$

$$p_{0_2}/p_\infty = \left[ \frac{(1+\gamma)^2 M^2}{4\gamma M^2 - 2(\gamma-1)} \right]^{\frac{\gamma}{\gamma-1}} \frac{1-\gamma+2\gamma M^2}{\gamma+1} \quad (6.8)$$

For high angle of attacks, where  $\alpha > \theta_c$ , Eq. (6.4) and Eq. (6.5) need to be modified to Eq. (6.9) and Eq. (6.10) <sup>49</sup>

$$C_A = \left[ \frac{2\beta_u + \pi}{2\pi} \right] \left[ C_{p,max} \sin^2 \theta_c + \sin^2 \alpha (1 - 3 \sin^2 \theta_c) \right] + \frac{3}{4\pi} \cos \beta_u \sin 2\alpha \sin 2\theta_c \quad (6.9)$$

$$C_N = \frac{C_{p,max}}{2} \cos^2 \theta_c \sin 2\alpha \left[ \frac{2\beta_u + \pi}{2\pi} + \frac{1}{3\pi} \cos \beta_u (\cot \alpha \tan \theta_c + 2 \tan \alpha \cot \theta_c) \right] \quad (6.10)$$

<sup>48</sup>[https://solarsystem.nasa.gov/docs/27\\_ong.chester2.paper1.pdf](https://solarsystem.nasa.gov/docs/27_ong.chester2.paper1.pdf)

<sup>49</sup><http://www.dtic.mil/dtic/tr/fulltext/u2/a013598.pdf>

$$\beta_u = \arcsin\left(\frac{\tan\theta_c}{\tan\alpha}\right) \quad (6.11)$$

Once the  $C_A$  and  $C_N$  have been determined, a simple rotation of  $\alpha$  degrees is performed to get the  $C_D$  and  $C_L$  as shown in Eq. (6.12) and Eq. (6.13)

$$C_D = C_N \sin\alpha + C_A \cos\alpha \quad (6.12)$$

$$C_L = C_N \cos\alpha - C_A \sin\alpha \quad (6.13)$$

The results of the analysis of the aeroshell are shown in Fig. 6.2, Fig. 6.3 and Fig. 6.4. From these plots the necessary stability coefficients needed for entry simulations can be determined.

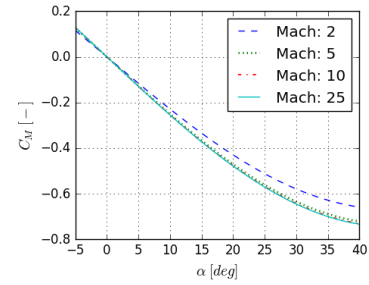
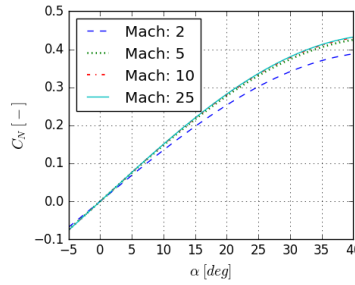
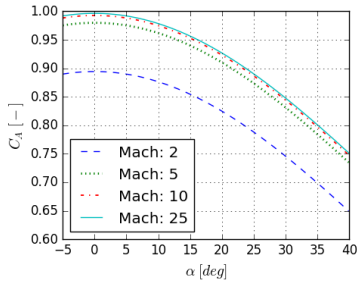


Figure 6.2:  $C_A$  entry vehicle coefficient vs  $\alpha$  for Mach 2, 5, 10 and 25

Figure 6.3:  $C_N$  entry vehicle coefficient vs  $\alpha$  for Mach 2, 5, 10 and 25

Figure 6.4:  $C_M$  entry vehicle coefficient vs  $\alpha$  for Mach 2, 5, 10 and 25

Using the aerodynamic coefficients calculated it is possible to perform an entry simulation. Due to the restrictions of the MNF, the simulation does not account for roll and yaw. The simulation needs to be piecewise simulated due to changes in constant parameters. Due to the piecewise simulation the assumption made for the derivative  $\gamma_\gamma$  is not valid and in the simulation used the derivative is taken as 0. The results with the initial parameters listed in Table 6.1 can be seen in Fig. 6.5. A parachute of  $50 \text{ m}^2$  with a  $C_D = 0.8$  is deployed after 60 seconds. This is simulated as additional drag once the parachute has been deployed and can be seen as a spike in the acceleration plot in Fig. 6.5c.

Parameter	Initial value
Mass	1500 kg
Flight path angle	-10 deg
Velocity	7260 $\frac{\text{m}}{\text{s}}$
Venusian Radius	6052 km
Altitude	260 km
Pitch angle	0 deg
Angle of attack	0 deg
$I_{yy}$	6000 $\text{kg m}^2$

Table 6.1: Initial entry simulation values

From the simulation we can determine that the maximum acceleration is  $26.1 \text{ g}$  at an altitude of  $172 \text{ km}$ . Noteworthy is the high oscillatory behaviour in pitch rate and angle of attack. This is due to the limitations of the linear state space and can be neglected [55] [50]. The pitch rate is unstable due to the breakdown of the MNF for subsonic speeds. Also visible is the parachute deployment at 60s. The induced acceleration is  $14 \text{ g}$ , which is low due to the nature of the linear simulation.

### 6.3. DEPLOYMENT SEQUENCE

The deployment sequence begins with a parachute release when the aeroshell reaches an altitude of  $93 \text{ km}$ , during which it will be travelling at a velocity of  $50 \text{ m/s}$ . Once the parachute has been deployed, the heatshield

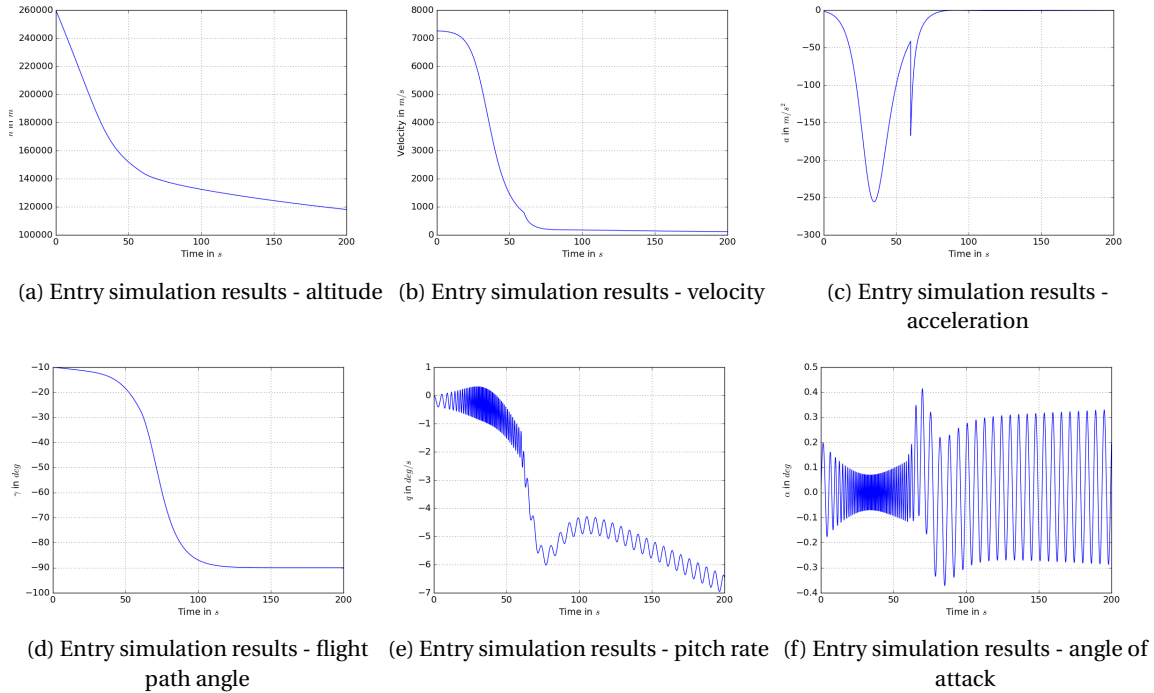


Figure 6.5: Entry simulation results

will be ejected to the side. Once the heatshield has been cleared, the lander is dropped. The lander will descend to the surface and begin the investigation of the surface of Venus. Once the lander has been cleared from the aeroshell, the aircraft is released.

The aircraft has been folded and stowed in such a way that all surfaces will be able to unfold and snap into place due to the aerodynamic forces. This optimally happens when the nose is pointed toward the surface, thus pointed towards the free stream. Since the aircraft will be upside down at the moment of deployment, it must perform a slight rolling manoeuvre to align with the correct position. The front and side views of the folding of both the main wing and the tail are depicted in Fig. 6.6. The arrows in the figure indicate in which direction the surfaces will unfold.

The main wings will be the first surfaces to unfold. The tail booms will then unfold into their fixed position, while the tips of the horizontal tail will also unfold into place. Once the booms have fully rotated, they will then telescopically extend to their full length. When the aircraft is fully unfolded with surfaces locked into operational position, it will glide to the upper track altitude where it can begin its mission. The top view of the operational aircraft is given in Fig. 6.7.

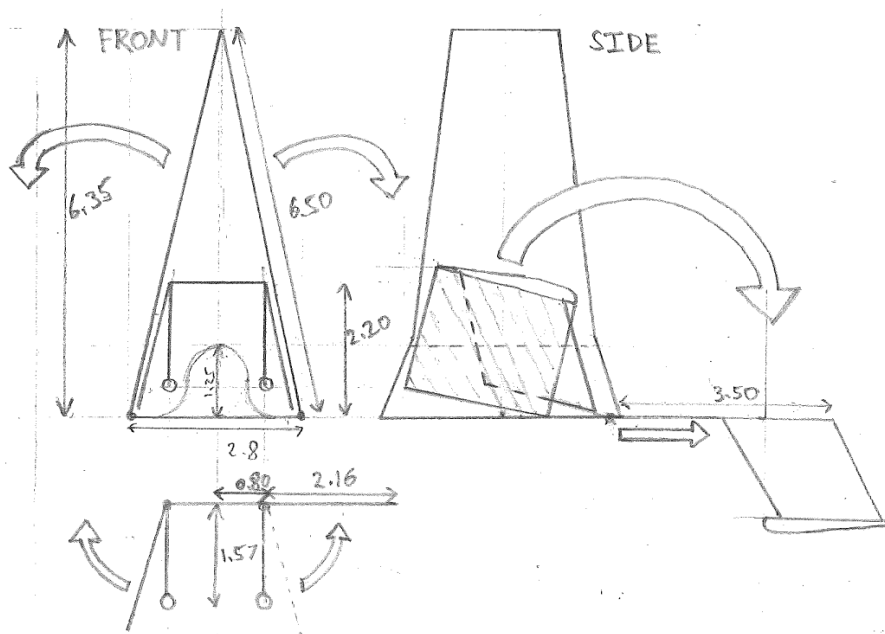


Figure 6.6: Folding of aircraft surfaces

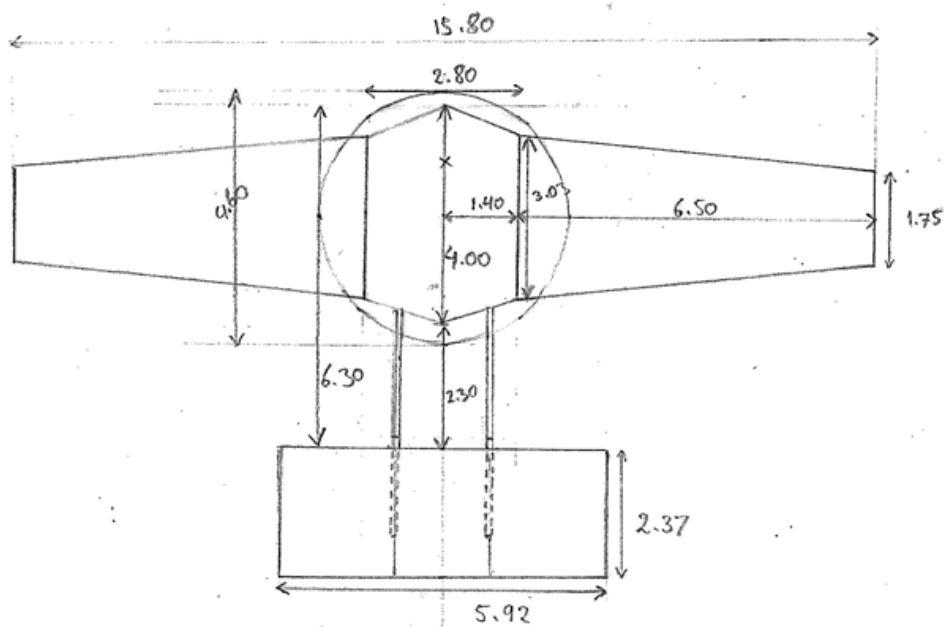


Figure 6.7: Unfolded aircraft, top view

# 7

## SPACECRAFT

The aircraft and landers need to arrive at Venus. To facilitate the travel a spacecraft needs to be designed. This chapter will treat the design of the spacecraft.

### 7.1. PAYLOAD

The spacecraft will carry four instruments, a Synthetic Aperture Radar (SAR), a Venus Emissivity Mapper (VEM), a camera and a Doppler Wind Lidar (DWL). The SAR, DWL, and camera are treated in Sections 7.1.1 to 7.1.3, respectively. The VEM was already discussed in Section 5.1.2. It should be noted that the VEM on the spacecraft will have a different resolution and a different swath width than the one on the aircraft. The spacecraft VEM has a ground resolution of 43.65 km with a swath width of 288 km.

#### 7.1.1. SYNTHETIC APERTURE RADAR

The SAR will be used to map the surface of Venus. The data gathered is intended to be compared to the data gathered by the Magellan mission, any geological changes around volcanoes would indicate could proof the presence of active volcanoes before any objects have to be send into the hostile atmosphere of Venus. This is of course dependent on any volcanoes having erupted in the decades between the Magellan mission and this new mission, so there is no certainty that this instrument will actually obtain proof of active volcanoes. Furthermore, the new radar images of Venus will have a higher resolution than the ones taken by Magellan, so they will allow for an increased understanding of the Venusian surface, even if no proof of active volcanism can be found.

#### 7.1.2. DOPPLER WIND LIDAR

The DWL is an instrument that uses a laser to gather information about the wind speeds in Venus' upper cloud layer and the overlying haze layer. In addition to information about wind speeds, it will provide information about the height of the cloud tops and the aerosol concentration and distribution within the upper cloud layer. This data can be used to find out more about the composition of and processes within the Venusian atmosphere.

#### 7.1.3. CAMERA

The camera that will be used on board of the spacecraft is based on the Venus Monitoring Camera (VMC) [63] that was used on the Venus express mission. It consists of a single Charge Coupled Device (CCD) detector and four different sets of optics for four different spectral bands ranging from UV to the near infrared. These images will be useful for a wide variation of science goals related to the Venusian clouds and upper atmosphere.

Table 7.1: SAR specifications. The power and weight estimations are based on [64]. The swath width is determined by the orbit, while the ground resolution is limited by transmitting power.

Synthetic Aperture Radar	
Power consumption [W]	350
Mass [kg]	154
Swath width [km]	100
Ground resolution [m]	60

Table 7.2: Specifications of a Doppler Wind Lidar proposed to NASA for measurements around Venus [65]

Doppler Wind Lidar	
Power consumption [W]	10
Mass [kg]	50
Vertical resolution (wind) [m]	1000
Cloud top range precision [m]	100

### 7.2. CONFIGURATION

In this section the layout of the spacecraft is discussed.

Table 7.3: Specifications of spacecraft camera [63]

VMC	
Power consumption [W]	5.2
Mass [kg]	1.5
Image dimensions [pixels]	1032x1024
Viewing angle [degrees]	17.5

In Fig. 7.2 one can see the general layout of the spacecraft in deployed configuration. During launch the SAR, high gain antenna and solar arrays will be in a folded position. The folded spacecraft needs to fit inside of the launcher fairing since all the feasible launchers have approximately the same fairing size. The smallest fairing was used and the spacecraft was sized to fit in that fairing including margins for vibrations. In Fig. 7.1 one can see that the spacecraft fits very comfortably inside of the launcher fairing. The spacecraft body is 4x2.5x2.5 m and carries the large aeroshell on top. The front view of the spacecraft in Fig. 7.2 is the side that is facing Venus, on this side all the instruments are located. The back side of the satellite is mostly empty because the retracted high gain antenna occupies most of the area. The right and left side of the spacecraft are symmetric and are dominated by the presence of the solar arrays. The solar arrays are on rotary hinges to provide the lowest possible incidence angle of the solar light on the array, maximising its performance.

### 7.3. STRUCTURE

The spacecraft structure is designed to carry the loads on the spacecraft during the whole mission and to prevent resonance of the structure. In the first step, the different load cases and required frequencies were analysed. Using the associated requirements, the required structural parameters are calculated and a weight estimation is made.

The spacecraft will experience the highest loads during launch. Depending on the launcher, the maximum acceleration will be approximately 4g. Acoustic noise, engine oscillations and other random vibration give requirements on the natural frequency of the spacecraft. Typical required frequencies for spacecraft are 15 Hz in the lateral direction and 30 Hz in the launch direction depending on the launcher [66]. In the case of this spacecraft the requirement for the lateral frequency is driving.

In the calculation of the natural frequencies, the spacecraft was considered to be a cantilever beam with an end mass and an equally distributed mass (Eq.7.1 and 7.2 [67]). The end mass is in this case the aeroshell and the distributed mass is the structural mass of the spacecraft. The rest of the spacecraft weight is attached to the bottom of the spacecraft and therefore does not contribute to the natural frequency. The location of the end mass is considered to be seven meters above the support and the beam stiffness is assumed to be constant. The actual beam stiffness and effected length depend on the moment of inertia and weight distribution along the spacecraft and aeroshell. The seven meters is based on an estimation of the effects of these parameters.

$$f = \frac{1}{2\pi} \sqrt{\frac{3EI}{L^3(M + 0.23m)}} \quad (7.1)$$

$$f = \frac{1}{2\pi} \sqrt{\frac{EA}{L(M + \frac{m}{3})}} \quad (7.2)$$

For both the launch loads and the required natural frequencies of the spacecraft, a safety factor of 1.5 is used. This safety factor is used to assure the structure will not fail when unexpected loads occur, the material changes due to fatigue or if the joints or the material do not have the expected quality. The structure of the spacecraft consists of the following parts to achieve these requirements:

- Vertical beams: The main loads in the spacecraft are carried by four vertical beams with a squared thin-walled cross section.
- Horizontal beams: At the sides of the top and bottom of the aircraft, horizontal beams give structural support. Furthermore, horizontal beams for the parabolic antenna and the solar panels will transfer their acceleration loads to the vertical beams.

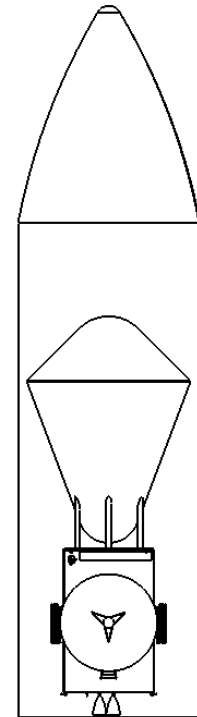


Figure 7.1: Spacecraft inside the fairing

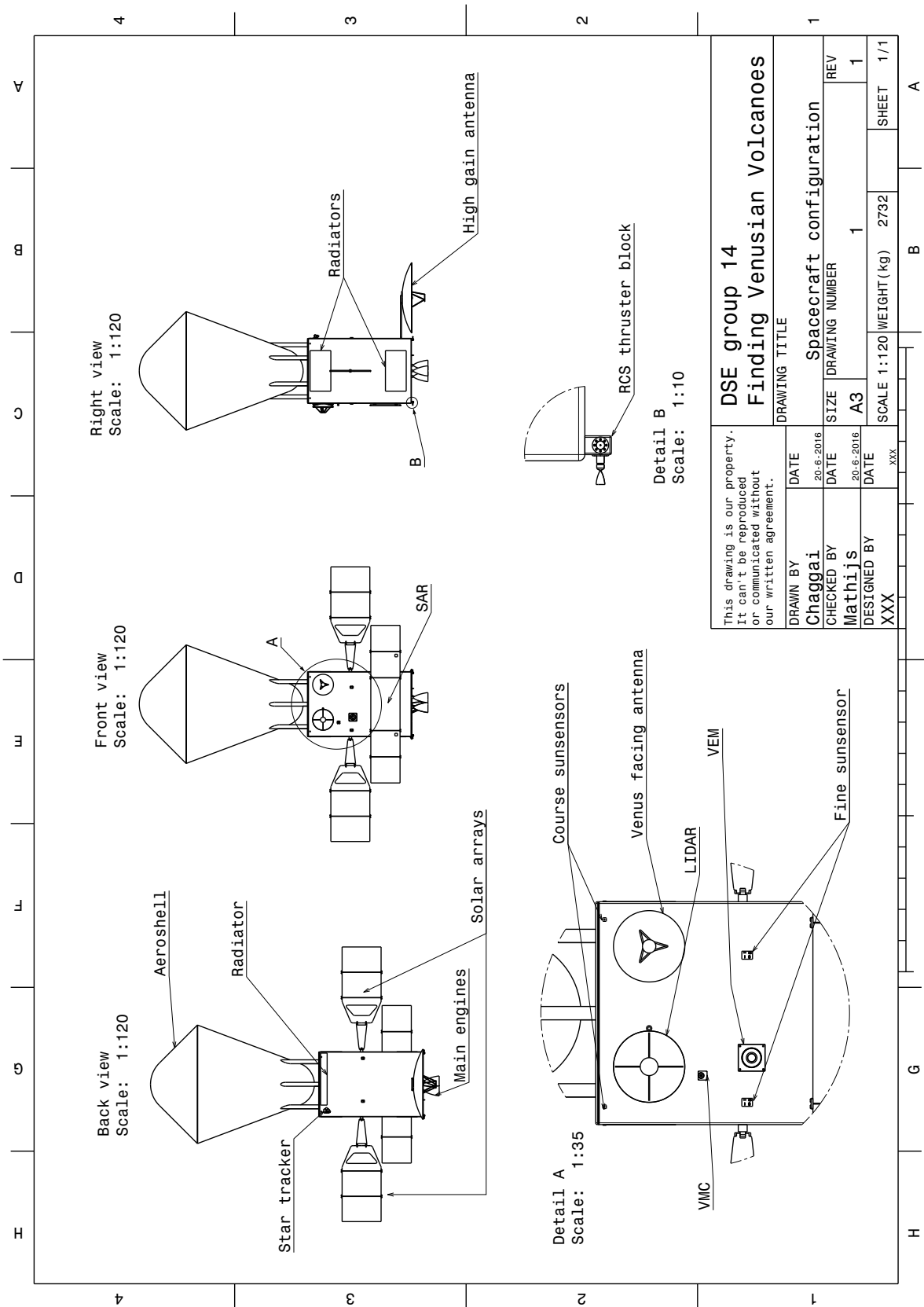


Figure 7.2: Spacecraft configuration

- Bottom structure: At the bottom, a web of four additional diagonal beams will transport the loads from the engines. Together with the beams at the sides, they will also transport all the acceleration loads from the spacecraft to a conical support. This conical support transport is part of the launcher.
- Exterior plates: The exterior plates will next to assure a closed spacecraft and give extra stiffness to the structure by increasing the moment of inertia.

With this structure, the lateral natural frequency of the spacecraft is 23 Hz and the axial frequency 101 Hz. The mass of the structure is 521 kg.

## 7.4. THERMAL

The thermal subsystem of the spacecraft needs to keep all the components of the spacecraft within acceptable temperature regions. The components that have to be kept within a specific temperature range include but are not limited to: payload, electronics, and fuel. After all the components have been identified, the temperature limits of the spacecraft are determined. The maximum temperature of the spacecraft can not exceed 323.15 K and the minimum temperature will not exceed 273.15 K. These limits are valid during all phases of the mission.

In the case of the spacecraft the best way to maintain temperatures was found to be a combination of Multi-Layer Insulation (MLI), radiators and electric heaters. The MLI is necessary to prevent the internal temperatures from dropping too much during interplanetary travel and during the eclipses around Venus. However, during the transfer to Venus, MLI is not sufficient to keep the internal temperature of the spacecraft above 273.15 K. Therefore, electric heaters need to be implemented that have a total heat output of 240 W, as this will keep the internal temperature at 273.15 K. It is possible that less heat is required from the heaters due to a different orientation then expected for example. To regulate this the spacecraft thermal system is equipped with multiple thermostats spread out over the spacecraft. These monitor the local temperature inside the spacecraft and activate or deactivate the heaters when necessary.

During the operational phase the spacecraft does not cool down as much in the eclipse as during the interplanetary travel. However, the spacecraft temperature still gets below the lower acceptable limit. Again, electric heaters are necessary, now they need to have a total heat output of 120 W to raise the temperature above the lower limit. While the spacecraft is orbiting Venus it will be heated up extra from sunlight that is reflected by the planet and the black body radiation of the planet itself. This all combined would cause the spacecraft to overheat when it is in sunlight. To counter this, the spacecraft is fitted with radiators to reduce the temperature to acceptable limits. These radiators have a surface area of 5.5 m<sup>2</sup> and are spread out over the sides of the spacecraft body that do not face the planet during the telecommunications phase. This is done to prevent increased black body radiation intake from the planet. This keeps the temperature of the spacecraft within the limits. The use of radiators has been applied in previous missions such as Venus Express. In Table 7.4 the maximum and the minimum temperature during the different phases with the full thermal system implemented are tabulated.

Table 7.4: Temperatures during different mission phases

Phase	Temperature cold situation [K]	Temperature hot situation [K]
Interplanetary travel	273.42	319.21
Mapping phase	291.92	312.60
telecommunications-relay phase	291.92	312.60

## 7.5. PROPULSION

The spacecraft needs to perform the orbit insertion burn to get in orbit around Venus. Besides this, it will also need to maintain this orbit. To do this, a propulsion system is necessary that is able to provide the required thrust. In this section the selection of the engines, type of propellant, and tank design will be treated.

### 7.5.1. MAIN ENGINE

With the spacecraft mass, the necessary  $\Delta V$ , and the available burn time, the required main engine thrust is calculated. This thrust was found to be 2609 N. With the necessary thrust known, an engine can be selected. Looking at the thrust and the engines that are currently available the choice was made to use three Aerojet

R-42 engines<sup>50</sup>. The type of engines can change in the final product if new engines get developed. However, currently (June 2016) the R-42 is a very acceptable option and its specifications can be used for reference. Three of these engines have a combined thrust of 2670 N, a specific impulse of 303 seconds and can fire long enough without overheating to complete the insertion burn.

### 7.5.2. TYPE OF PROPELLANT

The R-42 Engines use MMH and MON-3 as propellant which is a common combination for engines on planetary missions. Relative to other bi-propellants, this combination has a high specific impulse between 300-340 s [12] and a decent impulse density of 325 kg-s/l. The combination of MMH and MON is hypergolic and therefore requires no ignition source in the propulsion system. This leads to a less complicated and lighter system which is beneficial to the launch weight.

Furthermore, MMH and MON-3 have very good boil off properties, meaning they can be easily stored for prolonged periods of time without much propellant boiling off. This is favourable property for the fuel in planetary missions. The downside of MMH and MON-3 is that the fuel is highly toxic and needs to be treated with the utmost care during processing. Although MMH is toxic, so are most other bi-propellant combinations [12]. Therefore, toxicity was not seen as an argument to not select this propellant.

### 7.5.3. TANK DESIGN

For the tank design one can choose between a regulated system or a blow down system. In a blow down system the pressure in the tank decreases because the fuel or oxygen is flowing out. This decreases the specific impulse and therefore increases the required fuel mass. A regulated system uses a pressurant to control the tank pressure. With a constant pressure, a constant specific impulse can be achieved. However, a pressurant is needed and has to be stored in a separate tank, increasing the mass.

A regulated system has a larger fill ratio: 80-90% with respect to a 50-60% of a blow down system<sup>51</sup>. For larger tanks, the regulated system becomes more efficient. As a large amount of  $\Delta V$ , and therefore propellant, is required to get into an orbit around Venus, a regulated system will be used.

There are two pressurants used for spacecraft: Helium and nitrogen [68]. In this spacecraft helium will be used because nitrogen will dissolve more in MMH, meaning that more nitrogen has to be stored on the spacecraft. The tanks were designed, assuming a maximum temperature of 324 K, a pressure of seven bar in the fuel and oxidiser tanks, and a pressure of 276 bar in the pressurant tank based on [69].

Increasing the fuel or oxidiser tank pressure almost linearly increases the mass of the tank. Other parameters such as the shape, pressure of the pressurant tank, and the number of tanks have a low effect on the tank mass. Concerning the size, the pressure in the pressurant tank has the most influence. Due to the high pressure of 276 bar a small tank is possible. This is not the case for the other tanks as these contain liquids. With the  $\Delta V$  necessary and the storage pressure known the volume of the tanks can be calculated. The volumes of the tanks are found in Table 7.5.

Table 7.5: Tank volume

Tank	Volume [ $m^3$ ]
Oxidizer (MON-3)	0.717
Fuel (MMH)	0.704
Pressurant (He)	0.08

## 7.6. COMMUNICATIONS

The data that is gathered by the scientific instruments and housekeeping sensors on the spacecraft, aircraft, and lander has to be transmitted to Earth. For this, a communications subsystem is necessary. In this section first the Command and Data Handling System (CDHS) will be treated followed by the method of transmitting this to Earth.

### 7.6.1. CDHS

The CDHS collects, stores and prepares all data for transmission. It also receives the incoming commands from Earth and distributes the commands over the appropriate subsystems. The data storage on the space-

<sup>50</sup><http://www.rocket.com/files/aerojet/documents/Capabilities/PDFs/Bipropellant%20Data%20Sheets.pdf>

<sup>51</sup><http://www.lr.tudelft.nl/nl/organisatie/afdelingen/space-engineering/space-systems-engineering/expertise-areas/space-propulsion/design-data/data-for-rocket-propulsion-system-size-estimation/>

craft needs to have enough capacity to store the data produced by the spacecraft, aircraft, and lander combined, and needs to be able to hold on to it for at least two orbits in the telecommunications phase. This time is equal to 23.92 hours. The length of this time was determined by the duration that Venus is behind the Sun and therefore does not have a line of sight with Earth. The data generation by the spacecraft itself is 513 kbit/s. To properly store all the data from the lander, aircraft and spacecraft a storage size of 22.7 Gbit is necessary. This value is based on calculating the amount of data that will be gathered by the instruments and household equipment of all the vehicles during the maximum non-contact period possible.

Before the data can be transmitted or even stored, it needs to be compressed. This compression will be performed by a processor, which will not only be reserved for compressing data but also act as the central brain of the spacecraft. Therefore it needs to be a rather powerful processor. Furthermore, the processor will also interpret the commands coming from Earth and distribute them over the subsystems.

To fulfil these objectives the CDHS is made out of the components listed below. The specific models mentioned at each part are examples that would fulfil the specification. However, the specific model might change in the final product due to a cheaper or better alternative.

- Airbus DS solid state recorder<sup>52</sup>: This solid state recorder based on new flash memory will provide the 22.7 Gbit storage space necessary. Two of these solid state recorders will be used for redundancy.
- The BAE RAD 5545<sup>53</sup>: Will provide the computational power necessary. The processor is radiation hardened to reduce the risk of bit flipping due to radiation. The RAD 5545 is currently one of the fastest radiation hardened processors with four physical cores running at 2.2 GHz. For three multiple of these processors will be used in the design.

### 7.6.2. TT&C

The Telemetry Tracking and Command (TT&C) system is responsible for the transmitting of data and receiving of commands. The spacecraft will also act as a relay station between the aircraft and the lander and will therefore need to facilitate the communications to Earth. The spacecraft will have two high gain antennas used for high data rate communications, one to Earth and one to the aircraft and lander. Next to the two high gain antenna the spacecraft will have two low gain omnidirectional antennas to communicate during phases in which the high gain antennas cannot be pointed correctly, such as detumbling and safe mode. These two low gain antennas will be located at the top and bottom of the spacecraft to make sure that at least one antenna is always pointing in the general correct direction.

The sizing of the antennas and the power required for them is determined by the need to close the link budget. To close the link budget, the antenna specifications listed in Table 7.6 are required.

Table 7.6: Specifications of spacecraft telemetry system

specifications	Spacecraft To aircraft and lander	Spacecraft to Earth
Antenna type	Parabolic dish	Parabolic dish
Antenna size/diameter [m]	0.8	2.7
Transmitter power [W]	5	390
Data transmission band	X-band [8.0-8.4 GHz]	Ka-band [32.1-34.5 GHz]

On Earth the antenna that will be used is part of the NASA Deep Space Network (DSN). The reason for selecting DSN over other communication networks is explained in Section 9.1. The 34 meter dishes are sufficient to close the link budget of the spacecraft. As with the lander in Section 4.5.2, the required BER is  $10^{-6}$  as this will provide enough data clarity to process the data [12]. Also, for the communication of the aircraft QPSK 1/4 code was selected. With the selected forward error correcting code, QPSK 1/4, a SNR of 2.31 dB is necessary to achieve the BER of  $10^{-6}$  [12].

With the system as described above the link budget between Earth and the spacecraft can be closed as is shown in Table 7.7. For the downlink to Earth, the data rate is 2.81 Mbit/s, this combines the data of all vehicles. For the uplink a data rate of 10 kbit/s is assumed per vehicle, so a total of 30 kbit/s is sent to the spacecraft, this value was based on past missions. In the table it can be seen that even with this data rate the margin in the uplink is large, which means that the data rate can potentially be increased to 48 Mbit/s for each vehicle. Alternatively the power used by the DSN dish for transmitting can be reduced.

<sup>52</sup>[http://www.space-airbusds.com/media/document/ens\\_5\\_ssr\\_2014\\_bd.pdf](http://www.space-airbusds.com/media/document/ens_5_ssr_2014_bd.pdf)

<sup>53</sup><http://www.baesystems.com/en-us/download-en-us/20151124120253/1434571328901.pdf>

Table 7.7: Linkbudget Spacecraft-Ground station

Parameter [dB]	Downlink	Uplink
S/C antenna gain	57.18	
S/C pointing loss	-0.0085	
S/C power	25.91	N/A
S/C loss factor	-0.97	
GS antenna gain	78.99	
GS pointing loss	-1.29	
GS power	N/A	43.01
GS loss factor	-0.97	
Space loss	-291.12	
Atmospheric loss	-0.22	
System noise temperature	-26.27	
Boltzmann	228.60	
Data rate	-64.49	-44.77
QPSK 1/4 required margin	2.31	
Required margin to close	3.00	
<b>Total required <math>E_b/N_0</math></b>	<b>5.31</b>	
<b>Total <math>E_b/N_0</math></b>	5.34	42.16
<b>Total margin</b>	<b>0.03</b>	<b>36.85</b>

## 7.7. ADCS

The Attitude Determination and Control System (ADCS) needs to provide the necessary stability and pointing accuracy for the payload and communications system. The pointing accuracy necessary was determined by taking the pointing accuracy of the instruments and comparing them with the calculated pointing accuracy necessary for the communications. Using simple geometry it was found that the pointing accuracy is driven by the communications system to Earth with a required pointing accuracy of 5.285 arcseconds or less. For stability the mapping phase is leading for which the SAR needs a stability of 4.8 arcseconds/ms. For attitude determination a combination of sensors has to be used which are listed below. In the list typical models of the sensors are mentioned which can be used as reference but can change in the final product:

- Three Sodern Hydra star trackers<sup>54</sup>: These will provide the high accuracy for determining the attitude during the operational phase of the mission in which the highest accuracy is required. A set of three is selected to be fully redundant.
- Two Honeywell Miniature Inertial Measurement Units(MIMU's)<sup>55</sup>: These will provide the determination of sudden and small perturbation forces that can not be detected by the star sensors. Two MIMU's are implemented for redundancy.
- Four Adcole Two-Axis Fine Sun Sensors<sup>56</sup>: A pair will be located on opposite sides of the spacecraft. This leads to a set of Sun sensors always facing the Sun. The Sun sensors are selected to check the information provided by the star sensors. By using two on each side they will also be redundant.
- 12 Adcole coarse Sun sensors<sup>57</sup>: Two coarse Sun sensors will be located on each side of the spacecraft to provide redundancy. These sensors do not need a lot of power to work because they are simple small photo-diodes. They are also very light, but are not very accurate and will therefore only be used during the de-tumbling phase after launch and during safe mode.

This combination of sensors will be able to determine the attitude of the spacecraft to an acceptable degree during all mission phases. To control the attitude, actuators are necessary. The actuators that have been selected are listed below:

- Four Bradford space W45E reaction wheels<sup>58</sup>: These four reaction-wheels will provide the accurate attitude control and will be positioned in a pyramid configuration for redundancy.

<sup>54</sup>[http://www.sodern.com/sites/docs\\_wsw/RUB\\_51/2015\\_SODERN\\_HYDRA.pdf](http://www.sodern.com/sites/docs_wsw/RUB_51/2015_SODERN_HYDRA.pdf)

<sup>55</sup><http://www51.honeywell.com/aero/common/documents/myaerospacecatalog-documents/MIMU.pdf>

<sup>56</sup><http://www.adcole.com/aerospace/high-accuracy-fine-sun-sensors/two-axis-fine-sensor-system/>

<sup>57</sup><http://www.adcole.com/aerospace/analog-sun-sensors/coarse-sun-sensor-detector/>

<sup>58</sup>[http://bradford-space.com/userfiles/SCC\\_Heerle\\_Reaction%20Wheel%20Unit%20LR.pdf](http://bradford-space.com/userfiles/SCC_Heerle_Reaction%20Wheel%20Unit%20LR.pdf)

- Eight Aerojet MR-106E thrusters<sup>59</sup>: These are located in four pairs of two. Previous missions to Venus, such as Venus express and AKATSUKI, have shown that full 3-axis control can be provided with 4 thrusters. The thrusters will be used to de-saturate the reaction wheels. For redundancy two pairs of four thrusters will be used.

The reaction wheels are selected based on the required torque and angular momentum storage. The thrusters were selected to be able to de-saturate the wheels and to provide some thrust in case the main engines have unexpected problems. With the selected combination of sensors and actuators the spacecraft will be able to point itself and be stable enough during all mission phases.

## 7.8. EPS

To operate all the spacecraft systems need power, which first needs to be generated and then distributed properly. Energy also needs to be stored for use during eclipses. This all is the job of the Electronic Power System (EPS). The EPS of the spacecraft will consist of solar panels combined with rechargeable batteries. In this section first the solar panels will be discussed followed by the battery sizing.

### 7.8.1. SOLAR ARRAY

To size the solar array the required power needs to be determined first. To do so, the power usage needs to be known during the day and during eclipse. Knowing the orbit eclipse time for both the mapping and telecommunications phase the energy used can be calculated during day and eclipse. The necessary energy also heavily depends on the efficiency of the EPS. For example, during eclipse the batteries also have their own discharge efficiency causing some more energy loss. All these efficiencies have been taken into account and can be seen in Table 7.8. The total energy used by the spacecraft during one orbit needs to be generated by the solar array in the time it is in Sunlight. The equations used and a more detailed description of the calculation procedure can be found in [12].

Table 7.8: parameters solar array sizing

Parameter	Value
$\eta_{PV}$	0.29
$\eta_{EPS}$	0.8
$\eta_{battery}$	0.88
mean incidence angle [deg]	45

The size of the solar array depends on the type of solar cell that is used. For the spacecraft GaAs triple junction cells have been selected because of the experience in spacecraft with these cells, their high efficiency and their low annual degradation. The datasheet of the selected solar cells can be found at<sup>60</sup>.

With these solar cells the required array area was calculated for each of the three mission phases. In this calculation an average incidence angle of 45° was assumed so that there will always be enough solar power available. If there is too much or too little solar power the solar array can rotate on its rotatory hinge as described in Section 7.2 to adjust the incidence angle. The required size of the solar array was calculated for all mission phases and the largest required size was used. This lead to a solar array of 5.88 m<sup>2</sup>.

### 7.8.2. BATTERIES

During the eclipse the spacecraft is powered by batteries. These batteries need to be sized such that they can store all the energy needed. The mass and volume of the batteries depends heavily on the type of battery that is used. For the battery in the spacecraft a Li-ion battery is selected because of its high specific energy, energy density and the experience with this battery in space application. Because of the high specific energy and energy density the volume and mass of the batteries will be lower.

The only unknown that has to be determined for the calculation of the mass of the battery is the depth of discharge that will be used. Depth of discharge affects the lifetime of the battery and therefore needs to be carefully considered. In<sup>61</sup> the depth of discharge against amount of charge/discharge cycles can be found for space application Li-ion batteries. From the orbital parameters and the mission lifetime, the amount of charge/discharge cycles can then be calculated. The corresponding depth of discharge, that was found<sup>61</sup>

<sup>59</sup><http://www.rocket.com/files/aerojet/documents/Capabilities/PDFs/Monopropellant%20Data%20Sheets.pdf>

<sup>60</sup><http://www.spectrolab.com/DataSheets/cells/2015%20XTJ%20CIC%20Datsheet.pdf>

<sup>61</sup>[http://www.saftbatteries.com/force\\_download/li\\_ion\\_battery\\_life\\_\\_TechnicalSheet\\_en\\_0514\\_Protected.pdf](http://www.saftbatteries.com/force_download/li_ion_battery_life__TechnicalSheet_en_0514_Protected.pdf)

turned out to be around 70%. However, the source indicates that beyond 65% the data becomes unreliable, so the depth of discharge was chosen to be 55% to add a margin. The battery size was calculated for all the mission phases and the battery mass is found to be 48.4 kg. The used equations and method to calculate the battery mass can be found in section 21.2 of [12]. The specifications of the battery can be found in Table 7.9<sup>62</sup>.

Table 7.9: Battery specifications

Parameter	Value
Specific energy [Wh/kg]	170
Energy density [Wh/l]	250
Depth of discharge [%]	55

## 7.9. AEROSHELL DEPLOYMENT

The aeroshell was already described in Section 6.1. The deployment method from the spacecraft will be discussed in this section.

The aeroshell is attached to the spacecraft with struts. The struts are connected to the aeroshell using pyrotechnic fasteners. These fasteners have been used in the space industry for a long time. To release the aeroshell the pyrotechnic fasteners will explode to sever the connection with the spacecraft. From that moment the aeroshell fires small cold gas thrusters to guide itself into the correct entry trajectory. The deployment sequence will take place at the end of the mapping phase, thus before the inclination change to reduce that the necessary  $\Delta V$  that the aeroshell requires to position itself on the correct entry trajectory.

## 7.10. BUDGETS

In this section the different budgets of the spacecraft are shown. Note that in the mass budget, the mass of the aircraft and landers has been included in the aircraft aeroshell mass. However, in the cost budget, the costs of the landers and the aircraft have been omitted and the aircraft aeroshell entry is just the cost of the entry vehicle. Furthermore, a margin of 25 million Euro has been included to account for fluctuating prices of labour and products, as well as other unforeseen expenses. All values have been taken of data sheets of the products that have been used for reference which are mentioned in the sections above and if data was not available statistical data was used from [12] and previous missions.

## 7.11. BLOCK DIAGRAMS

In this section the different block diagrams of the spacecraft systems are shown. These are the hardware, software, data handling and electrical diagram.

### 7.11.1. HARDWARE

The hardware diagram of the spacecraft shown in Fig. 7.3 indicates the interactions between the different systems that comprise the spacecraft. The diagram shows the barrier between the inside and outside of the spacecraft that is formed by the structure and MLI, with the heat flow going through that system. It should be noted that the heat inflow, both from outside and from electric heaters, is spread over all systems on the inside, and all outflow originates from the systems inside. The antennas, aeroshell and solar panels are all located on the outside. Also, the aeroshell will only be connected to the spacecraft for the first part of the mission.

### 7.11.2. S/W DIAGRAM

The software block diagram of the spacecraft Fig. 7.4 is similar to that of the lander in Fig. 4.5, but it has more systems which communicate with each other. One of the main additions is the ADCS software that calculates the attitude and required orientation. The power software monitors the battery power level, turns the solar panels to face the Sun if more power is required and turns heaters on and off depending on the temperature. Also, the housekeeping software has several thermal probes to determine whether the spacecraft needs heating or cooling to keep the instruments in the optimal temperature range.

<sup>62</sup>[http://www.saftbatteries.com/force\\_download/1602\\_Saft-SpaceBrochure\\_8.5x11.pdf](http://www.saftbatteries.com/force_download/1602_Saft-SpaceBrochure_8.5x11.pdf)

Table 7.10: Mass budget of the spacecraft

Element	Allocated [kg]
1.0 Payload	1710.9
1.1 Aircraft aeroshell	1500.0
1.2 SAR	154.0
1.3 VEM	5.4
1.4 VMC	1.5
1.5 LIDAR	50.0
2.0 Spacecraft Bus (dry)	1021.5
2.1 Propulsion	101.8
2.2 ADCS	80.2
2.3 Communications	98.4
2.4 CDHS	48.1
2.5 Power	87.6
2.6 Structure	521.0
2.7 Thermal	84.4
3.0 Spacecraft dry mass	2732.4
4.0 Propellant	2800.2
4.1 MMH	1036.4
4.2 MON-3	1731.6
4.3 Presurrant He	3.2
4.4 Monoprop. Hydrazine	29
5.0 Loaded mass	5532.6
6.0 Launch Vehicle adapter	83.5
<b>Total mass</b>	<b>5616.1</b>

Table 7.11: Power budget of the spacecraft

Element	Power [W]
1.0 Payload	533.7
1.1 SAR	350
1.2 Camera	5.2
1.3 LIDAR	10
1.4 VEM	18.5
1.5 Aircraft power	150
2.0 Subsystem power	1,443.1
2.1 ADCS	227
2.2 TT&C	430
2.3 CDHS	162.1
2.4 Power	161
2.5 Propulsion	223
2.6 Thermal	240
<b>Total</b>	<b>1976.8</b>

Table 7.12: Cost budget of the spacecraft

Element	Allocated [€ × 1000 (FY2016)]
1.0 Payload	98,900
1.1 Aircraft aeroshell	61,600
1.2 SAR	26,400
1.3 VEM	2000
1.4 VMC	900
1.5 LIDAR	8000
2.0 Subsystems	164,164
2.1 Propulsion	13,776
2.2 ADCS	30,176
2.3 Communications	20,664
2.4 CDHS	28,044
2.5 Power	38,212
2.6 Structure	30,012
2.7 Thermal	3280
4.0 Propellant	449.7
4.1 MMH	293
4.2 MON-3	151
4.3 Presurrant He	0.2
4.4 Monoprop. Hydrazine	5.5
5.0 Margin	25,000
<b>Total cost</b>	<b>288,513.7</b>

### 7.11.3. DATA HANDLING

The spacecraft will need to handle a range of data flow, as it also acts as a relay station for communications to Earth. Once the aircraft or lander are operational and in range, the spacecraft will receive modulated

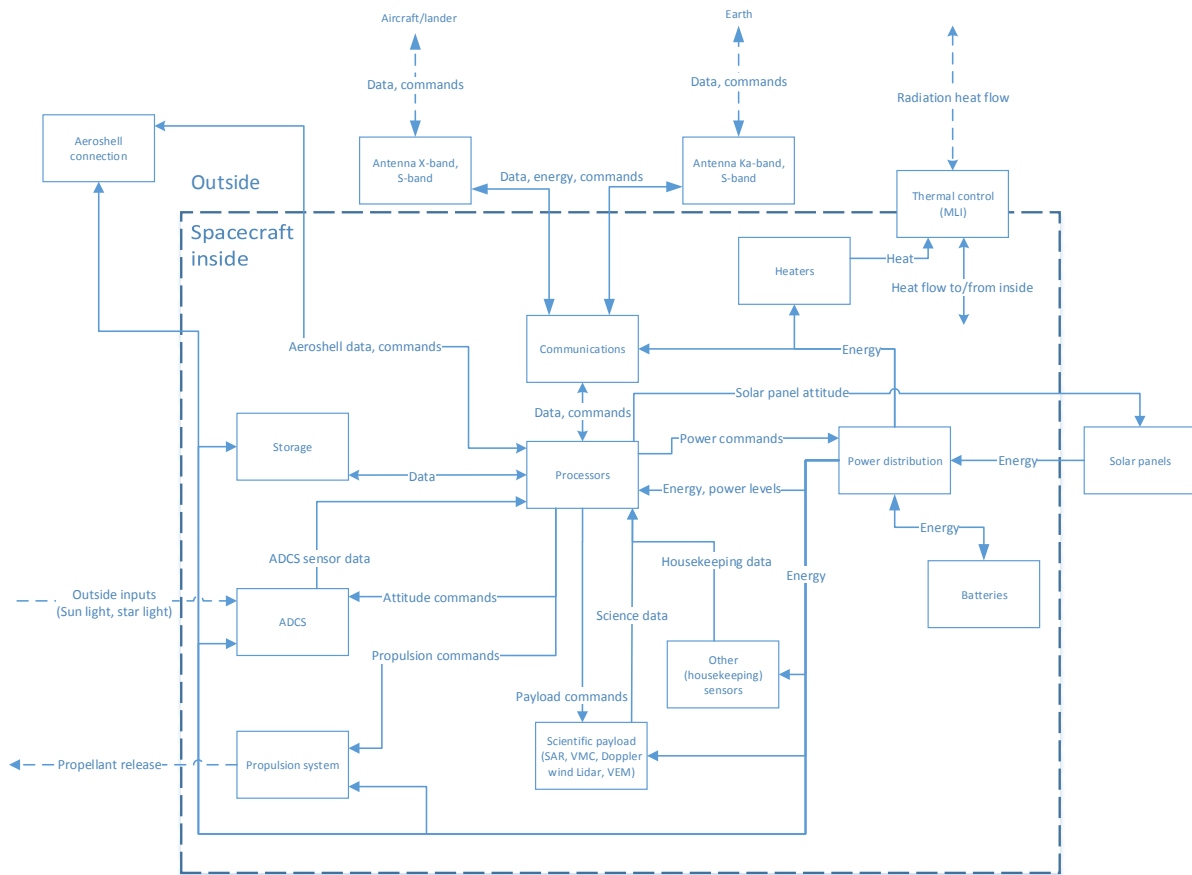


Figure 7.3: Spacecraft hardware diagram

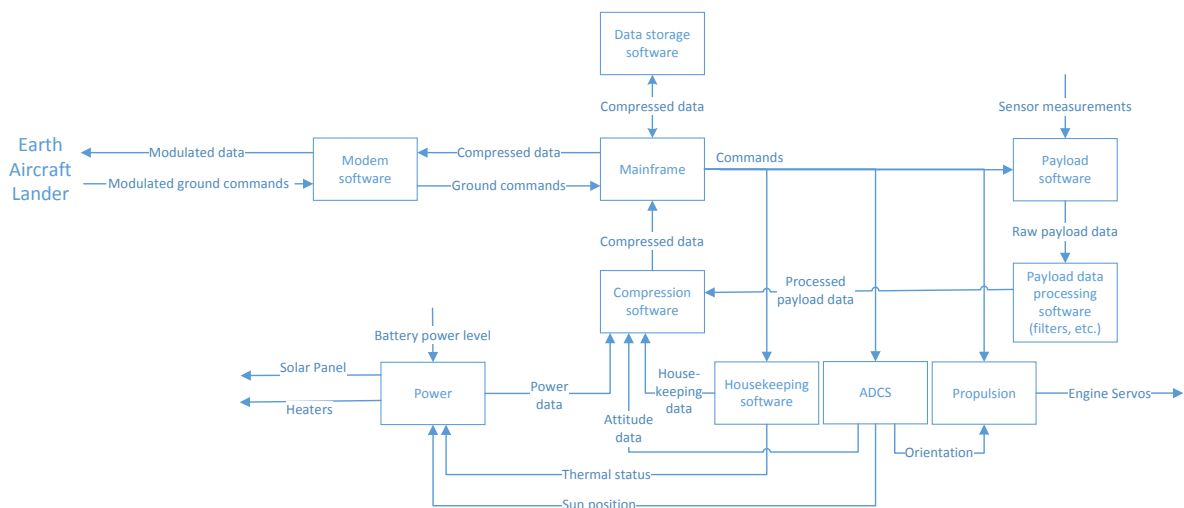


Figure 7.4: Spacecraft software block diagram

compressed data generated by those vehicles. This data is then demodulated and stored in the spacecraft data storage. The spacecraft itself will also be generating data with its scientific payload. This data is compressed by the processor and then usually stored in the onboard data storage. Once the spacecraft reaches a position in which it can contact Earth, it will start to pull compressed data from the data storage and compressed data from the processor and provide it to the modem, that will modulate the data. Once this is done, the signal

will be transmitted to Earth. Alternatively, if there are commands for the aircraft, these will also be relayed to the aircraft, even though this is not shown in the diagram.

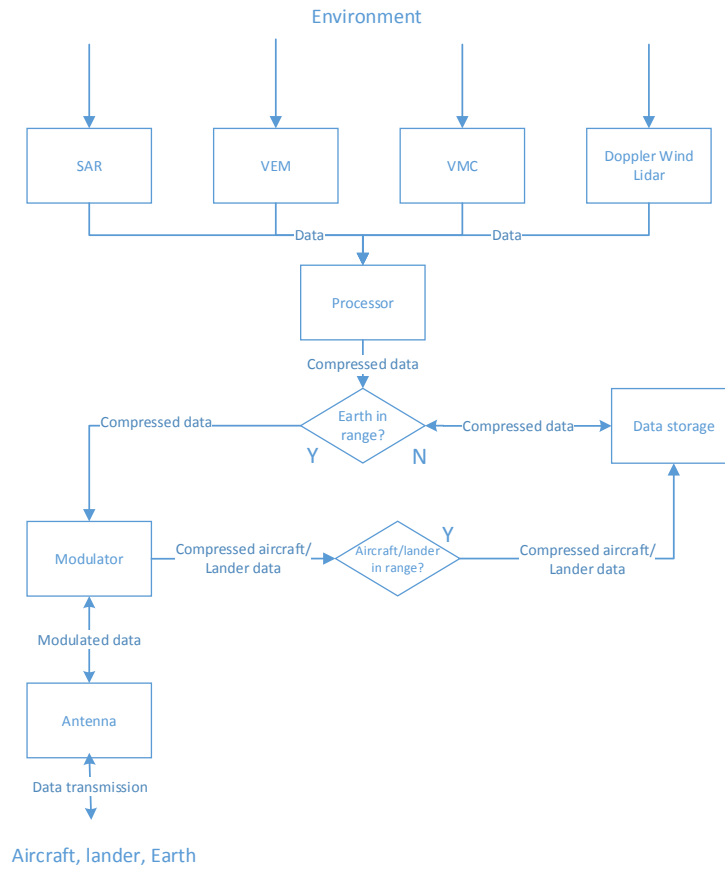


Figure 7.5: Spacecraft data handling block diagram

#### 7.11.4. ELECTRICAL BLOCK DIAGRAM

The electrical block diagram of the spacecraft is similar to the diagram for the aircraft (Fig.5.76). However there is one specific difference. In case of the spacecraft, the solar arrays have to be pointed to the Sun. A Solar Array Drive (SAD) will provide this. The electrical block diagram is shown in Fig. 7.6.

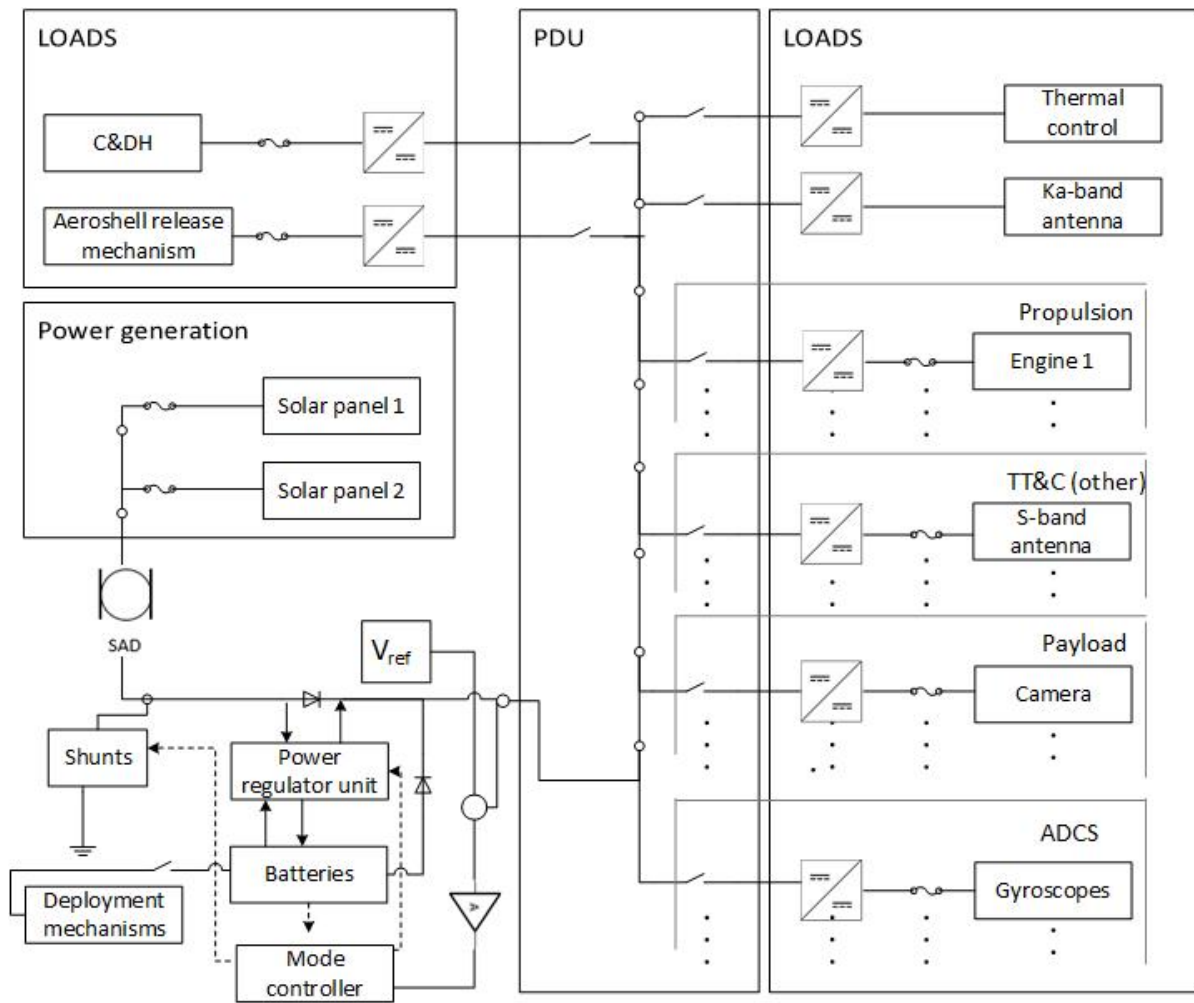


Figure 7.6: Spacecraft electrical block diagram

# 8

## SENSITIVITY

This chapter describes the sensitivity of the lander and spacecraft to changes in the design. For the aircraft no sensitivity analysis is performed because of the high complexity of the system. A mass change could change not only change sizes of other systems but also design decisions.

### 8.1. LANDER

The results of the sensitivity analysis of the lander show that some parts will have a very large impact on other components, while others can be changed without critical consequences. The results are shown in Table 8.1.

The main reason for the total mass to increase when the inner radius is increased while keeping the same lifetime is the increase of the outer radius shell. This radius increases exponentially with the inner radius because of the required insulation gas in between. This can also be seen when the inner radius is increased while keeping the outer radius the same. The mass will increase by a little, while the lifetime will decrease significantly.

Since the mass of the lander is mostly determined by the pressure shells as mentioned above, an increase in payload mass does not affect the overall mass significantly.

Table 8.1: Sensitivity of the lander design

Change	Result
Increase inner radius by 0.05 m, same lifetime	Total mass increases by 47.2 kg
Increase inner radius by 0.05 m, same outer radius	Decrease lifetime by 40 minutes
Increase payload mass by 1 kg	No significant impact on other components

### 8.2. SPACECRAFT

Possible changes in requirements could change the mass of one of the spacecraft subsystems and the required  $\Delta V$ . The results of the sensitivity analyses can be found in Table 8.2.

Table 8.2: Sensitivity of the spacecraft design

Change	Result
Increase data rate with 1 kbit	Power required increase 0.13 W
Increase in eclipse time with 1 minute	Increase in dry mass of 0.374 kg
Increase power required with 1 W	Increase in dry mass of 0.114 kg
Increase dry mass with 1kg	Increase in propulsion mass of 1.5 kg
Increase $\Delta V$ with 1 m/s	Increase in propulsion mass of 2.46 kg

# 9

## OPERATIONS AND LOGISTICS

Operations and logistics are an essential part of achieving the mission goals. Operations include all actions that are required during mission life and these will be described in Section 9.1 to Section 9.3. The logistics is then graphically shown in a logistic flow block diagram in Section 9.4.

### 9.1. GROUND SUPPORT

After the launch no changes or repairs can be performed on the hardware. The software, however, can still be changed and corrected if necessary. As the satellite performs its mission, it sends household data down to the ground station, in addition to the scientific data it gathers. This data can then be used to gauge the health of the system. If needed, changes and updates can be sent to the on-board software to improve the operations of the mission or to correct for any deficiencies.

This is a relatively common practice on modern space missions. The Curiosity Mars rover, for example, has had more than 10 software updates<sup>63</sup>. As such, the spacecraft exploring Venus will have to be designed in such a way that it can safely be updated, including the option for autonomous reversal to a previous version if the update introduces unexpected software errors. During the spacecraft's planned life there must be a team monitoring the system health. If irregularities are detected, the capability to update the spacecraft's operating system to resolve issues must be available. Otherwise the spacecraft's effective lifetime might decrease significantly.

For communication with the spacecraft a 34 meter antenna will be needed. There are two ground station networks with both global coverage and dishes with the right size, namely ESA's Estrack [70] and NASA's Deep Space Network (DSN) [71].

The main advantage of Estrack is the fact that it's 34 meter dishes are already capable of receiving and transmitting on the Ka-band,[70] while this is not yet the case with the DSN, which is scheduled to be upgraded by 2018[72]. The DSN has more 34-meter dishes per site, though. Furthermore, all three of the DSN sites have 34-meter antennas capable of sending and receiving on the S-band, while this capability only exist in one Estrack site. The DSN also provides a lot more additional services and support with receiving data and planning activities (AMMOS [71]) than ESA's Estrack. This is because The DSN can be hired for non-NASA missions, while Estrack is solely available for ESA or ESA-affiliated missions. The DSN does not come for free. While Estrack would be available to ESA missions without additional costs for the mission, the same is not true for the DSN.

Based on this, it was decided to use NASA's DSN, as it has increased availability of mission support and is available no matter what space agency funds the mission.

### 9.2. COMMUNICATION

In Fig. 9.1 and Fig. 9.2 the communication flow diagram is shown for the uplink and downlink. As can be seen in the diagrams, all communication with the lander and aircraft will be performed via the satellite. This will decrease the signal to noise ratio for the lander and aircraft communication. The uplink in this case is all data coming from Earth and the downlink all data going to Earth. This means that the communication from the lander/aircraft to the bus is part of the downlink and the communication from the bus to the lander/aircraft part of the uplink. The data of the uplink contains the commands given by the ground station. The downlink data contains information about the state of the bus, aircraft and lander and the data obtained by the scientific payloads. Both data lines will contain acknowledgements when establishing a connection.

In the diagrams, it can also be seen that three frequency bands will be used: S-band, X-band and Ka-band. The S-band frequencies will be used for all the initial communication and in case the main satellite dish malfunctions. The initial communication includes start-up commands and data of the state of the aircraft,

<sup>63</sup><https://www.nasa.gov/jpl/msl/mars-rover-curiosity-20131220/#.Vx9hRvmLRD8>

lander and bus. For this communication, low gain antennas are required because at this stage the parabolic antennas are not pointed in the right direction yet.

The Ka-band will be used for the communication between the bus and Earth. . At this frequency band, higher data rates are possible which increases the signal to noise ratio. Because of higher gain losses, a frequency in the X-band will be used for the communication between the bus and the lander or the aircraft instead of a Ka-band frequency.

In total, four antennas will be used on the bus: two low gain S-band antennas, a high gain X-band antenna and a high gain Ka-band antenna. The low-gain S-band antennas are used for communication with earth when the satellite is in Safe-mode. The lander and aircraft will both a high gain X-band antenna. All antennas are reciprocal: they will be used for both uplink and downlink. This means that the transmitting X-band antenna for the uplink will be the receiving X-band antenna for the downlink.

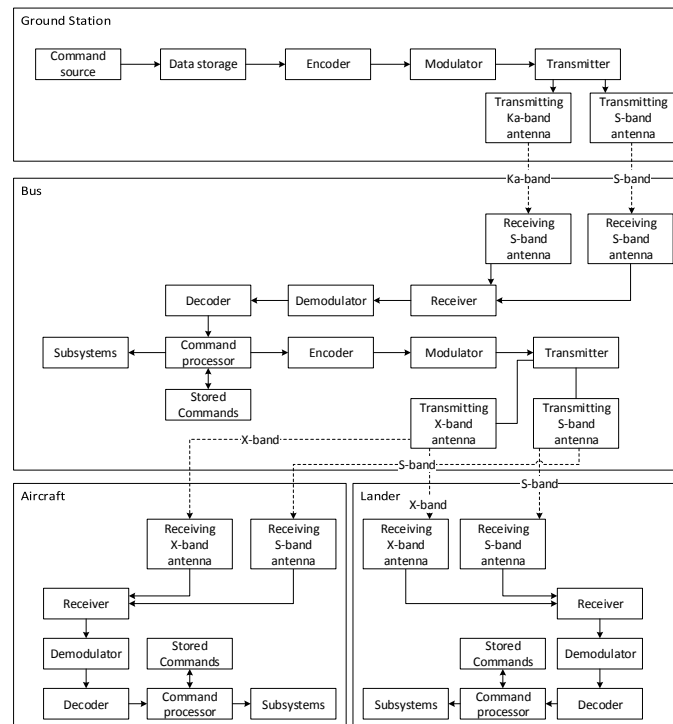


Figure 9.1: Uplink communication flow diagram

### 9.3. DATA PROCESSING

Data measured by instruments will be send to receiving antennas using the spacecraft's telemetry system. Stars, the Sun, molecular clouds, and gas giants are natural emitters of electromagnetic radiation, which appears as noise to deep space communication antennas and receivers. Sophisticated signal processing is then applied to filter out the noise<sup>64</sup>.

Once that is done, the properly filtered data received at the antennas of the DSN flows through a string of computers and communication links known collectively as the Ground Data System (GDS). The Advanced Multi-Mission Operations System (AMMOS) provides most of the ground data system functions needed to design, implement, and operate a mission operations system<sup>65</sup>. The functions of the GDS can be viewed as generally divided into two segments: front end and back end.

To make the data usable for scientists and engineers, front end processing is applied. This includes frame-synchronising the data stream and restoring the formats created by the spacecraft computers. In addition, front-end processing should provide a way in which engineers and scientists can easily track the incoming data.

<sup>64</sup><http://www.qrg.northwestern.edu/projects/vss/docs/communications/3-how-is-data-processing-managed.html>

<sup>65</sup><https://ammos.jpl.nasa.gov/>

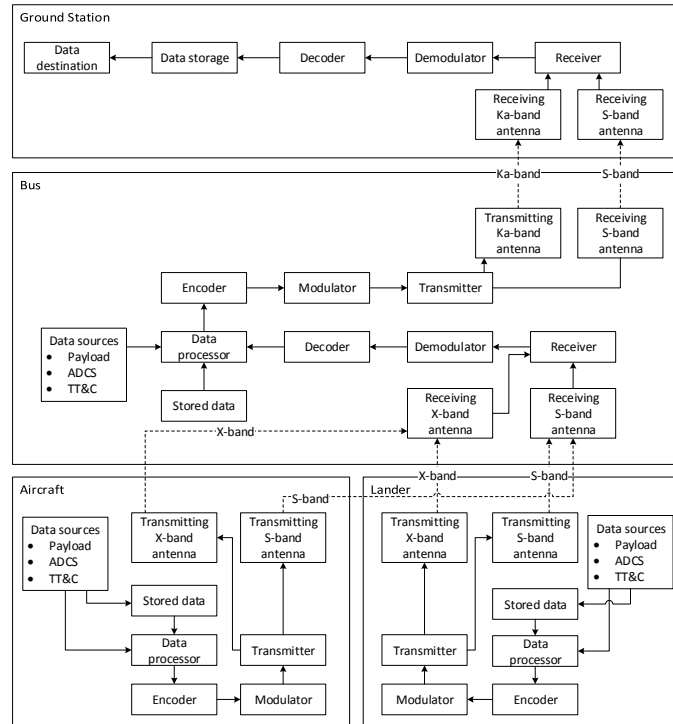


Figure 9.2: Downlink communication flow diagram

Back end processing includes storing and organising of the data, as well as other activities intended to make the data more easily available for scientists. Access to the data is mainly gotten through the back-end systems. This whole process is graphically shown in figure 9.3.

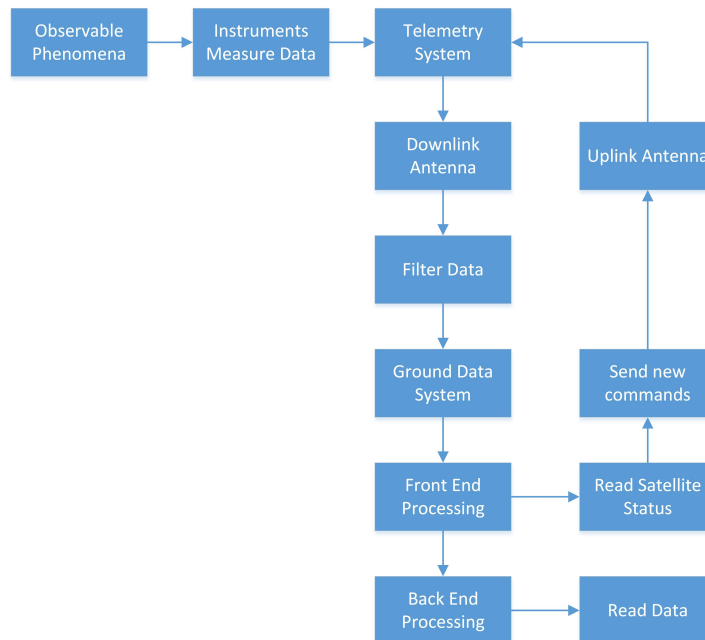


Figure 9.3: Data processing

### 9.4. LOGISTIC FLOW BLOCK DIAGRAM

A logistic flow block diagram can be found in figure 9.4. It describes all the logistical actions required to realise the mission. These actions include the hiring and organising of the team that will finish the design and production of the mission, as well as the acquiring of funding, finding manufacturers for the different parts necessary for the aircraft and other actions that do not directly relate to building the mission but that are nonetheless vital for its success. Communicating and operating the spacecraft is also considered to be part of the logistical actions.

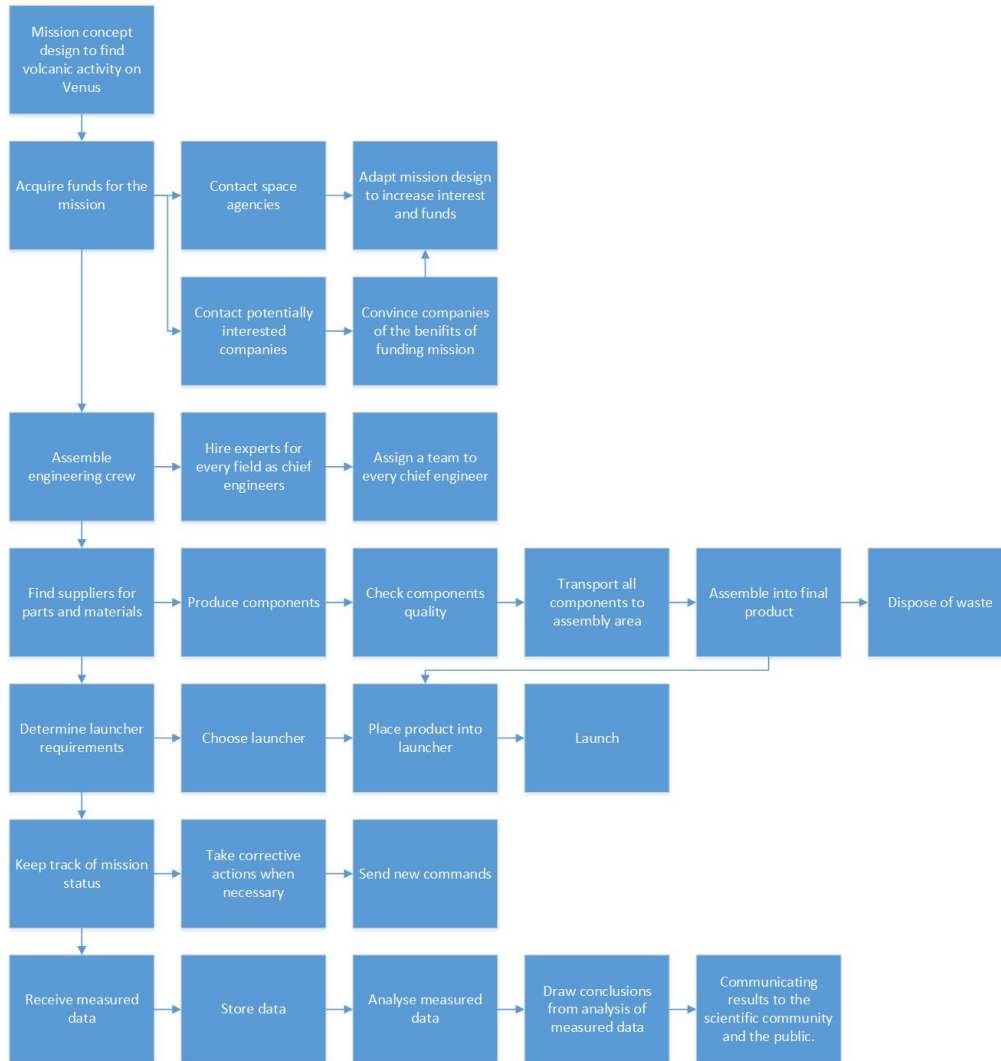


Figure 9.4: Logistic flow block diagram

# 10

## RISK ANALYSIS

In this chapter, a risk assessment is performed for the mission to Venus. To be able to do that, Section 10.1 will give a short explanation of risk as well as the method that is applied in the assessment. After this, the initial risk assessment is performed in Section 10.2. To reduce some of the risks, risk mitigation is applied. This process is described in Section 10.3. All this is followed by the final risk map with the mitigated risks.

### 10.1. RISK ANALYSIS METHOD

Risk is defined as the likelihood of a failure occurring multiplied by the consequence of that failure for the mission [73]. To visualise the risks and get a better overview, a risk map will be created. Risk maps have 'probability of occurrence' along the horizontal axis, and 'impact of failure' along the vertical axis. This means that the failures located furthest to the top right pose the highest risk to the mission, while those in the bottom left corner are much less important. Based on this, priorities can be set as to how resources should be assigned to reduce the risks.

The probability of occurrence is qualitatively ranked from 1 to 5 and this scale is explained in Table 10.1. The impact of the consequences also has a scale that is shown in Table 10.2. Secondary objectives are mentioned in that table as well. Secondary objectives involve performing scientific experiments and gathering data that will be beneficial to the scientific community. However, if these objectives are not performed they will not compromise the main mission.

Table 10.1: The scale of probability

Scale	Elaboration
5	Near certain to occur
4	Highly likely to occur
3	Likely to occur
2	Unlikely to occur
1	Highly unlikely

Table 10.2: The scale of impact of consequences

Scale	Elaboration
Catastrophic	Mission failure
Critical	Mission success questionable
Moderate	Secondary mission failure
Minor	Secondary mission questionable
Negligible	Solvable inconvenience, no impact on mission success

To further visualise these effects three different colours are used in the risk map to indicate the difference in risk. These are shown in Table 10.3.

Table 10.3: Risk map color descriptions

Name	Description	Colour
Red	Significant risks that could severely harm the mission	Red
Yellow	Risks that can harm the mission, but are less critical than the red risks	Yellow
Green	Risks of lowest importance. Not considered in risk mitigation.	Green

### 10.2. INITIAL RISK ANALYSIS

In this section the initial risk analysis is performed. The first step is to identify the risks and then classify them in terms of probability and consequence as mentioned in Section 10.1. This first step is done in Section 10.2.1. Based on the classifications the risk map will be created in Section 10.2.2.

#### 10.2.1. IDENTIFICATION AND CLASSIFICATION OF RISKS

The risks listed here are based on the different system functions that are expected in the final design. Currently it is assumed that systems are not redundant if it was not mentioned in this report. As the design matures risks may be added, removed or adjusted.

1. Launch failure
  - (a) Launch failure: Catastrophic because it is a total failure which means the mission cannot be performed leading to large scheduling problems. However, looking at the recent launches by the Atlas V 551 and Delta V Heavy combined, they were successful 11 out of 12 launches, so it is considered highly unlikely that launch failure occurs.
  - (b) Wrong orbit insertion by launcher: Depending on the mistake in the orbit, propellant and  $\Delta V$  that is lost, the impact changes. It is assumed that the impact is moderate since most occurrences of wrong orbit insertions can be solved. Unlikely to have a significant insertion error as overall the launchers have a good accuracy.
2. Propulsion system
  - (a) Not having enough  $\Delta V$ : Catastrophic because it can prevent the satellite from reaching Venus. Unless terrible contingency management has been applied it is highly unlikely.
  - (b) Sudden death of system: Catastrophic because the satellite will be dead in space. Unlikely to occur since most times that the propulsion system has a problem it will still perform but not to specifications.
  - (c) Unexpected malfunctioning of the system: This was for instance the case of Akatsuki. Unforeseen failures caused the initial orbit insertion to fail. The impact of such an event can range from negligible to critical depending on the event, but to be conservative the impact for now is assumed to be critical. The occurrence of such an event is considered to be highly unlikely because of past experience.
  - (d) Damaged propellers on the aircraft: A damaged propeller of the aircraft can cause the thrust of the aircraft to differ from the design value and therefore force an alternate mission profile. As the aircraft has multiple propellers, a single failure will not lead to total mission failure, so its impact is critical rather than catastrophic. Propeller damage is expected to be unlikely to occur due to the experience with propellers on Earth.
3. Electronic Power System (EPS)
  - (a) Failure to deploy solar panels: Critical, because it is not possible for the satellite or aircraft to reach and/or operate at Venus solely on battery power. Because of the large amount of experience with solar panels it is considered to be highly unlikely that this occurs.
  - (b) Short circuit leading to system overload: Catastrophic, because the entire system stops functioning. Probability is highly unlikely since the amount of experience with insulation and electric systems is large in space engineering and testing is also performed prior to launch.
  - (c) Battery failure: Catastrophic, because the satellite generally communicates to Earth while in eclipse and aircraft will not be able to descend into the Venusian atmosphere. In either case, the mission is significantly compromised. This failure is highly unlikely due to the large amounts of experience with batteries in space.
  - (d) Solar panels damaged by the acid on Venus: The solar panels on the aircraft can be damaged by the acid of the Venusian clouds. This would cause a decrease in performance and might lead to insufficient power for the aircraft to fly, leading to it crashing on the surface. The impact of this event is moderate because it is expected that the primary mission can be performed before significant damage is taken. Also, the application of protective coatings leads to only having a likely occurrence of this damage.
4. Structural
  - (a) Damage to spacecraft and/or payload due to launch loads/vibrations: Critical because if important systems are damaged then parts of the mission can be impossible. Highly unlikely to occur as everything is well tested on the ground before launch by applying a launch loads and vibrations test.
  - (b) Damage due to Venus' atmosphere: It is highly likely to happen due to the very hostile atmosphere. Moderate impact because it is expected that the damage will only affect the vehicle after it has completed its primary objectives.
5. Communication
  - (a) Loss of communication between spacecraft and ground station: Catastrophic since the satellite will be unresponsive to commands and will not transmit any data, causing the mission to end. This is highly unlikely to occur because of experience, the application of verification and validation in the design process and the inclusion of a low gain back-up antenna.
  - (b) Loss of communication between spacecraft and aircraft: Catastrophic since the aircraft will con-

- tinue to fly but no data on possible active volcanoes will be returned. This is unlikely to occur because of experience and the application of verification and validation in the design process.
- (c) Loss of communication between lander and spacecraft: Catastrophic since the lander will continue functioning but it will die before the data can be transmitted. This is unlikely to occur because of experience with the Venera landers.
6. Payload
- (a) Payload not functioning as expected at arrival (damaged etc.): Catastrophic, because mission cannot be (completely) fulfilled. Highly unlikely due to experience and the application of verification and validation on Earth.
  - (b) Aeroshell not detaching: Catastrophic because mission of aircraft and lander can not be performed. This is highly unlikely because of experience with detaching payloads from a satellite.
7. Entry and Landing
- (a) Failure to deploy aircraft: After the aircraft has entered the Venusian atmosphere, the aircraft needs to unfold and start flying. This could go wrong causing the aircraft to crash and therefore making completion of the primary mission impossible. Thus this is catastrophic and the probability of occurrence is estimated to be highly likely since there is no previous experience in deployment of an aircraft during a free fall after entry of an atmosphere.
  - (b) Wrong landing location: If the lander is deployed but ends up in a wrong location due to, for example uncertainty in winds, it might not be able to analyse an active volcano, but will still provide significant scientific data. Thus the impact is critical. Based on experience from previous missions, the occurrence of such an event is likely.
  - (c) Lander not deploying from aircraft: If the lander does not deploy it will not be able to analyse the volcanoes at the surface. However, the aircraft can possibly complete the primary objectives. Therefore, it is critical. Highly unlikely because of experience with dropping payloads such as bombs from aircraft on Earth.
8. ADCS
- (a) System pointing error: Moderate impact, because it is possible to update the software of the ADCS to compensate for such an error. Considered unlikely that the error will be large enough to pose issues.
  - (b) Malfunctioning actuators leading to partial loss of spacecraft control: Critical because the spacecraft becomes more difficult to properly control, but a number of actuators are expected to still be functioning. Partial failures are likely as a result of the complexity of the ADCS. An example of this is the Kepler telescope where two of the four reaction wheels failed leading to a reduction in performance. However, it was mentioned in Chapter 7 that there is redundancy so the probability of this event is reduced to highly unlikely.
  - (c) Loss of sensor: Critical as the loss of a sensor can lead to total loss of the determination of spacecraft attitude. Unlikely to occur based on data from previous missions. However, redundancy was applied in Chapter 7 so the probability is further reduced to highly unlikely.
  - (d) Aircraft control surface failure: Moderate, because the aircraft is designed to be very stable by itself, and can therefore still perform some parts of the mission. Likely due to inexperience with flying on Venus.
9. CDHS
- (a) Too little data storage: Moderate impact as part of data is lost. Still, actions can be taken to distribute available storage more evenly to compensate for this, and data can still be sent to Earth so main mission functions are not impaired. Highly unlikely as sizing should already take contingencies into account.
  - (b) Bit flipping in main processor: Minor impact as it only affects small parts of the data processing and because of the inclusion of software that identifies and corrects bit flipping. Likely to happen even to radiation-hardened processors.
  - (c) Complete failure of processor: Catastrophic as most subsystems require a functioning processor (e.g. actuators, signal processing, etc.) or become useless (e.g. sensors, data storage, etc.). Unlikely because of experience and application of verification and validation. The probability is further reduced by adding extra processors as was described in Chapter 7. The new probability is highly unlikely.
10. Thermal
- (a) Faulty thermostat measurement: Critical as errors are not expected to be too large to cause total

- mission failure, but can still lead to reduction of mission life. The reduction in mission life will be caused by components not being heated or cooled sufficiently. Considered unlikely to happen because of experience with the systems and the application of verification and validation.
- (b) Faulty heaters/coolers: Critical as system will still function, but lifetime is expected to be compromised. Unlikely to occur as they are relative simple systems, in contrast to active coolers/heaters.
  - (c) Damaged coatings: Negligible as the heaters/coolers can be used to compensate for (partial) loss of coatings and because this was already considered in the design. Furthermore, it is expected that the mission life is too short to severely damage the coatings. Highly likely as there is radiation in space which will damage the coatings eventually.
  - (d) Overheating in Venusian environment: Catastrophic if the electrical system fail before completion of the mission. Likely to occur because the temperature at the surface is high, but some steps were already taken during lander design to reduce the likelihood.
11. Volume
- (a) Volume of spacecraft too big for selected launcher fairing: Critical as it endangers the entire project schedule, and might also increase costs. Highly unlikely as this is checked continuously during the design process by application of contingency management.
12. Mass
- (a) Mass of spacecraft higher than expected (snowball effect, Launcher etc): Catastrophic, because schedule, costs etc. will be strongly affected by the issue, as effort needs to be put into fixing the issue and salvage the mission. Highly unlikely as this will be checked continuously during the design process through the application of contingency management.
13. End-of-life disposal
- (a) No more propellant remaining for disposal: Negligible as the effect of debris around Venus is not very important at this time. The spacecraft might also deorbit by itself over time depending on the orbit. If the mission is properly designed this is unlikely to happen.
  - (b) Faulty orbit for deorbiting: Negligible as the effect of debris around Venus is not very important at this time. This is highly unlikely to happen if the system is properly tested.
14. Cost
- (a) Going over budget: Catastrophic as the mission might be cancelled, if no corrective actions are possible or if it is considered too expensive. Highly likely to happen during the process, because a project like this one has never been done before and costs are already difficult to predict for more standard missions.

### 10.2.2. INITIAL RISK MAP

All the risks discussed in the previous section are located in the risk map in Table 10.4. Note that the width of the columns in the risk map does not represent the importance of that column.

Table 10.4: Initial risk map

	1	2	3	4	5
Catastrophic	1a,2a,3b,3c,5a,6a,6b,9c,12a	2b,5b,5c	10d	7a,14a	
Critical	2c,3a,4a,7c,8b,8c,11a	2d,10a,10b	7b		
Moderate	9a	1b,8a	3d,8d	4b	
Minor			9b		
Negligible	13b	13a		10c	

From the risk map it can be seen that the largest concentration of risks are located in the top half of the map, which means they can potentially threaten mission success. The two risks in red are critical and have top priority for the mitigation planning.

## 10.3. RISK MITIGATION

With the risks determined it is now possible to relocate the available resources in such a way that the most critical risks are mitigated. This has the effect that the system has an increased chance of successfully completing the mission. The steps taken to mitigate the most pressing risks are shown in Section 10.3.1. Based on these mitigating measures, the risks will reduce, and this is shown in the revised risk map. This risk map is shown in Section 10.3.2.

### 10.3.1. RISK MITIGATION PLAN

For the risk mitigation the first priority are the risks located in the red region (high risk region) of the risk map, as these form the biggest threat to completing the mission. After this, resources are assigned to mitigating the risks located in the yellow region (medium risk region) of the risk map. The green risks are left unchanged as mitigation on them is considered a waste of resources as they already have a low enough risk.

#### High risk events (Red)

- 7a) **Failure to deploy aircraft** The probability can be reduced by extensively testing deployment of the aircraft during a fall on Earth. The new probability will become highly unlikely.
- 14a) **Going over budget** By applying appropriate contingency management the probability of going over budget will decrease. Also, current estimates for the budget indicate that there is a significant margin available for unforeseen costs. Because of this, it is highly unlikely that this happens.

#### Medium risk events (Yellow)

- 2b) **Sudden death of propulsion system** Adding redundancy to the system allows it to perform its mission even if some parts fail. In turn, this causes the probability of system failure to become highly unlikely.
- 2d) **Damaged propellers on the aircraft** The impact of a damaged propeller can be reduced by adding more propellers to the aircraft, so that a single propeller failure still allows for the mission to be performed. Therefore the impact is moderate, while the probability is still unlikely.
- 3d) **Solar panels damaged by the acid on Venus** By performing additional testing under Venusian conditions, the probability of this risk is reduced to unlikely.
- 4b) **Damage due to Venus' atmosphere** By testing the system in Venusian conditions the probability of structural damage is reduced to unlikely.
- 5b) **Loss of communication between spacecraft and aircraft** Through extensive verification and validation the probability of failure can be reduced to highly unlikely.
- 5c) **Loss of communication between lander and spacecraft** Through extensive verification and validation the probability of failure can be reduced to highly unlikely.
- 7b) **Wrong landing location** If the lander is launched from the aircraft the accuracy will become better since no entry effects need to be taken into account and the winds will already be better known due to the data gathered by the aircraft. By doing this the probability will be reduced to highly unlikely.
- 8d) **Aircraft control surface failure** By applying thorough verification and validation of the system the probability decreases to unlikely.
- 10a) **Faulty thermostat measurement** The risk of a faulty thermostat can be reduced by adding additional thermostats, thus by using the principle of redundancy.
- 10b) **Faulty heaters/coolers** By adding redundancy, even if some heaters/coolers fail, the other heaters/-coolers will be able to take over the function, reducing probability of thermal system failure.
- 10d) **Overheating in Venusian environment** Using new technology in insulation and heatproof instruments the lander and aircraft can survive longer, thereby extending their lifetime. This will give them enough time to fulfil their mission, reducing the impact of the risk to moderate. Further testing, and verification and validation can decrease the probability to unlikely.

### 10.3.2. FINAL RISK MAP

With all the different risk mitigation measures described previously part of the failure risks have been mitigated. Table 10.5 shows the final risk map. All mitigated risks are indicated between brackets, while those that were not mitigated are not between brackets.

Table 10.5: Revised risk map

	1	2	3	4	5
Catastrophic	1a,2a,3b,3c,5a,6a,6b,9c,12a (2b,5b,5c,7a,14a)				
Critical	2c,3a,4a,7c,8b,8c,11a (7b,10a,10b)				
Moderate	9a	1b,8a(2d,3d,4b,8d,10d)			
Minor			9b		
Negligible	13b	13a		10c	

It can be seen that the mitigation plan has significantly mitigated the total risk of the mission. No failures are in the red and yellow zones, which means that the probability of mission success increased.

# 11

## RAMS

This chapter elaborates on the Reliability, Availability, Maintainability, and Safety (RAMS) analysis. This analysis will be mostly focused on the reliability, while the availability, maintainability, and safety will be discussed very briefly. It should be noted that there is not a lot of statistical data available from comparable missions, as space missions are often mission specific and diverse.

### 11.1. RELIABILITY

Reliability is the probability that a system will perform in a satisfactory manner for a given period of time when used under specified operating conditions. Since nothing of the hardware can be repaired or replaced after launch, a high reliability is required to maximise mission success. In this case, reliability means without failure that impairs the mission, and not that any kind of failure is not allowed. Therefore, reliability can be increased by applying redundancy.

If budget allows, redundancy is applied to every subsystem, but since this increases the cost, a trade-off between the two has to be made. Applying redundancy is more important for components that are crucial for mission success or have a low reliability. During the design, this was constantly taken into account, and multiple forms of redundancy were applied [12], as mentioned below.

#### 11.1.1. REDUNDANCY STRATEGIES

Replication consists of installing two or more of the same components with switches allowing to make one of them active if needed. This type of redundancy minimises the chance of random failures, but not failures due to design deficiencies. This is applied to parts such as the aircraft propellers and lander cameras.

Diverse design redundancy means that different designs are used that do the same. The structural components of the lander are an example, since there are both the ring for structural integrity and the internal struts. This type of redundancy offers high protection against failures due to design deficiencies.

Functional redundancy is applied to the attitude determination of the spacecraft, amongst others. The spacecraft uses star trackers, initial measurement units, fine sun sensors, and coarse sun sensors. All of these measure different things to determine the attitude. This type of redundancy also reduces failures due to design deficiencies.

The aircraft will constantly try to communicate with the spacecraft, when an attempt fails, it will try again. This is an example of temporal redundancy, a repetition of an unsuccessful operation. Temporal redundancy is a low cost technique when applied to communication.

#### 11.1.2. EXPECTED RELIABILITY

From historical data, the expected reliability of different components can be determined. Table 11.1 shows an overview of the failure rates of different components. These values were used to determine the necessity of redundancy of several components.

### 11.2. AVAILABILITY

Material wise, there will be no problem obtaining the needed material to produce all designs. The availability of commonly used radioactive materials, such as plutonium-238, is limited, but the use of such materials was avoided. Some technologies are not currently ready to use yet, but are expected to be so well before the launch date of 2023. These include the batteries and solar cells used on the aircraft.

During the further design, new technology currently not available should also be taken into account. If certain new products become available in the future that are beneficial for the mission, they should be considered for implementation.

Table 11.1: Frequency of spacecraft failures between 1990 and 2008 [12]

Subsystem	30 days	1 year	5 years	10 years
Attitude control	8%	12%	11%	18%
Thruster/fuel	13%	20%	16%	13%
Control processor	0%	0%	4%	5%
Mechanisms/structures/thermal	8%	10%	11%	7%
Payload instruments	0%	2%	3%	4%
Battery/cell	6%	2%	10%	6%
Electrical distribution	12%	8%	10%	11%
Solar array	25%	17%	12%	12%
TT&C	22%	23%	18%	19%
Unknown	8%	6%	5%	5%

### 11.3. MAINTAINABILITY

From the launch onwards, it will not be possible to maintain the spacecraft or its components physically. The only maintenance that can be performed on the spacecraft are software updates. All components will have to be designed in such a way that they can safely be updated, including the option for autonomous reversal to a previous version if the update introduces unexpected errors.

The necessity of maintenance of the parts that will be designed first should be avoided as much as possible by storing them with caution. It should however be taken into account that they might require maintenance before or after assembly, to solve unforeseen issues.

### 11.4. SAFETY

As this will be an unmanned mission, no humans are exposed to hazardous situations after launch. There are, however, some hazards present during production, as discussed in Chapter 13. The risks that the equipment and vehicles encounter were discussed in Chapter 10. The fact that no radioactive material is used contributes a lot to the safety of all personnel involved.

When the time of manned missions to Venus arrives, lots of extra safety precautions should be taken. The mission should ensure for example the survivability on Venus and human friendly launch, transfer, and entry. Another safety attribute would be the launch safety, but this is the responsibility of the launch vehicle provider.

# 12

## VERIFICATION AND VALIDATION

In the detailed design phase a large number of programs have been used to end up with the best possible final design. To check that the programs are accurate enough to be used in the design process they have to be verified and validated. First, Section 12.1 describes the general procedures that have to be applied on all of the programs. After this, Section 12.2 briefly discusses the procedures applied to the different programs. With the different programs checked, systems can be built and then verified as is explained in Section 12.3. Finally, Section 12.4 gives a global description of some system validation that is expected to take place after system verification is completed.

### 12.1. GENERAL PROGRAM PROCEDURES

In this section a number of general steps are described that have been performed for each of the programs used in the design process. These involve the checking for coding errors, as explained in Section 12.1.1, the application of unit tests to the programs as discussed in Section 12.1.2 and the application of the complete program tests in Section 12.1.3. After this, Section 12.1.4 briefly describes the general program validation procedure.

#### 12.1.1. CODING ERRORS

In the detailed design phase a large number of programs have been created to help automate and thereby streamline the process. It is expected that during the coding, errors will be made. It is assumed that these errors will be small, like using the wrong type of brackets or integer division. By simply running the codes, most of the bugs will show in the programming environment, allowing for them to be fixed. Despite the ease of finding programming errors, it is still necessary to properly check the programs to see whether they are running properly, as some mistakes will not be detected by the programming environment. Once the coding errors have all been removed from the different modules, they can be verified for other kinds of mistakes.

#### 12.1.2. UNIT TESTS

Before the complete program can be verified, it will be necessary to verify the individual modules of which it is built. In order to test the individual modules, so-called unit tests are applied. During a unit test the module being tested will receive a number of inputs for which the outputs are known. A simple example is that if a 1 N bending force is applied at free the end of a 50 m cantilever beam, the bending moment near the root will be 50 Nm. If the result provided by the module is not close to the expected result, this indicates the presence of a discrepancy, and means that the module is not correct. The origin of the discrepancy then has to be located and fixed. All discrepancies should preferably be solved so that the results of the module can be considered accurate. In case there is a discrepancy that cannot be solved, it has to be decided whether it is acceptable to still use the module. If so, some type of precaution should be applied in the program to account for the discrepancy.

#### 12.1.3. COMPLETE PROGRAM VERIFICATION

With the unit tests completed, and all modules verified, they are combined in a single program. Once compiled, the first step is to check that the inputs and outputs of the different modules match. If for example one module provides a value in meters, while another module requires that value to be provided in kilometres, this will cause incorrect results. To prevent or at least minimise the risk of this happening, a general programming approach was decided upon. This included the decision that all programs use SI units as inputs, and that proper documentation should be present in the codes.

Once it has been checked that all of the modules work together properly, the complete system can be tested. For relatively simple programs it is possible to verify the system by comparing it to an analytical solution. Such analytical solutions can potentially also be found on the internet, although the quality can be questionable. However, it is expected that most of the programs will be too complex, with many equations,

relations between modules, iterative loops, etc. This makes it very hard, if not impossible to verify the program with an analytical solution. A method to overcome this issue is to apply simplifications to make the analytical solution less complex. In that case, care should be taken when comparing the results, because the simplifications can lead to significant differences in the results, and make it seem as if the program is wrong, when in reality it is not.

Instead, for such situations, it is possible to look for other programs created by other companies that have already been verified, to verify the group's program. Should this also not be possible, because no similar code exists or because it is paid software, then another option is literature. It can be that literature offers plots of similar programs used in different situations. Then, the general shape and magnitude of the results can be found and compared to the program results. Although this does not prove that the program is accurate, it does show that the program has similar behaviour and generates results in a correct range.

#### 12.1.4. COMPLETE PROGRAM VALIDATION

With verification completed, it has been checked that the program is calculating the proper parameters which is done by validation. During validation proof is provided that the program matches with the results obtained from real life experiments [74]. As validation requires experiments, for which no resources are available, the experiments will be briefly discussed in Section 12.2 along with the verification.

## 12.2. PROGRAM VERIFICATION AND VALIDATION

In this section, the verification and validation methods that were applied to specific programs are discussed. Since the aircraft, lander and spacecraft have a large number of very similar subsystems, those will only be described once. Such systems include the thermal control system, structure, power system, communications system and CDHS.

The individual unit-tests to be performed will not be discussed as these are all based on the same principle described earlier. Furthermore, it is assumed that the individual modules have been verified.

#### 12.2.1. STABILITY AND CONTROL

The stability and controllability program was verified by comparing its shape to that found in [47, 48]. The second part of the program to validate was the eigenmotion analysis. For the aircraft, a large number of parameters need to be known to place in a matrix. This matrix can be solved relatively easily by the program, but is nearly impossible to solve by hand. A reference that was readily available is the Cessna Citation of the TU Delft that was used during the flight test of SVV. Using the same inputs and comparing the results, the eigenmotion was verified. A last part of the verification was the sizing of the aileron, elevator and rudder. These were verified by comparing the results to those from [49] by using the same inputs.

To validate the program, it will be necessary to perform flight or wind tunnel tests with a model of the Venusian aircraft. However, as the Venusian atmosphere is much different from that on Earth, it is expected to be difficult to perform the experiments under the same conditions as in the lower altitudes of Venus.

#### 12.2.2. POWER SYSTEM

The equations used in the power system program were not complex, so analytical solutions were used to verify them. For further validation of the spacecraft power program, the solar panel and battery size were looked up for Venus Express [75]. From this comparison, the results were deemed to be accurate, and as such the program was verified.

The validation of the spacecraft program is not expected to pose any issues, as there is much experience with these systems and relatively simple test rigs can be used to perform experiments. The validation of the aircraft power program is expected to be more difficult as the aircraft will be operating in the Venusian atmosphere and partially inside or below the clouds. The solar cell program is currently based on the data from an article by NASA from 2013 [25]. An experiment similar to this should be performed, but this time the solar power on the bottom cells should preferably also be measured. Also, potential improvements in solar cell efficiency from 2013 to 2026 should be taken into account in the results.

#### 12.2.3. AERODYNAMICS

The aerodynamic program was used to determine a large number of design characteristics. These include, but are not limited to the airfoil, lift and drag coefficients, the wing span, mean aerodynamic chord and area of the different wing surfaces. For several parts it was not possible to verify the program as insufficient resources were available, but parts like the lift and drag coefficients were verified by making use of other open source

programs such as JavaFoil<sup>66</sup> and Xfoil<sup>67</sup>. An example of this is that if the program shows that the best airfoil, is the NACA0012, with a lift coefficient of 1.5 at 4° angle of attack, that JavaFoil will return a similar value, with the same atmospheric inputs. As long as the aerodynamic program remained in the inviscid region, the accuracy of the results was considered adequate. Once viscous flow is implemented, the results are expected to become less accurate, as this is difficult to implement properly. Due to lack of resources no viscous flow was implemented in the program. For the mean aerodynamic chord and other general wing dimensions, some analytical formula's are available from literature to verify those parts of the program.

To validate the program, some wind tunnel experiments should be performed in which the different aerodynamic characteristics can be determined for a wide range of flight situations. As the flight environment of Venus is very hard to reproduce care should be taken to get as close to it as possible by matching the non-dimensional parameters like the Reynolds number.

#### 12.2.4. ADCS

For the ADCS program the sizing of the different components of the ADCS used to store and dump momentum, allowing the satellite to remain stable enough to do measurements, had to be verified. For initial verification, analytical solutions were used to get an estimate of the different specifications of the ADCS. These were then compared to past planetary missions which showed that the results were accurate and that they could be used for the sizing of the ADCS.

Validation of the ADCS will be done by applying the program to design the ADCS of a already existing spacecraft if the values are close to the actual values of the spacecraft then the program is validated.

#### 12.2.5. ENTRY SYSTEM

For the entry system, the key method for verifying the program were the results of another simulation. This simulation was made of the entry of the Venera 4<sup>68</sup> and 8<sup>69</sup>. Also, [62] was used to check that the lift and drag coefficients used in the program were correct.

For the validation of the entry system data from other spacecraft (re-)entering the Earth or Venusian atmosphere will be used. By entering the same initial conditions into the program it can be checked that the resulting trajectory is similar to that experienced in real life.

#### 12.2.6. GRAVITY PROGRAM

The gravity program will be verified by making use of data available from online sources. The program will be used to generate an image of the gravity field around Venus. This image is then compared to gravity maps generated in [76] to see if there are any discrepancies.

To validate the program, it is used to predict the orbit of a satellite and then compared to the actual orbit of that satellite. If the program provides accurate results that match the motion of the satellite, it is considered validated.

#### 12.2.7. THERMAL PROGRAM

The thermal program was verified by making use of an analytical solution and showed that the program was accurate. As there were differences between the aircraft, lander and spacecraft thermal programs, they were verified individually. Furthermore, for the lander it was possible to check whether the results were in a similar range as those in [14]. Similarly, for the spacecraft program, data from past missions was used to check that the amount of layers in the MLI was reasonable.

To validate these programs, a number of experiments have to be performed on programs or data from past experiments or missions can be used. By giving the same dimensions and thermal characteristics as inputs to the programs, the results can be compared to check that the programs are valid.

#### 12.2.8. AIRCRAFT PROPULSION PROGRAM

The aircraft propulsion program was verified by comparing the results it generated to those that the open source programme JavaProp<sup>70</sup> generated.

For validating the aircraft propulsion program, experiments with a propeller could be performed to check that the outcomes match for similar inputs. Alternatively, to save resources measurements from past experi-

<sup>66</sup><http://www.mh-aerotools.de/airfoils/javafoil.htm>

<sup>67</sup><http://web.mit.edu/drela/Public/web/xfoil/>

<sup>68</sup><http://www.braeunig.us/misc/Venera4sim.pdf>

<sup>69</sup><http://www.braeunig.us/misc/Venera8sim.pdf>

<sup>70</sup><http://www.mh-aerotools.de/airfoils/javaprop.htm>

ments could be used to validate the program in a similar manner.

#### 12.2.9. STRUCTURE PROGRAM

For the verification of the structural program a number of methods were applied. The first was to create a number of force, shear flow and moment diagrams for several simple load cases. Statics and structural analysis methods were then used to create the same diagrams, or at least determine the load values at a number of points large enough to see a trend. A comparison will then indicate whether the program is accurate. The second method that was applied was to use the finite element analysis software Nastran In-CAD<sup>71</sup>. The results from the two programs were then compared to further verify the program.

To validate the structure program, a number of material tests should be performed or data from past experiments can be used. Comparison of the data can help locate discrepancies and in the end validate the program.

#### 12.2.10. COMMUNICATIONS PROGRAM

The communications system was designed using a program capable of determining the signal to noise ratio that is produced by a certain combination of factors such as the diameter of receiver and transmitter, frequency used and the transmitter power. As long as the signal to noise ratio is too low, the system can not function. Therefore, verification was important. The equations used in the program are not too complex, and could be calculated by analytically. Therefore, to verify the outcomes multiple cases were compared to see that the same inputs result in the same outputs.

To validate the program characteristics from past mission communications systems can be used to check that the results are accurate.

#### 12.2.11. CDHS PROGRAM

The CDHS program is based on a number of simple equations. The verification was therefore done by comparing numerical and analytical results. Another option that can be applied in the verification procedure was to look into past missions to see what the typical regions were for the outputs of the program. For the spacecraft, these references were other satellites, while for the aircraft and lander, the best reference was Curiosity. However, since the launch of Curiosity computer systems have developed further, which meant that large difference in characteristics were found.

For validation of the program, an experiment can be performed in which a processor and data storage system are connected to a system that provides it with inputs and receives the outputs of the processor. This way, it can be checked that for a range of data flow rates, the system will function properly.

### 12.3. SYSTEM VERIFICATION

The main goal of system verification is to proof that the different systems meet the requirements. As much experience is already available for the spacecraft systems, while the lander and especially the aircraft are more or less unique, the verification of those systems is considered to be more important and more resources should be directed towards their verification. Several examples of verifications will be given in the following subsections.

#### 12.3.1. VOLUME

The volume for the systems are largely based on the requirement that the entire system has to fit inside the launcher fairing. During the early stages of the detailed design it was found that volume is one of the most stringent parameters of the entire design. For verification, a form of inspection is used with Computer Animated Drawings (CADs). These can give an accurate representation of the volume that the different components will occupy, and it can thereby be verified that they do not exceed these limits. Another option is to construct the systems and then measure their volume to take factors into account that were not envisioned in the CADs.

#### 12.3.2. STRUCTURE

The structure of the different vehicles each have a number of requirements in common. Each of them will need to withstand the launch loads and launch vibrations, but also other loads. To verify that the systems can survive those situations, a few tests should be performed:

<sup>71</sup><http://www.autodesk.com/products/nastran-in-cad/overview>

- Loading test: All of the different systems can be placed in a test rig that will apply the expected maximum loads or for example the launch load cycles on those parts. That way it can be checked that they will not only be able to take on the loads, but also still be functioning after the loads are no longer applied.
- Shaker test: The different systems will be placed on a platform that will introduce vibrations similar to those expected in the mission envelope of that particular system. For the subsystems of the aircraft it will for example be necessary to not only apply the launch vibrations, but also those generated during Venusian entry.
- Landing test: The legs of the landers will need to be able to take on the loads caused by the impact with the Venusian surface. To check that this is accomplished, the landers can be dropped from an altitude that will result in them landing at the speed calculated by programs. Alternatively, the lander can be attached to a moving system that can speed it up before impacting with the surface, similar to a car crash test.
- Flight test: During the flight test the aircraft will go through a number of flight cycles in the Earth atmosphere. This will allow for looking into the bending of the wing caused by the lift generation and turbulence. As this was the reason for the crash of NASA's Helios aircraft, this should certainly be tested [77].

### 12.3.3. AIRCRAFT DEPLOYMENT AND OPERATIONS

The deployment of the aircraft is a very important stage in the mission. If the aircraft does not deploy properly it will not be able to perform its mission, and both aircraft and the lander it contains will be lost. As a result completing the primary objectives of the mission is expected to be impossible. To test this aircraft deployment there are two main options available. The first is to have a model of the aircraft dropped from an aircraft or balloon at a relatively low altitude. This is necessary because the atmospheric parameters are then in a similar range as those expected to be present in the atmospheric region of Venus in which the aircraft is deployed.

The second option is to have a scale model tested in a wind tunnel. As the conditions in the wind tunnel can be controlled more effectively, it will be possible to analyse a wide range of situations to reduce the risk of deployment failure. As the temperature at which the aircraft unfolds are similar to sea-level temperature on Earth not many adjustments have to be made to the tunnel. However, in each case, care should be taken to account for the different chemical composition of the atmospheres.

Once deployed, it should be checked that the aircraft can offer the desired handling characteristics and is properly stabilised. Here, the same two options are again available for the verification. However, testing the aircraft over the entire range of atmospheric conditions that are expected on Venus will be very difficult as it requires both high temperatures and high densities. A possible wind tunnel is the 8- by 6-Foot Supersonic Wind Tunnel of NASA's Glenn research center, as it can go to temperatures of 126° Celsius while still providing the option of measuring at subsonic flight regimes<sup>72</sup>. No other wind tunnels in [78] were found to have similar performance, as they either had too high Mach numbers or lower operating temperatures. Furthermore, the wind tunnel allows for testing the aircraft propulsion. Still, its upper temperature limit does not allow for the entire flight regime of the aircraft, but it is the best tunnel for which data is currently (June 2016) available. To compensate for this, corrections should be applied to the results, and it should be checked that the tests take place at similar Reynolds numbers as those anticipated on Venus.

### 12.3.4. AIRCRAFT CONTROL

The aircraft control system should be thoroughly verified, because if it does not operate properly, mission success will be at risk. Furthermore, as no aircraft has ever flown on another planet before, it is considered of prime importance to verify it. In order to do so, a model of the aircraft should be created and tested over a wide range of situations. Initially, the model should simply be allowed to make a number of climb and descend cycles in calm conditions without any significant turbulence. This will allow for removing a large number of potential bugs from the control algorithm. After this, the number of cycles should be increased. Once the aircraft has passed this part, it should be tested in much more turbulent conditions, in which it is expected that the control system will have much more difficulties maintaining its programmed flight path. To account for temperature changes these tests should preferably be performed in cold and warm regions. The functioning of the control surfaces can be tested a bit further in wind tunnels.

<sup>72</sup><http://facilities.grc.nasa.gov/documents/TOPS/Top8x6.pdf>

However, the higher densities and high temperatures on Venus can not be encountered during these tests, and can not be properly tested for by other means than simulations. Therefore, the entire control system can only be fully verified once the aircraft is flying on Venus.

### 12.3.5. AIRCRAFT POWER SYSTEM

As during the early stages of the detailed design it was found that the power system of the aircraft is stringent in the wing sizing, it should be thoroughly verified. The solar cells should be placed in test rig similar to that mentioned earlier in Section 12.2.2 and then be tested continuously for the expected aircraft mission lifetime. This way, it is possible to look into the degradation of the panels in Venusian conditions with temperature, pressure, and density cycles matching those of the aircraft. However, as the aircraft is expected to operate for at least a few months, another option is to apply more simulations for the verification.

The other key component of the aircraft power system are the rechargeable batteries. As the batteries are of a new type, their performance should be properly verified<sup>73</sup>. The batteries will be charged and discharged while exposed to the same temperature cycles that are expected in the insulated part of the aircraft. This way it can be checked that their performance adheres the specification provided by the producer, and guarantees that they will perform their functions on Venus.

### 12.3.6. OTHER SYSTEMS

For many other systems similar test will be applied to verify them. Apart from applying a test, verification can also be performed by [79]:

- **Analysis:** Method of theoretical or empirical verification by evaluating properties using commonly accepted techniques. These analysis techniques are systematic, statistical and qualitative methods of analysis as well as simulation tests or verification by similarity of space systems [80].
- **Inspection:** Inspect the design documentation or the product to show compliance with the requirement.
- **Review of Design:** Method characterised by using validation data, design documents, technical specifications and other plans for verification. This documentation must show that the design complies with the requirements [80].

Decisions on what method to apply will vary per system and potentially per requirement, and should be properly selected in further design stages.

## 12.4. SYSTEM VALIDATION

Once the systems have been verified, the last step is to apply validation. Validation will take place during or after the integration of all systems into one or more assemblies. In this design, they will be the lander, aircraft, aeroshell and spacecraft, but in later stages the lander will be integrated in the aircraft, the aircraft in the aeroshell, etc. During the validation, it is checked that the stakeholder intentions were met<sup>74</sup>. Several of these tests are listed next:

- **Launch vehicle adapter matching:** It can be checked that the full vehicle can be connected properly to the launch vehicle adapter of the launcher.
- **Volume measurements:** With all systems integrated, the volumes of entire vehicle can be tested in the fairing of the launcher to be used for the mission. Should this show that the vehicle does not fit in the launcher, changes should be made, although it is expected to be very unlikely to happen.
- **Weighing:** It will now be possible to exactly measure the weight of the different assemblies as well as the total weight, including the launch vehicle adapter. Thereby it is possible to validate that the vehicle can indeed be launched with the selected launcher.
- **Launch loads:** It should again be checked that the full vehicle can withstand the launch loads and vibrations. In order to do so similar tests to the structure verification can be applied except on a larger scale this time.

Other validation methods will be selected later on in the design.

<sup>73</sup><http://www.oxisenergy.com/technology/product/>

<sup>74</sup>[http://ocw.mit.edu/courses/aeronautics-and-astronautics/16-842-fundamentals-of-systems-engineering-fall-2009/lecture-notes/MIT16\\_842F09\\_lec09.pdf](http://ocw.mit.edu/courses/aeronautics-and-astronautics/16-842-fundamentals-of-systems-engineering-fall-2009/lecture-notes/MIT16_842F09_lec09.pdf)

## SUSTAINABLE DEVELOPMENT STRATEGY

The Brundtland Commission (formerly known as the World Commission on Environment and Development) defines sustainable development as “development that meets the needs and aspirations of the present without compromising the ability of future generations to meet their own needs” [81]. In this chapter, the sustainable development strategy applied in this project will be discussed.

Throughout the design process, a sustainable mindset will be applied. The sustainability practises following from this mindset can be split into those that will reduce the mission impact on Earth and those that reduce the mission impact on Venus. The following green engineering practises for reducing the environmental impact on Earth have been adopted and will be used during the further steps leading up to launch:

- Whenever a material is selected in the design process, its impact on the environment during its extraction, manufacturing and decay shall be evaluated. Furthermore, hazardous materials shall be avoided to minimise risk of exposure for employees. The main examples of this are:
  - **PETI-330 resin** is solvent free, contains no volatiles, and is considered non-toxic. Furthermore, its curing stage does not require an autoclave [82], which is an expensive and energy-intensive process.
  - **Carbon Fibre** recycling is a relatively recent development which has been commercialised [83], where the reclaimed carbon fibres can retain most of their mechanical properties [84]. While this would be a sustainable practice on Earth, this mission’s aircraft will unfortunately not be reclaimable. On another note, dust created during machining can cause mechanical irritation or abrasion, and is a hazard to electrical equipment due to its conductivity <sup>75</sup>.
  - **Teflon** can release vapours during hot processing which may be hazardous when inhaled. Furthermore, perfluorooctanic acid (PFOA) can degrade under high temperatures and be released as gas, which is toxic for humans and animals [85]. Therefore, workplaces must be well ventilated, and employees must handle the product with the utmost care. Smoking tobacco contaminated with Teflon can induce polymer fume fever. However, no special environmental precautions are required [86].
  - **Aerogel** is physically considered to be non hazardous. However, it contains titanium dioxide, which is considered a category 2 carcinogen [87]. Precautions must therefore be taken to prevent inhalation of dust. Aerogels are not expected to produce hazardous decomposition products for the environment, however it is not water soluble. Therefore, it must be disposed of in an approved landfill [87].
  - **Titanium** does not present a health, fire or explosion risk in its usual solid form under normal conditions. However, a machining process may create dust which can be irritating to the eyes and respiratory system. Furthermore, a dust cloud can ignite between 330 - 590°C. While titanium itself is not listed as a known carcinogen, chronic overexposure to metals with which it is alloyed can cause pulmonary fibrosis or chronic bronchitis. Environmentally, it is an abundant metal which is chemically inert, and has little tendency to bio accumulate along a food chain. No particular ecological measures are required [88].
- Transport distances of materials and spacecraft parts shall be minimised to limit impacts on the environment.
- While selecting launchers, budget and reliability permitting, the most sustainable one will be selected.
- The different launcher stages (except for the kick stage which is slung to deep space) will re-enter the Earth atmosphere so as to not result in additional space debris around Earth.
- Fuel saving methods such as aerocapture and aerobraking are explored to reduce the amount of propellant required. This reduces the launch mass, and thus the fuel required for the launch.
- The use of radioactive materials for power generation has been avoided in the final mission designs.

<sup>75</sup><https://www.monash.edu/ohs/information-and-documents/workshop-safety/carbon-fibre-composites-ohs-information-sheet>

- The weight of different components has been kept as low as possible while still meeting all of the requirements. Lower weight results in lower fuel consumption, which reduces its impact on the environment.
- If cost, power, and mass budgets permit it, the amount of embedded scientific tools shall be maximised to make the most out of this mission.
- Use is made of existing ground stations on Earth such as the Deep Space Network, so that no new ground stations have to be constructed.
- The transfer trajectory to Venus shall be optimised to reduce the required  $\Delta V$  and reduce the amount of propellant needed. In turn, this reduces the launch mass, and the fuel required by the launcher.
- If possible, the spacecraft is launched along with a number of other spacecraft to optimise the use of the launcher. This can be done by looking into other missions having similar launch windows and targets.

For Venus, the measures taken are:

- The risk of forward contamination will be minimised even though Venus has a very hostile environment. Venus is considered to be a Category 2 target body by the Office of Planetary Protection<sup>76</sup>. This means that it is expected that there is only a remote chance that contamination carried on a spacecraft or aerial vehicle can jeopardise future exploration, and requires only simple documentation in the form of a planetary protection plan<sup>77</sup>.
- The spacecraft bus shall be used as a communications relay station to reduce the power required by the communications system in the aircraft and lander. This can help limit the size of the aircraft and lander, which can help reduce the footprint of the aircraft and lander on Venus.
- A clear end-of-life strategy will be researched, especially for the bus and power sources.
- Creation of space debris shall be minimised to limit the risks for future missions to Venus.
- The aircraft will make use of electric engines instead of other fuel types that would otherwise introduce combustion reaction products to the Venusian atmosphere.
- The kick stage will be slung into deep space and will therefore not result in Venusian space debris.

---

<sup>76</sup><https://planetaryprotection.arc.nasa.gov/solarsystem/bodies>

<sup>77</sup><https://planetaryprotection.arc.nasa.gov/about-categories/>

# 14

## PROJECT DEVELOPMENT

This chapter will detail the activities that should be completed after the end of the DSE project if the mission to Venus would be performed. In Section 14.1 the activities will be listed and explained. In Section 14.2 the timeline of the activities will be detailed. Finally, in Section 14.3 the costs of the different activities will be detailed.

### 14.1. ACTIVITIES

The activities can be split up into four major phases. These are the design, production, launch and operations phase, which will be discussed in Sections 14.1.1 to 14.1.4 respectively.

#### 14.1.1. DESIGN

The design phase includes all activities related to finishing the detailed design. These activities are:

1. Completing the Detail design.
2. Producing and testing samples at the coupon, element, detail and sub-component levels.
3. Producing and testing components.

Completing the design is the overarching activity, which includes designing everything that has not been treated in the DSE. This includes all the small parts, like fasteners, bolts and circuit-boards. The testing of all the different parts happens in parallel and will inform changes in the design during the process. The testing of the components is treated as a separate activity, as it would involve a lot more in-depth testing than the other components.

#### 14.1.2. PRODUCTION

The production phase includes all activities involving full-scale production of the design. Therefore it will also include the activities related to building and testing the prototypes. The production activities are listed below.

1. Producing and testing full-scale prototypes.
2. Improving final design based on prototype test results.
3. Producing the final design.

#### 14.1.3. LAUNCH

The launch phase includes the activities related to facilitating the launch of the spacecraft and obtaining the facilities needed for the operations phase.

1. Procure Launch vehicle.
2. Obtain DSN contract.
3. Launch.

#### 14.1.4. OPERATIONS

The Operations phase includes all activities related to operating the spacecraft after launch. These activities include:

1. Monitoring and correcting the course of the satellite on its way to Venus.
2. Performing the orbit insertion at Venus.
3. Monitoring the satellite as it performs the mapping phase.
4. Initiating the release of the aeroshell containing the aircraft.
5. Changing the spacecraft orbit for its communication phase.
6. Monitoring the aircraft health.
7. Determining the landing location for the lander.
8. Initiating lander deployment and monitoring it during operations.
9. Initiating end-of-life strategies for the different mission segments.
10. Processing and publishing mission data.

## 14.2. TIMELINE

Fig. 14.1 contains the information about the times every activity and phase is expected to take. Note the long period of inactive time in the launch phase. This is caused by the limited launch window each year. May 2023 is the earliest launch window after production is finished. This also means that there is a decent period in which schedule overruns will not have too large an effect on the overall schedule.

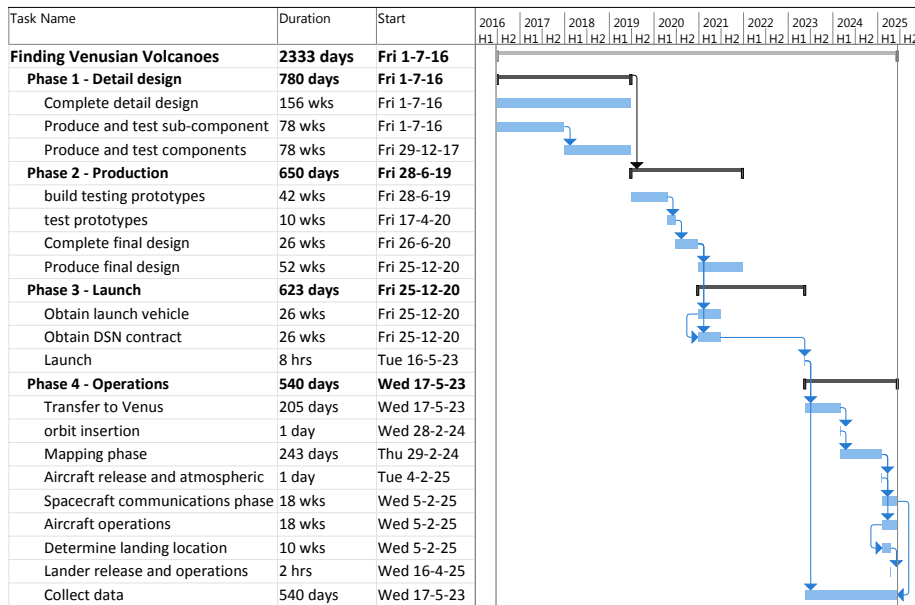


Figure 14.1: This chart shows the time the different project phases will take, as well as the interrelations between the different project activities.

## 14.3. COSTS

The costs for the different activities are detailed in their respective sections below. The costs for each of the phases are detailed separately. This section will go more in-depth on the facility and personnel costs. The costs of producing the actual vehicle will be discussed in Sections 14.3.1 to 14.3.4 respectively. Finally, Section 14.3.5 contains the cost-breakdown of the entire project.

### 14.3.1. DESIGN

For the design phase, a team of engineers is needed. The cost per engineer is detailed in Table 14.1. A total of 353 engineers will be on staff for the duration of the Design phase. The cost per engineer includes the cost of performing the tests on sub-component and lower levels of the design. The cost for testing on the component level of the design will be equal to 40% of the total cost. This relatively low percentage was chosen as producing component-level parts is less intensive when compared to a full-size product. No time and resources need to be spend on integration. In addition, not all components need to be tested as extensively as others.

Table 14.1: The cost per engineer per month. the workspace costs includes the costs of hiring a space and providing necessities like computers and software. The Workshop costs include all costs associated with small-scale experiments and tests the engineer needs to perform.

Engineer cost breakdown [€/month]	
Salary (gross)	5000
Workspace	1000
Workshop	2000
<b>Total</b>	<b>8000</b>

Table 14.2: Cost of the Lander and aircraft. The spacecraft is not included here, as it's cost has been calculated using SMAD and this includes the costs for developing and testing prototypes and components for testing.

Section	[Cost M€]
Landers (2 included in mission)	90
Aircraft	160
<b>Total</b>	<b>250</b>

From Section 14.2, we can see that the design phase takes 156 weeks, which is 3 years or 36 months. This means that the total cost for the engineers comes down to 101.664 million euros.

For the cost for component testing, first the total cost of the different parts of the missions needs to be known. The relevant values are given in Table 14.2. The mission will have two landers, so the total cost comes down to 250 million. This means that the cost for testing components totals up to 25 million.

### 14.3.2. PRODUCTION

For the production, the same overall cost for the engineers is assumed. Likewise, the same number of engineers is expected to be on staff. The cost for the production of the prototypes is taken at 70% of the total system cost. This relative low cost is the result of the fact that only the aircraft needs to be tested destructively, and that model would not require any of the costly instruments.

The production phase takes in total 130 weeks, or 30 months, as listed in Section 14.2. The total cost for the engineers totals up to 84.72 million. The cost for the prototypes is equal to 70% of the system production costs, which is 175 million.

### 14.3.3. LAUNCH

The costs of the Launch phase are determined by three factors, being the cost of the launcher and of the Deep Space Network (DSN) contract. These are tabulated in Table 14.3.

Table 14.3: The costs for the Launch and the DSN contract. The launch costs are based on the costs for the Ariane 64. If our mission is funded by ESA, that's the launcher we would have to use. Otherwise, the Atlas V launcher can be used, which is cheaper.

Section	[Cost M€]
Launch	130
DSN	30 [71]
<b>Total</b>	160

Table 14.4: The cost per ground control specialist per month. Their salary is equal to that of an engineer, while the costs associated with the workspace are less, as the biggest cost-driver is treated separately in the DSN contract.

Ground control cost breakdown [€/month]	
Salary (gross)	5000
Workspace	800
<b>Total</b>	5800

### 14.3.4. OPERATIONS

Operations costs consist of the cost of maintaining the communications equipment and the hiring of the specialists needed to handle the mission operations. The cost for the communication equipment is already part of the DSN contract, so that leaves the costs for the ground control specialists. This cost is broken down in Table 14.4. A total of 30 ground control specialists will be hired for the mission. This relatively low amount is chosen because the mission is automated to a large degree.

As can be read in Section 14.2 the mission time is 25 months. The total costs for the personnel then amounts to 4.35 million euros.

### 14.3.5. COST BREAKDOWN

This section contains the full project costs breakdown. The breakdown is displayed in Tables 14.5 and 14.6. Table 14.5 contains all the costs related to design and production. These are the costs for which a budget limit of one billion euros has been established. Table 14.6 details the costs for the launch and operations. These costs are treated separately as they are not part of the budget.

Table 14.5: Cost breakdown for the design and production phases constrained by budget of 1 billion euros.

Item	[Cost M€]
<b>Personnel design and production</b>	
Engineers design phase	101.664
Engineers production phase	84.72
<b>Production and testing</b>	
Component testing	100
Prototype testing	175
Aircraft production	160
Landers production	90
Spacecraft production and testing	288.5
<b>Design and production total</b>	999.884

Table 14.6: This table contains the cost for the launch and operations. These costs are not part of the 1 billion budget that has been established for this project.

Item	[Cost M€]
<b>Personnel launch and operations</b>	
Ground support	4.35
<b>Additional costs</b>	
DSN contract	30
Launch	130
<b>Design and production sub-total</b>	164.35

# 15

## COMPLIANCE MATRIX

With the detailed design phase completed, it is necessary to show that our mission complies with all of the top level requirements that were provided at the start of the project. These requirements are [1]:

1. The observations shall be able to unambiguously detect volcanic activity, if present.
2. Once an active volcano has been identified, the eruption products shall be analysed.
3. The spatial resolution of the eruption product measurements shall be high enough to identify sources and sinks of eruption products.
4. The launch date shall be no later than 2026.
5. Any exposure to hazardous materials shall be avoided for all personnel involved.
6. A clear end-of-life strategy shall be included in the mission design.
7. The used of radioactive materials shall be avoided, unless there are strong and compelling reasons to do so.
8. At any time it shall be demonstrated that the chosen solutions fulfil the mission requirements.
9. The mission cost shall not exceed €1.0 billion (FY2016), excluding launch and operations.
10. An itemised budget for launch and operations shall be provided.
11. A market analysis shall establish additional science goals and their impact on the nominal mission design.
12. The design shall be presented as a "begin-to-end" design, including launcher selection, interplanetary transfer, deployment, in-situ operations, data-transfer, and end-of-life strategy.
13. The launcher selection shall be based on existing launchers.

To give a brief description of the compliance of the design with each of the requirements, a compliance matrix is created as shown in Table 15.1. The table also refers to the locations where more detailed information on the compliance can be found. The ID in the table matches with the numbered list of requirements mentioned above. If a more detailed discussion on the specific requirement is present in the report, a reference is also provided.

Table 15.1: Compliance table

ID	Requirement met?	Reference
1	Yes. It is expected that the scientific instruments will be able to detect volcanic activity, in case that there is such activity.	Sections 4.1, 5.1 and 7.1
2	Yes. Once identified, the scientific equipment on the lander will be capable of measuring the eruption products. However, to do so it is necessary that the lander lands in the correct location.	Sections 4.1, 5.1 and 7.1
3	Yes. With the scientific equipment selected for the mission, it should be possible to provide sufficient spatial resolution in the measurements.	Sections 4.1, 5.1 and 7.1
4	Yes. The launch date will be May 16 2023.	Section 14.2
5	Yes. Attempts were made to avoid hazardous materials, but they will still be used in parts of the design. During further development of the design, it might be that better less hazardous materials are found that can replace other materials. However, the employees will be properly protected from the hazardous materials during production.	Section 5.5 and Chapter 13

6	Yes. For the different vehicles, end-of-life strategies have been devised. However, for the lander and aircraft these are simply based on staying and crashing on the surface, respectively. For the spacecraft, a decaying orbit can be initiated that will cause it to burn up in the Venusian atmosphere. Alternatively, if no actions are taken, the satellite will still burn up in the atmosphere eventually.	
7	Yes. No radioactive materials are used in the design.	Chapter 13
8	Yes. This compliance matrix is one such check and other checks were performed during the design process.	
9	Yes. As can be seen in the cost breakdown of the design, the costs are €999.884 million, excluding the launch and DSN costs.	Section 14.3.5
10	Yes. For the detailed design, launch and operations, an itemised budget was created.	Section 14.3.5
11	Yes. In the market analysis, additional science goals were identified. Also, several secondary objectives were defined that could be accomplished by the mission.	Section 2.1.2
12	Yes. In the report all these factors have been discussed.	
13	Yes. All launchers considered are expected to be in operation by the time of launch.	Section 3.7

It can be concluded from the compliance matrix that the design fully complies with all of the requirements set by the client.

# 16

## FOLLOW-UP RESEARCH

In this section, a list of possible improvements through further research is given.

- Improve the aerodynamic model of the aircraft by implementing any of the following:
  - Including fuselage effects in analysis: In the current aerodynamic analysis, the aircraft fuselage is not taken into account. As the fuselage affects the lifting performance of the wing close to it, these should be taken into account to improve the accuracy of the results.
  - Implement viscous flow: By adding viscous flow to the aerodynamic analysis of the aircraft, the results of the model will become more accurate. However, implementing this does add a significant amount of complexity.
  - Development of an airfoil specifically designed for mission: The current airfoil is created from a combination of pre-defined airfoils from the NACA 6-series. Although these airfoils have good performance, they were designed for aircraft on Earth rather than on Venus. The latter imposing differing airfoil design requirements due to the large wing planform area.
- Measure stability coefficients: During the design process, the stability coefficients of the aircraft were all determined by making use of approximate equations. Therefore, it is best to create a model of the aircraft to test for similar Reynolds numbers. With these tests, the actual values of the stability coefficients can be determined. The test and its results also allow for an accurate determination of the eigenmotions of the aircraft.
- Aircraft solar panel testing: The solar panels used in the design were tested under Venusian atmospheric conditions in [25]. However, in the case of the aircraft, solar panels are also implemented on the bottom of the aircraft, and do not face the Sun. Within the Venusian clouds, the light is scattered and also reaches these panels. In the design, the assumption was made that inside the lower cloud levels, the light would be nearly homogeneous. This assumption needs to be tested by either applying a test, or by making a simulation of the light scattering inside the clouds.
- Dynamic analysis of aircraft release: The phase during which the aircraft is released from the aeroshell on Venus and unfolds its wings is critical as the aircraft will otherwise crash on the Venusian surface before it can perform its mission. In this detailed design, the aircraft deployment process is only described, and not analysed. It is suggested that future research should be performed to simulate the entire deployment procedure of the aircraft by making use of a dynamic model. To complement this model, also tests in the Earth atmosphere can be performed with aircraft models that are dropped from an aircraft or parachute to see whether the unfolding procedure works.
- More detailed analysis under Venusian conditions: The propeller sizing method applied during the detailed design was a relatively simple method. In order to be more accurate, it is recommended that a more detailed analysis, either by simulation or by testing, of propeller blades under Venusian conditions is performed. As the propulsion system on the aircraft is the main power consumer, this detailed analysis could lead to a change in engine power and a change in the overall aircraft weight.
- Investigate the thermal situation including localised temperatures: In the thermal analysis of for example, the spacecraft, the different components on the inside such as propellant tanks and batteries were approximated as a single block with a single thermal capacity value. As a result, all inside components have the same temperature. In reality, the components will all have a different thermal capacity, and also interact with each other. This means that their temperature will vary throughout the spacecraft. An advanced thermal study can help clarify these differences and improve the spacecraft thermal model. The same can also be done for the lander and aircraft thermal models.

# 17

## CONCLUSION

Project Matryoshka aims to unambiguously detect volcanic activity and characterise the eruption products on Venus, such that the sources and sinks can be identified. To do so, it will make use of a spacecraft, an aircraft and two landers. The spacecraft will compare its topography data with the data gathered by Magellan to find active volcanoes. The aircraft with its superior manoeuvrability will be able to analyse and locate active volcanoes with a higher certainty, since it can dive below the clouds. In addition, it will be able to complete a series of secondary objectives. The lander will be able to analyse the ground and by using the other lander as reference draw definite conclusions on the eruption products characteristics.

The Visual Near-InfraRed camera and the Laser Induced Breakdown Spectroscope are needed for the lander to unambiguously determine volcanic activity. The layout of the lander is made out of two shells with insulation between. This delays the overheating problem for a hundred minutes once on the surface and resolves the pressure problem, which is enough to perform all necessary tasks with some room to spare.

The aircraft will carry a camera, Venus Emissivity Mapper and Spectropolarimeter for Planetary Exploration for the primary objective. The track generation takes into considerations the aerodynamic efficiency, propellers efficiency, thermal control, power production, battery sizing. Various tracks were generated for different atmospheric conditions. The horizontal tail, vertical stabilisers and control surfaces were sized such that the center of gravity shift induced by deploying the lander will not destabilise the aircraft for both static and dynamic scenarios. The horizontal tail is mounted on a telescopic boom that is folded inwards while inside the aeroshell.

The aeroshell is designed with a 45 degree angled conical heat shield with a spherical nose to enter the atmosphere at a shallow flightpath angle. After peak deceleration, the parachute is deployed to decelerate further. The heatshield is then ejected and once cleared, the reference lander and aircraft are deployed. The aircraft will then perform a rolling manoeuvre to turn right side up.

The spacecraft will use the Synthetic Aperture Radar, Venus Emissivity Mapper, a camera and a Doppler Wind Lidar. The spacecraft's life consists of two phases, the mapping and the relay phase. The mapping phase is performed in a highly elliptical orbit and takes 8 months. An inclination change will mark the start of the the relay stage where the spacecraft receives data form the landers and aircraft and transmits them to earth.

Next steps in the design process are to further optimise the propeller design and fit it for specific tracks. After that, all design algorithms should be into one optimisation program to determine the optimal aircraft design. The internal layout of all mission vehicles can be designed to a higher detail, which includes the deployment mechanisms. This allows for calculating the exact moment of inertia, which improves the accuracy of simulations.

Further improvements to the mission can be made through advanced simulation techniques to determine aerodynamic coefficients and stability derivatives. Once the layout is designed in detail, a finite element method approach can be used to calculate the thermal resistivity.

New breakthroughs into more advanced power generation and power storage will improve the aircraft qualities. The thermal constraints would be reduced if high temperature electronics will become available. The mission lifetime will also benefit from a coating that is more abrasion, high temperature and corrosion resistant.

# ACKNOWLEDGEMENTS

We would like to thank our tutor Dr. D.M. Stam for the enormous amount of help she provided during the project. She guided the group through the project and provided us with very useful constructive criticism.

We would also like to express our gratitude towards our coaches, Dr. S. Teixeira De Freitas and MSc. Z. Hong, for their assistance in the design process of the materials and structural elements of the design.

Furthermore, we would like to thank the following people for their time and support:

- Dr. A. Cervone
- Ir. B.T.C. Zandbergen
- Dr. Ir. M. Wagemaker
- E.J. van den Bos
- Dr. C. Kassapoglou
- Dr. C. Wilson
- Dr. L. Rossi
- Dr. Ir. E. Mooij
- Dr. S.J. Garcia Espallargas
- Dr. I. Fernandez Villegas
- Prof. Dr. T.J. Dingemans
- Dr. W.T. Fowler
- K. Siemonsma
- Aspen Aerogels®
- TU Delft
- OSSC
- OSSA

## BIBLIOGRAPHY

- [1] D.M. Stam. Project Guide Design Synthesis Exercise: Finding Venusian Volcanoes. Blackboard, April 2016.
- [2] R. Herrick and et al. Goals, Objectives, and Investigations for Venus Exploration. Technical report, VEXAG, May 2014.
- [3] K.H. Baines and et al. Exploring Venus with Balloons: Science Objectives and Mission Architectures for Small and Medium class Missions, April 2016.
- [4] F. Snik and et al. Spex: An in-orbit spectropolarimeter for planetary exploration. *Proceedings of SPIE*, 7010, 2008.
- [5] L.V. Zasova and et al. Structure of the venus atmosphere. *Planetary and Space Science*, 2007.
- [6] et al. Seiff, A. Models of the structure of the atmosphere of venus from the surface to 100 kilometers altitude. *Advances in Space Research*, 5(11):3–58, 1985.
- [7] G.M. Keating and et al. Models of venus neutral upper atmosphere: Structure and composition. *Advances in Space Research*, 5(11):117–171, 1985.
- [8] R.D. Lorenz. Surface winds on venus: Probability distribution from in-situ measurements. *Icarus*, 264:311–315, 2016.
- [9] E.V. Shalygin and et al. Active volcanism on Venus in the Ganiki Chasma rift zone. *AGU Publications*, 42(12):4762 – 4769, June 2015.
- [10] I. de Pater and J.J. Lissauer. *Planetary Sciences*. Cambridge Universitt Press, New York, fifth edition, 2007.
- [11] A.T. Basilevsky and J.W. Head. The surface of Venus. *Institute of Physics Publishing*, 66:1699–1734, September 2003.
- [12] J.R. Wertz and et al. *Space Mission engineering: The New SMAD*. Space Technology library, 2011.
- [13] M5 call-Technical Annex. Technical report, ESA, April 2016.
- [14] B. Bugby and et al. Novel Architecture for a Long Life, Lightweight Venus Lander. *AIP Conference Proceedings*, 1103:39–50, 2009.
- [15] A. Ashab, Y.C. Wong, G. LU, and D. Ruan. Indentation tests of aluminium honeycombs. *Journal of Physics*, 2013.
- [16] A. Ball and et al. *Planetary Landers and Entry Probes*. Cambridge Books Online, 2010.
- [17] I. Cowie. All About Batteries, 2014.
- [18] R.C. Wiens and et al. *The ChemCam Instrument Suite on the Mars Science Laboratory (MSL) Rover: Body Unit and Combined System Tests*. Space Science Reviews, 2012.
- [19] S. Maurice and et al. *The ChemCam Instrument Suite on the Mars Science Laboratory (MSL) Rover: Science Objectives and MastUnit Description*. Space Science Reviews, 2011.
- [20] J. Helbert, N. Müller, A. Maturilli, R. Nadalini, S. Smrekar, P. D’Incecco, and M. D’Amore. Observing the surface of Venus after VIRTIS on VEX: new concepts and laboratory work. In *Infrared Remote Sensing and Instrumentation XXI*, volume 8867 of *Proceedings of SPIE*, page 88670C, September 2013.
- [21] IMPERX. *IMPERX B6620 specification*, 2014.
- [22] A. Sánchez-Lavega and et al. Variable winds on venus mapped in three dimensions. *Geophysical research Letters*, 35, 2008.
- [23] M.G. Tomasko and et al. Measurements of the flux of sunlight in the atmosphere of venus. *Journal of Geophysical Research*, 85(A13):8167–8186, 1980.
- [24] R.L. Burder and J.D. Faires. *Numerical Analysis*, volume 9. Brooks/Cole Cengage Learning, 2011.
- [25] G.A. Landis and E. Haag. Analysis of solar cell efficiency for venus atmosphere and surface missions. In *International Energy Conversion Engineering Conference*, July 2013.
- [26] M. Wagemaker. Personal communications.

- [27] J.D. Jr. Anderson. *Fundamentals of Aerodynamics*, volume 5. McGraw-Hill Education, 2011.
- [28] K. Fujii and et al. Scaling Analysis of Propeller-Driven Aircraft for Mars Exploration. *Journal of aircraft*, March 2013.
- [29] K.P. Valavanis. *Advances in Unmanned Aerial Vehicles: State of the Art and the Road to Autonomy*. Springer, 2007.
- [30] Structures and ESA Mechanisms Division. *Structural Materials Handbook*, volume Volume 1 - Polymer Composites. European Space Agency, Noordwijk, The Netherlands, April 1995.
- [31] S. Ghose and et al. Processing and Characterization of PETI Composites Fabricated by High Temperature VARTM. Technical report, U.S. Government, 2011.
- [32] J.W. Connell and et al. High Temperature Transfer Molding Resins: Status of PETI-298 and PETI-330. Technical report, U.S. Government, 2003.
- [33] Upilex, UBE Industries Ltd. *Data Sheet: PETI-330*, h edition, 2008.
- [34] M.C.Y. Niu. *Composite Airframe Structures*. Practical Design Information and Data. Hong Kong Conmilit Press Ltd., 1992.
- [35] N.L. Hancox and R.M. Mayer. *Design Data for Reinforced Plastics - A Guide fpr Engineers and Designers*. Chapman & Hall, London, 1994.
- [36] Firehole Composites. Fatigue Life Prediction in Composite Materials. White paper series, Firehole Composites, 2010.
- [37] A. Yavrouian and et al. High Temperature Materials for Venus Balloon Envelopes. *AIAA*, 11th Lighter-than-Air Systems Technology Conference:68–76, 1995.
- [38] Chemours. *Teflon PTFE DISP 30*, 2015.
- [39] DuPont. *Teflon PTFE Properties Handbook*.
- [40] C.T. Russell and J.L. Phillips. The Ashen Light. *Adv. Space Res.*, 10(5):137–141, 1990.
- [41] S. Black. Lightning strike protection strategies for composite aircraft. *CompositesWorld*, 21(3), May 2013.
- [42] LORD. *LORD UltraConductive Film and Coatings for Lightning Strike Protection*, 2012.
- [43] P.T. Arévalo. Design Optimization of a Composite Wing Box for High-Altitude Long-Endurance Aircraft. Master's thesis, Embry-Riddle Aeronautical University - Daytona Beach, 2014.
- [44] T.H.G. Megson. *An Introduction to Aircraft Structural Analysis*. Butterworth-Heinemann, 4th edition, 2010.
- [45] M.D. Ardena and et al. Analytical Fuselage and Wing Weight Estimation of Transport Aircraft. Technical report, 1996.
- [46] T. Gleason and P. Fahlstrom. *Introduction to UAV Systems*. Aerospace Series. Wiley, fourth edition, 2012.
- [47] G. La Rocca. Systems engineering and aerospace design lecture 4. Blackboard, March 2016.
- [48] G. La Rocca. Systems engineering and aerospace design lecture 5. Blackboard, March 2016.
- [49] S.H. Mohammad. *Aircraft Design: A Systems Engineering Approach*. Aerospace Series. Wiley, first edition, 2012.
- [50] J.A. Mulder and et al. Flight Dynamics Lecture Lecture Notes. Blackboard, March 2013.
- [51] D.P. Raymer. *Aircraft Design: A Conceptual Approach*. American Institute of Aeronautics and Astronautics, 1992.
- [52] W. Jaworski and R.G. Nagler. A parametric analysis of venus entry heat-shield requirements. Technical report, National Aeronautics and Space Administration, 1970.
- [53] Avco corporation. Venus Flyby/Entry probe mission study. Technical report, 1968.
- [54] S.J. Duasai and et al. Planetary Systems-Venus Probe Study. Technical report, Martin Marietta Corporation, 1968.
- [55] E. Mooij. Re-entry Systems Lecture Notes. Blackboard, March 2013.
- [56] E. Mooij. Personal communication.
- [57] D.R. Chapman. An approximate analytical method for studying entry into planetary atmospheres. Technical report, National advisory committee for aeronautics, May 1958.

- [58] W.C. Pitts and R.M. Wakefield. Performance of Entry Heat Shields on Pioneer Venus Probes. *Journal of Geophysical Research*, 85(A13):8333–8337, 1980.
- [59] M.A. Covington and et al. Performance of a low density ablative heat shield material. *Journal of Spacecraft and Rockets*, 45(2), 2008.
- [60] A. Sengupta and L. Hall. Challenges of a Venus Entry Mission. Technical report, Jet Propulsion Laboratory, December 2010.
- [61] F.J. Regan and et al. *Dynamics of atmosphere re-entry*. AIAA, 1993.
- [62] F.J. Regan. *Re-Entry Vehicle Dynamics*. Education Series. AIAA, 1984.
- [63] W.J. Markiewicz and et al. VMC: The Venus Monitoring Camera. *ESA SP-1295*, 2007.
- [64] P.A. Fox, K.V. James, and A. Thompson. WiSAR: A New Solution for High-Performance, Smallsat-Base Synthetic Aperture Radar Missions. Technical report, 2008.
- [65] U.N. Singh, G.D. Emmit, S. Limaye, J. Levine, J. Yu, and M.J. Kavaya. Coherent Doppler Lidar for Wind Measurements on Venus. Technical report, NASA Langley research centre, 2013.
- [66] J.J. Wijker. *Spacecraft structures*. Springer, 2008.
- [67] G. Allan and et al. *Harris' Shock and Vibration Handbook*. McGraw-Hill, sixth edition, 2010.
- [68] C.D. Brown. *Elements of spacecraft design*. AIAA, 2000.
- [69] F. Valencia Bel and M. Lang. The Role of Different Parameters in the Pressurant Budget of Venus Express and its Dynamic Evolution during the Mission. In *4th International Spacecraft Propulsion Conference*, volume 555 of *ESA Special Publication*, page 115.1, October 2004.
- [70] ESA. *ESA's deep space tracking network*, 2015.
- [71] NASA. *Deep Space Network Services Catalog*, 2015.
- [72] B. Geldzahler. Future Plans for the Deep Space Network (DSN). 2009.
- [73] R. Curren. *Lecture 08 Risk Management & Reliability Engineering*. BlackBoard, 2016. Retrieved on 22 April, 2016.
- [74] E. Mooij and Z. Papp. Simulation, Verification and Validation Lecture Notes. Blackboard, February 2015.
- [75] P. Sivac and T. Schirmann. The venus express spacecraft system design. *ESA Special Publication*, SP1295, 2007.
- [76] Li, F. and Yan, J. and Xu, L. and Jin, S. and Rodriguez, J.A.P. and Dohm, J.H. A 10 km-resolution synthetic Venus gravity field model based on topography. *Icarus*, 247:103–111, February 2015.
- [77] T.E. Noll and et al. Investigation of the Helios Prototype Aircraft Mishap. Technical report, NASA, 2004.
- [78] M. Goodrich and J. Gorham. Wind Tunnels of the Western Hemisphere. Technical report, The Library of Congress, June 2008.
- [79] A. Cervone. *Lecture 07 Verification & Validation for Spacecraft Propulsion*. BlackBoard, 2016. Retrieved on 13 June, 2016.
- [80] C.H. Verlag and et al. *Handbook of Space Technology*. Wiley, first edition, 2009.
- [81] UN. Report of the World Commission on Environment and Development: Our Common Future, April 2016.
- [82] UBE Industries Ltd. *High Temperature Composite Materials: PETI-330*.
- [83] G. Gardiner. Recycled carbon fiber update: Closing the CFRP lifecycle loop. *Composites World*, December 2014.
- [84] K. Wood. Carbon fiber reclamation: Going commercial. *Composites World*, April 2010.
- [85] DuPont. *DuPont Teflon PTFE 613A fluoropolymer resin*, 2005.
- [86] DuPont. *Safety Data Sheet: PTFE Fine Powder*, 202 edition, 2015.
- [87] Aspen Aerogels. *Safety Data Sheet: Pyrogel XT*, July 2012.
- [88] Wyman-Gordon Company. *Material Safety Data Sheet: Titanium Alloys*, 2009.

# A

## SOURCE CODE

Throughout the design of the project, a lot of programming was used to determine and optimise the code. The programming language used is Python. This code is online available for the public at the GitHub repository <https://github.com/MaxHenger/dse14-finding-venusian-volcanoes>. At the moment of writing (28nd June 2016) all the python files together amount to 14550 lines of code excluding comments and empty lines.

# B

## WORK ALLOCATION

In this appendix an overview is provided to show who contributed to what part of the report. In this overview a difference is made between contributing by writing a part and contributing by providing the content to be written. The content part can include but is not limited to collecting data, calculating values etc. In Table B.1 contributing by content is represent by a black × symbol and contributing by writing is represented by a red × symbol. The amount of crosses does not portray the actual amount of work put in. For example: Max Henger (M.H.), Yuyang Luan (Y.L.) and Akhil Gunesse (A.G.) only worked on up to two sections according to the table. However, they went into minute detail such that even though working just as hard as everyone else, they did not have much time to work on much else.

Table B.1: Work allocation overview

Section	M.B.	A.B.	C.G.	A.G.	S.H.	M.H.	J.H.	T.K.	Y.L.	J.W.
Executive Summary	×, ×									
Introduction	×, ×									×, ×
General Mission Description	×, ×					×	×, ×			×, ×
Astrodynamics			×, ×	×, ×						
Lander	×, ×		×, ×		×, ×		×, ×	×, ×		
Aircraft	×, ×	×, ×	×, ×		×, ×	×, ×		×, ×	×, ×	×, ×
Entry		×, ×	×				×, ×			×, ×
Spacecraft	×, ×		×, ×		×, ×			×, ×		×, ×
Sensitivity			×, ×				×, ×			
Operations and Logistics					×		×	×, ×		
Risk analysis	×, ×		×, ×							
RAMS							×, ×			
Verification and Validation	×, ×								×	
Sustainable development strategy	×, ×	×, ×								
Project development								×, ×		
Compliance matrix	×, ×									
Follow up research	×, ×									
Conclusion										×, ×
Catia	×	×	×				×	×	×	×